Ion Beam Assisted Deposition of Biaxially Aligned Oxide Thin Films

by

Kevin Glenn Ressler

B.S. Ceramic Science and Engineering
Penn State University, 1992

Submitted to the Department of Materials Science and Engineering on August 9, 1996 in partial fulfillment of the requirements for the degree of Doctor of Philosophy in Electronic Materials.

Massachusetts Institute of Technology
September 1996

copyright 1996 Massachusetts Institute of Technology
All rights reserved

Signature of Author . . . .
Department of Materials Science and Engineering
August 9, 1996

Certified by . . . .
Professor Michael J. Cima
Norton Professor of Ceramics
Thesis Supervisor

Accepted by . . . .
Linn W. Hobbs
John F. Elliott Professor of Materials
Chairman, Departmental Committee on Graduate Students

ARCHIVES

MASSACHUSETTS INSTITUTE
OF TECHNOLOGY

SEP 27 1996

LIBRARIES

Ion Beam Assisted Deposition of Biaxially Aligned Oxide Thin Films

by

Kevin G. Ressler

Submitted to the Department of Materials Science and Engineering
on August 9, 1996 in partial fulfillment of the requirements for the
degree of Doctor of Philosophy in Electronic Materials.

Abstract

The mechanism of biaxial alignment in oxide thin films fabricated by ion beam assisted deposition (IBAD) was examined. Biaxially aligned yttria-stabilized zirconia (YSZ) films were fabricated by two IBAD techniques both without active substrate heating and at 600°C on several single crystal, polycrystalline, and amorphous substrates. Biaxially aligned $La_{1-x}Ca_xMnO_3$ (LCMO) films were deposited by dual ion beam deposition on various substrates.

IBAD biaxial alignment resulted from anisotropy in ion induced damage on various crystal surfaces. IBAD biaxial alignment occurs so that damage tolerant planes face the assisting ion beam. Damage accumulation causes the crystal growth direction to change. Biaxially aligned films were obtained at all ion bombardment angles investigated, including those which did not correspond to channeling directions in the film. The observed IBAD YSZ and IBAD LCMO biaxial alignment did not occur due to ion channeling.

Two growth modes were observed in IBAD films fabricated without active substrate heating and at 600°C. IBAD film growth without active substrate heating occurs through granular renucleation, while IBAD film growth at elevated substrate temperature occurs through growth rate competition. Substrate-independent biaxial alignment was observed for YSZ films fabricated by both IBAD techniques without active substrate heating. The biaxial alignment of IBAD YSZ and IBAD LCMO films deposited at 600°C was substrate dependent, with epitaxial films deposited on single crystal substrates and differing biaxial alignment observed on several polycrystalline and amorphous substrates. Anisotropy in ion damage tolerance determined the development of IBAD biaxial alignment for both growth modes.

Thesis Supervisor: Michael J. Cima
Title: Norton Professor of Ceramics

TABLE OF CONTENTS

		Page
	TITLE PAGE	1
	ABSTRACT	2
	TABLE OF CONTENTS	3
	LIST OF FIGURES	8
	LIST OF TABLES	16
	ACKNOWLEDGEMENTS	17
Chapter 1	INTRODUCTION	18
Chapter 2	BACKGROUND	23
	2.1 Thin Film Microstructural Development	23
	2.2 Thin Film Texture Development	26
	2.2.1 Pre-coalescence Texture Development	28
	2.2.2 Texture Development During Coalescence	32
	2.2.3 Post-coalescence Texture Evolution	32
	2.3 Ion Beam Assisted Deposition	36
	2.3.1 Proposed Mechanisms of IBAD Biaxial Alignment	36
	2.3.2 Ion Beam Assisted Deposition of YSZ	38
	2.4 Summary	39
Chapter 3	THIN FILM FABRICATION AND CHARACTERIZATION TECHNIQUES	43
	3.1 Substrates	43
	3.1.1 Substrate Preparation	43
	3.1.2 Substrate Heater Block Mounting	43
	3.2 Ion Beam Assisted Deposition	44
	3.2.1 Ion Assisted Electron Beam Evaporation System Description	44
	3.2.2 E-Beam Evaporation and Ion Assisted Electron Beam Evaporation Procedure	46
	3.2.3 Dual Ion Beam Deposition System Description	47
	3.2.4 Dual Ion Beam Deposition Procedure	49
	3.3 X-Ray Diffraction	49

3.3.1 Out-of-Plane Orientation 50
3.3.2 In-Plane Orientation 50
3.3.2.1 X-ray ϕ Scans 52
3.3.2.2 X-ray Pole Figure Measurements 52
3.3.3 Experimental Conditions 53
3.4 Film Microstructure 53
3.5 Determination of Ion Etch Rates and R Values 54

Chapter 4 ION ASSISTED ELECTRON BEAM EVAPORATION 58

4.1 Introduction 58
4.2 Experimental Procedure 58
4.2.1 Ion Assisted Electron Beam Evaporation of YSZ at 600°C 58
4.2.2 Ion Assisted Electron Beam Evaporation of YSZ with Varied Substrate Heating 59
4.2.3 Film Characterization 61
4.3 Results: Ion Assisted E-Beam Evaporation 61
4.3.1 Ion Assisted Electron Beam Evaporation of YSZ at 600°C 61
4.3.1.1 Effects of IBAD Parameters on YSZ Biaxial Alignment on Pyrex 61
4.3.1.2 Substrate Dependent Film Orientation 64
4.3.1.3 Development of (200) Biaxial Alignment on Pyrex: X-ray Examination 67
4.3.1.4 Model Experiments on Amorphous Substrates 70
4.3.1.5 Development of (200) Biaxial Alignment on Pyrex: Microstructural Examination 71
4.3.2 Ion Assisted E-Beam Evaporation of YSZ with Varied Substrate Heating 80
4.3.2.1 X-ray Investigation 80
4.3.2.2 Film Microstructure 84
4.4 Discussion: Ion Assisted E-Beam YSZ Biaxial Alignment 87
4.4.1 Growth Extinction Model for Ion Assisted E-beam Biaxial Alignment at 600°C 87
4.4.2 Biaxial Alignment of IBAD YSZ Films Evaporated with Varied Substrate Heating 91
4.5 Summary 92

Chapter 5 DUAL ION BEAM DEPOSITION OF YSZ 94

5.1 Introduction 94
5.2 Experimental Procedure 94
5.2.1 Dual Ion Beam Deposition of YSZ without Active Substrate Heating 94
5.2.2 Dual Ion Beam Deposition of YSZ at 600°C 96
5.2.3 Film Characterization 99
5.3 Results: Dual Ion Beam Deposition of YSZ 99
5.3.1 Dual Ion Beam Deposition of YSZ without Active Substrate Heating 99
5.3.1.1 Substrate-Independent Biaxial Alignment 99
5.3.1.2 Dependence of FWHM on R Value 101
5.3.1.3 X-ray Diffraction and Electron Microscopy Investigation of Biaxial Alignment Evolution 105
5.3.2 Dual Ion Beam Deposition of YSZ at 600°C 114
5.3.2.1 35° Bombardment Angle 114
5.3.2.2 45° Bombardment Angle 114
5.3.2.3 SEM Microstructure Characterization 122
5.4 Discussion: Dual Ion Beam Deposition of YSZ 122
5.4.1 Dual Ion Beam Deposition of YSZ without Active Substrate Heating 124
5.4.2 Dual Ion Beam Deposition of YSZ at 600°C 125
5.4.2.1 35° Bombardment Angle 125
5.4.2.2 45° Bombardment Angle 125
5.4.3 Film Microstructure and Comments on Dual Ion Beam Deposition Biaxial Alignment at 600°C 129
5.5 Summary 130

Chapter 6 DUAL ION BEAM DEPOSITION OF LCMO 131

6.1 Introduction 131
6.2 Experimental Procedure 132
6.2.1 Dual Ion Beam Deposition of LCMO 132
6.2.2 Film Characterization 132
6.3 Results and Discussion: Dual Ion Beam Deposition of LCMO 133
6.3.1 X-ray Diffraction 133
6.3.2 LCMO Film Microstructure 133
6.3.3 Electrical Resistance Measurements 137
6.4 Summary 137

Chapter 7 ROLE OF THE ASSISTING ION BEAM IN THE DEVELOPMENT OF IBAD BIAXIAL ALIGNMENT 139

7.1 Introduction 139
7.2 In-Plane Orientation of (200) Biaxially Aligned Films 140
7.3 Texturing Mechanism of the Assisting Ion Beam 148
7.3.1 ADESH and TRIM92 Software 148
7.3.1.1 YSZ Lattice Constant and Density 148
7.3.1.2 Potential Function for YSZ in ADESH 150
7.3.1.3 TRIM92 153
7.3.1.3.1 Binary Collision Approximation 153
7.3.1.3.2 TRIM92 Simulation Algorithm 154
7.3.1.3.3 TRIM Calculation of Ion Energy Loss and Ion Range 155
7.3.1.3.4 Determination of Bulk Binding Energy and Bulk Displacement Energy 161
7.3.2 Ar^+ Range in Zirconia and Channeling in Zirconia and LCMO 167
7.3.3 Etch Rate Anisotropy 179
7.3.4 Anisotropy in Damage 182
7.4 Summary 193

Chapter 8 MODEL EXPERIMENTS ON YSZ SINGLE CRYSTALS AND THE ROLE OF SUBSTRATE TEMPERATURE IN THE DEVELOPMENT OF IBAD BIAXIAL ALIGNMENT 194

8.1 Introduction 194
8.2 Experimental Procedure 194
8.3 Dual Ion Beam Deposition of YSZ Single Crystals 195
8.4 IBAD YSZ Biaxial Alignment on YSZ Single Crystals 202
8.5 Summary 205

Chapter 9 CONCLUSIONS AND FUTURE WORK 207
9.1 Conclusions 207
9.2 Future Work 209

Appendix A INTERATOMIC POTENTIAL CALCULATION 211

Appendix B BULK MODULUS DETERMINATION 213

BIBLIOGRAPHY 216

LIST OF FIGURES

Page

CHAPTER 1

Figure 1.1 Dependence of YBCO critical current on in-plane mosaic spread (from Reference 12). 20

CHAPTER 2

Figure 2.1 Thin film structure zone model of Grovenor *et al.* showing microstructure regimes as a function of $\frac{T_s}{T_m}$, the ratio of substrate temperature to the melting temperature of the film material (from Reference 26). 24

Figure 2.2 Columnar film growth illustrating the tangent rule (from Reference 31). 27

Figure 2.3 Schematic of a spherical cap-shaped film particle on a substrate which it partially wets. γ_i is the surface interface energy of the particle/substrate interface, γ_s is the substrate surface energy, and γ_f is the surface energy of the free particle surface. θ is the equilibrium contact angle between the particle and the substrate (from Reference 32). 31

Figure 2.4 Schematic of uniaxial texture evolution during columnar growth from randomly oriented equidistant nuclei. Grains with their fastest growth direction aligned closest to the substrate normal grow faster than misoriented grains. Favorably oriented grains grow to extinguish misoriented grains to establish uniaxial texture along the fast growth direction (from Reference 35). 34

Figure 2.5 (111) X-ray pole figure of a (200) biaxially aligned YSZ film fabricated by Iijima *et al.* using dual ion beam deposition without active substrate heating. The in-plane film orientation features a (111) pole in the direction of the assisting ion beam projection as illustrated above (from Reference 6). 40

Figure 2.6	Schematic showing relationship between {111} in-plane orientation of (200) biaxially aligned YSZ film and the assisting ion beam incident at 55° from the substrate normal.	41

CHAPTER 3

Figure 3.1	Schematic of ion assisted electron beam evaporation system.	45
Figure 3.2	Schematic of dual ion beam deposition system.	48
Figure 3.3	Schematic of four circle X-ray diffraction geometry.	51
Figure 3.4	Measured assisting ion beam fluence at normal incidence as a function of distance from the RF ion source.	55
Figure 3.5	Schematic showing ion fluence dependence on ion bombardment angle	56

CHAPTER 4

Figure 4.1	θ-2θ X-ray trace and (111) X-ray pole figure of YSZ film fabricated by electron beam evaporation at 600°C on Pyrex.	62
Figure 4.2	θ-2θ X-ray trace and (111) X-ray pole figure of YSZ film fabricated by ion assisted electron beam evaporation at 600°C on Pyrex.	63
Figure 4.3	(111) X-ray pole figure of IBAD YSZ film exhibiting two biaxially aligned grain populations.	65
Figure 4.4	(111) X-ray pole figures of IBAD YSZ films showing in-plane orientations of (200) biaxially aligned YSZ films as a function of ion bombardment angle.	66
Figure 4.5	(111) X-ray pole figures for films deposited on (a) Pyrex and (b) quartz by ion assisted e-beam evaporation at 600°C.	68
Figure 4.6	θ-2θ X-ray trace intensities and (111) X-ray pole figures showing development of YSZ (200) biaxial alignment on Pyrex as a function of film thickness.	69

Figure 4.7 (111) X-ray pole figures for films evaporated on Pyrex (a) without ion assist (b) with 75eV ion assist throughout deposition (c) with 75eV ion assist during the first 50nm and by standard e-beam evaporation to final thickness of 1 μm and (d) without ion assist during first 60nm, ion etched at 75eV for 10 min, and evaporated to final thickness of 1 μm. 72

Figure 4.8 SEM micrograph of ion assisted e-beam YSZ film deposited on Pyrex at 600°C. 73

Figure 4.9 Low magnification cross-sectional TEM image of IBAD YSZ film deposited on Pyrex at 600°C. 74

Figure 4.10 Selected area electron diffraction pattern of (200) biaxially aligned film shown in Fig. 4.9. Diffraction spots can be attributed to three (200) grain populations. 76

Figure 4.11 Cross-sectional TEM image of IBAD YSZ film showing secondary dendrites of (200) YSZ columns. 77

Figure 4.12 Cross-sectional TEM image of IBAD YSZ film near the top film surface. 79

Figure 4.13 Hypothetical model of faceted YSZ column structure observed in films deposited on Pyrex at 600°C. 81

Figure 4.14 (a) θ-2θ X-ray traces of YSZ films deposited on Pyrex, quartz, and Hastelloy substrates by ion assisted e-beam evaporation without active substrate heating. (b) (111) X-ray pole figure of film deposited on Pyrex. 83

Figure 4.15 SEM micrograph of ion assisted e-beam YSZ film deposited on Pyrex without active substrate heating. 85

Figure 4.16 Low magnification cross-sectional TEM micrograph of ion assisted e-beam YSZ film deposited on Pyrex without active substrate heating. 86

Figure 4.17 Schematic of (200) YSZ biaxial alignment development on Pyrex resulting from growth rate anisotropy during IBAD. 90

CHAPTER 5

Figure 5.1	Normalized plots of film thickness versus deposition time for a poorly controlled deposition (Run 090895) and a well controlled deposition (Run 010996).	97
Figure 5.2	Periodic r value variation during Run 111595.	98
Figure 5.3	θ-2θ X-ray traces of YSZ films sputtered without active substrate heating.	100
Figure 5.4	θ-2θ X-ray traces of dual IBAD YSZ films deposited without active substrate heating on several substrates.	102
Figure 5.5	(111) X-ray φ scans of dual IBAD YSZ films deposited without active substrate heating on several substrates.	103
Figure 5.6	FWHM values obtained from (111) X-ray φ scans of the nine films fabricated at ideally constant r value.	104
Figure 5.7	FWHM values obtained from (111) X-ray φ scans of films fabricated with varied r value during deposition.	106
Figure 5.8	SEM micrograph of YSZ film fabricated by dual ion beam deposition without active substrate heating.	107
Figure 5.9	Cross-sectional TEM micrograph of dual ion beam YSZ film deposited on quartz.	108
Figure 5.10	Micrograph highlighting several of the twins and dislocations present in Fig. 5.9.	110
Figure 5.11	X-ray data from (a) (220) χ scan and (b) (220) φ scan of a biaxially aligned YSZ film fabricated by dual ion beam deposition without active substrate heating.	112
Figure 5.12	(220) and (200) stereographic projections for YSZ grains in the film/substrate interfacial region and grains constituting most of the film.	113
Figure 5.13	θ-2θ X-ray traces of films deposited on quartz and silicon substrates by dual ion beam deposition at 600°C with a 35° ion bombardment angle.	115

Figure 5.14 (111) X-ray ϕ scans of YSZ films deposited on quartz and silicon substrates by dual ion beam deposition at 600°C with a 35° ion bombardment angle. 116

Figure 5.15 (111) X-ray pole figure of YSZ film deposited on quartz by dual ion beam deposition at 600°C with a 35° ion bombardment angle showing {111} reflection parallel to assisting ion beam at χ=35° and ϕ=0°. 117

Figure 5.16 θ-2θ X-ray traces for YSZ films deposited on quartz and silicon substrates by dual ion beam deposition at 600°C with a 45° ion bombardment angle. 119

Figure 5.17 (111) X-ray ϕ scans for YSZ films deposited on quartz and silicon substrates by dual ion beam deposition at 600°C with a 45° ion bombardment angle. 120

Figure 5.18 (111), (200), and (220) X-ray pole figures ϕ scans for YSZ films deposited on silicon and quartz substrates by dual ion beam deposition at 600°C with a 45° ion bombardment angle. 121

Figure 5.19 SEM micrograph of YSZ film fabricated by dual ion beam deposition at 600°C. 123

Figure 5.20 Schematic of Σ13 coincident site lattice consistent with biaxial alignment of YSZ film deposited on quartz at 600°C by dual ion beam deposition with an ion bombardment angle of 35°. 126

Figure 5.21 Representation of (111), (200), and (220) biaxially aligned grain populations and corresponding X-ray pole figure reflection positions. 128

CHAPTER 6

Figure 6.1 θ-2θ XRD trace of control LCMO film sputtered on $SrTiO_3$ at 600°C. 134

Figure 6.2 θ-2θ XRD traces of LCMO films fabricated by dual ion beam deposition at 600°C on quartz with and without ion assist. 134

Figure 6.3 (110) X-ray ϕ scan of (h00) biaxially aligned LCMO film on quartz. 135

Figure 6.4 SEM micrograph of LCMO film fabricated by dual ion beam deposition at 600°C. 136

Figure 6.5 Electrical resistivity of IBAD LCMO film on quartz versus absolute temperature. 138

CHAPTER 7

Figure 7.1 (111) X-ray pole figures of (200) biaxially aligned YSZ films fabricated at 600°C on Pyrex by ion assisted electron beam evaporation. Angle shown is the ion bombardment angle. 142

Figure 7.2 Field plot showing in-plane orientation of (200) biaxially aligned YSZ films fabricated by both IBAD techniques without active substrate heating and at 600°C. Filled symbols indicate (111) oriented parallel to assisting ion beam projection. Open symbols indicate (220) oriented parallel to assisting ion beam projection. 145

Figure 7.3 Field plot comparing results from this work to the in-plane orientation observed by Iijima *et al.*[3,6] and Arendt *et al.*[9] for YSZ films fabricated by dual ion beam deposition without active substrate heating. Filled symbols indicate (111) oriented parallel to assisting ion beam projection. Open symbols indicate (220) oriented parallel to assisting ion beam projection. 147

Figure 7.4 Schematic showing ion pathlength and ion range as defined in equation 7-11. 156

Figure 7.5 Schematic of projectile/target collisions in Newtonian laboratory coordinates and in center-of-mass coordinates (from Reference 67). 158

Figure 7.6 Stopping power of an ion as a function of ion energy. Nuclear stopping is the dominant ion stopping mechanism in the low energy IBAD regime (from Reference 82). 162

Figure 7.7 Zirconium ion energy as a function of distance from correct lattice site. Local energy minimum exists at interstitial site. 165

Figure 7.8 Oxygen ion energy as a function of distance from correct lattice site. Local energy minima exist only at energies greater than that needed to remove ion from lattice. 166

Figure 7.9 Ion ranges for 100eV and 300eV Ar^+ incident on zirconia as a function of ion bombardment angle. Angle of 90° corresponds to normal incidence. 168

Figure 7.10 (100), (110), and (111) ZrO_2 planes with ionic radii of Shannon[83] and radii consistent with nuclear stopping cross-sections for 75eV and 300eV argon bombardment. 172

Figure 7.11 (100), (110), and (111) $LaMnO_3$ planes with ionic radii of Shannon[83] and radii consistent with nuclear stopping cross-sections for 75eV eV argon bombardment. 176

Figure 7.12 EDAX spectra of (200) biaxially aligned YSZ films fabricated by ion assisted electron beam evaporation on Pyrex at 600°C (Specimen 1) and by dual ion beam deposition on quartz without active substrate heating (Specimen 2). Argon was detected in both specimens. 177

Figure 7.13 Ion etch rates of (200) biaxially aligned YSZ films for (a) 150eV beam energy and 19μA/cm^2 ion fluence and (b) 300eV beam energy and 96μA/cm^2 ion bombardment. 181

Figure 7.14 Ion displacements for (a) (110) and (b) (111) ZrO_2 computational cells. 185

Figure 7.15 Atomic densities as a function of distance from (110) and (111) ZrO_2 surfaces. 187

Figure 7.16 Calculated (a) Zr^{4+} and (b) O^{2-} energies from open (110) and (111) surfaces into bulk ZrO_2. 188

CHAPTER 8

Figure 8.1	(111) X-ray ϕ scans of dual IBAD YSZ films, YSZ single crystal substrates, and epitaxially evaporated ceria layers for YSZ films fabricated by dual ion beam deposition at 600°C.	196
Figure 8.2	(111) X-ray ϕ scans of YSZ single crystal substrates, dual IBAD YSZ films, and epitaxially evaporated ceria layers for YSZ films fabricated by dual ion beam deposition without active substrate heating.	198
Figure 8.3	Schematic of coincident site lattice between (200) YSZ film and (110) YSZ substrate with (100) YSZ ‖ (110) YSZ; $[00\bar{1}]$ YSZ ‖ $[00\bar{1}]$ YSZ.	200
Figure 8.4	Cross-sectional TEM micrograph of YSZ film deposited on (110) YSZ by dual ion beam deposition at 600°C.	201
Figure 8.5	TEM micrograph showing both CSL and IBAD YSZ grains and respective orientations.	203
Figure 8.6	TEM micrograph along the IBAD YSZ/evaporated CeO_2 interface showing epitaxial CeO_2 growth on both YSZ granular orientations.	204

LIST OF TABLES

Page

CHAPTER 4

Table 4.1 Deposition conditions for films deposited without active substrate heating and at 400°C by ion assisted electron beam evaporation. 60

Table 4.2 X-ray diffraction results as a function of IBAD conditions and substrate for films deposited without active substrate heating and at 400°C by ion assisted electron beam evaporation. 82

CHAPTER 7

Table 7.1 IBAD parameters used to fabricate (200) biaxially aligned YSZ films. 141

Table 7.2 Summary of in-plane film orientation for Series 1-4. 143

Table 7.3 ε Values for 75eV and 300eV Ar^+ bombardment of Zr^{4+} and O^{2-} in ZrO_2. 163

Table 7.4 Nuclear stopping cross section radii and Ionic Radii for Zr^{4+} and O^{2-}. 170

Table 7.5 Nonexcluded areas for zirconia planes as a function of Ar^+ energy. 173

Table 7.6 Ionic radii and nuclear stopping cross-section radii for LCMO. 175

Table 7.7 Chemical composition of biaxially aligned YSZ films. 178

Table 7.8 ZrO_2 ion coordination numbers. 189

Table 7.9 $LaMnO_3$ ion coordination numbers. 192

ACKNOWLEDGEMENTS

There are a number of people I wish to thank for contributions toward my thesis. I would like to thank my advisor, Professor Michael J. Cima, for providing the guidance and suggestions that helped turn this thesis into a work of which I am proud. I would also like to thank Professor Harry L. Tuller and Professor Carl V. Thompson II for taking the time to serve on my thesis committee. John Centorino and Lenny Rigione provided greatly appreciated assistance in the laboratory. Both were also active participants in the sports debates held in Room 12-002. I would like to thank Barbara Layne for her assistance in everything from handling purchase orders to guarding the Soda Club horde. Thanks are extended to Dr. Paul C. McIntyre for teaching me TEM sample preparation. I wish to thank Mike Frongillo for many spirited sessions of high resolution TEM. I also wish to thank the Consortium for Superconducting Electronics, the Office for Naval Research, and Defense Advanced Research Projects Agency for their support of this research.

Graduate school is both an individual and a group journey; this is especially true for CPRL students. I wish to thank the CPRLers for their encouragement and camaraderie. All of my fellow students have contributed to my MIT experience.

I wish to thank Dr. Neville Sonnenberg for serving as a mentor during the past four years. Neville tutored me in thin film deposition and many related technical subjects. He has also been a good friend.

I want to thank my family for their love and support. I am especially grateful for their support during my first few years of graduate school. Finally, I wish to thank my wife Barbara. Her love and understanding helped me immeasurably. I am blessed to have all of them in my life.

CHAPTER 1
INTRODUCTION

Fabrication of highly crystallographically textured thin films on nonepitaxial single crystal, polycrystalline, and amorphous substrates is of tremendous technological importance. This is particularly true for oxide thin film fabrication. Single crystal oxide substrates are typically expensive, are available only in small sizes, and often feature materials properties that compromise their utility in device fabrication, such as high dielectric constant for perovskite single crystals and twinning in $LaAlO_3$. Elevated deposition temperatures are frequently employed to ensure epitaxial oxide film growth in instances where suitable single crystal substrates are available. Maintaining elevated substrate temperature for extended periods of time imposes a thermal budget incompatible with metallization and precludes the use of polymers in oxide device structures.

Ion beam assisted deposition (IBAD) is a thin film fabrication technique capable of producing highly textured thin films independent of substrate crystalline nature. The utility of IBAD was first demonstrated by Yu *et al.*[1,2] when they reported fabrication of highly oriented Nb thin films on amorphous silica substrates at room temperature by employing off-axis ion bombardment during film growth. The resulting Nb films featured both out-of-plane and in-plane crystallographic orientation, or biaxial alignment.

Research began toward fabrication of biaxially aligned yttria-stabilized zirconia (YSZ) thin films by IBAD soon after the work of Yu *et al.*[1,2] was published. The motivation was to create (200) biaxially aligned YSZ films on polycrystalline metal ribbons to serve as crystallographic templates for subsequently deposited $YBa_2Cu_3O_{7-x}$ (YBCO) thin films. Significant progress has been made in this effort. (200) Biaxially aligned YSZ thin films have been prepared by several IBAD techniques, including dual ion beam deposition[3-12], ion assisted pulsed laser ablation[13], RF bias sputtering[14-19], and

ion assisted electron beam evaporation.[20-25] The work of Iijima *et al.*[3-8] and Arendt *et al.*[9-12] using dual ion beam deposition is particularly noteworthy, as both groups report in-plane mosaic spreads of less than 6° FWHM for IBAD YSZ films deposited on polycrystalline nickel ribbons. The orientation of YBCO films mimics that of the YSZ beneath. YSZ in-plane mosaic spread is therefore manifested in subsequently deposited YBCO films. The importance of restricted in-plane orientation can be appreciated by noting the exponential decrease in YBCO critical current with increased mosaic spread shown in Fig. 1.1. Iijima *et al.*[3-8] and Arendt *et al.*[9-12] both attain the highly textured IBAD YSZ films without active substrate heating; the measured substrate temperature during fabrication does not exceed 200°C.

Low temperature fabrication of other textured oxide films would be useful in myriad applications. Biaxially aligned $BaFe_{12}O_{19}$ films on plastic substrates could be used for magnetooptic recording media. $LaMnO_3$-based oxide films could be utilized for colossal magnetoresistive recording heads on polycrystalline Al_2O_3-TiC substrates if the deposition temperature could be reduced to that where metallization is stable. Biaxially aligned $LiNbO_3$ films on glass substrates could be used for electrooptic waveguides. All of these applications are presently limited by the requirements of high deposition temperature for oxide film crystallinity and single crystal substrates for film texture.

Thesis Motivation and Scope of Thesis

Biaxially aligned YSZ thin films have been fabricated by several IBAD techniques. The mechanism by which IBAD biaxial alignment evolves has not been thoroughly investigated. The primary objective of this thesis is to identify the mechanism of IBAD biaxial alignment. The second is to fabricate IBAD thin films of a different oxide material to demonstrate the general applicability of IBAD and to determine if the same mechanism of IBAD biaxial alignment operative for YSZ holds in general.

(200) Biaxially aligned YSZ films are fabricated using ion assisted, electron beam evaporation and dual ion beam deposition in this thesis. A major reason for investigating two different IBAD fabrication techniques in this work is to determine whether the

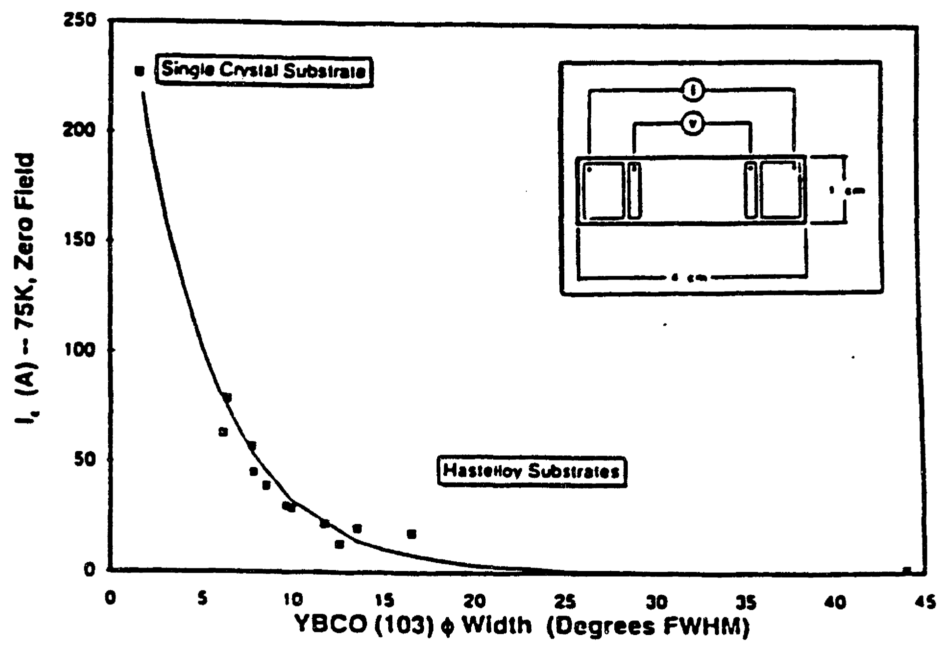

Figure 1.1 Dependence of YBCO critical current on in-plane mosaic spread (from Reference 12).

evolution of IBAD biaxial alignment is specific to individual fabrication techniques or whether the mechanism is common to ion assisted film growth by any technique.

The first set of experiments focuses on fabrication of (200) biaxially aligned YSZ by ion assisted electron beam evaporation on amorphous and polycrystalline substrates. The dependence of YSZ biaxial alignment on deposition rate, substrate temperature, ion bombardment angle, ion beam energy, and assisting ion fluence is determined. Cross-sectional transmission electron microscopy (TEM) is used to evaluate the microstructures of two (200) biaxially aligned YSZ films, one fabricated without active substrate heating and the other fabricated at elevated substrate temperature.

The second set of experiments evaluates the effects of the same IBAD parameters for dual ion beam deposition of (200) biaxially aligned films. The relationship between in-plane mosaic spread and the ion to molecule arrival ratio is studied. The microstructural evolution of (200) biaxial alignment is examined by cross-sectional TEM of a YSZ film deposited on an amorphous quartz substrate without active substrate heating.

Dual ion beam deposition of $La_{1-x}Ca_xMnO_3$ (LCMO) thin films on single crystal, polycrystalline, and amorphous substrates is then investigated. The biaxial alignment in these films is compared to that observed in IBAD YSZ films.

The role of the assisting ion beam is investigated in the next section of the thesis. Two alternative theories to explain the development of IBAD biaxial alignment are tested to explain the observation of two different IBAD YSZ in-plane orientations and the conditions for which each is obtained. Two software packages, ADESH and TRIM92, are used as complementary tools to model low energy ion bombardment of YSZ and to determine the influence of the assisting ion beam.

The next set of experiments are model experiments studying IBAD biaxial alignment development on single crystal YSZ substrates in two substrate temperature regimes. The single crystal substrates represent a nucleation seed acting to fix both the out-of-plane and in-plane film orientations. The mechanisms of IBAD biaxial alignment are discussed based on these results in conjunction with the results on nonepitaxial substrates.

Thesis Organization

Chapter 2 reviews the IBAD YSZ literature and discusses several mechanisms of thin film texturing. Chapter 3 details the deposition and characterization techniques used in this work. Ion assisted electron beam evaporation of YSZ is discussed in Chapter 4. Dual ion beam deposition of YSZ is the focus of Chapter 5. Dual ion beam deposition of LCMO is discussed in Chapter 6. The role of the assisting ion beam is examined in Chapter 7. The role of substrate temperature in determining the mechanism of IBAD biaxial alignment is shown in Chapter 8. The investigation of IBAD biaxial alignment is concluded and future work is suggested in Chapter 9.

CHAPTER 2
BACKGROUND

This chapter provides the background information for the research in this thesis. The focus of this thesis is the development of biaxial alignment in thin films fabricated by ion beam assisted deposition. Microstructural development in conventionally deposited thin films is discussed first using the structure zone diagram of Grovenor *et al.*[26] Texture development during thin film fabrication is then described. Fabrication of biaxially aligned thin films on nonepitaxial substrates using IBAD is then detailed, along with several proposed mechanisms for IBAD biaxial alignment. Finally, biaxially aligned YSZ fabrication by IBAD is reviewed to establish the starting point for this research.

2.1 THIN FILM MICROSTRUCTURAL DEVELOPMENT

Several models have been proposed to model the fully developed grain structure of thick polycrystalline films. The earliest model was proposed by Movchan and Demchisin[27] for microstructures observed in electron-beam deposited films of several metals and oxides. The general film features were schematically illustrated as a function of the homologous substrate temperature T_s/T_m, the ratio of the absolute substrate temperature to the melting temperature of the film material. Thornton[28] modified this structure zone model to include an axis accounting for the pressure of the sputtering gas during magnetron sputtering of several metal coatings. Finally, Grovenor *et al.*[26] advanced a refined structure zone model based on elemental metal films evaporated at a number of substrate temperatures. The structure zone model of Grovenor *et al.*[26] is shown in Fig. 2.1.

Four microstructural regions, or zones, are noted in the diagram. Equiaxed grains with diameters of less than 200Å were observed for films fabricated at $T_s/T_m<0.15$ (Zone

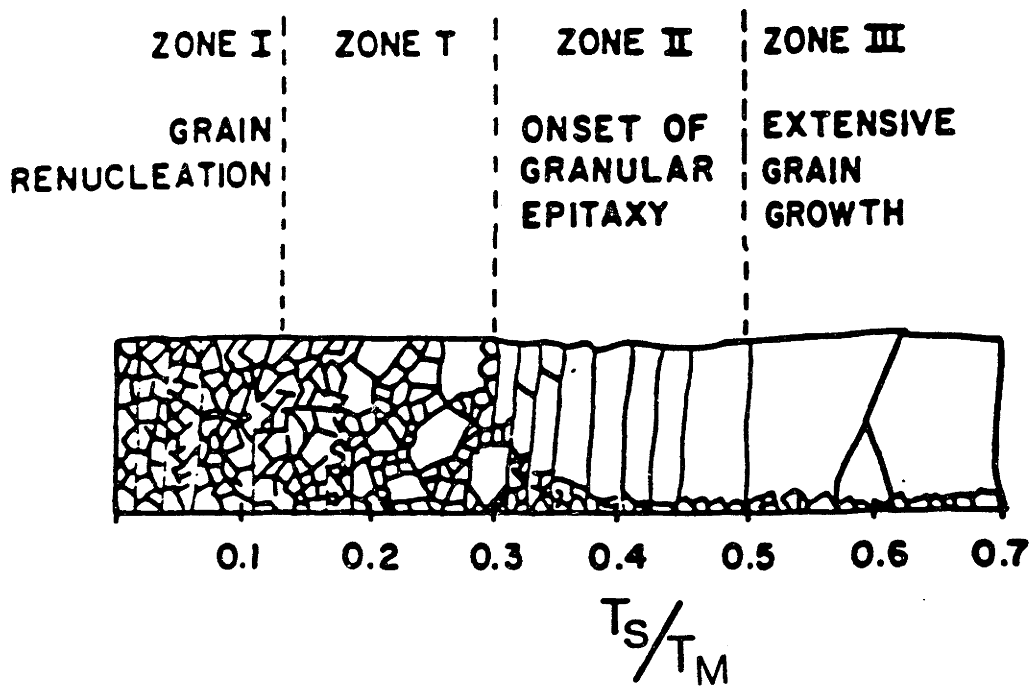

Figure 2.1 Thin film structure zone model of Grovenor *et al.* showing microstructure regimes as a function of $\frac{T_s}{T_m}$, the ratio of substrate temperature to the melting temperature of the film material (from Reference 26).

I). A bimodal grain distribution was observed for films fabricated at $0.15<T_s/T_m<0.3$ (Zone T) with large 500Å grains surrounded by smaller grains. Columnar grains appear in Zone II at $T_s/T_m>0.3$. Bulk grains with widths in excess of the film thickness are observed for films deposited at $T_s/T_m>0.5$.

The presence of four microstructural zones was attributed to the combined effects of surface diffusion, bulk diffusion, granular epitaxy, and grain boundary mobility, all of which are temperature-dependent. Grovenor *et al.*[26] place great emphasis on the temperature dependence of grain boundary mobility in explaining the origin of the thin film structure zones. Grain growth in the context of the structure zone diagram occurs during film deposition rather than post-deposition heat treatment. The mobility and migration activation energy of a grain boundary depend on its crystallography.[29] There is a distribution of the number of mobile grain boundaries at a given substrate temperature. Grovenor *et al.*[26] proposed phenomenologically that the four zones corresponded to grain growth situations where (a) one or zero, (b) two, or (c) all grain boundaries of a particular grain are mobile.

The Zone I microstructure at the lowest homologous substrate temperature results from the small fraction of mobile grain boundaries at low temperature. The change in crystallography produces a new grain boundary when a mobile grain boundary encounters a stationary grain boundary. The new grain boundary is statistically unlikely to be mobile in this temperature regime, precluding further grain growth. Little grain growth in expected in Zone I. Grains that do grow expand to approximately twice their initial diameters. The characteristic microstructure of Zone I is comprised of clumped equiaxed grains on the order of 200Å diameter. Grain renucleation occurs continually throughout film deposition at low homologous temperature. The mechanism by which the renucleation occurs is not clear. Renucleation may occur at low homologous temperature for two reasons. Relatively high undercooling provides a thermodynamic incentive for nucleation, while low grain boundary mobility may provide a kinetic impetus for renucleation rather than continued growth of a given grain at low substrate temperature.

Zone T microstructures occur at higher homologous substrate temperatures and result from type (b) grain growth where two grain boundaries are mobile. Grains with

more than one mobile boundary achieve size advantage over smaller neighboring grains. Large grains surrounded by numerous smaller grains are statistically more likely to continue growth, while smaller grains do not grow at all. This leads to the bimodal grain size distribution characteristic of Zone T. The larger grains are somewhat misrepresented in Fig. 2.1. Large grains in many experimentally observed Zone T microstructures continue through the entire thickness of the film rather than terminating within the film as shown in Fig. 2.1.[30]

All grain boundaries are mobile in type (c) grain growth in both Zones II and III. There is increased probability of any grain boundary sweeping across a grain and reacting to form another mobile boundary. Surface diffusion, grain boundary diffusion, and bulk diffusion are all operative elevated substrate temperatures. Granular epitaxy and type (c) grain growth both occur at these homologous temperatures, but by different mechanisms. The balance between film thickening, continued granular epitaxy, and lateral grain growth leads to a microstructure dominated by long, thin columns in Zone II. A squat columnar microstructure is observed at higher homologous temperatures in Zone III where more lateral grain growth occurs relative to thickening by deposition.

The film columns shown in the Grovenor *et al.*[26] structure zone model are aligned normal to the substrate. Actual film columns are frequently tilted in the direction of the vapor source in thin films fabricated by physical vapor deposition techniques. An experimental observation based on Al films evaporated at oblique incidence as shown in Fig. 2.2. is the tangent rule, which relates the angle β between the columns and the substrate normal and the angle α between the vapor source direction and the substrate normal by

$$\tan\alpha = 2\tan\beta. \tag{2-1}$$

Geometric shadowing as a result of low adatom mobility is the generally accepted cause of column tilting toward the vapor source direction.

2.2 THIN FILM TEXTURE DEVELOPMENT

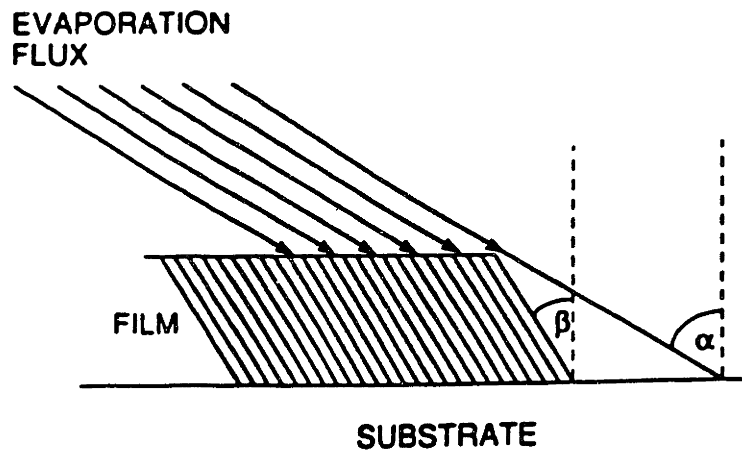

Figure 2.2 Columnar film growth illustrating the tangent rule (from Reference 31).

The preceding section characterized the fully developed grain structure of polycrystalline films as a function of substrate temperature. The evolution of film texture throughout all stages of microstructural development is discussed in this section in light of the structure zone diagram in Fig. 2.1. Thin film microstructural development begins with nucleation. There are three principal modes of thin film growth: Volmer-Weber, or island growth, Frank-van der Merwe, or two-dimensional layer-by-layer growth, and Stranski-Krastanov growth. Volmer-Weber growth prevails when film atoms are more strongly bound to each other than to the substrate, as is frequently the case in oxide film deposition. The film materials does not completely wet the substrate in Volmer-Weber growth, so the film grows from independently nucleated islands which grow into the vapor along the vapor-substrate interface. These islands eventually coalesce into a continuous film with further deposition. This continuous film then thickens with further deposition. Polycrystalline films can develop texture during any of these three stages, as discussed by Thompson and Carel.[32]

2.2.1 Pre-coalescence Texture Development

Volmer and Weber[33] proposed the capillary model for heterogeneous nucleation from the vapor phase. Neugebauer[34] modified the treatment to examine the thermodynamic stability of adatom clusters on a substrate. The idealized geometry of the adatom clusters is a spherical cap on the substrate. Consider a spherical adatom cluster of radius r. The total free energy of the cluster with respect to dissociation into the vapor phase is

$$\Delta G = \left(\frac{4\pi r^3}{3}\right)\Delta G_v + 4\pi r^2 \Gamma_{cv} \tag{2-2}$$

where ΔG_v is the volume free energy of the adatom aggregate and Γ_{cv} is the surface free energy between the aggregate and the vapor phase. The positive surface free energy term typically dominates the volume free energy term for small aggregates. The condition of maximum free energy corresponds to minimum stability of the adatom aggregate. The

aggregate radius that corresponds to the maximum free energy is obtained by setting $\frac{d\Delta G}{dr} = 0$ and solving to obtain

$$r^* = \frac{-2\Gamma_{cv}}{\Delta G_v}. \tag{2-3}$$

Aggregates smaller than the critical radius r^* are energetically unfavorable and will dissolve. Aggregates of radius r^* and larger are thermodynamically stable nuclei and, on average, will grow to form permanent islands on the substrate. The free energy barrier to nucleation ΔG^* is obtained by substituting equation (2-3) into equation (2-2) to yield

$$\Delta G^* = \frac{16\Gamma_{cv}^3}{3(\Delta G_v)^2}. \tag{2-4}$$

The nucleation frequency I^* is defined as the number of supercritical aggregates created per unit are and time and is given by

$$I^* = C \operatorname{Re} xp\left(\frac{\Delta G_{des} - \Delta G_s - \Delta G^*}{kT}\right) \tag{2-5}$$

where C is a geometric constant that includes the nucleus size, R is the deposition rate, ΔG_s is the activation free energy for adatom surface diffusion, k is Boltzmann's constant, and T is the substrate temperature.

A number of important observations can be drawn from these equations. A primary component of ΔG_v is the enthalpy of sublimation. Many oxides such as zirconia have high boiling points and correspondingly high enthalpies of sublimation. Such materials have large ΔG_v and small critical radii r^*. Common f.c.c. metals feature calculated r^* of about 1Å.[30] The enthalpy of sublimation of most f.c.c. metals is smaller than that for most oxides; therefore the calculated r^* values for oxides would be even smaller. Secondly, the nucleation frequency is linearly proportional to the deposition rate R and is exponentially dependent on the substrate temperature. Both observations have implications with respect to film texture. First, it is not meaningful to discuss texture development due to preferential nucleation when the critical nucleus size is so small.[32] Secondly, substrate temperature is expected to have a much greater influence on

nucleation than deposition rate. The nucleation frequency can be altered by many orders of magnitude by altering substrate temperature, while altering the deposition rate will yield small differences in nucleation rate.

The growth energetics of the supercritical adatom cluster can be described by macroscopic surface energies once the nucleus is sufficiently large. The surface energies affecting the growth of a spherical cap are shown in Fig. 2.3. γ_i is the surface interface energy of the particle-substrate interface, γ_s is the surface energy of the substrate, and γ_f is the surface energy of the free particle surface. The equilibrium contact angle between the spherical cap and the substrate is θ. The interface energy γ_i is a strong function of the crystallographic orientations of the particle and substrate. A coordinate system referenced to the particle crystal lattice with one axis normal to the film plane is shown in Fig. 2.3. γ_i would be expected to vary for rotations through β and δ but not α on an amorphous substrate. Minimization of γ_i on an amorphous substrate would lead to uniaxial texture normal to the substrate but would impose no constraint on in-plane orientation. γ_i typically depends on α, β, and δ for films deposited on single crystalline substrates. Minimization of γ_i on single crystal substrates would therefore lead to restricted in-plane and out-of-plane texture. The favored nucleus orientation will be affected by anisotropy of γ_s as well as the orientation dependence of γ_i if γ_s is not isotropic, as would be the case for a polycrystalline substrate.[32]

Growth laws in terms of the rate of change of the spherical cap radius r_i can be determined for diffusion-limited and interface-limited growth if it is assumed that most of the particles attaching to the cluster arrive by adatom diffusion rather than direct incorporation from the vapor. Particles with minimum γ_i and γ_s will grow at slightly higher rates than particles with the same volume but with higher surface energies.

van der Drift[35] listed four cases in which film texture could be formed during nucleation as a result of substrate crystallography. The first case is epitaxial nucleation on a single crystal substrate. The second is epitaxial nucleation on a polycrystalline substrate. The third case arises in the instance that a certain set of crystal planes preferentially form parallel to a smooth amorphous substrate surface. The fourth case is

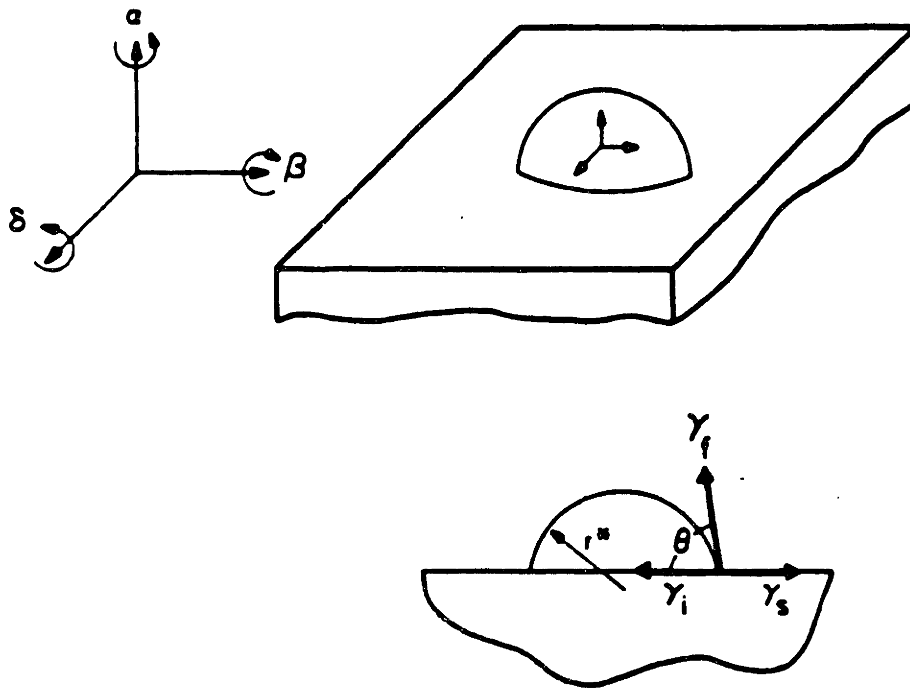

Figure 2.3 Schematic of a spherical cap-shaped film particle on a substrate which it partially wets. γ_i is the surface interface energy of the particle/substrate interface, γ_s is the substrate surface energy, and γ_f is the surface energy of the free particle surface. θ is the equilibrium contact angle between the particle and the substrate (from Reference 32).

preferential growth of crystal planes on a rough substrate. The latter three cases establish uniaxial texture normal to the substrate but impose no alignment in the plane of the film.

2.2.2 Texture Development During Coalescence

Islands undergo coarsening processes with material exchange through self-diffusion on particle surfaces and through grain boundary motion. The driving force for coalescence is reduction in surface energy. Coalescence energetically favors particles with low surface energy to volume ratios. During coalescence the total projected area of islands decreases and their height increases. Grain growth and corresponding texture development during coalescence have been experimentally observed but has not been extensively studied, even though coalescence can determine the final film texture.[32] An example of coalescence-controlled texture is gold deposition onto oxidized Si at room temperature. Randomly oriented Au islands were observed before complete coalescence. A few grains with (111) texture grew large at the late stage of coalescence. The (111) texture became dominant and was maintained with increased thickness.

Coalescence could reduce the orientation present after nucleation, as shown for two of van der Drift's cases. The nucleation texture on an amorphous substrate remains constant during the horizontal growth of nuclei, but reorientation of islands upon coalescence may decrease the film texture. The texture on a rough substrate would increase during the horizontal growth of nuclei but could again decrease during coalescence. The effects of coalescence on film texture for a given deposition situation cannot be assumed a priori. That coalescence can alter film texture should be acknowledged.

2.2.3 Post-coalescence Texture Evolution

The temperature dependence of texture development during nucleation and coalescence was not emphasized in the preceding sections, as both processes qualitatively occur in the same manner regardless of substrate temperature. This is consistent with the coalesced islands depicted near the interface of all four zones of the Grovenor structure zone model in Fig. 2.1. Grovenor *et al.*[26] proposed that the initial structure of a thin film

was composed of fine equiaxed grains at all substrate temperatures. The film texture that evolves after coalescence is a strong function of substrate temperature.

The initial fine equiaxed grain structure is maintained throughout the film by grain renucleation for films fabricated under Zone I conditions. TEM investigations of metal films deposited at low homologous substrate temperature reveal highly textured regions in the film comprised of groups of grains of approximately the same orientation.[25] How the texture varies with increased film thickness has not been examined.

Strong uniaxial texture is frequently observed in columnar thin films fabricated under Zone II conditions. van der Drift[35] used a geometric analysis to model the development of uniaxial texture in columnar thin films. A cross-sectional schematic of the columnar microstructure evolution is shown in Fig. 2.4 starting from randomly oriented, equidistant nuclei. The vertical growth rate of a crystal, the rate at which the apex of the crystal rises, is a function of the crystal orientation. Grains with their fastest growth directions aligned closest to the substrate normal grow faster than misoriented neighboring grains. Favorably oriented grains grow to extinguish misoriented grains to establish a pronounced texture normal to the substrate along the fast growth direction. The growth competition in this case does not produce restricted in-plane orientation. The same type of growth competition could occur among uniaxially textured nuclei to produce a uniaxially aligned columnar microstructure.

Thin film texture can also be altered by twinning. Fahey *et al.*[36] fabricated $SrRuO_3$ and $BaTiO_3$ thin films on both (100) $SrTiO_3$ and (100) MgO substrates using off-axis RF magnetron sputtering. The substrate temperature was 600 to 650°C, high enough to ensure epitaxial growth. The crystallographic effects of different film/substrate mismatches and argon and oxygen atmospheres were examined. θ-2θ X-ray diffraction revealed (100) normal orientation in all of the films. X-ray ϕ scans at several χ positions revealed a set of four twins along with the primary (100) orientation. Nonorthogonal twinning equivalent to a 60° rotation of twinned crystallites about the <111> directions in the (100) oriented films were observed by x-ray diffraction for $BaTiO_3$ and $SrRuO_3$ films on substrates with large mismatch. The twins were not detected in the θ-2θ scan because the twins were not oriented normal to the substrate. Films fabricated in oxygen deficient

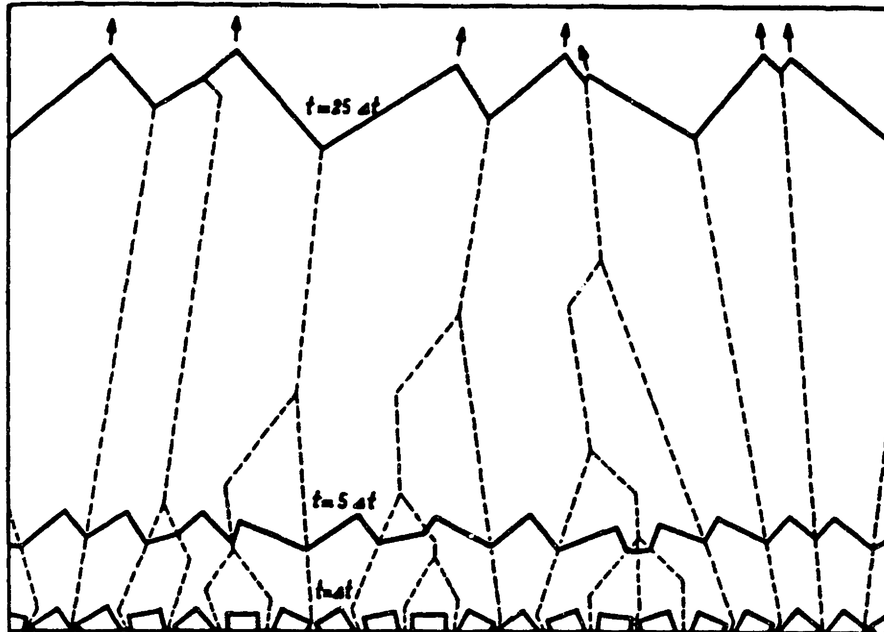

Figure 2.4 Schematic of uniaxial texture evolution during columnar growth from randomly oriented equidistant nuclei. Grains with their fastest growth direction aligned closest to the substrate normal grow faster than misoriented grains. Favorably oriented grains grow to extinguish misoriented grains to establish uniaxial texture along the fast growth direction (from Reference 35).

atmospheres featured the same twins. An epitaxial, twin-free $SrRuO_3$ film was deposited on a $SrTiO_3$ substrate with a processing atmosphere of 80mT O_2 and 120mT Ar. The mismatch for this combination is -0.6%. $SrRuO_3$ films deposited on $SrTiO_3$ with an atmosphere of 100mT Ar were twinned. $BaTiO_3$ films deposited on untwinned $SrRuO_3$ films were epitaxial and twin-free. $BaTiO_3$ films deposited on twinned $SrRuO_3$ films were also twinned, indicating granular epitaxial growth of the top film. The authors proposed that the twinning occurred in the mismatched films to remove biaxial in-plane strain. No explanation was offered to explain the twinning observed in oxygen-poor environments with low film/substrate mismatch.

Thin films can develop texture long after coalescence is complete. Karpenko *et al.*[37] sputtered biaxially aligned Mo films onto the native oxide of Si(100) wafers without active substrate heating. The substrate temperature did not exceed 200°C during fabrication. Films were fabricated at 34 nm/min and 67 nm/min. No evidence of texture was observed in films thinner than 80nm. Films deposited at both deposition rates exhibited (110) normal orientation after was observed at a film thickness of 80nm. No in-plane orientation was evident at this thickness. In-plane orientation was first observed at a film thickness of 500nm for films deposited at both deposition rates. Films deposited to 1 μm thickness at 34 nm/min and 67 nm/min exhibited (110) and (111) in-plane textures, respectively.

TEM and SEM were used to examine the film microstructures. Randomly oriented polycrystalline grains were observed in films less than 10nm thick. The randomly oriented grains began to form columnar features with faceted growth fronts with increased thickness. Cross-sectional TEM revealed that (110) planes for films deposited at 34 nm/min and (111) planes for films deposited at 67 nm/min had aligned with the growth direction at a film thickness of 200nm. The normal orientation became more pronounced with increased film thickness. In-plane orientation was noted in electron diffraction patterns of films 2μm thick. Thicker films exhibited a porous, columnar microstructure. Plan view and cross-sectional electron diffraction patterns indicated the individual columnar were single crystals. Karpenko *et al.*[37] described the microstructure observed in the thick Mo films as a Zone 2 microstructure. The

observation of a Zone 2 microstructure was surprising, given the low fabrication temperature.

Karpenko *et al.*[37] suggested that the change from Mo (110) to (111) biaxial alignment was related to the mean energy of the sputtered flux. The mean kinetic energy of the sputtered flux had been shown to influence thin film texture for several materials and sputtering gases.[38,39] The mass of the sputtering gas species influenced the Mo texture. Mo films sputtered under similar deposition conditions exhibited (110) biaxial alignment when neon was the sputtering gas but (111) biaxial alignment when argon was the sputtering gas. The mean kinetic energy of the Mo flux sputtered in the lighter neon gas was greater than that sputtered in Ar. Films fabricated at higher deposition rates with a higher power Ar plasma exhibited (111) biaxial alignment while films fabricated at lower deposition rates with less power exhibited (110) biaxial alignment. The mean kinetic energy of the Mo flux was greater for films fabricated with greater plasma power.

2.3 ION BEAM ASSISTED DEPOSITION BIAXIAL ALIGNMENT

2.3.1 Proposed Mechanisms of IBAD Biaxial Alignment

Yu *et al.*[1,2] were the first to demonstrate thin film texturing using low energy off-axis ion bombardment when they fabricated biaxially aligned niobium films on amorphous silica substrates at room temperature using dual ion beam deposition. One ion beam sputtered a Nb target while a second 200 eV Ar ion beam was incident at an angle of 20° from the substrate plane during deposition. A channeling direction of the niobium crystallites in the film was shown to align with the direction of the incident ion beam. Yu *et al.*[1] attributed the development of biaxial Nb alignment to the variation of sputtering yield with azimuthal angle of incidence. The angular dependence of sputtering yields for ion energies of 20keV and greater is well established.[40] They noted that decreases in the sputtering yields of single crystals by factors of 2-5 occur when the ion beam is parallel to a channeling direction in the sample, even for ion energies below 1000eV. Yu *et al.*[1,2] proposed that ions would channel through grains oriented favorably

with respect to the assisting ion beam while relatively preferentially sputtering grains misoriented with respect to the ion beam.

Bradley[41] expanded on the idea of preferential sputtering of misoriented grains to describe the development of biaxial alignment during IBAD. The model assumes that the crystal axis normal to the substrate plane is fixed while the in-plane axes are random. Such uniaxial texture could arise for a variety of reasons, as described in Section 2.2. Crystallites oriented in such a way that they are sputtered less relative to others start to dominate the microstructure. The development of a biaxially textured microstructure is thought to be the result of the higher sputtering yields of all grains other than those corresponding to the channeling direction. By balancing the deposition rate and the ion sputtering rate a net deposition would occur of only crystallites oriented in the low sputtering yield direction.

Ensinger[42] proposed an alternative ion texturing mechanism following work on TiN thin film fabrication by IBAD. TiN films were fabricated by evaporating Ti in a nitrogen atmosphere with N^+ ion assist at normal incidence during growth. Ensinger examined the texturing effects of both ion beam energy and the N^+ ion to Ti atom arrival ratio during IBAD. Control films fabricated by evaporating Ti in a nitrogen atmosphere at room temperature produced weakly crystalline films with some (111) texture. TiN films fabricated with N^+ ion assist at low ion energies and low ion to molecule arrival ratios at room temperature were highly crystalline and exhibited (111) orientation. Ensinger observed increased (200) TiN intensity relative to (111) intensity in X-ray θ-2θ scans with increased assisting ion irradiation, whether in by increased ion to atom arrival ratio or, in a less straightforward manner, to assisting ion beam energy. The (200) to (111) intensity ratio increased linearly with ion to atom arrival ratio with the N^+ energy fixed at 30keV. The (200) to (111) ratio increased with increasing ion energy from 100eV to 1keV, but slowly decreased with increased ion energy up to 30keV for a fixed N^+ to Ti atom arrival ratio of 1. The N^+ penetration depth into TiN was calculated using TRIM code and was found to monatonically increase with ion energy. The assisting ion energy for high energy ions therefore distributed over a greater volume into the film, which correlated with the slight decrease in (200) texture observed for ion energies

greater than 1keV at fixed ion to atom arrival ratio. Ensinger observed that ion induced texture formation correlated more with momentum transfer per unit volume rather than the average ion energy transferred to a film atom. Improved (200) TiN texture relative to (111) obtained by IBAD was attributed to lesser ion damage of (200) planes relative to (111) TiN. Ensinger argued that (111) TiN appeared more close-packed than (100) TiN planes for ion bombardment at normal incidence. Therefore (111) planes suffered greater ion damage in the form of lattice rearrangement and sputtering while N^+ ion channeled through open (100) planes, leaving them relatively undisturbed during growth and enabling (100) texture evolution to occur during IBAD.

2.3.2 Ion Beam Assisted Deposition of YSZ

Ion beam assisted deposition has been used to fabricate thin films of several oxide species. Yttria-stabilized zirconia (YSZ) has received the most attention of any oxide because of the potential of coating long lengths of polycrystalline metal tape with biaxially aligned YSZ acting as a crystallographic template for subsequently deposited high J_c $YBa_2Cu_3O_{7-x}$ superconducting strips. Biaxially aligned YSZ thin films have been prepared by several IBAD techniques, including dual ion beam deposition[3-12], ion assisted pulsed laser ablation[13], RF bias sputtering[14-19], and ion assisted electron beam evaporation.[20-25] Iijima *et al.*[3-8] and Arendt *et al.*[9-12] have fabricated the best biaxially aligned YSZ films by dual ion beam deposition. Both groups have reported YSZ films with exclusive (200) alignment normal to the film plane and in-plane mosaic spreads of less than 6° FWHM for IBAD YSZ films deposited on polycrystalline nickel substrates. The orientation of subsequently deposited YBCO films fabricated by pulsed laser deposition mimicked the biaxial alignment of the IBAD YSZ film. Both groups fabricated the IBAD YSZ films without active substrate heating; the measured substrate temperature during fabrication does not exceed 200°C. The other IBAD parameters such as deposition rate, ion bombardment angle, assisting ion beam energy, and assisting ion fluence were also similar.

Given the technical and potential commercial importance of biaxially aligned YSZ fabrication by IBAD, a thorough understanding of the mechanism by which biaxial

alignment develops during IBAD is desirable. The microstructural and mechanistic development of YSZ biaxial alignment during IBAD has not been examined by either group. Iijima *et al.*[3-8] and Arendt *et al.*[9-12] have observed that one of the {111} poles in a (111) X-ray phi scan or (111) X-ray pole figure of the (200) biaxially aligned YSZ films always corresponds to the projection of the assisting ion beam for all IBAD fabrication conditions. A (111) X-ray pole figure of a (200) biaxially aligned YSZ film fabricated by IBAD reported by Iijima *et al.*[6] is shown in Fig. 2.5. The projection of the assisting ion beam lies at 0° ϕ in Fig. 2.5. The smallest in-plane YSZ mosaic spread was obtained with the assisting ion beam incident at an angle of 55° from the film normal. This is the angle between [200] and [111] for a cubic material with [200] fixed normal to the substrate, as shown in Fig. 2.6. Degraded in-plane orientation was reported for ion bombardment angles both greater than and less than 55° from the substrate normal. Iijima *et al.*[6] observed that the biaxial alignment was enhanced by interaxial ion channeling along the YSZ <111> axis. The in-plane YSZ orientation was attributed to selective resputtering due to ion channeling, as suggested by Yu *et al.*[1,2] and Bradley.[41]

2.4 SUMMARY

Texture development in thin films during nucleation, coalescence, and growth was discussed in light of the structure zone diagram of Grovenor *et al.*[26] Several mechanisms by which texture could evolve during thin film were discussed. Uniaxial alignment normal to the substrate results from most of the texturing scenarios, and is the most alignment that can be obtained on amorphous and polycrystalline substrates for films fabricated by conventional vapor deposition techniques. Only two situations lead to oxide film biaxial alignment, alignment both normal to and within the film plane: epitaxial growth on a single crystal substrate and nonorthogonal twinning from a film epitaxially grown on a single crystal substrate.

Ion beam assisted deposition has been used to fabricate biaxially aligned films of several materials on amorphous and polycrystalline substrates. Off-normal ion bombardment during film deposition was required to obtain biaxial alignment. Two

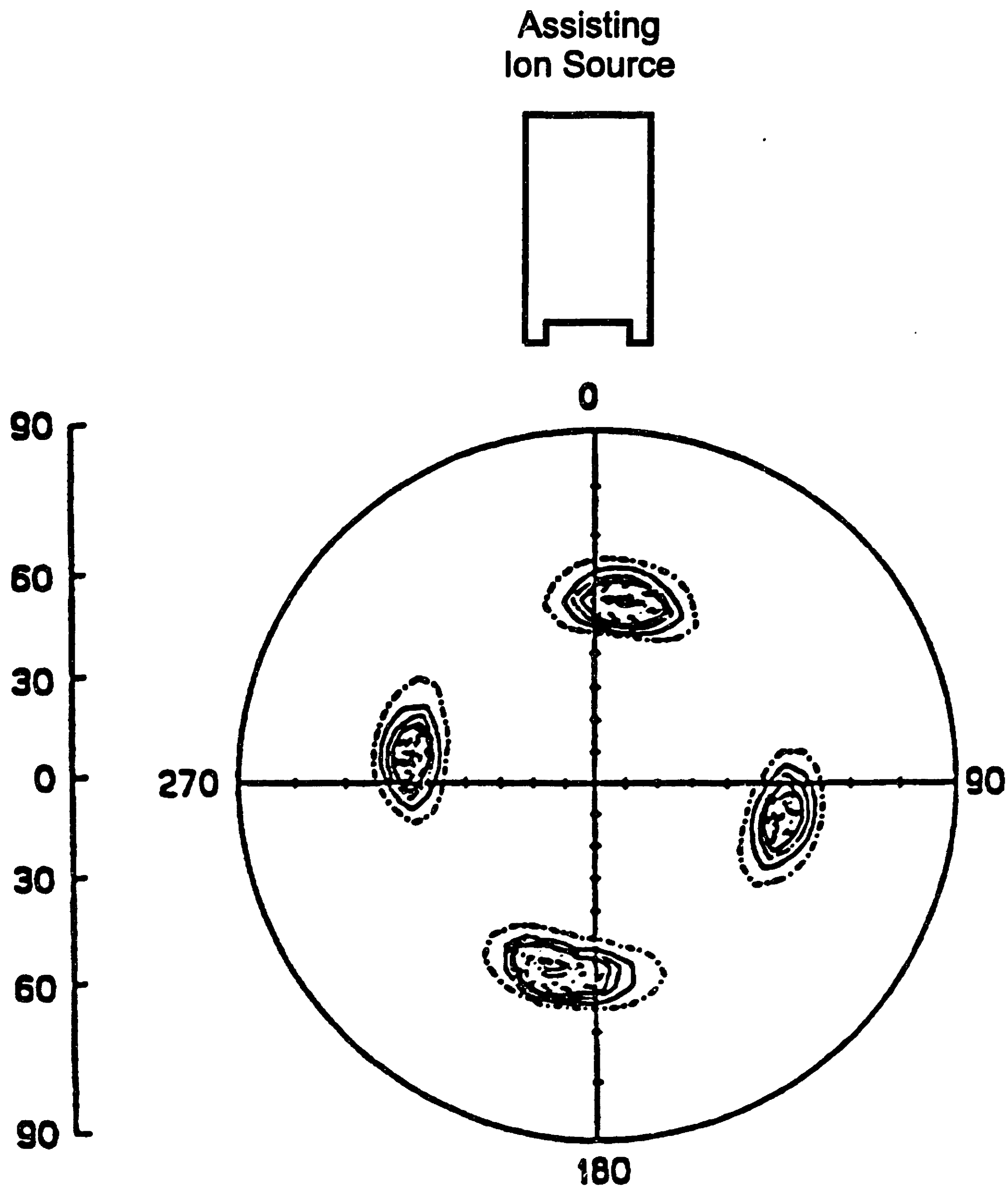

Figure 2.5 (111) X-ray pole figure of a (200) biaxially aligned YSZ film fabricated by Iijima *et al.* using dual ion beam deposition without active substrate heating. The in-plane film orientation features a (111) pole in the direction of the assisting ion beam projection as illustrated above (from Reference 6).

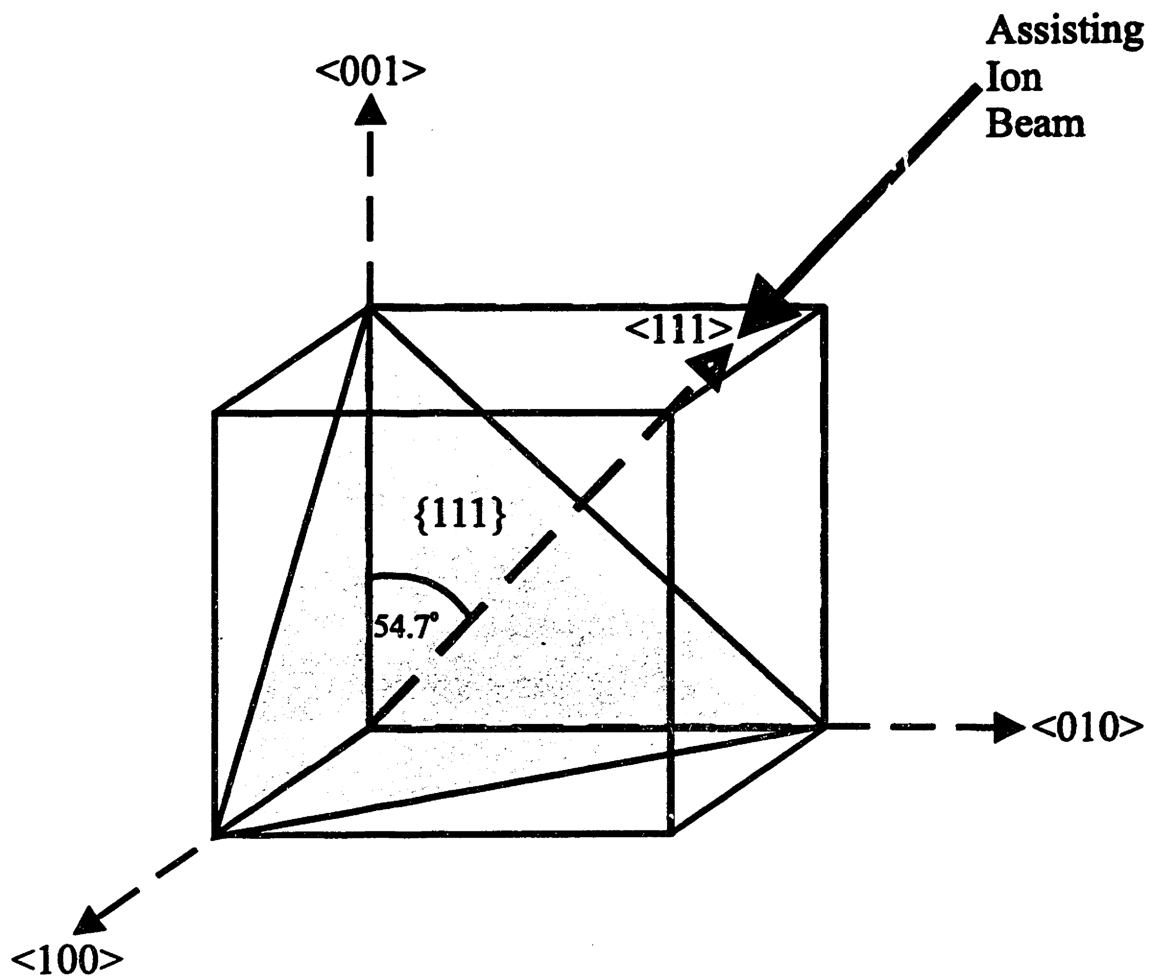

Figure 2.6 Schematic showing relationship between {111} in-plane orientation of (200) biaxially aligned YSZ film and the assisting ion beam incident at 55° from the substrate normal.

theories explaining the development of ion induced texturing were examined. Both are predicated on ion channeling occurring along open crystallographic directions of the film. Yu *et al.*[1,2] and Bradley[41] argue that IBAD biaxial alignment develops as a result of anisotropic sputtering of misoriented grains, while Ensinger argues that ion texturing results from anisotropic damage of nonchanneling crystallographic planes. Iijima *et al.*[3-8] were in agreement with Yu *et al.*[1,2] and Bradley[41] in suggesting that IBAD YSZ biaxial alignment resulted from anisotropic sputtering of grains misoriented with respect to the assisting ion beam. The development of IBAD YSZ biaxial alignment has not previously been systematically examined from either microstructural or mechanistic standpoints.

CHAPTER 3

THIN FILM FABRICATION AND CHARACTERIZATION TECHNIQUES

This chapter details the experimental techniques used in this thesis research. Substrate preparation, film fabrication, X-ray characterization, and electron microscopy conditions are described in this chapter. Any departures from the techniques and procedures described in this chapter are explicitly noted in the following chapters.

3.1 SUBSTRATES

3.1.1 Substrate Preparation

Most of the substrates used in this research were commercially available, including type 7740 Pyrex[43], amorphous quartz[44], Hastelloy C-276[45], (100) Si[46], and (100), (110), and (111) YSZ single crystals[47]. Yttria-stabilized tetragonal zirconia polycrystals (Y-TZP) were manufactured in-house. The Hastelloy and Y-TZP substrates were ground and polished to ~250 nm finish. The YSZ single crystals were polished to an optical finish by the vendor. The Pyrex, quartz, hastelloy, and Si substrates were cut into ¼" x ¼" squares. Larger as-received substrates were diced in-house using a diamond-impregnated wire saw.[48] The native oxide was not removed from the Si substrates. All substrates were cleaned by ultrasonication in successive baths of trichloroethane, acetone, and methyl alcohol for ~15 minutes each.

3.1.2 Substrate Heater Block Mounting

Stainless steel substrate blocks were polished clean with a Scotch Brite[49] cloth and rinsed with acetone. Substrates were attached to the steel blocks using a thin layer of silver paste[50] to ensure good thermal contact between the substrates and the substrate block. Organic components were removed from the silver paste *ex situ* with a slow

bakeout procedure after the substrates had been mounted. The block was heated for 2 hours at 80°C in an oven before being transferred to a Neytech furnace where it was heated in air to 220°C at 1°/min, held for 4 hours, heated to 400°C at 1°/min, and held for another 4 hours before furnace cooling to room temperature. The block was then mounted in the vacuum deposition chamber prior to pumpdown.

3.2 ION BEAM ASSISTED DEPOSITION

IBAD is a thin film fabrication technique that incorporates ion bombardment of a growing film during deposition. IBAD has been performed with a variety of deposition equipment configurations, including those used in this thesis research, ion assisted electron beam evaporation and dual ion beam deposition. Both IBAD configurations were incorporated into the same vacuum deposition system.

3.2.1 Ion Assisted Electron Beam Evaporation System Description

Figure 3.1 is a schematic of the ion assisted electron beam evaporation system used in this research. The evaporation source was a multiturret, water cooled, copper crucible and a 14 kW electron gun.[51] The source material was 8 mol% yttria-stabilized zirconia powder[52] that was pressed uniaxially and isostatically, fired, and crushed into ~3 mm pieces. A 3cm ion beam generated from an RF ion source[53] bombarded the film during depositions with ion assist. A mixture of argon with 8% oxygen (by volume) was used as the assisting ion source gas. A plasma bridge neutralizer (PBN) was used to neutralize the ion beam. Argon was used as the PBN gas. The chamber pressure rose to ~2×10^{-4} Torr with the introduction of the ion source and PBN gas flows, which was maintained during all depositions, whether or not ion assist was employed.

The stainless steel mounting block was attached on a heated substrate stage located above the RF ion source. The ion bombardment angle between the substrate plane and the ion beam could be varied by adjusting the block support mechanism. The ion bombardment angle is defined as the angle between the assisting ion beam and the substrate plane. Normal incidence ion bombardment would therefore correspond to an

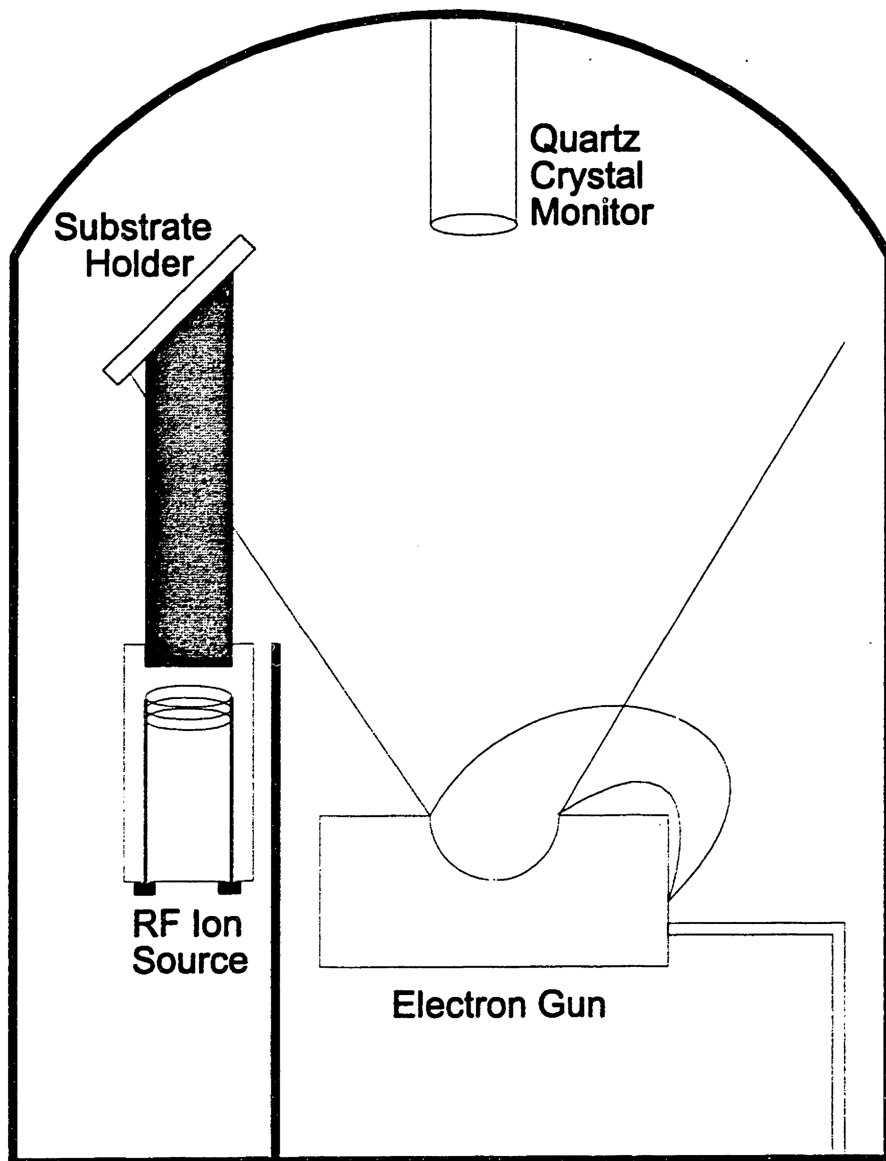

Figure 3.1 Schematic of ion assisted electron beam evaporation system.

ion bombardment angle of 90°, although ion bombardment always occurred at off-normal incidence in the IBAD work in this thesis. The mounting block was attached to a Boroelectric heater[54] on the substrate stage. Block temperatures were monitored using two independent Inconel sheathed Type K thermocouples inserted inside the sample block. Silver paste was used to ensure thermal contact between the block and the thermocouples. Heater control was provided by an Omega 2010 SSR temperature control.[55] All deposition temperatures reported in this thesis are the measured block temperatures.

Deposition rate and film thickness were measured using a quartz crystal film thickness monitor.[56] The measured deposition rates differed from the actual values in part due to electromagnetic interactions between the RF plasma and the thickness monitor. The net deposition rate also differs from the gross deposition rate measured with the thickness monitor due to sputtering from the assisting ion beam. Transmittance envelopes from film deposited on transparent substrates were obtained using a UV/Vis spectrophotometer[57] and film thickness was calculated using the interference fringe envelope technique developed by Swanepeol.[58] This thickness value was compared to that obtained from cross-sectional SEM fracture surfaces. The deposition rates reported in this thesis are net deposition rates unless otherwise noted. The net deposition rates were determined by dividing the film thickness measured by the optical and/or SEM techniques by the deposition time.

3.2.2 E-Beam Evaporation and Ion Assisted Electron Beam Evaporation Procedure

Several YSZ and CeO_2 films were fabricated by e-beam evaporation without ion assist. The vacuum chamber was evacuated to a pressure $<5x10^{-7}$ Torr before starting the Boroelectric heater for runs in which active substrate heating was desired. Most films were fabricated at a constant substrate temperature of 600°C. The substrate block was heated to 100°C in 30 minutes and then to 600°C in 2 hours. The evaporation source was slowly heated to the desired power level and allowed to equilibrate prior to deposition. A shutter above the crucible prevented deposition on the substrates during source conditioning. Deposition commenced once the desired substrate temperature had been

reached and the evaporation source had been equilibrated. Deposition to the desired film thickness occurred, after which the electron gun power was terminated and the substrate block cooled to room temperature over a period of three hours. The chamber pressure during evaporation was typically 2×10^{-6} Torr.

The heater warmup and evaporation source conditioning procedure for ion assisted electron beam evaporation was identical to that for evaporation alone. Gas flows to the ion source and PBN commenced after the substrate temperature had reached the desired value and the evaporation source was at the desired power level. Introduction of these gases increased the chamber pressure to 2×10^{-4} Torr, which was maintained throughout deposition. The ion source was ignited and stabilized for a 2 minutes, after which the ion beam was ignited and the crucible shutter was removed simultaneously. The ion source and electron gun power were shut off after depositing to the desired film thickness. Gas flow continued through the unignited ion source and PBN after deposition to help cool the substrates to room temperature in 3 hours.

3.2.3 Dual Ion Beam Deposition System Description

The dual ion beam deposition configuration is similar to the configuration used for ion assisted electron beam evaporation. Figure 3.2 shows a schematic of the dual ion beam deposition system. A 3 cm Kaufmann ion source[59] was used as the sputtering ion source. Argon was used as the sputtering gas. A sintered block of 8 mol% YSZ was the sputtering target. The RF ion source[53] was the assisting ion source, and a mixture of argon with 8 vol% oxygen was used as the assisting ion source gas. The PBN was used to neutralize both the RF and Kaufmann ion sources and to minimize charging on the insulating YSZ target. Argon was the PBN gas.

Substrates were attached with silver paste to stainless steel blocks and positioned above the RF ion source, and the ion bombardment angle θ is the same as was defined in the ion assisted electron beam evaporation setup. The Omega 2010 SSR temperature control was used as the heater control and the same quartz crystal monitor was used to monitor film thickness and deposition rate. Cross-sectional SEM fracture surfaces and the interference fringe envelope technique developed by Swanepeol[58] for films deposited

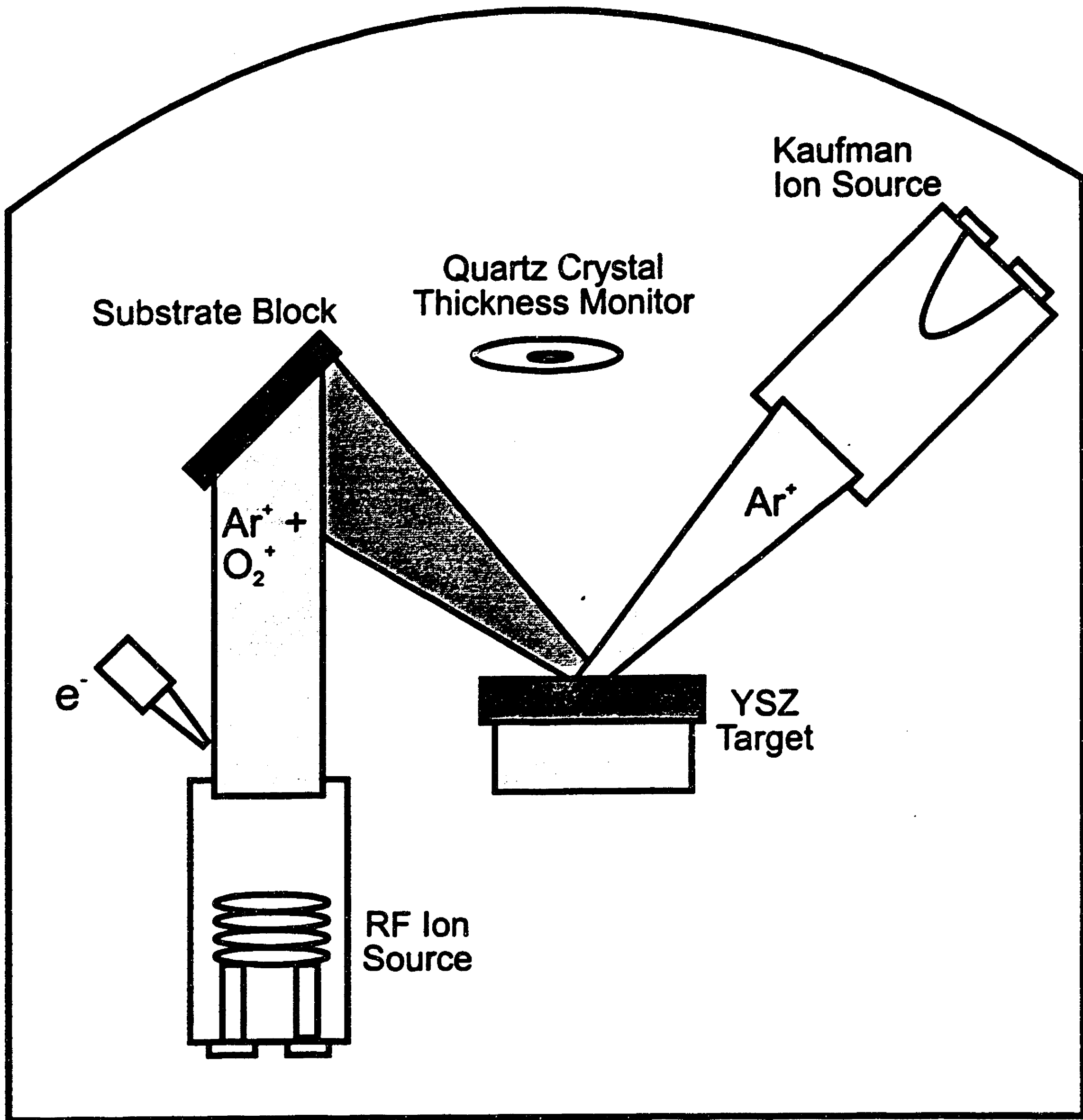

Figure 3.2 Schematic of dual ion beam deposition system.

on transparent substrates were used to determine film thickness. The net deposition rates were determined by dividing the film thickness measured by the optical and/or SEM techniques by the deposition time.

3.2.4 Dual Ion Beam Deposition Procedure

The vacuum chamber was evacuated to a pressure $<5x10^{-7}$ Torr before deposition. Several films were deposited at a constant substrate temperature of 600°C; for these runs the substrate block was heated to 100°C in 30 minutes and then to 600°C in 2 hours. Gas flows were initiated to the PBN, the Kaufmann ion source, and the RF ion source after the substrate temperature had stabilized at the desired value. The chamber pressure rose to $2x10^{-4}$ Torr with introduction of these gas flows, and the chamber pressure remained at that value throughout deposition. The RF ion source was ignited, followed by the Kaufmann ion source. The Kaufmann ion beam was started. The RF ion beam was ignited after the Kaufmann ion beam was stable. The RF ion beam characteristics (beam voltage, accelerator voltage, etc.) remained constant throughout deposition. LabVIEW software code with PID feedback was used to control the Kaufmann ion source beam current. The beam current was modulated in order to meet an desired deposition rate, as measured using the quartz crystal monitor. The beam current value was changed every minute in proportion to the measured film thickness compared to the ideal film thickness that should have been present with the desired deposition rate a given time in the deposition. Films were fabricated by dual ion beam deposition both at constant deposition rate and with a deposition rate that linearly increased throughout deposition. The ion sources were turned off after depositing to the desired film thickness. Gas flow continued thorough the PBN and both ion sources to help cool the substrates to room temperature.

3.3 X-RAY DIFFRACTION

Several X-ray diffraction (XRD) techniques were used to characterize thin film crystalline orientation. θ-2θ measurements were used to evaluate the film orientation

normal to the substrate, or the out-of-plane orientation. X-ray ϕ scans and X-ray pole figures were used to measure the in-plane film orientation. Films which feature both out-of-plane and in-plane texture are called biaxially aligned. The crystallographic and microstructural evolution of biaxially aligned films is the focus of this thesis.

3.3.1 Out-of-Plane Orientation

The crystalline planes parallel the sample surface are measured in θ-2θ XRD. The X-ray detector was placed in a position 2θ in order to measure diffracted intensity originating at an angle of incidence θ. The diffraction pattern exhibited by a sample will fall between two extremes. A randomly oriented polycrystalline sample will feature diffraction peaks from all allowed (hkl) planes. The relative peak intensities are governed by several factors, including the respective scattering factors for the (hkl) planes. A single crystal sample only has one family of planes aligned parallel to the sample surface and therefore diffracts from one set of parallel (hkl) planes. Samples that yield diffraction patterns with relative peak intensities which differ from those for a polycrystalline sample are said to exhibit out-of-plane texture, or preferred normal orientation.

3.3.2 In-Plane Orientation

Measurement of in-plane sample orientation is an extension of that used in θ-2θ X-ray diffraction. The X-ray detector is positioned at the same 2θ location to receive diffracted intensity from an angle of incidence θ. In-plane film orientation is examined by measuring diffracted intensity from planes at off-normal incidence. Two techniques were used in this thesis to probe in-plane orientation: X-ray ϕ scans and X-ray pole figures. Most X-ray ϕ scans and X-ray pole figures were measured using a diffractometer with a pole figure apparatus. The remaining X-ray ϕ scans and all of the X-ray χ scans were measured using a four circle X-ray diffractometer. The difference between a pole figure apparatus and a four circle diffractometer can be shown by referring to the diffraction geometry shown in Fig. 3.3. The pole figure apparatus allows independent control of only one of the four variables θ, 2θ, χ, and ϕ at a given time. The remaining

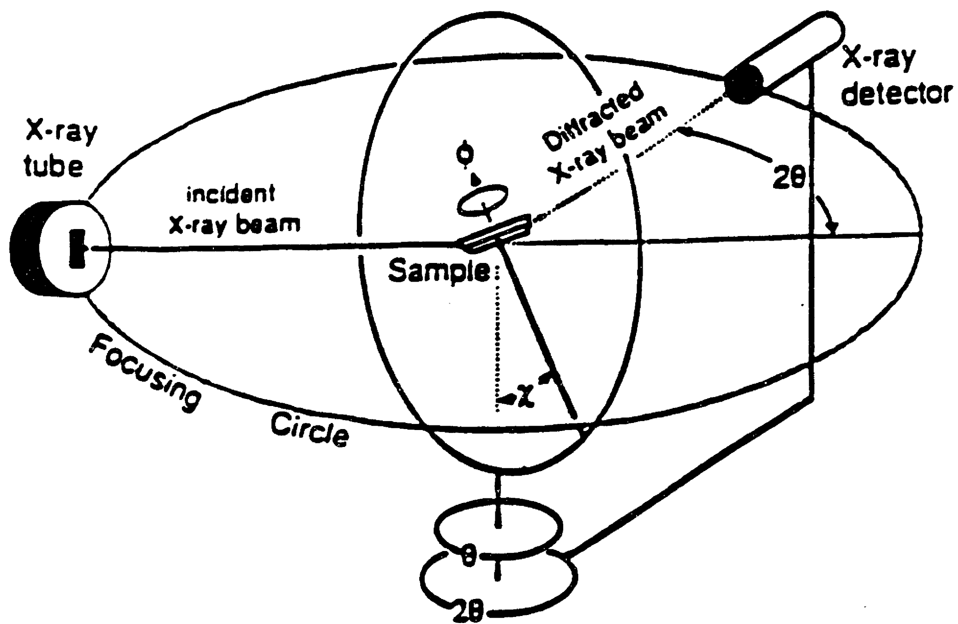

Figure 3.3 Schematic of four circle X-ray diffraction geometry.

three are fixed during a scan. The four circle diffractometer enables independent simultaneous control of all four variables. The procedures used to measure X-ray ϕ scans and X-ray pole figures are discussed below. The experimental conditions used for special four circle diffractometer scans, such as X-ray χ scans, are specifically noted in the text.

3.3.2.1 X-ray ϕ Scans

X-ray ϕ scans measure the X-ray intensity from a sample positioned in the diffractometer at constant values of θ, 2θ, and χ during a rotation through 360 degrees ϕ. The experimental procedure for examining a (200) biaxially aligned IBAD YSZ film is detailed as an example. The specimen is first examined in a powder diffractometer and is shown to exhibit strong (200) preferred orientation according to XRD. X-ray ϕ scans about any crystalline reflection other then (h00) can be used to probe the in-plane crystalline orientation. (111) X-ray ϕ scans were routinely measured to examine the in-plane orientation of YSZ films which exhibited strong (200) preferred normal orientation. The four (111) X-ray poles for a YSZ film with (200) parallel to the substrate plane lie 90° ϕ apart from each other and 55° χ from the (200) planes. The pole figure apparatus is positioned to χ=35° and the specimen is aligned to that the projection of the assisting ion beam is aligned with ϕ=0°. The goniometer is positioned at the appropriate θ and 2θ for the (111) YSZ X-ray reflection. The X-ray intensity is then measured as the specimen is rotated through 360° ϕ. The observation of four intense reflections separated by 90° confirmed in-plane alignment, while other results would indicate either random in-plane alignment or multiple in-plane texturing.

3.3.2.2 X-ray Pole Figure Measurements

X-ray pole figures are X-ray intensity contour plots comprised of X-ray ϕ scans taken at several values of χ. Pole figures are stereographic representations of in-plane crystalline orientation that can provide a more complete evaluation of sample texture than can be obtained from a single X-ray ϕ scan. A pole figure comprised of concentric circles

extending radially from $\chi=90°$ represents random in-plane orientation, just as a flat line does for an X-ray scan taken at the (hkl) reflection of interest. Pole figures of specimens with a single in-plane orientation show complete X-ray contour poles, whereas an individual X-ray ϕ scan would show the azimuthal intensity variation through the center of the poles. Pole figures have a distinct advantage over X-ray ϕ scans in cases of multiple textured orientation since the location and symmetry of multiple reflections can be matched to their parent (hkl) reflections by symmetry relations.

3.3.3 Experimental Conditions

All θ-2θ XRD measurements were measured using a Rigaku[60] RU300 diffractometer with a rotating Cu anode. CuK_α radiation was used with a voltage of 50kV and a current of 200 mA. The divergence and scatter slits were 0.5° and the receiving slit was 0.15mm. All samples were scanned from $2\theta=10°$ to 100° at 10°/min with a sampling interval of 0.02° 2θ. The X-ray ϕ scan and X-ray pole figure measurements were conducted on a Rigaku RU200 diffractometer with a pole figure apparatus. CuK_α radiation was used at a voltage of 50kV and a current of 180 mA. The divergence and scatter slits were 0.5° and the receiving slit was 0.15mm. X-ray ϕ scans were carried out at 180° ϕ/min with a ϕ step of 1°. The X-ray pole figure apparatus was aligned such that $\chi=90°$ corresponded to normal incidence on the sample. X-ray pole figures were measured from $\chi=15°$ to 85° with a step of 10° and a ϕ step of 1°.

3.4 FILM MICROSTRUCTURE

Scanning electron microscopy (SEM) and transmission electron microscopy (TEM) were used to examine the film microstructure. A Hitachi[61] S-530 scanning electron microscope was used with an accelerating voltage of 25kV. All specimens were sputter-coated with gold prior to SEM observation. Cross-sectional TEM specimens were prepared by a sequence of mechanical thinning steps, dimpling to <10μm thickness,

and ion milling with 4 kV argon ions. Low resolution TEM was performed using a JOEL 200CX microscope[62] operating at 100 kV and high resolution TEM was performed using a Topcon 002B microscope[63] operating at 200 kV.

3.5 DETERINATION OF ION ETCH RATES AND R VALUES

The ion current density, or ion fluence, emitted from the RF ion source was measured using a Faraday cup with a bias of -30V. This bias was selected in order to measure the current from positively charged ions while repelling electrons used to neutralize the plasma. The Faraday cup was placed at normal incidence with respect to the RF plasma. The ion fluence for given values of beam energy, beam current, accelerating voltage, and neutralizer emission current decreases approximately linearly with distance from the RF ion source as a result of beam divergence. Ion beam divergence is specific to a given set of operating conditions. The measured ion fluence data for a beam energy of 300eV, a beam current of 30mA, an accelerating voltage of 600V, and a neutralizer emission current of 120mA is shown as a function of distance from the RF ion source in Fig. 3.4. The ion fluence for a given experiment depends on the ion bombardment angle. The actual current density impinging on a film during IBAD depends on the projected area of the film with respect to the assisting ion beam. The Faraday cup measures the ion fluence corresponding to normal incidence. The ion fluence reported in this thesis for a given bombardment angle is equal to the fluence measured with the Faraday cup at the appropriate distance between the RF ion source and substrate block times the sine of the ion bombardment angle. The geometric proof of this relation is shown using view factors in Fig. 3.5. The ion fluence is measured in current per unit area. Consider equal unit areas A for the substrate block and RF ion source beam area. Assisting ion bombardment at 90° results in all the ion beam current emitted from the RF ion source striking an equal area on the substrate block. Assisting ion bombardment at 0° bombardment angle results in none of the plasma striking the face of the substrate block. Finally, consider ion bombardment at angle θ. The beam current emitted per unit area A bombards a projected substrate block area $A\sin\theta$. Therefore, the

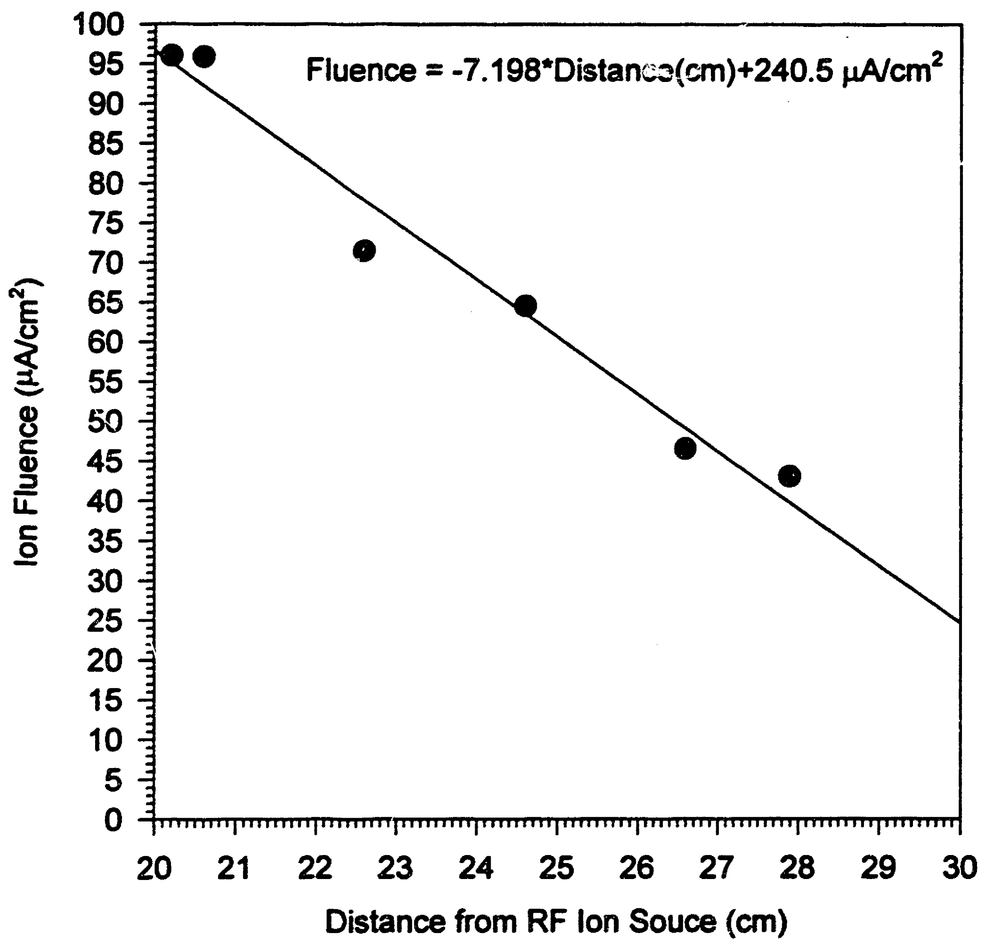

Figure 3.4 Measured assisting ion beam fluence at normal incidence as a function of distance from the RF ion source.

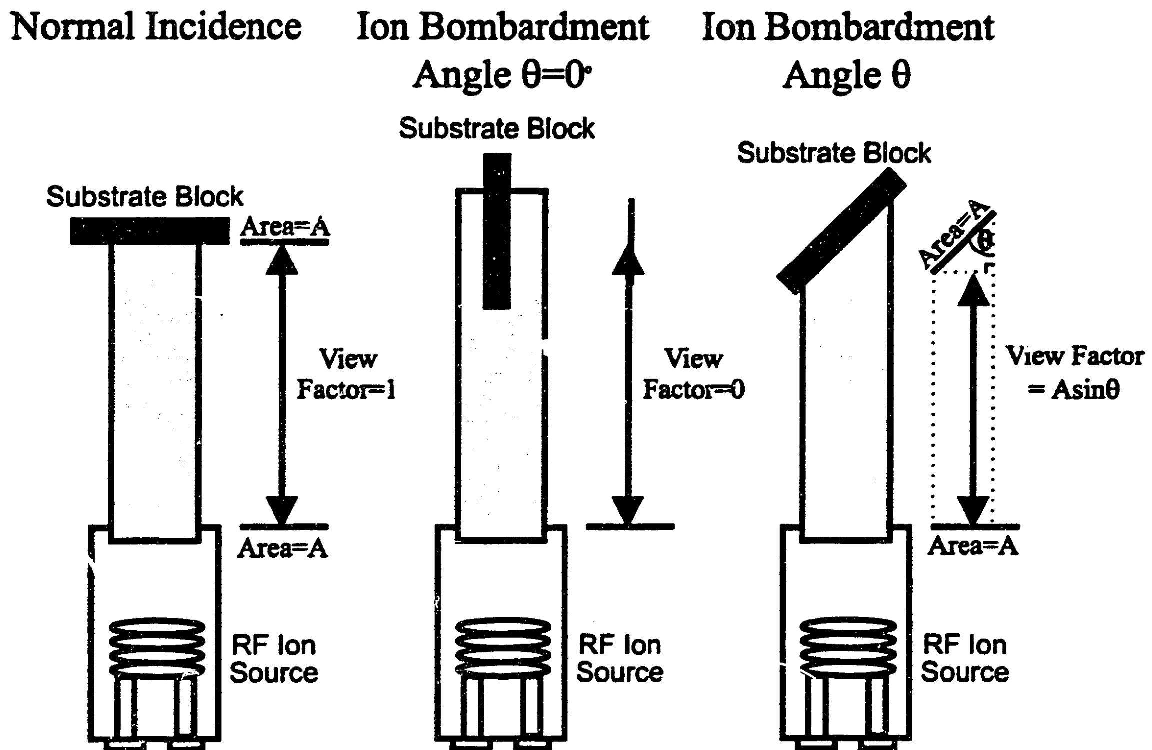

Figure 3.5 Schematic showing ion fluence dependence on ion bombardment angle.

ion fluence bombarding a film at bombardment angle θ is equal to the fluence measured at normal incidence times the sine of the bombardment angle.

The ion etching rate of a film is an important parameter in ion beam assisted deposition. Ion etching rates of YSZ films were measured in the following manner. The thickness of a previously deposited film was calculated using the envelope technique of Swanepoel.[58] The specimen was mounted on a substrate block using the procedure detailed in Section 3.2.2. The film was then ion milled by the RF ion source for a fixed period of time. The specimen was then removed from the substrate block and the thickness was again measured. The ion etching rate was determined by dividing the thickness of material removed by the ion bombardment time.

The r value is defined as the flux of incident ions divided by the flux of arriving adatom molecules. The r value provides a measure of the influence of the assisting ion beam during IBAD. Films fabricated with high r values experience numerous ion/film collisions during fabrication, while films fabricated with low r values are modified by the assisting ion beam to a lesser extent. It is necessary to know the gross deposition rate in order to exactly determine the r value. The gross deposition rate is unknown for most IBAD depositions. For IBAD depositions with low assisting ion beam fluence and/or low beam energy, a reasonable approximation of the r value can be obtained by dividing the assisting ion flux by the net deposition flux calculated using the envelope technique of Swanepoel.[53] This estimate is not adequate for IBAD depositions where considerable ion etching occurs. The ion etching rate is first determined, after which the r value is obtained by dividing the known assisting ion flux by the gross deposition flux calculated by adding the net deposition flux and the ion etching rate.

CHAPTER 4
ION ASSISTED ELECTRON BEAM EVAPORATION

4.1 INTRODUCTION

Biaxially aligned zirconia thin films have been fabricated by several deposition techniques. Dual ion beam deposition has been used in most of the research of biaxially aligned zirconia for high T_c superconductor applications. Ion assisted electron beam evaporation of zirconia has not been examined as much as of dual ion beam deposition of YSZ, even though ion assisted e-beam evaporation may prove to be of more commercial importance. Ion assisted electron beam evaporation can produce textured thin films at much higher deposition rates than can be attained by dual ion beam deposition. High deposition rates are a prerequisite for many commercial applications where thick films are employed. Examining the evolution of biaxial alignment during ion assisted electron beam evaporation and the establishing the balance of ion bombardment to deposition needed to obtain biaxial alignment are important from mechanistic standpoints.

This chapter focuses solely on ion assisted electron beam evaporation of YSZ. Several IBAD parameters are varied in this study, including the deposition rate, ion bombardment angle, assisting ion beam energy, the assisting ion beam fluence, and the substrate temperature. The dependence of YSZ film biaxial alignment on these parameters is established using X-ray diffraction.

4.2 EXPERIMENTAL PROCEDURE

4.2.1 Ion Assisted Electron Beam Evaporation of YSZ at 600°C

Amorphous quartz, type 7740 Pyrex, polished Hastelloy, (100) Si, and polished Y-TZP substrates were mounted on stainless steel heater blocks using the procedures

described in Chapter 3. The majority of work centers on films deposited on Pyrex, where desired (200) biaxial alignment was observed. The angle of ion incidence was varied from 8° to 48° from the substrate plane in this study.

The substrate temperature was 600°C for all YSZ depositions unless otherwise noted. Substrates were etched with the ion beam for 10 min. prior to film deposition to ensure surface cleanliness. Films were deposited at rates of either 1.2 or 2.4 Å/s, as measured from SEM fracture micrographs, and final film thicknesses were approximately 1 μm. The ion beam energy was either 75 or 300 eV, and the current density was either 18 or 84 $\mu A/cm^2$.

4.2.2 Ion Assisted Electron Beam Evaporation of YSZ with Varied Substrate Heating

Amorphous quartz, type 7740 Pyrex, and polished Hastelloy substrates were mounted on stainless steel heater blocks using the procedures described in Chapter 3. The gross deposition rate was 4.4 Å/s for all films. The net deposition rate for films deposited with ion assist at 45° bombardment angle, 300eV beam energy, and 57$\mu A/cm^2$ ion fluence was nearly the same, as determined using the envelope technique of Swanepoel.[58] The ionized gas was a mixture of Ar with 8 vol% O_2. Films were deposited to a thickness of 1.3 μm. A control and an IBAD film were deposited without active substrate heating. The substrate temperature rose from an initial temperature of 20°C to a steady state temperature of 220°C during the control deposition due to radiant heat from the electron beam evaporator. The substrate temperature rose to 250°C during the ion assisted electron beam deposition due to heating from the ion beam and radiant heat from the ion source. These runs are referred to as Runs 1 and 2, respectively in Table 4.1. A control film and an IBAD film were fabricated at 400°C in Runs 3 and 4. Two differing substrate heating segments were used in Runs 5 and 6. The first 4400Å were evaporated by IBAD without active substrate heating in Run 5, followed by 8800Å deposited at 400°C. The substrate temperature was 400°C for the first 4400Å of Run 6. Deposition was stopped to allow the substrate block to cool to 20°C before depositing the final 8800Å.

Table 4.1 Deposition conditions for films deposited without active substrate heating and at 400°C by ion assisted electron beam evaporation

Deposition Conditions			
Run	Substrate Temperature (°C)	Thickness	Ion Assist
1	RT	1.3μm	No
2	RT	1.3μm	Yes
3	400	1.3μm	No
4	400	1.3μm	Yes
5	RT 400	4400Å 8800Å	Yes Yes
6	400 RT	4400Å 8800Å	Yes Yes

RT - Run started at 20°C, with substrate temperature reaching ~250°C by end of deposition.

4.2.3 Film Characterization

Film orientation was examined using θ-2θ X-ray diffraction, four-circle diffractometry, X-ray pole figures, and X-ray phi scans using a CuKα radiation source, as described in Chapter 3. Selected samples was observed using scanning electron microscopy and cross-sectional transmission electron microscopy. Dr. Paul C. McIntyre performed the high resolution TEM microscopy featured in this chapter.

4.3 RESULTS: ION ASSISTED E-BEAM EVAPORATION

4.3.1 Ion Assisted Electron Beam Evaporation of YSZ at 600°C

4.3.1.1 Effects of IBAD Parameters on YSZ Biaxial Alignment on Pyrex

YSZ films deposited at 600°C without ion assist are crystalline and feature strong (200) preferred uniaxial orientation. The θ-2θ XRD trace for a film deposited at 2.5Å/s at 600°C without ion assist is shown in Fig. 4.1. The principal reflection of randomly oriented polycrystalline YSZ is (111), which is hardly evident in the XRD trace. The (111) pole figure for this film, shown in Fig. 4.1, confirms the presence of random in-plane orientation. The (111) reflection intensity corresponding to the (200) uniaxial film alignment normal to the substrate is distributed uniformly at χ=35°. Only uniaxial (200) orientation was observed in YSZ films deposited on Pyrex at 600°C without ion assist.

A film fabricated with ion assist of 75eV beam energy and 8 $\mu A/cm^2$ at 45° bombardment angle at the same deposition rate and substrate temperature features (200) biaxial alignment. The (200) normal orientation is evident in the θ-2θ trace in Fig. 4.2. The (111) X-ray pole figure for the film is shown in Fig. 4.2. The four poles at χ=35° are the in-plane {111} reflections for (200) grains aligned parallel to the substrate plane. The projection of the assisting ion beam lies at ϕ=0°. This in-plane orientation is consistent with {220} in the film plane aligned normal to the assisting ion beam at χ=45° and ϕ=0°. All films fabricated on Pyrex with ion assist exhibited strongly (200) preferred orientation normal to the substrate, although small (111) and (311) reflections were

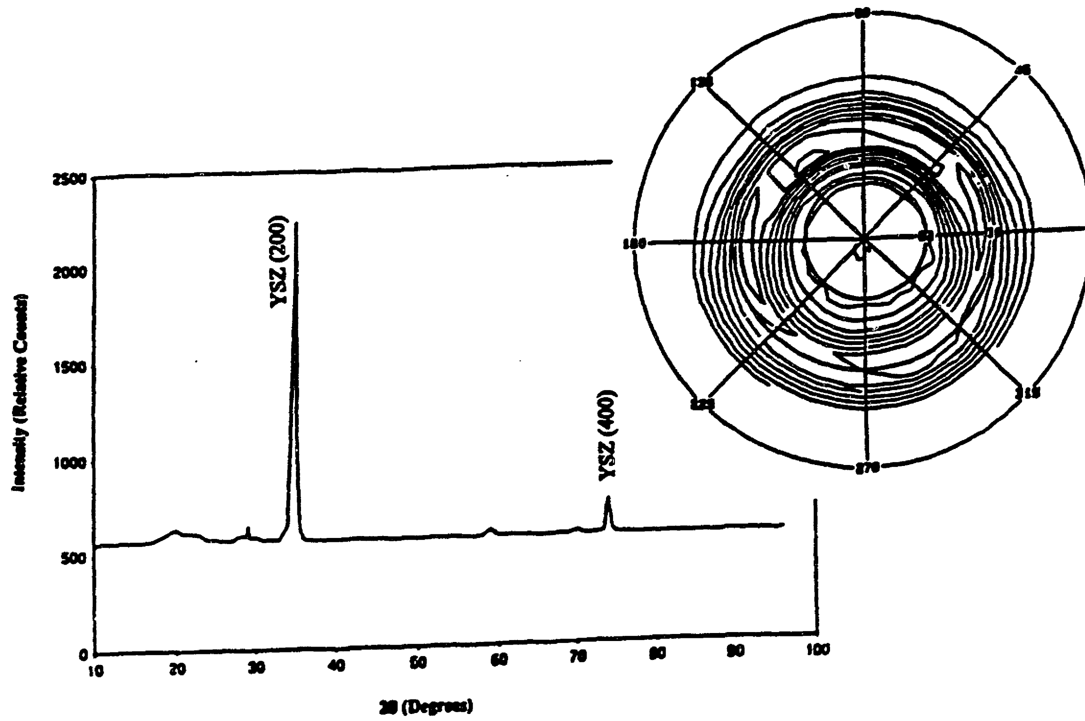

Figure 4.1 θ-2θ X-ray trace and (111) X-ray pole figure of YSZ film fabricated by electron beam evaporation at 600°C on Pyrex.

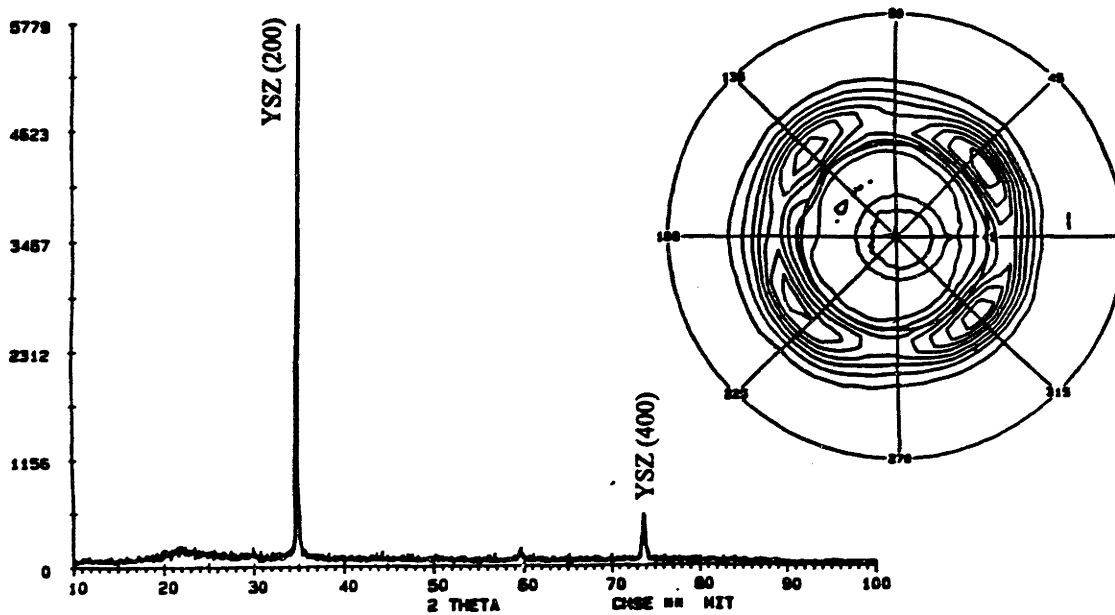

Figure 4.2 θ-2θ X-ray trace and (111) X-ray pole figure of YSZ film fabricated by ion assisted electron beam evaporation at 600°C on Pyrex.

sometimes observed. IBAD film orientation is a complex function of deposition rate, bombardment angle, assisting beam energy, and substrate temperature. Biaxial alignment of several grain populations occurs under appropriate IBAD conditions. Fig. 4.3 shows the (111) pole figure for YSZ deposited at 1.1 Å/s with a beam energy of 75 eV, a bombardment angle of 38° and a substrate temperature of 600°C. Eight superimposed (111) reflections contribute to each pole figure. The superposition of multiple reflections obscures the individual poles. Two reflections cause the broad pole from ϕ=190° to ϕ=270°. The film texture results from biaxially aligned populations of (200) and (311) grains. The four poles at χ=35° are the (111) reflections of the grains with (200) normal orientation, as shown in the upper inset of Fig. 4.3. The remaining poles are the (111) poles of grains with (311) near-normal orientation. The (311) grains are not aligned parallel to the substrate normal, but are slightly tilted in the direction of the incident ion beam. The (111) reflection for the (311) normal orientation should lie at χ=60.5° in the stereographic projection, not at χ=43°. The (111) poles of the (200) normal orientation are offset 45° from the ion beam projection, indicating the (220) axis of the (200) biaxially aligned grains is aligned with the ion beam. Both the (200) and (311) grain populations are aligned with respect to the ion beam.

A series of films was fabricated by ion assisted, electron beam evaporation on Pyrex with a deposition rate 2.5 Å/s and assisting ion beam energy of 75 eV at bombardment angles of 8°, 23°, 38°, and 48° with respect to the substrate plane. The (111) pole figures for these films are shown in Fig. 4.4. All of the films are biaxially aligned. Several different in-plane orientations are obtained under these conditions. While the 38° and 48° angles are close to the [111] and [110] channeling directions with <200> fixed normal to the substrate, 8° and 23° do not correspond to channeling directions. Biaxial alignment is obtained at all bombardment angles with IBAD, not just those corresponding to channeling directions.

4.3.1.2 Substrate Dependent Film Orientation

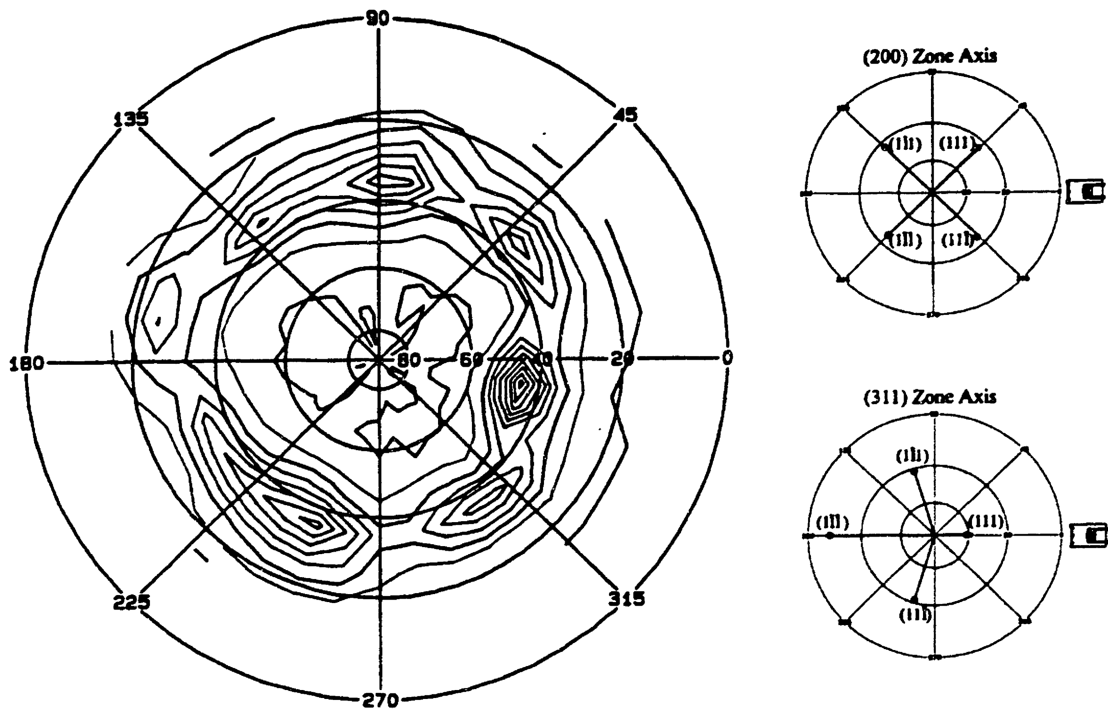

Figure 4.3 (111) X-ray pole figure of IBAD YSZ film exhibiting two biaxially aligned grain populations.

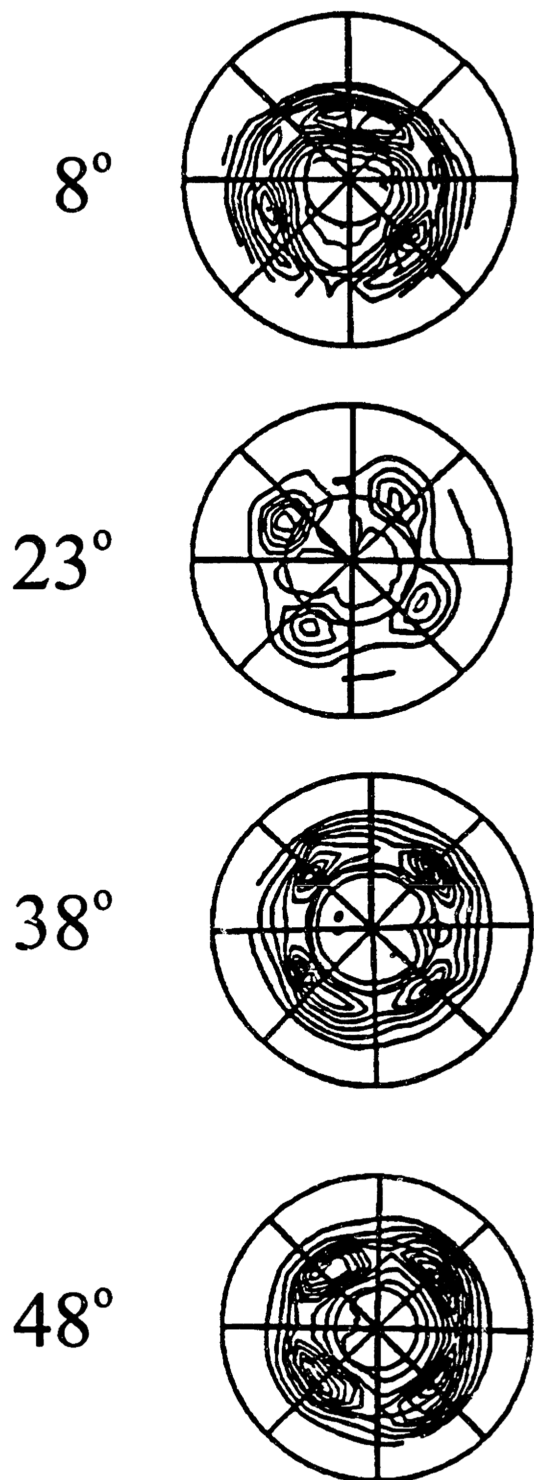

Figure 4.4 (111) X-ray pole figures of IBAD YSZ films showing in-plane orientations of (200) biaxially aligned YSZ films as a function of ion bombardment angle.

Crystalline YSZ films are observed on all substrates for films deposited at 600°C, both with and without ion assist. Films deposited under identical conditions on different substrates featured different orientations normal to the substrate, both with and without ion assist. Films deposited on Pyrex and quartz under identical conditions often exhibited different in-plane orientations even when the θ-2θ XRD traces were similar. YSZ films were deposited at 2.5Å/s, 45° bombardment angle, 75 eV beam energy, and 600°C substrate temperature to the same nominal thickness of 1 μm. Both films exhibited preferred (200) normal alignment. The relative (311) θ-2θ X-ray intensity was greater for the film on quartz. The film on Pyrex exhibited (200) biaxial alignment, as shown in Fig. 4.5(a). The film deposited on quartz exhibited primarily (311) biaxial alignment, as shown in Fig. 4.5(b). The in-plane orientation difference between the two films may be attributed to different relative populations of (200) and (311) grains nucleated on Pyrex and quartz.

4.3.1.3 Development of (200) Biaxial Alignment on Pyrex: X-ray Examination

The development of (200) YSZ biaxial alignment on Pyrex was examined by depositing a series of films to 2600Å, 5200Å, and 10,400Å thickness at a deposition rate of 2.5 Å/s, a bombardment angle of 45°, an assisting ion beam energy of 75 eV, and a constant substrate temperature of 600°C. The θ-2θ X-ray trace information and (111) X-ray pole figures for the films are shown in Fig. 4.6. It should be noted that the θ-2θ X-ray data provides only a qualitative measure of the true orientation normal to the substrate, as the (311) grain normals are tilted in the direction of the ion beam, precluding quantitative comparisons of the (111), (200), and (311) orientations normal to the substrate.

Preferred (200) normal orientation has been established within the first 2600Å. Smaller (311) and (111) reflections of nearly identical intensity are also present. Biaxially aligned (111), (200), and (311) grains contribute to the (111) pole figure for the 2600Å film. Grains with (111) biaxial alignment cause the pole about the zone axis. The region around ϕ=0°, the projection of the incident ion beam, has contributions from the

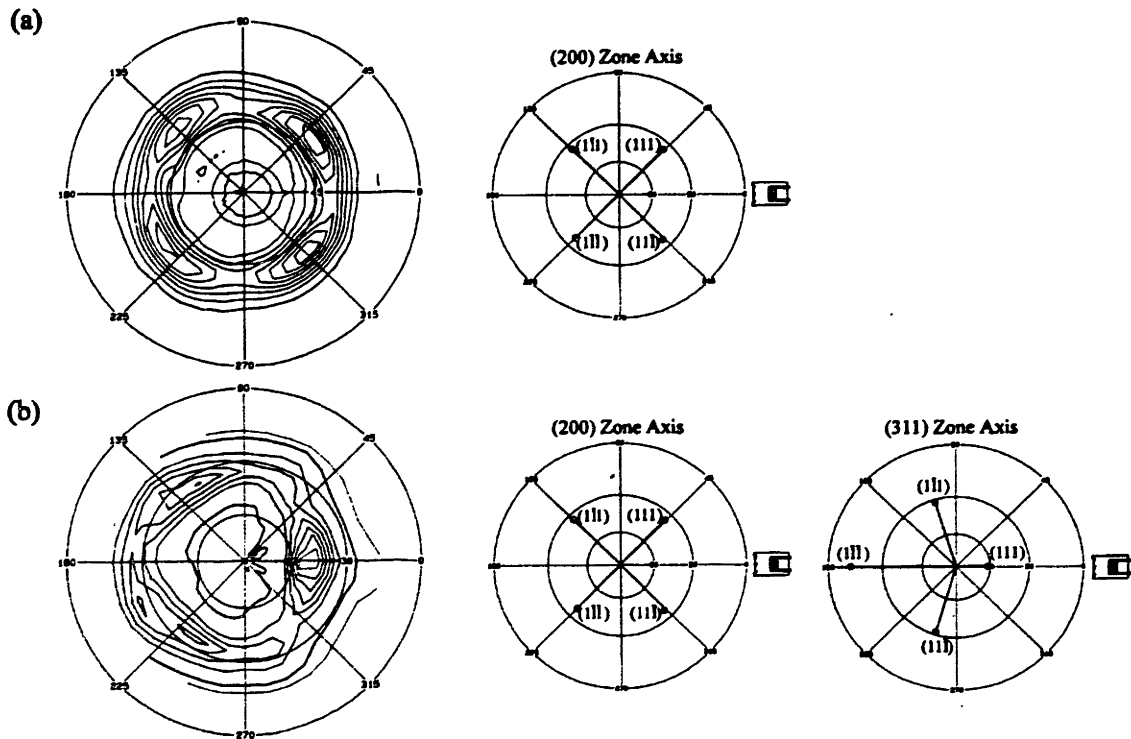

Figure 4.5 (111) X-ray pole figures for films deposited on (a) Pyrex and (b) quartz by ion assisted e-beam evaporation at 600°C.

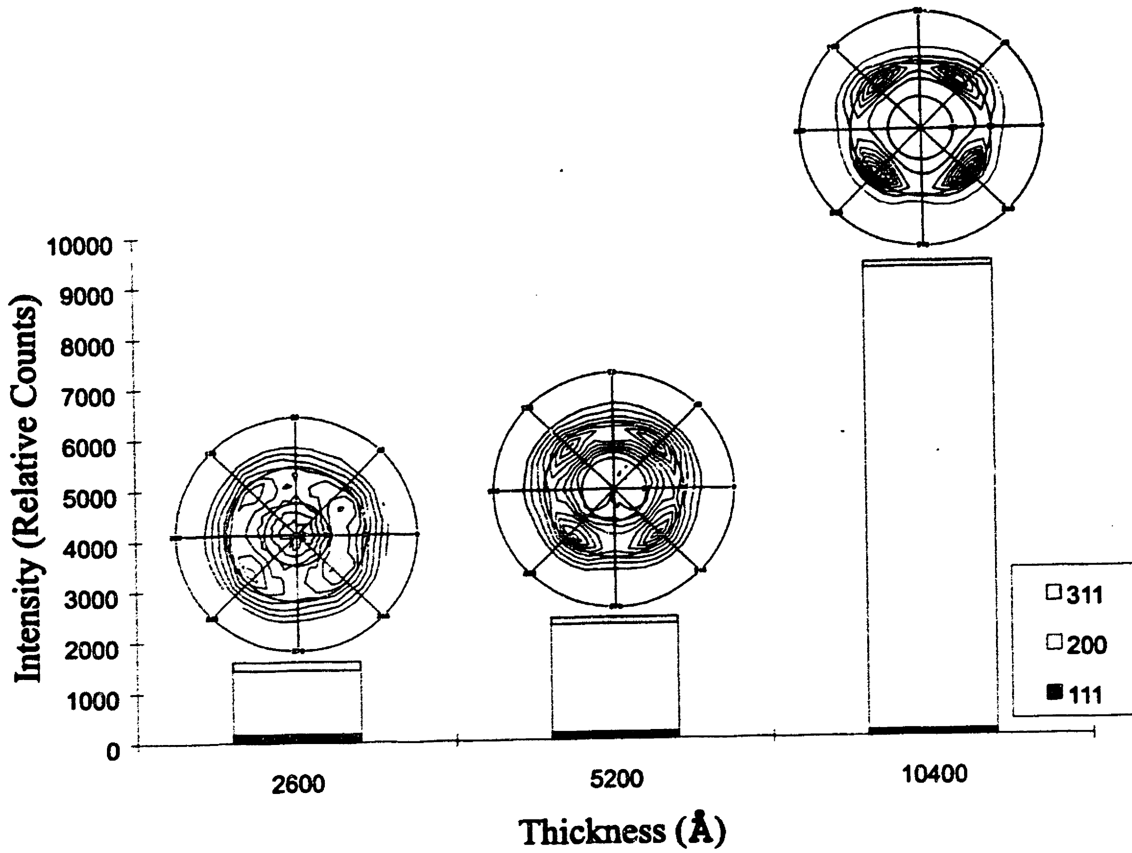

Figure 4.6 θ-2θ X-ray trace intensities and (111) X-ray pole figures showing development of YSZ (200) biaxial alignment on Pyrex as a function of film thickness.

(111) pole of the (311) near-normal orientation at $\phi=0°$ and the (111) poles of the (200) normal orientation at $\phi=45°$ and $\phi=315°$.

Improved (200) biaxial alignment is clearly evident from the θ-2θ X-ray trace and (111) X-ray pole figure of the 5200Å film. The absolute intensities of the (311) and (111) reflections were nearly identical to those from the 2600Å film, while the (200) θ-2θ intensity increased significantly. The relative (200) grain intensity increased substantially over this thickness range. The improved (200) biaxial alignment is evident in the pole figure for the 5200Å film. The in-plane intensities from the (111) and (311) grain populations are negligible in comparison to that of the biaxially aligned (200) grains, indicating that the relative (200) X-ray intensity increased significantly within the second 2600Å of deposition.

The (200) intensity in both the θ-2θ X-ray trace and (111) X-ray pole figure of the 10400Å film are increased compared to that present in the 5200Å film. The relative (200) X-ray intensity increased continually with film thickness, as the absolute (111) and (311) θ-2θ X-ray intensities are nearly identical in all three films while the absolute (200) intensity increased monatonically. The (200) biaxial alignment present in the film had apparently been established within the first 2600Å of deposition, as the relative (111) and (311) contributions decreased continuously with increased film thickness.

4.3.1.4 Model Experiments on Amorphous Substrates

Four YSZ films were deposited on Pyrex under modified deposition conditions to clarify the mechanism of biaxial alignment. All films were deposited at 2.5Å/s to 1 μm thickness on Pyrex substrates held at 600°C. The orientation of the substrates was such that the bombardment angle with respect to the substrate plane was 45°, whether or not ion assist was employed. All films were deposited with gases flowing through the assisting ion source to maintain identical chamber pressures for all depositions. The first film (film 1) was a control in which the YSZ was evaporated without ion assist. The second film (film 2) was deposited with 75eV ion assist throughout deposition. In the third film (film 3), the 75eV ion beam was active during the first 500Å of deposition after

which deposition continued to 1 μm without ion assist. The fourth film (film 4) was fabricated by standard electron beam evaporation during the first 600Å. The shutter over the evaporation source was then closed, and the ion beam was ignited so that the existing YSZ film was bombarded with 75 eV ions for ten minutes. The ion beam was then turned off and the shutter over the evaporation source was removed. Deposition continued without ion assist until the film reached a thickness of 1 μm.

All films featured (200) preferred normal orientation as determined using θ-2θ X-ray diffraction. The (111) X-ray pole figures for films 1-4 are shown in Figs. 4.7(a) - 4.7(d), respectively. The control film deposited without ion assist (film 1) featured (200) uniaxial alignment normal to the substrate, but random in-plane alignment as indicated by the pole figure in Fig. 4.7(a). Films 2-4 all exhibited (200) biaxial alignment, although to different extents, as shown in Fig. 4.7(b)-4.7(d). The in-plane alignment is best defined for film 2, which was fabricated with ion assist during the entire deposition.

4.3.1.5 Development of (200) Biaxial Alignment on Pyrex: Microstructural Examination

Cross-sectional TEM specimens were prepared from the specimens discussed in the previous section. The films prepared both with and without ion assist feature similar columnar microstructures. A typical SEM cross section of a biaxially aligned YSZ film is shown in Fig. 4.8. A granular region is present near the film/substrate interface. The remainder of the film is dominated by well-defined columns of approximately 1000Å width. Columns were observed to tilt toward the directions of the ion beam and evaporation source. Similar tilted columnar microstructures were observed on all substrates for films fabricated both with and without ion assist.

Figure 4.9 is a low magnification cross-sectional micrograph from an IBAD YSZ film fabricated under the same conditions as film 2. The specimen was thinned so that (200) biaxially aligned columns were viewed near a <100> zone axis. The path of the incident ion beam in the cross section plane is marked by a large arrow at the top of Fig. 4.9. A tilt of the columns toward the ion beam and evaporation source is evident in this image. The column structure developed from initial nuclei on the substrate surface

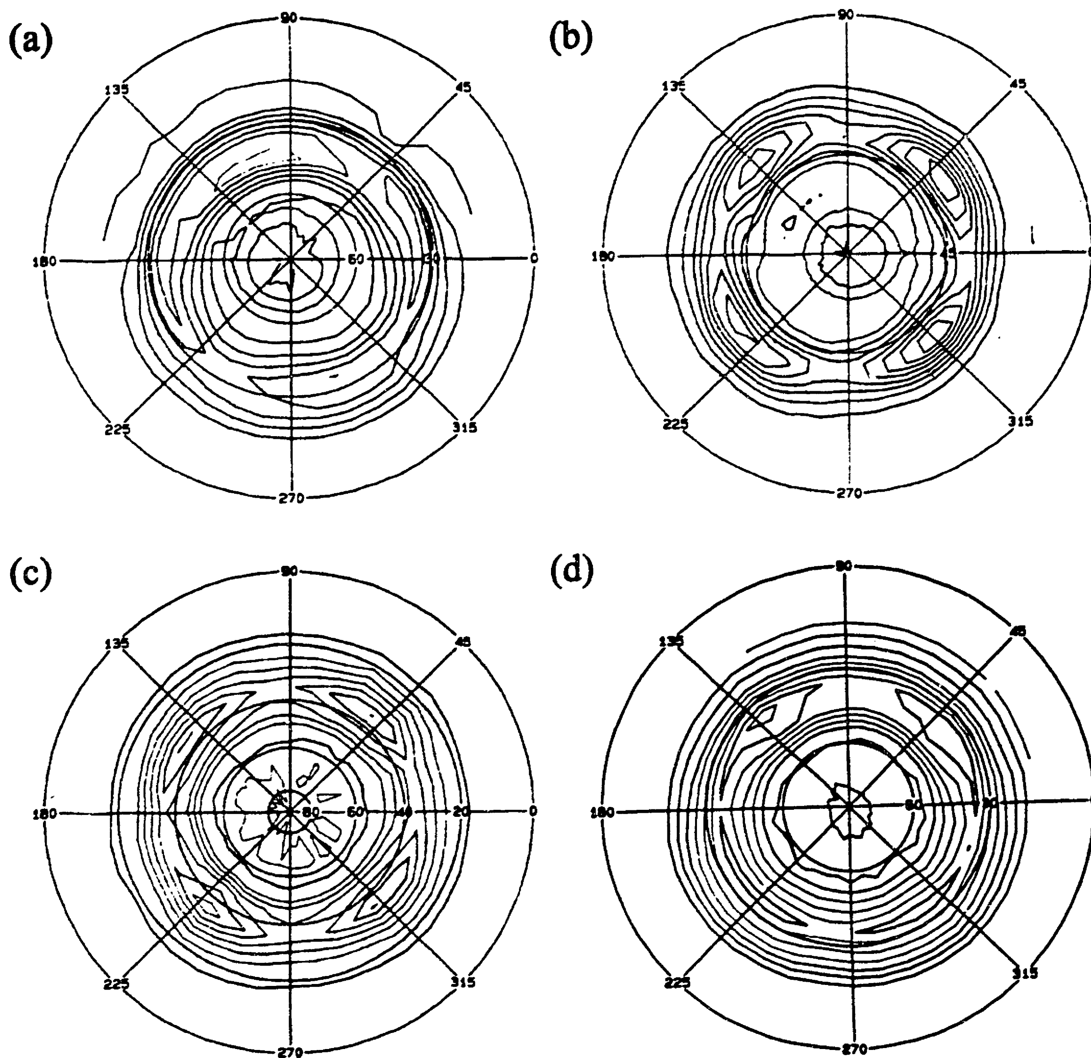

Figure 4.7 (111) X-ray pole figures for films evaporated on Pyrex (a) without ion assist (b) with 75eV ion assist throughout deposition (c) with 75eV ion assist during the first 50nm and by standard e-beam evaporation to final thickness of 1 μm and (d) without ion assist during first 60nm, ion etched at 75eV for 10 min, and evaporated to final thickness of 1 μm.

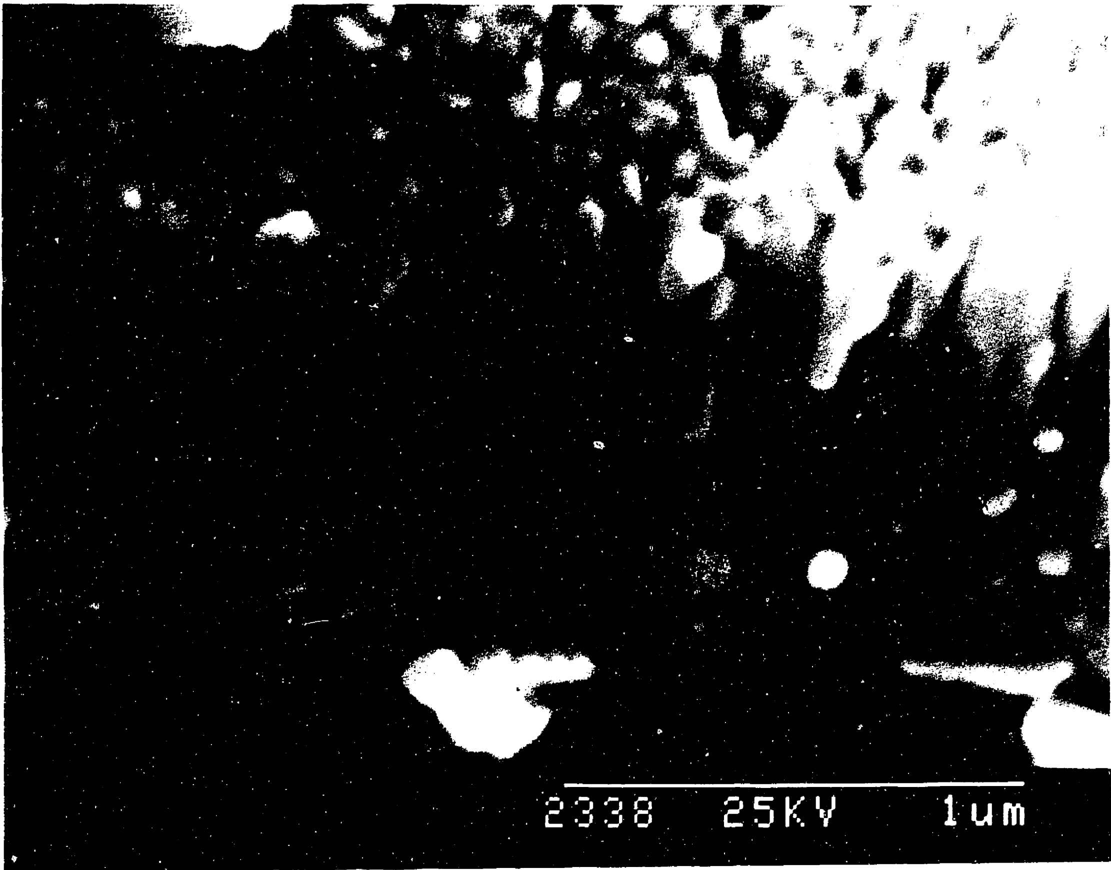

Figure 4.8 SEM micrograph of ion assisted e-beam YSZ film deposited on Pyrex at 600°C.

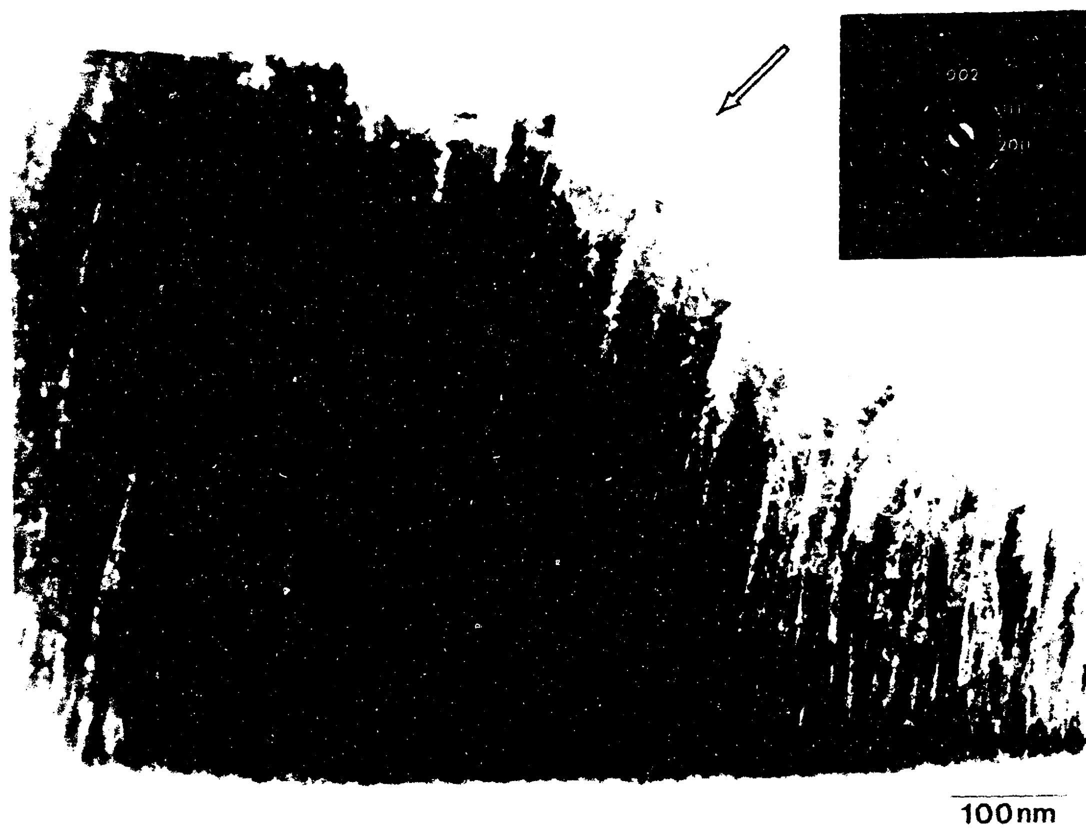

Figure 4.9 Low magnification cross-sectional TEM image of IBAD YSZ film deposited on Pyrex at 600°C.

during the first 600-800Å of deposition. The columns grew wider, on average, with increasing deposition until a relatively thickness-independent column diameter of ~200Å developed after 1600 to 1800Å of deposited film.

The presence of several grain populations is evident in the inset electron diffraction pattern in Fig. 4.9. The diffraction pattern results from a superposition of reflections from three (200) grain populations, as shown in Fig. 4.10. The majority of the columns in Fig. 4.9 are (200) biaxially aligned columns viewed along a <100> zone axis. These columns contribute (200) and (002) reflections in the diffraction pattern. Two (200) YSZ reflections present in the inset electron diffraction pattern indicate several of the (200) oriented columns in this region had other in-plane alignments. There are a number of (200) oriented columns viewed down a <110> zone axis. The in-plane alignment of these columns is rotated 45° relative to that of the majority of (200) biaxially aligned grains. This is the YSZ in-plane alignment noted by Iijima *et al.*[3-8] Second, there is a reflection contribution from (200) uniaixally aligned columns. Several populations contribute to the diffracted intensity of the {111} planes. The strength of the (111) reflections is consistent with a number of (200) oriented columns being viewed down a <110> zone axis. There is also a (111) reflection from (200) uniaxially aligned columns. The latter two (200) column populations contribute several {111}, {200}, {220}, and {311} reflections.

Figure 4.11 is a bright field TEM image taken from film 3, the film deposited with ion assist during the first 500Å of deposition and without ion assist during deposition of the remaining ~1 μm YSZ film thickness. The region in Fig. 4.11 is in the upper portion of the IBAD YSZ layer. Ion milling of the foil during TEM specimen preparation resulted in removal of the Pyrex substrate and the film immediately adjacent to the substrate interface. The TEM specimen was sectioned and thinned so that the majority of the (200) biaxially aligned columns were imaged near a <100> zone axis. Interpretation of the microstructure as viewed in cross section is complicated by the frequent overlap of YSZ columns. The YSZ column in the center of the image is, however, easily resolved from its neighbors. The column has a faceted dendritic character, with obvious sidebranch development. Analysis of the lattice fringes in the

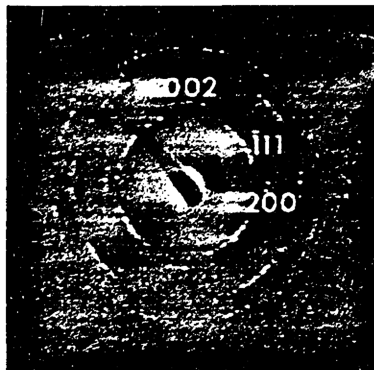

Majority (200) Biaxially Aligned Grains

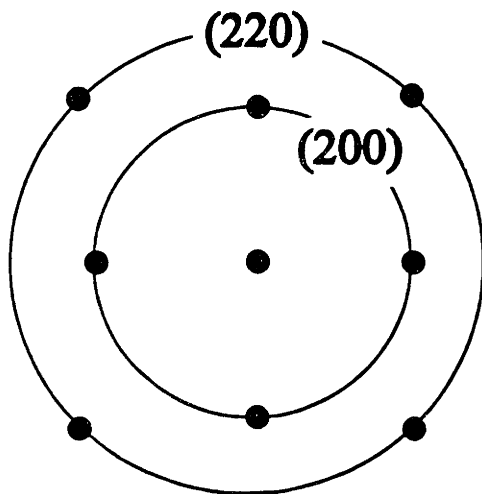

Minority (200) Biaxially Aligned and (200) Uniaxially Aligned Grains

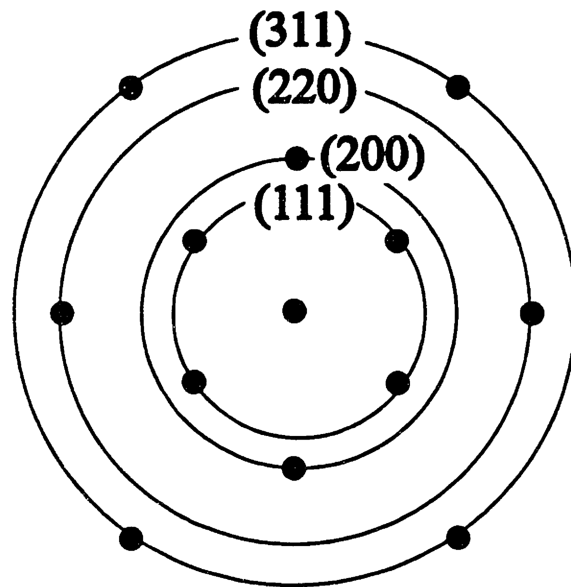

Figure 4.10 Selected area electron diffraction pattern of (200) biaxially aligned film shown in Fig. 4.9. Diffraction spots can be attributed to three (200) grain populations.

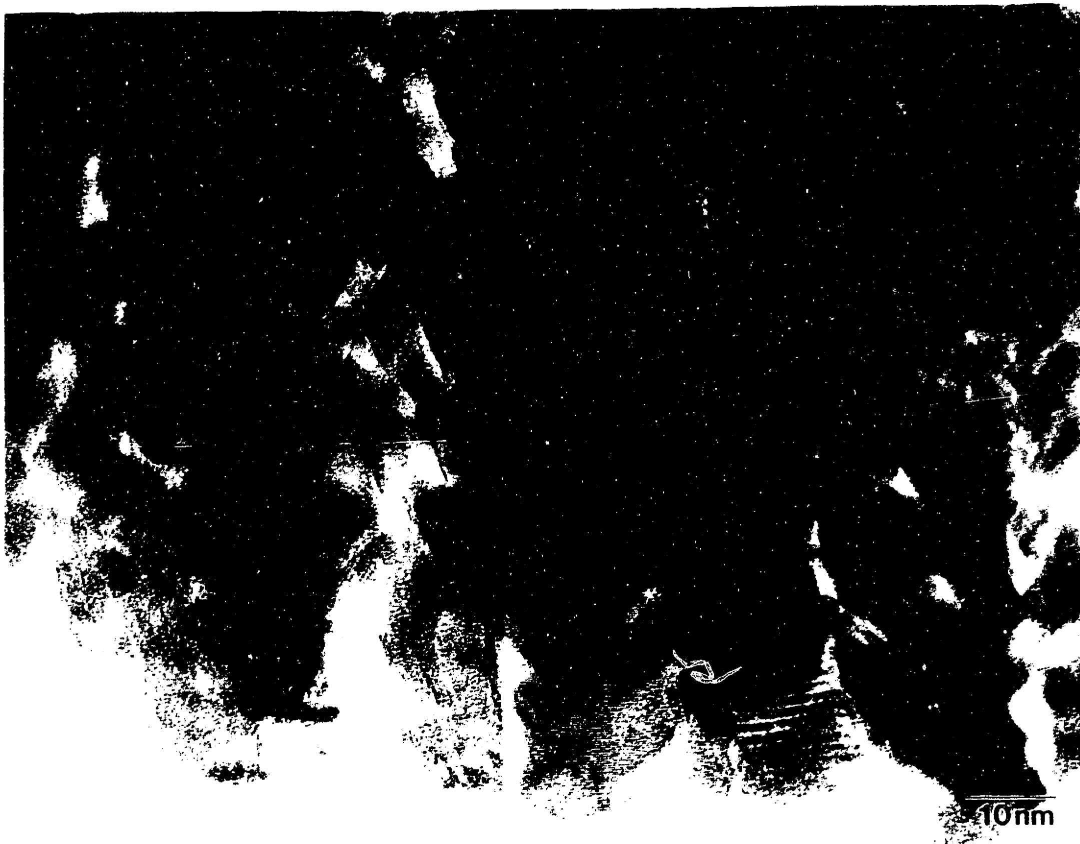

Figure 4.11 Cross-sectional TEM image of IBAD YSZ film showing secondary dendrites of (200) YSZ columns.

column indicated the (200) plane paralleled the film plane, consistent with the θ-2θ XRD patterns of all the YSZ films deposited at 600°C on Pyrex. Fringes of the (111) plane are also visible, and these make an angle of ~55° with the (200) fringes, indicating the columns was viewed very close to its [100] zone axis. The sidebranches visible in this portion of the dendritic column are oriented at angles of approximately 35° to the YSZ (200) fringes. This dendritic geometry is consistent with sidebranches parallel to the upward-pointing <111> axes of the columns. The sidebranch spacing was ~100Å in the IBAD YSZ layer and the sidebranch length was apparently constrained to 50-100Å by impingement with adjacent columns in this region.

The dendritic columnar structure was more pronounced near the film surface, as is evident in Fig. 4.12. The bright field image shows the tops of several adjacent columns and the beginning of the glue line in the same cross-sectional specimen shown in Fig. 4.11. The TEM specimen was maintained in the same orientation in both Figs. 4.11 and 4.12, with most (200) biaxially aligned columns viewed near their <100> zone axes. The columns appear to terminate in facets. The sidebranch development and spacing were similar to those observed in Fig. 4.11, although the increased column width in the upper portions of the film resulted in greater sidebranch lengths.

The faceted dendritic microstructure observed in these films provides a clue to the nature of film growth in this system. The dendrite sidebranches occur with a definite crystallographic habit for both IBAD and non-IBAD films: branches parallel to the upward-pointing <111> axes of the individual columns. The habit of sidebranches that form during growth of faceting crystals, including many ceramics and semiconductors, is a function of the orientation of layer source planes relative to the fast growth direction. Impingement of active layer source planes leads to the formation of ribs that, under conditions of high driving force, form sidebranches.[64] The resulting sidebranch directions are those midway between operating layer sources that make the greatest angle other than 90° with the fast growth direction. The fast growth case for the films under these conditions is the YSZ [100] axis, and the sidebranch directions are upward-pointing <111>. The geometry is consistent with faceted {101} layer source planes on the column

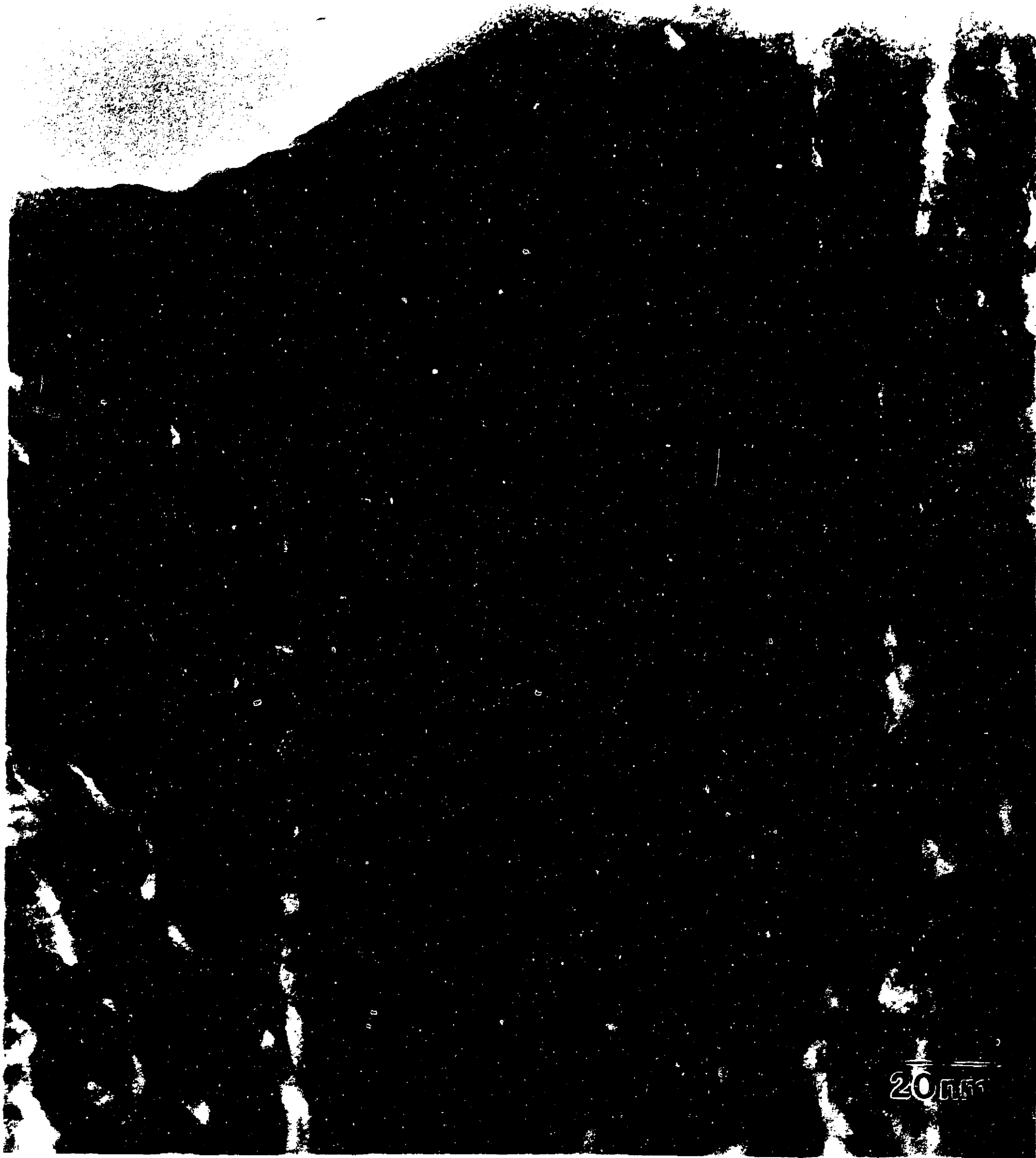

Figure 4.12 Cross-sectional TEM image of IBAD YSZ film near the top film surface.

sides. A hypothetical model of the column structure that incorporates these sidebranch and layer source orientations is shown in Fig. 4.13.

4.3.2 Ion Assisted E-Beam Evaporation of YSZ with Varied Substrate Heating

4.3.2.1 X-ray Investigation

The experimental conditions and X-ray diffraction results from this study are summarized in Table 4.2. Control films deposited at room temperature without ion assist were nearly amorphous, with a small (111) component present according to XRD (Run 1). The films deposited at 4.4Å/s at room temperature with 300 eV ion assist were crystalline and biaxially aligned on all three substrates (Run 2). The θ-2θ XRD scans for the films deposited in Run 2 are shown in Fig. 4.14(a). The (111) X-ray pole figure for the film deposited on Pyrex is shown in Fig. 4.14(b).

The films deposited at 4.4 Å/s at 400°C without ion assist (Run 3) featured (200) uniaxial alignment on Pyrex and quartz, and (111) uniaxial alignment on Hastelloy. The films deposited at 400°C with ion assist (Run 4) featured (200) uniaxial alignment on Pyrex, and (111) uniaxial alignment on quartz and Hastelloy. Runs 5 and 6 were performed in two differing substrate heating segments. In Run 5, 4400Å of YSZ was evaporated without active substrate heating. Subsequently, 8800Å of YSZ was deposited at 400°C with ion assist. The resulting films were (200) biaxially aligned on all substrates. Mixed orientations were observed for all three films deposited in Run 6, with 4400Å deposited at 400°C without ion assist followed by 8800Å deposited at room temperature with ion assist. The XRD trace for the film on Pyrex featured a (111) reflection with half the intensity of the dominant (200) reflection. The XRD traces for the films on quartz and Hastelloy featured (200) reflections with a third of the intensity of the dominant (111) reflections.

IBAD films deposited without active substrate heating featured the same crystallographic texture on all three substrates, as evidenced by Run 2. The substrate-independent biaxial alignment present in these films had not been observed for films fabricated at 600°C. Substrate-dependent alignment was observed in the control and

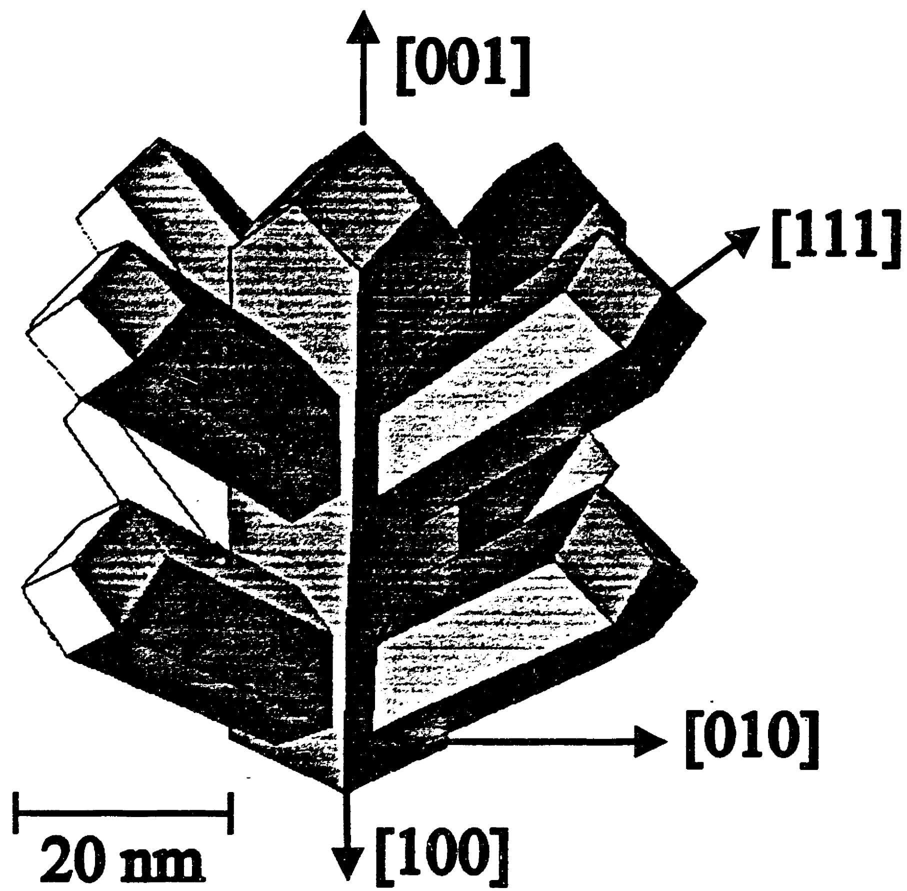

Figure 4.13 Hypothetical model of faceted YSZ column structure observed in films deposited on Pyrex at 600°C.

Table 4.2 X-ray diffraction results as a function of IBAD conditions and substrate for films deposited without active substrate heating and at 400°C by ion assisted electron beam evaporation

Deposition Conditions			Pyrex		Quartz		Hastelloy	
Run	Substrate Temperature (°C)	Ion Assist	Out of Plane	In Plane	Out of Plane	In Plane	Out of Plane	In Plane
1	RT	No	amor.	NA	amor.	NA	amor.	NA
2	RT	Yes	(200)	BA	(200)	BA	(200)	BA
3	400	No	(200)	NA	(200)	NA	(111)	NA
4	400	Yes	(200)	BA	(111)	BA	(111)	BA
5	RT, 400	Yes	(200)	BA	(200)	BA	(200)	BA
6	400, RT	Yes	(200); (111)	BA	(111); (200)	BA	(111); (200)	BA

RT - Run started at 20°C, with substrate temperature reaching ~250°C by end of deposition.

amor. - largely amorphous, with small (111) component present

NA - No in-plane alignment

BA - Biaxially aligned, with in-plane alignment

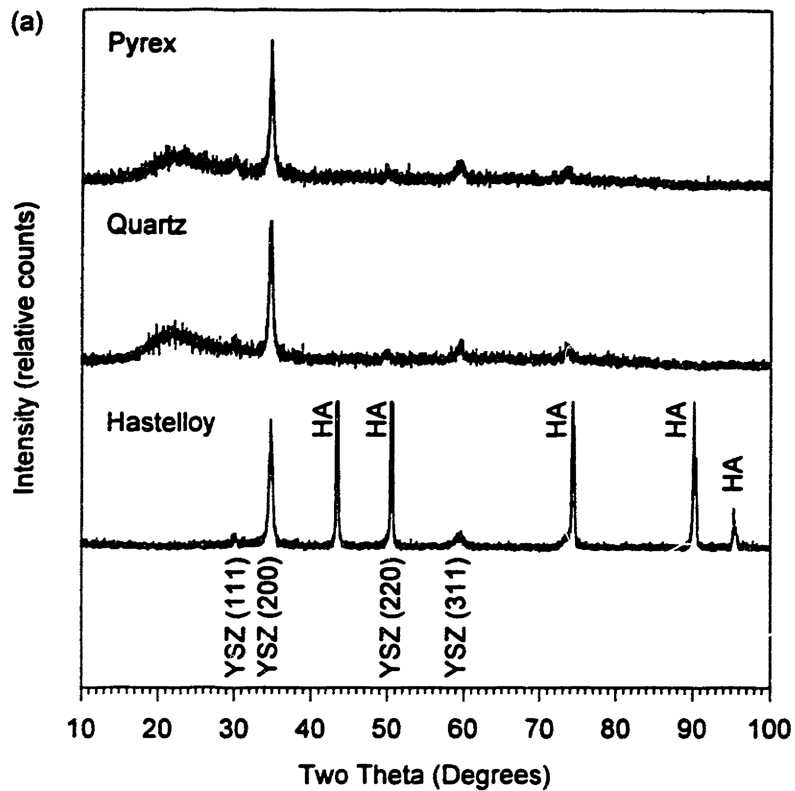

(b)

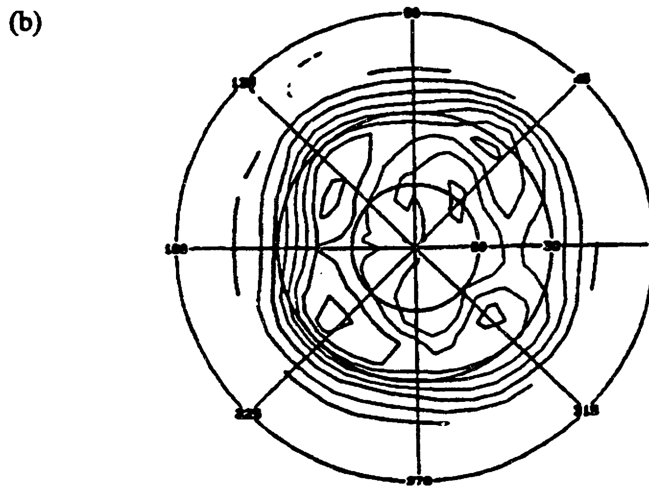

Figure 4.14 (a) θ-2θ X-ray traces of YSZ films deposited on Pyrex, quartz, and Hastelloy substrates by ion assisted e-beam evaporation without active substrate heating. (b) (111) X-ray pole figure of film deposited on Pyrex.

IBAD runs at 400°C, as had been observed for IBAD at 600°C. The films deposited in Run 5, with initial deposition at room temperature and final deposition at 400°C, featured substrate-independent (200) biaxial alignment. The crystalline orientation of the films deposited in Run 5 were similar to those observed from the films in Run 2. The orientation that was present after the deposition without active substrate heating was maintained throughout deposition at 400°C. Conversely, the films deposited in Run 6, with initial deposition at 400°C and subsequent deposition without active substrate heating, featured a substrate-dependent mixture of orientations. The film orientation was unlike that of either the films deposited at 400°C throughout deposition (Run 4) or without active substrate heating throughout deposition (Run 2). The predominant orientation of all substrates in Run 6 were identical to the orientation observed in Run 4. It appears that (200) oriented grains were formed on each during the last 8800Å of film deposited without active substrate heating. The film deposited in the second step of Run 6 without active substrate heating did not mimic the orientation of the film beneath.

4.3.2.2 Film Microstructure

SEM fracture micrographs of the IBAD film deposited at on Pyrex without active substrate heating are shown in Fig. 4.15. The film is composed of discontinuous columns, and the surface is rough. The column shapes are not as uniform as those observed for films deposited at 600°C.

A cross-sectional TEM micrograph of the IBAD YSZ film deposited on quartz in Run 2 is shown in Fig. 4.16. There microstructure features numerous diamond-shaped grains. The low magnification prevents evaluation of the grain crystalline orientations. It does appear that the grains are faceted. Assuming the (200) direction of each of the grains is aligned normal to the substrate, the angles made by the facets do not seem to match with either {110} or {111} planes. There appear to be distinct faceted boundaries between the grains. The grains are stacked vertically and at an angle, perhaps a shadowing effect from evaporation. These grain groupings are distinctly different from the continuous columns observed though the entire thickness of IBAD YSZ films deposited at 600°C.

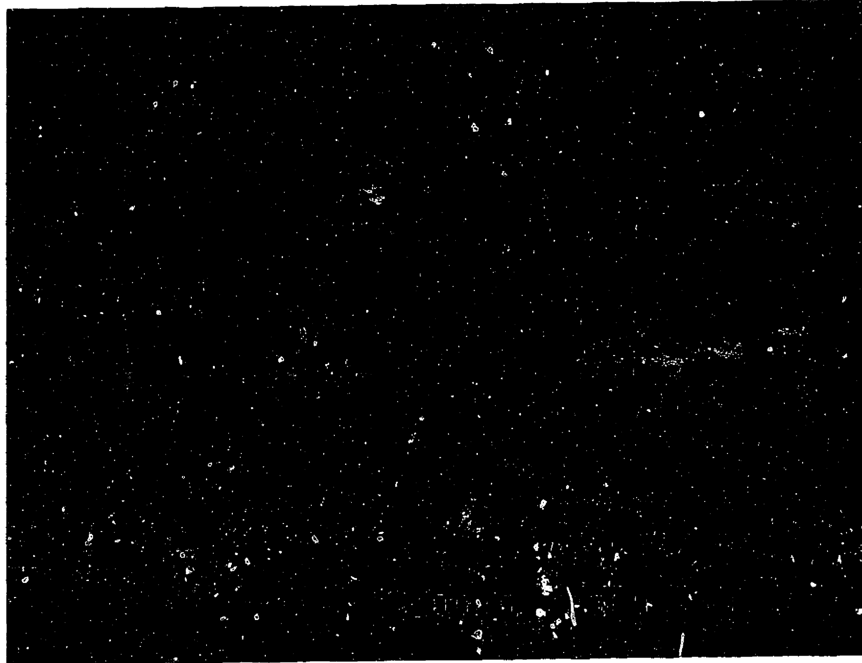

Figure 4.15 SEM micrograph of ion assisted e-beam YSZ film deposited on Pyrex without active substrate heating.

Figure 4.16 Low magnification cross-sectional TEM micrograph of ion assisted e-beam YSZ film deposited on Pyrex without active substrate heating.

4.4 DISCUSSION: ION ASSISTED E-BEAM YSZ BIAXIAL ALIGNMENT

(200) biaxially aligned YSZ films were fabricated by ion assisted e-beam evaporation without active substrate heating, at 400°C, and at 600°C substrate temperature. The in-plane orientation of films fabricated with and without active substrate heating are similar, with {220} planes are aligned with the projection of the assisting ion beam. This is contrary to the observation of {111} aligned with the assisting ion beam projection for YSZ films fabricated by dual ion beam deposition by Iijima *et al.*[3-8]

Several aspects of the ion assisted e-beam films fabricated without active substrate heating and at elevated substrate temperature are clearly different. The fine-grained microstructure observed for films fabricated without active substrate heating is similar to the Zone I microstructure observed by Grovenor *et al.*[26] at low substrate temperature. The columnar microstructure observed for films fabricated at 600°C is similar to the Zone II microstructure of the same structure zone diagram observed at higher homologous temperatures. The nature of biaxial alignment differed as well, as substrate-independent biaxial alignment was observed for films fabricated without active substrate heating while substrate-dependent biaxial alignment was observed for films fabricated at 400°C and 600°C.

4.4.1 Growth Extinction Model for Ion Assisted E-beam Biaxial Alignment at 600°C

Tilted columnar microstructures were observed for films evaporated at 600°C both with and without ion assist. Thin columnar film microstructures are consistent with Zone II fabrication on the Grovenor *et al.*[26] structure zone model. The angular columnar tilt as observed by SEM and the columnar microstructure as observed by SEM and TEM were similar for films fabricated with and without ion assist. These observations are consistent with shadowing with respect to the evaporant source and indicate that the assisting ion beam did not appreciably alter columnar development.

The results from the model experiments on Pyrex indicate that IBAD biaxial alignment is linked to growth rather than nucleation under these conditions. The development of film texture in the experiment where deposition and ion etching were carried out independently can only be explained by a growth-controlled mechanism. Random in-plane orientation was present in film 4 when electron beam evaporation was stopped after 600Å of film had been deposited. Cross-sectional TEM evidence shows a continuous film was present by that thickness. The subsequent 10 minute ion bombardment at 75eV was the only ion assist during the deposition. The experiment demonstrated that in-plane alignment does not occur upon nucleation under these conditions, but instead is a growth phenomenon. The in-plane alignment for this mechanism to occur must develop in films within the first 500Å. Film 3, fabricated with ion assist for the first 500Å and evaporated until a total thickness of 1 μm, exhibited in-plane alignment comparable to that observed in the film deposited with ion assist throughout deposition (Figs. 4.7(c) and 4.7(b)). Both films exhibited considerably better in-plane alignment that of the film etched for 10 minutes after 600Å had been deposited under standard electron beam evaporation. The XRD and TEM evidence indicate that the majority of biaxial alignment occurs within the thickness over which (200) columns extinguish polycrystalline grains of other orientations. Further deposition appears to perpetuate the biaxial alignment present at the onset of (200) columnar microstructure dominance.

Analysis of electron diffraction patterns obtained from various positions along the height of the columns failed to detect a significant improvement in biaxial alignment after the first 150nm of IBAD deposition. This suggests the biaxial alignment occurs primarily during the early stages of the deposition process. The (200) film orientation is established within the initial 80nm of film, both with and without ion assist. Randomly oriented polycrystalline grains are extinguished within this distance from the film/substrate interface. The column width observed in films prepared without ion assist was essentially constant after the first ~80Å had been deposited. Average column width will tend to increase as unfavorably oriented crystals are shadowed by their faster growing neighbors. The shadowing process is likely more effective when the columns

are relatively narrow. Small differences in growth rate among neighboring columns can effectively produce shadowing under these conditions. The TEM evidence suggests that the average column diameter remains relatively constant after the columns which survive the initial growth competition come into contact. Small differences in growth rate produced by IBAD do not dramatically improve the biaxial alignment thereafter. That may explain the presence of (200) columns with wire texture and the presence of (200) columns with the in-plane orientation featuring {111} planes in the direction of the incident ion beam in the selected area electron diffraction patterns.

Growth of preferred orientations and the extinction of others due to shadowing is well documented for columnar structures. Uniaxial texture evolution during columnar growth was modeled by van der Drift.[35] This growth model can be extended to explain the development of biaxial alignment during IBAD. Alignment will develop if the net growth rate of columnar grains varies with orientation with respect to the ion beam. Columnar grains of a specific orientation favorably aligned with the ion beam will begin to shadow grains that are growing more slowly. This surface roughness induces a growth instability such that the faster growing grains will begin to dominate the microstructure just as in the case of fiber texture development during film growth. A schematic detailing the development of biaxial alignment as a result of growth rate anisotropy is shown in Fig. 4.17 for the specific case of (200) biaxial alignment on Pyrex. The schematic is consistent with X-ray data in Section 4.3.1.3 and the SEM and cross-sectional transmission electron microscopy detailed in Section 4.3.1.5.

Relative grain growth rates could vary with respect to the assisting ion beam for a number of reasons. Grains oriented with channeling directions parallel to the assisting ion beam would presumably suffer less sputtering than grains with no open crystallographic planes exposed to the beam, as postulated by Yu *et al.*[1,2] and Bradley[41] The relative grain growth rates could differ in the absence of sputtering anisotropy if grains experience anisotropy in ion damage, as postulated by Ensinger.[42] It cannot be determined from the present data which mechanism is responsible for the growth rate variation leading to biaxial alignment under these conditions. This matter is the focus of Chapter 7.

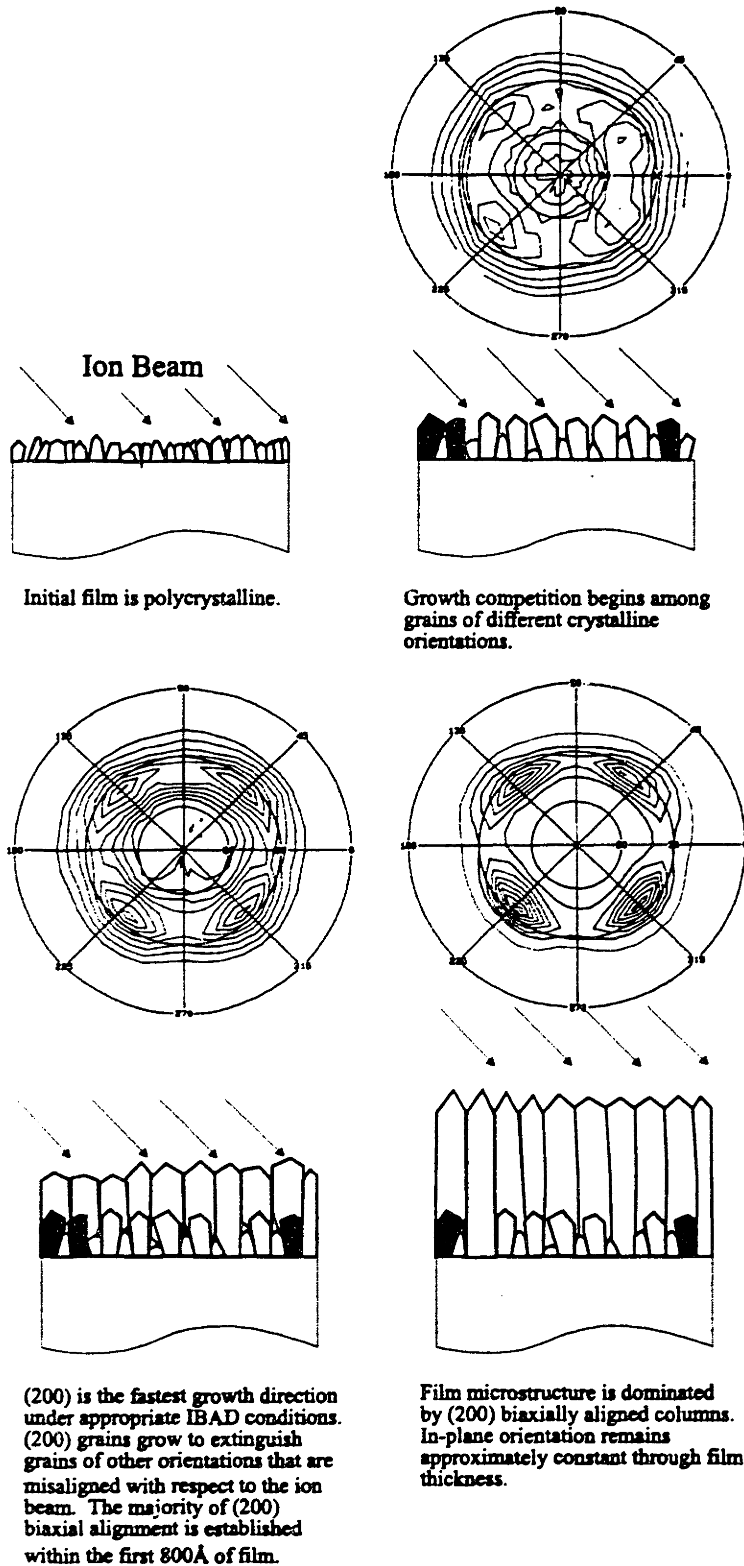

Figure 4.17 Schematic of (200) YSZ biaxial alignment development on Pyrex resulting from growth rate anistropy during IBAD.

4.4.2 Biaxial Alignment of IBAD YSZ Films Evaporated With Varied Substrate Heating

(200) biaxial alignment was observed for IBAD films fabricated without active substrate heating on Pyrex, quartz, and Hastelloy substrates. Films fabricated with ion assist at 400°C exhibited (200) biaxial alignment on Pyrex, but (111) biaxial alignment on quartz and Hastelloy. Films deposited by IBAD in Run 5 with the first 4400Å deposited at room temperature and the second 8800Å at 400°C exhibited (200) biaxial alignment on all substrates, as was observed when the entire film was fabricated without active substrate heating. Films deposited in Run 6 with the reverse temperature sequence exhibited a mixture of (200) and (111) biaxial alignment, with the dominant orientation consistent with that observed in Run 4 when the substrate temperature was 400°C throughout deposition. (200) biaxial alignment development on quartz and Hastelloy clearly took place upon during the deposition step without active substrate heating.

These results can be explained by noting the substrate temperature effect on granular film evolution. A faceted, fine-grained microstructure is present in the TEM micrograph shown in Fig. 4.16 for an IBAD film deposited without active substrate heating. This microstructure is similar to the Zone I microstructure described by Grovenor *et al.*[26] Grovenor *et al.*[26] observed grain renucleation for metallic films fabricated at low homologous temperature. The metal film microstructure consisted of highly textured groups of grains. Films evaporated without ion assist at room temperature were weakly crystalline according to XRD, but highly crystalline and textured films were obtained by evaporating YSZ at room temperature with ion assist. The microstructure in Fig. 4.16 is also consistent with continuous grain renucleation during fabrication without active substrate heating. Substrate-independent biaxial alignment is consistent with a renucleation process in which the assisting ion beam is responsible for inducing film crystallization. Texture evolution in such a situation would be regulated more by the assisting ion beam than by substrate crystallinity. This was observed in Run 2, with (200) biaxial alignment observed for films deposited on two amorphous glass and one polycrystalline metal substrate. The film orientation present after 4400Å deposited without active substrate heating was maintained through the final

8800Å deposited at 400°C. This is consistent with granular epitaxy becoming operative at higher substrate temperature. This argument also holds true for Run 6, in which the temperature sequence was reversed. Substrate-dependent biaxial alignment developed during the first 4400Å deposited at 400°C, and grain renucleation during the subsequent step without active substrate heating resulted in (200) biaxial alignment development on all substrates.

4.5 SUMMARY

The results of this research demonstrated that biaxially aligned YSZ films can be fabricated by ion assisted electron beam evaporation over a wide range of deposition rates, ion beam energies and fluences, bombardment angles, and substrate temperatures. It should be emphasized that IBAD biaxial alignment was observed at all angles of ion incidence, not just those corresponding to YSZ channeling directions. Substrate-independent biaxial alignment was observed for depositions without active substrate heating, while substrate-dependent biaxial alignment was observed for depositions at 400°C and 600°C, indicating that the development of IBAD biaxial alignment may be temperature dependent. Films fabricated by IBAD both without active substrate heating and at elevated temperatures featured similar biaxial alignment according to θ-2θ XRD, X-ray pole figures, and TEM selected area diffraction patterns even though their microstructures were distinctly different as shown by cross-sectional TEM. The in-plane orientation of (200) biaxially aligned YSZ films fabricated in both temperature regimes exhibited {220} poles in the direction of the assisting ion beam projection, in contrast to the {111} poles parallel to the assisting ion beam noted by Iijima *et al.*[3-8] for biaxially aligned YSZ films fabricated by dual ion beam deposition.

The microstructural differences were consistent with two different modes of IBAD film growth at low and elevated substrate temperature. IBAD film growth at elevated temperature occurred through growth rate competition. The biaxial alignment observed on different substrates at 600°C indicated that the outcome of the growth rate competition was substrate dependent. The microstructure observed in ion assisted e-

beam evaporated films fabricated without active substrate heating was consistent with continuous grain renucleation during deposition. The fact that substrate-independent biaxial alignment was observed for films fabricated without active substrate heating while substrate-dependent biaxial alignment was observed at 600°C indicates that the mode of film growth operative at low substrate temperatures is different from that operative above 400°C.

CHAPTER 5
DUAL ION BEAM DEPOSITION OF YSZ

5.1 INTRODUCTION

Fabrication of biaxially aligned YSZ films by dual ion beam deposition has been examined by several groups, including Iijima *et al.*[3-8] and Arendt *et al.*[9-12] Most of the work has focused on film fabrication without active substrate heating. Both the mechanism of biaxial alignment and microstructural development during dual ion beam deposition have not been addressed to a significant extent. Biaxial alignment development and microstructural evolution during dual ion beam deposition are examined in this chapter by combining X-ray diffraction with cross-sectional TEM.

The study in Chapter 4 detailed the influence of deposition rate, ion bombardment angle, assisting ion beam energy, the assisting ion beam fluence, the ion to molecule arrival ratio and the substrate temperature on YSZ biaxial alignment by ion assisted electron beam evaporation. The influence of the same IBAD parameters on YSZ biaxial alignment by dual ion beam deposition is examined in this chapter. The fabrication and examination of (200) biaxially aligned YSZ films fabricated by dual ion beam deposition both without active substrate heating and at 600°C is discussed.

5.2 EXPERIMENTAL PROCEDURE

5.2.1 Dual Ion Beam Deposition of YSZ without Active Substrate Heating

Substrates were mounted on stainless steel heater blocks using the procedures described in Chapter 3. Ar gas was flowed through the Kaufmann sputtering ion source, while a mixture of Ar and 8% O_2 flowed through the assisting RF ion source. A variety of deposition conditions were examined in this study. The RF ion source was set to

30mA beam current, 300eV beam energy, 600V accelerator voltage, and 120mA neutralizer emission current for all depositions. The ion bombardment angle was 35° for most depositions, while 45° was used for a few depositions. The sputtering Kaufmann ion source was set to 1000eV beam energy for all depositions, while the beam current was PID controlled to maintain a desired YSZ deposition rate.

The gross deposition rate, net deposition rate, and assisting ion fluence varied with the substrate block position relative to the YSZ sputtering target and RF ion source. The substrate block was fixed at one position relative to the assisting ion source and sputtering target for most depositions. The ion bombardment angle was 35°, the assisting ion fluence was 96μA/cm^2, and the ion etching rate was ~0.2Å/s. The substrate temperature rose from 20°C initially to a steady state value of 180°C during deposition. A variety of substrates were mounted for a deposition representative of the biaxial alignment observed without active substrate heating. Amorphous quartz, pyrex, (100) Si, a Si substrate with a spun-on polyimide film, TZP, and Hastelloy substrates were mounted on a stainless steel block with thermal grease. The net deposition rate was ~0.2Å/s as calculated from the ultraviolet/visible transmittance spectra of the film on quartz. The films were deposited to a thickness of 420nm.

Films were fabricated with a variety of deposition profiles to examine the dependence of the in-plane mosaic spread with ion to YSZ molecule arrival ratio. The assisting ion fluence linearly decreases with distance from the RF ion source, as shown in Fig. 3.4. Multiple quartz substrates were vertically mounted on the sample block so that films could be fabricated with several different assisting ion fluences and therefore several different ion to molecule arrival ratios during the same deposition. The ion bombardment angle was 35°, the assisting beam energy was 300eV, and the assisting ion fluence was 96μA/cm^2 for all depositions.

Nine depositions were undertaken in the first set of experiments. Three films were deposited with the sputtering ion source beam current held constant throughout deposition. The deposition rate was PID controlled by continuously adjusting the sputtering ion source beam current throughout deposition as described in Section 3.2.4 to maintain a constant deposition rate during fabrication of the other six films. The

deposition rate of the six PID controlled runs was well controlled, while the deposition rate of the three films fabricated with constant sputtering ion source beam current varied during deposition. Normalized plots of film thickness versus deposition time for runs representative of poorly controlled and well-controlled conditions are shown for Runs 090895 and 010996 respectively in Fig. 5.1. The r value was therefore constant during the PID-controlled depositions while the r value varied slightly during the other three runs.

The r value was intentionally varied in three other runs. The deposition rate in Run 102695 started at 0.1Å/s and was linearly increased using PID control to a final value of 0.45Å/s at the end of the 6h deposition. The corresponding initial and final r values were 15 and 2.7, respectively. The deposition rate in Run 102895 linearly increased from 0.1 to 0.4Å/s over the same 6h duration for initial and final r values of 15 and 3. The deposition rate was periodically varied in Run 111595, as shown in Fig. 5.2. The r value was maintained at 2.6 for 20 min., then was linearly increased to 20 ions:molecule YSZ over 5 min. and held at 20 for an additional 5 min. The deposition rate was then restored to its original value to commence a new cycle.

5.2.2 Dual Ion Beam Deposition of YSZ at 600°C

Three amorphous quartz substrates were vertically mounted on a substrate block using the procedures described in Chapter 3. A variety of IBAD conditions were examined in order to fabricate a (200) biaxially aligned YSZ film at 600°C. Ion bombardment angles of 35° and 45° were used. Films were fabricated with constant deposition rates for this series of experiments. The Kaufmann ion source was set to 1000eV beam energy for all depositions and the beam current was PID controlled to maintain a desired YSZ deposition rate. The net deposition rates ranged between 0.18 and 0.25Å/s. Ar gas was flowed through the Kaufmann sputtering ion source, while a mixture of Ar and 8% O_2 flowed through the assisting RF ion source. The RF ion source was set to 30mA beam current, 300eV beam energy, 600V accelerator voltage, and 120mA neutralizer emission current for a fluence of 96μA/cm^2 for all depositions.

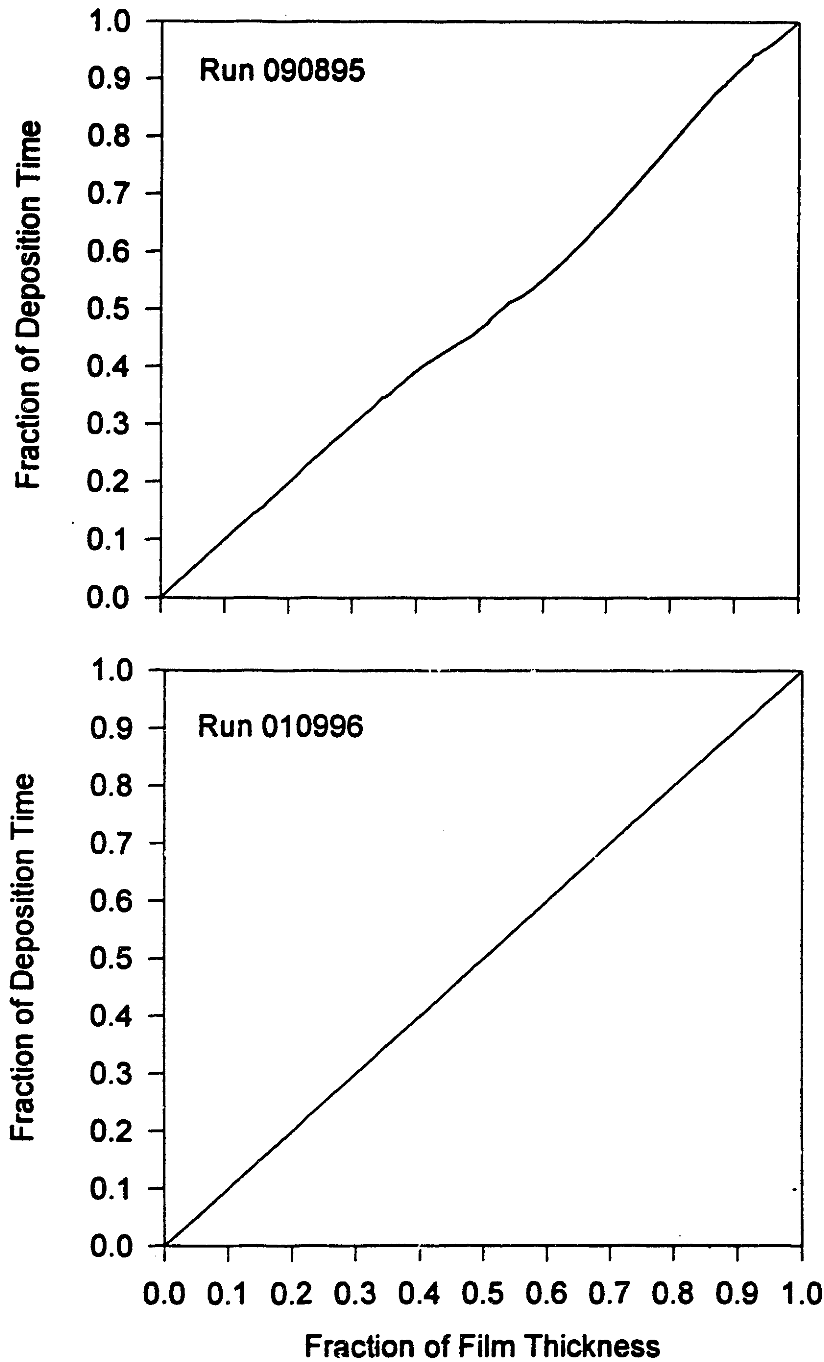

Figure 5.1 Normalized plots of film thickness versus deposition time for a poorly controlled deposition (Run 090895) and a well controlled deposition (Run 010996).

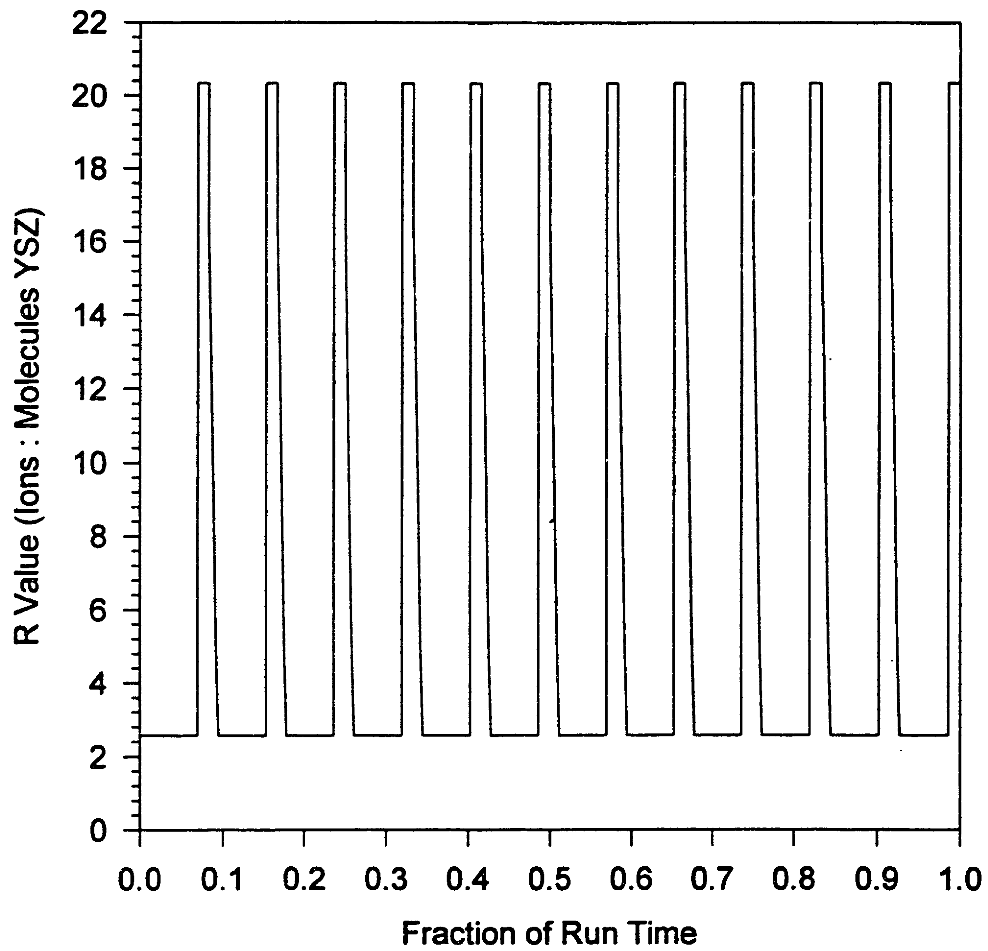

Figure 5.2 Periodic r value variation during Run 111595.

5.2.3 Film Characterization

Film orientation was examined using θ-2θ X-ray diffraction, four-circle diffractometry, X-ray pole figures, and X-ray ϕ scans using a CuK_α radiation source, as described in Chapter 3. Selected YSZ samples was observed using scanning electron microscopy. Several YSZ films were examined using cross-sectional high resolution transmission electron microscopy. Mr. Michael Frongillo performed the high resolution microscopy featured in this chapter.

5.3 RESULTS: DUAL ION BEAM DEPOSITION OF YSZ

5.3.1 Dual Ion Beam Deposition of YSZ without Active Substrate Heating

5.3.1.1 Substrate-Independent Biaxial Alignment

Pyrex, quartz, and Hastelloy substrates were positioned at an angle of 45° with respect to the assisting ion source for a control deposition without ion assist. The sputtering ion source beam current and voltage were 30mA and 1000eV, respectively. The substrate temperature rose from 20°C to a steady state temperature of 85°C during deposition. The deposition rate was ~0.4Å/s, as determined from the deposition time and the thickness calculated using the envelope technique of Swanepoel.[58] The YSZ films on all three substrates featured (220) uniaxial orientation, as indicated in the θ-2θ traces in Fig. 5.3, but the films exhibited random in-plane orientation.

All YSZ films deposited by dual ion beam deposition without active substrate heating featured strongly preferred (200) alignment on all substrates under all deposition conditions. A wide range of IBAD deposition conditions were examined; net deposition rates ranged from 0 to 0.3Å/s, assisting beam currents ranged from 20 to 30 mA and assisting beam energies ranged from 200 to 350eV resulting in ion fluences ranging from ~ 50 to 100 μA/cm^2. The corresponding r values ranged from 2 to 4.5 ions per YSZ molecule. Ion bombardment angles of 35° and 45° were used.

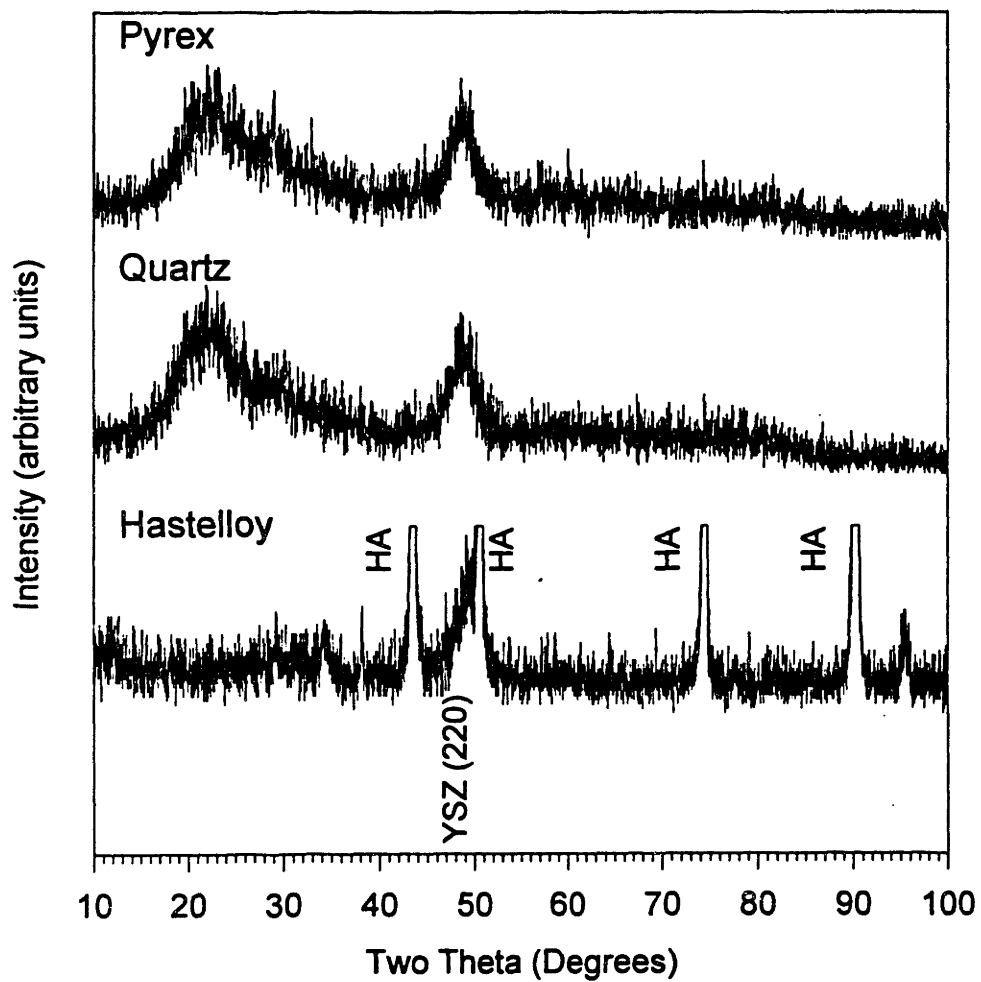

Figure 5.3 θ-2θ X-ray traces of YSZ films sputtered without active substrate heating.

Several amorphous, polycrystalline, and single crystal substrates were selected for a model deposition to demonstrate the substrate-independent nature of YSZ biaxial alignment observed with dual ion beam deposition without active substrate heating. Pyrex, quartz, Hastelloy, (100) Si, Y-TZP, and a (100) Si substrate with a spun-on polyimide film were adhered to a substrate block using thermal grease and placed at an angle of 35° with respect to the assisting ion beam. A YSZ film was deposited at a constant net deposition rate of 0.16 Å/s with an assisting beam energy of 300eV and fluence of 53 $\mu A/cm^2$. The r value was approximately 3.4 throughout the deposition. The θ-2θ X-ray traces and (111) X-ray ϕ scans for the films are shown in Figs. 5.4 and 5.5. (200) and (400) reflections were the only observed YSZ film reflections. The films exhibited similar in-plane alignment on all substrates, as shown in Fig. 5.5. The full width at half maximum (FWHM) breadths of the X-ray poles is indicated above the respective substrate traces. The X-ray ϕ scans indicate (111) poles were aligned toward the ion beam projection at $\phi=0°$. Similar θ-2θ and (111) X-ray ϕ scans were observed for all YSZ films deposited by dual ion beam deposition under all fabrication conditions.

5.3.1.2 Dependence of FWHM on R Value

The FWHM values obtained from (111) X-ray ϕ scans of the nine films fabricated at ideally constant r value is shown in Fig. 5.6 over the range of r values examined. The data are broken into two groups. The data indicated with hollow symbols correspond to films deposited under PID control, while the data for the three films deposited at constant sputtering ion source beam current are indicated by solid symbols. The FWHM values for the films deposited in poorly controlled Runs 090795 and 090895 were considerably better than those obtained in well controlled Runs 010996 and 092095, even though the films were deposited with similar r values. The smallest FWHM for a film deposited under PID control was 26°, while many of the films deposited under poorly controlled conditions, and correspondingly varied r values, featured in-plane mosaic spreads below 25°. The smallest in-plane mosaic spread of 22° FWHM was observed for a film deposited in Run 090895, in which the r value varied during deposition.

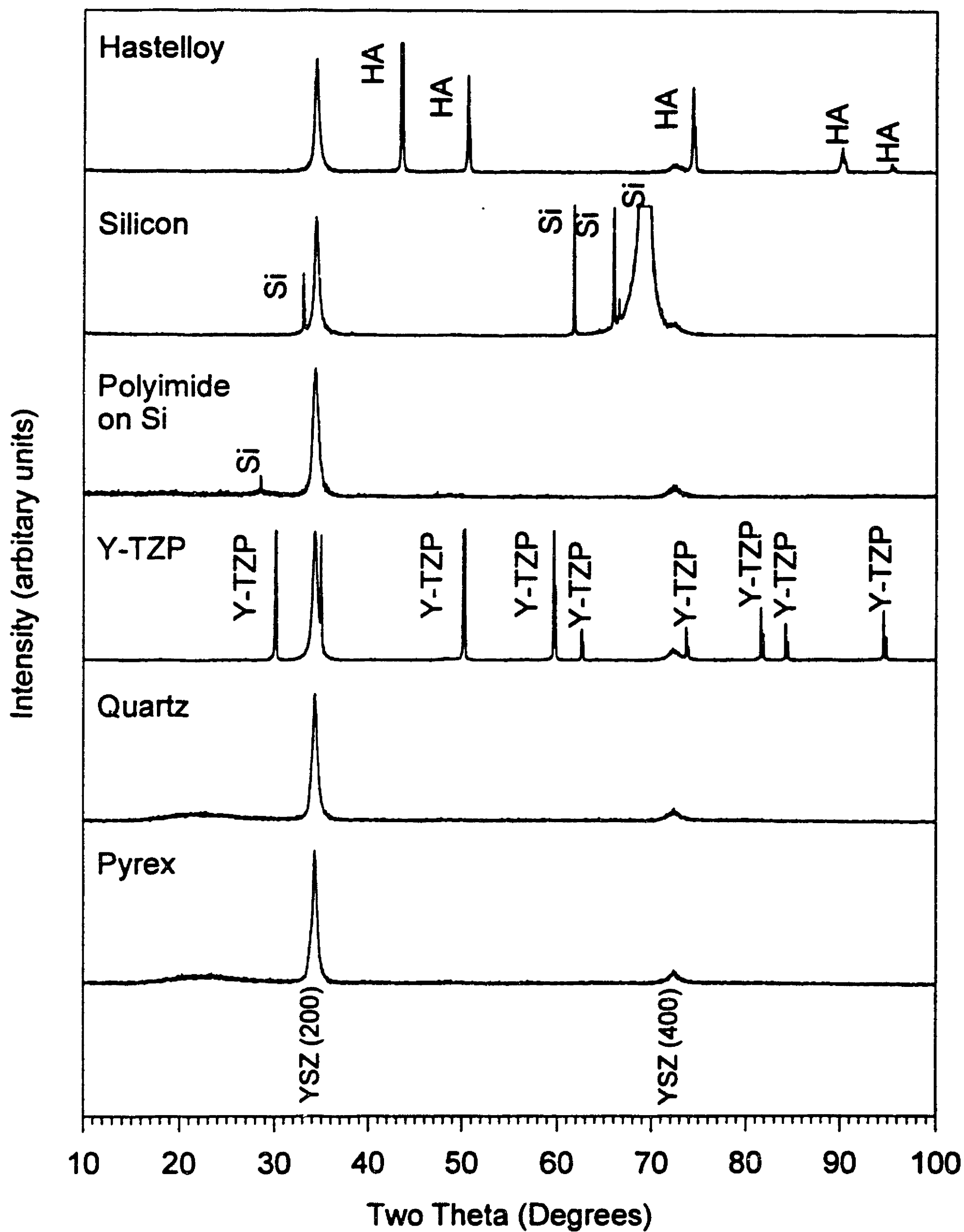

Figure 5.4 θ-2θ X-ray traces of dual IBAD YSZ films deposited without active substrate heating on several substrates.

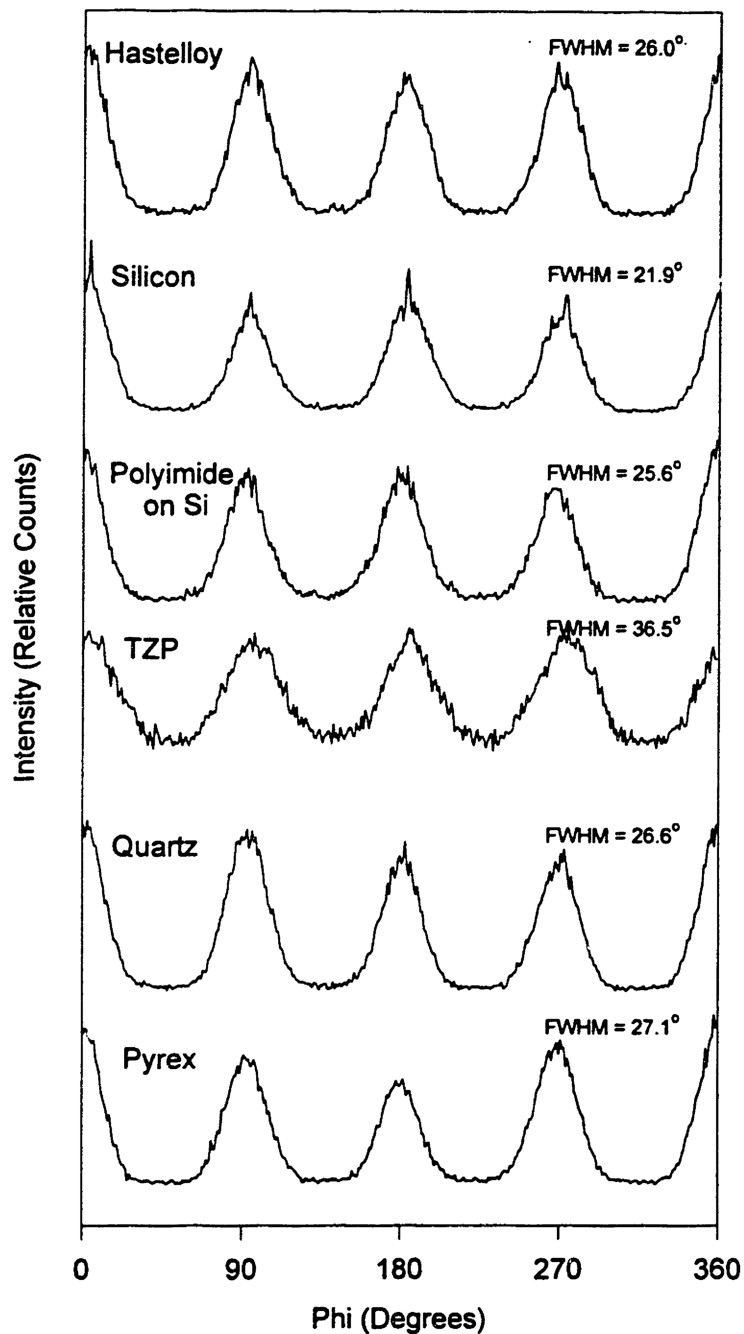

Figure 5.5 (111) X-ray φ scans of dual IBAD YSZ films deposited without active substrate heating on several substrates.

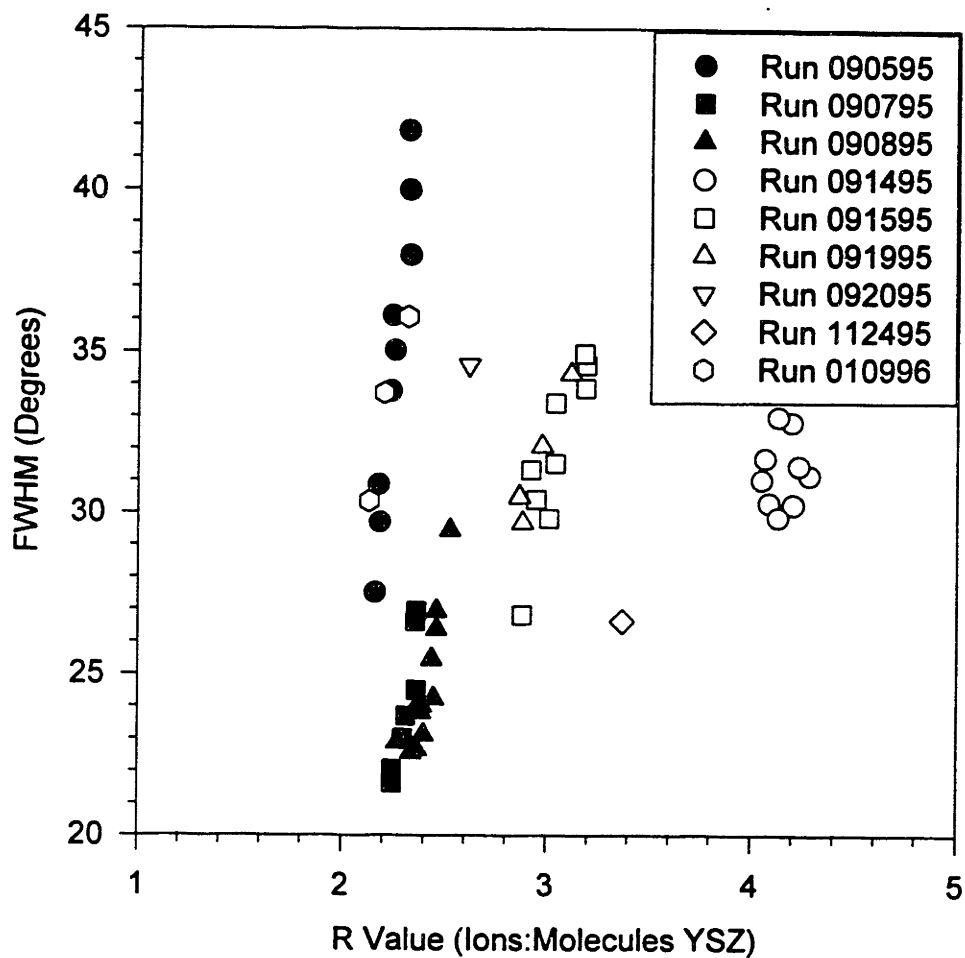

Figure 5.6 FWHM values obtained from (111) X-ray ϕ scans of the nine films fabricated at ideally constant r value.

The improved FWHM observed with slightly varied r values spurred several experiments where the r value was varied in a controlled manner during deposition. The YSZ films fabricated under all three sets of deposition conditions were (200) biaxially aligned. The FWHM of the (111) X-ray ϕ scan reflections for the three films are compared to the other well controlled depositions in Fig. 5.7. The FWHM of the films fabricated with linearly decreasing r value in Runs 102695 and 102895 were smaller than all but one of the films deposited under well controlled deposition conditions. The FWHM of the film fabricated with periodic r value conditions in Run 111595 was 4° less than that of Run 092095, fabricated with a constant r value of 2.6.

5.3.1.3 X-ray Diffraction and Electron Microscopy Investigation of Biaxial Alignment Evolution

A typical SEM fracture micrograph of a YSZ film deposited on quartz by dual ion beam deposition without active substrate heating is shown in Fig. 5.8. The film microstructure is dense, uniform, and featureless. This microstructure is markedly different from the highly columnar microstructure observed in films deposited by ion assisted, electron beam evaporation at 600°C.

Two films fabricated on quartz substrates during the same deposition (Run 090895) were used for X-ray diffraction and TEM characterization. The films were deposited at an ion bombardment angle of 35° using a constant net deposition rate of 0.14Å/s and assisting beam energy and fluences of 300eV and $55\mu A/cm^2$. A cross-sectional TEM micrograph of a (200) biaxially aligned film viewed along a <110> zone axis at the film/substrate interface is shown in Fig. 5.9. The specimen was prepared so that the assisting ion beam was incident from the right of the micrograph at an angle of 35° from the interface. Several sets of {111} lattice fringes are apparent in the micrograph along the interface. An interfacial YSZ grain with [220] tilted slightly toward the ion beam is indicated. This observation is consistent with the (220) orientation observed in control films deposited without ion assist. Most of the grains at the top of the micrograph are oriented with [200] approximately normal to the film/substrate interface. The transition from [220] normal orientation at the interface to [200] normal orientation

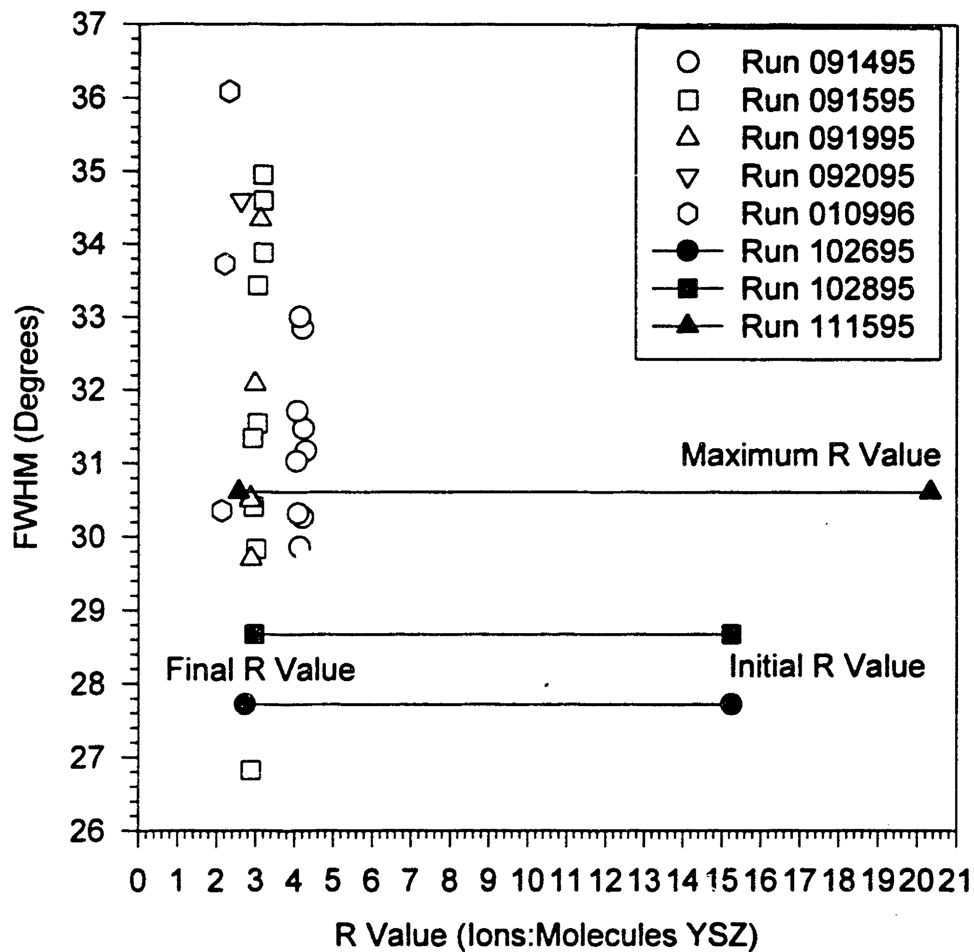

Figure 5.7 FWHM values obtained from (111) X-ray ϕ scans of films fabricated with varied r value during deposition.

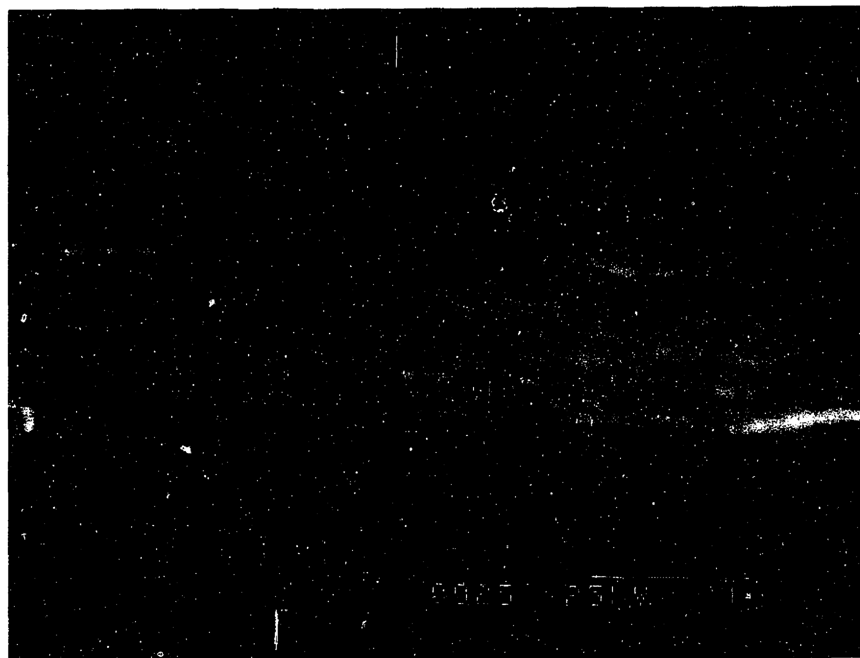

Figure 5.8 SEM micrograph of YSZ film fabricated by dual ion beam deposition without active substrate heating.

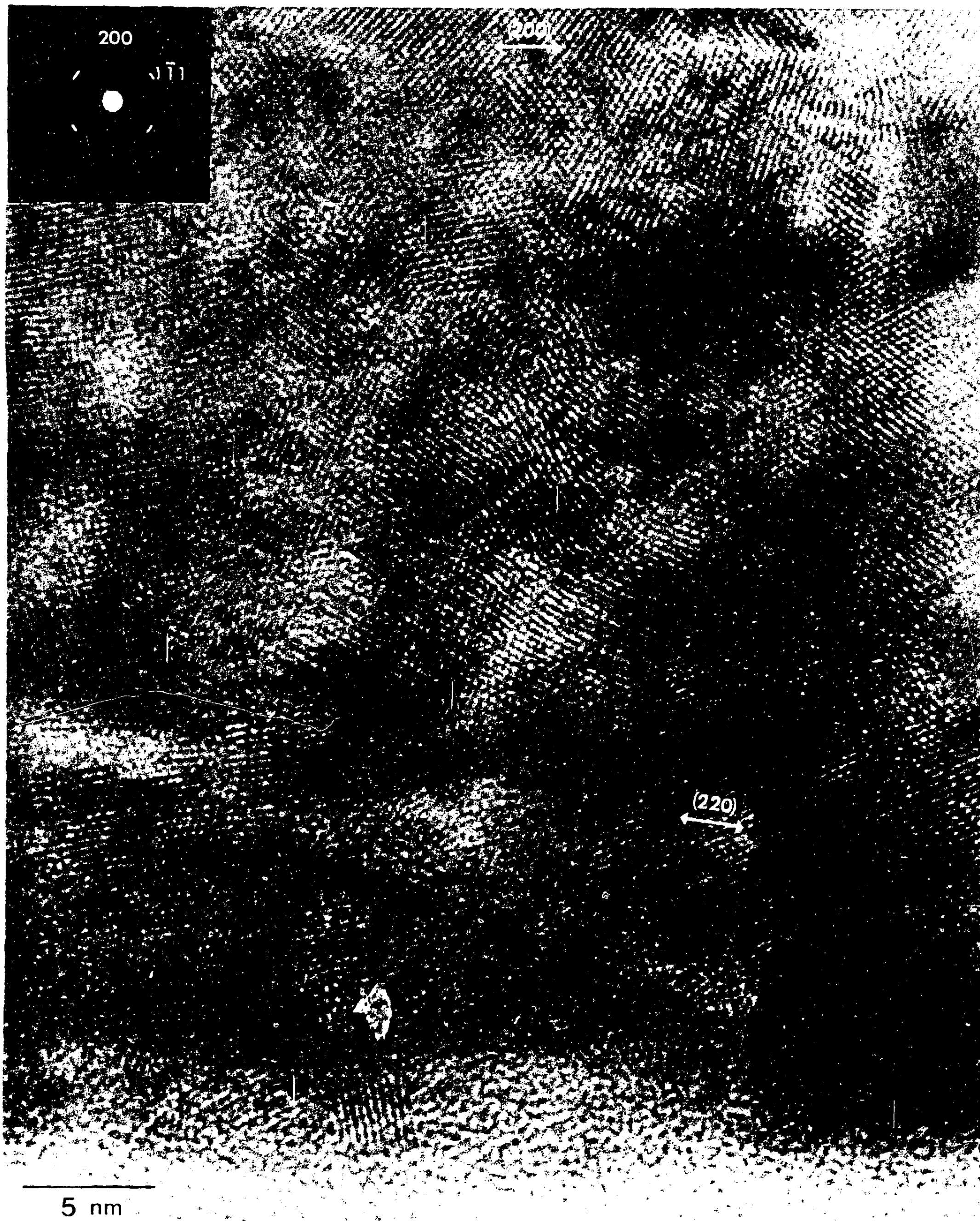

Figure 5.9 Cross-sectional TEM micrograph of dual ion beam YSZ film deposited on quartz.

is achieved within the first 50nm. Several twins and dislocations are associated with the transition. Figure 5.10 highlights several of the twins and dislocations present in Fig. 5.9. Disordered regions such as these are observed throughout the film along the intersections of grains misoriented with respect to each other. There are several regions within the micrographs where lattice fringes appear either distorted or are not visible. This is consistent with the in-plane mosaic spread observed in the X-ray ϕ scans. The majority of grains share similar azimuthal orientations, as is indicated by the restricted in-plane orientation. The zone axes for these individual grains are approximately parallel. The majority of grains therefore diffract along the same zone axis. The lattice fringes for these grains are clearly discerned in Fig. 5.9. Azimuthally misoriented grains do not share the same zone axis as the majority of grains and therefore do not diffract along the same zone axis as the majority grain population. The lattice fringes of misoriented grains appear distorted in Fig. 5.9 because the grains are not viewed along their zone axes.

Restricted crystallographic orientation is evident from the inset selected area electron diffraction pattern in Fig. 5.9. Similar electron diffraction patterns were observed through the remainder of the film. No discernible texture difference was evident with increased thickness. A textured polycrystalline microstructure was observed throughout the film. Grains with (200) near-normal orientation were observed through the entire film thickness beyond the interfacial (220) region. The crystallographic grain orientation was not in registry with that of the grains beneath them. (200) granular near-normal orientation persisted through the film, but not in an epitaxial manner.

A (220) X-ray χ scan was taken to confirm the presence of grains with (220) near-normal orientation in the film. The step size was 0.10° χ, the accelerating voltage and current were 50kV and 200mA, and the count time at each step was 40s. The χ scan was taken in two steps. First, the specimen was positioned in the four circle diffractometer specimen holder so that ϕ=0° corresponded to the projection of the assisting ion beam during fabrication. The X-ray detector was then positioned near the appropriate 2θ position for the (220) YSZ reflection. The specimen was positioned at χ=45° and ϕ=45° so that one of the (220) poles for the (200) biaxially aligned film satisfied the Bragg

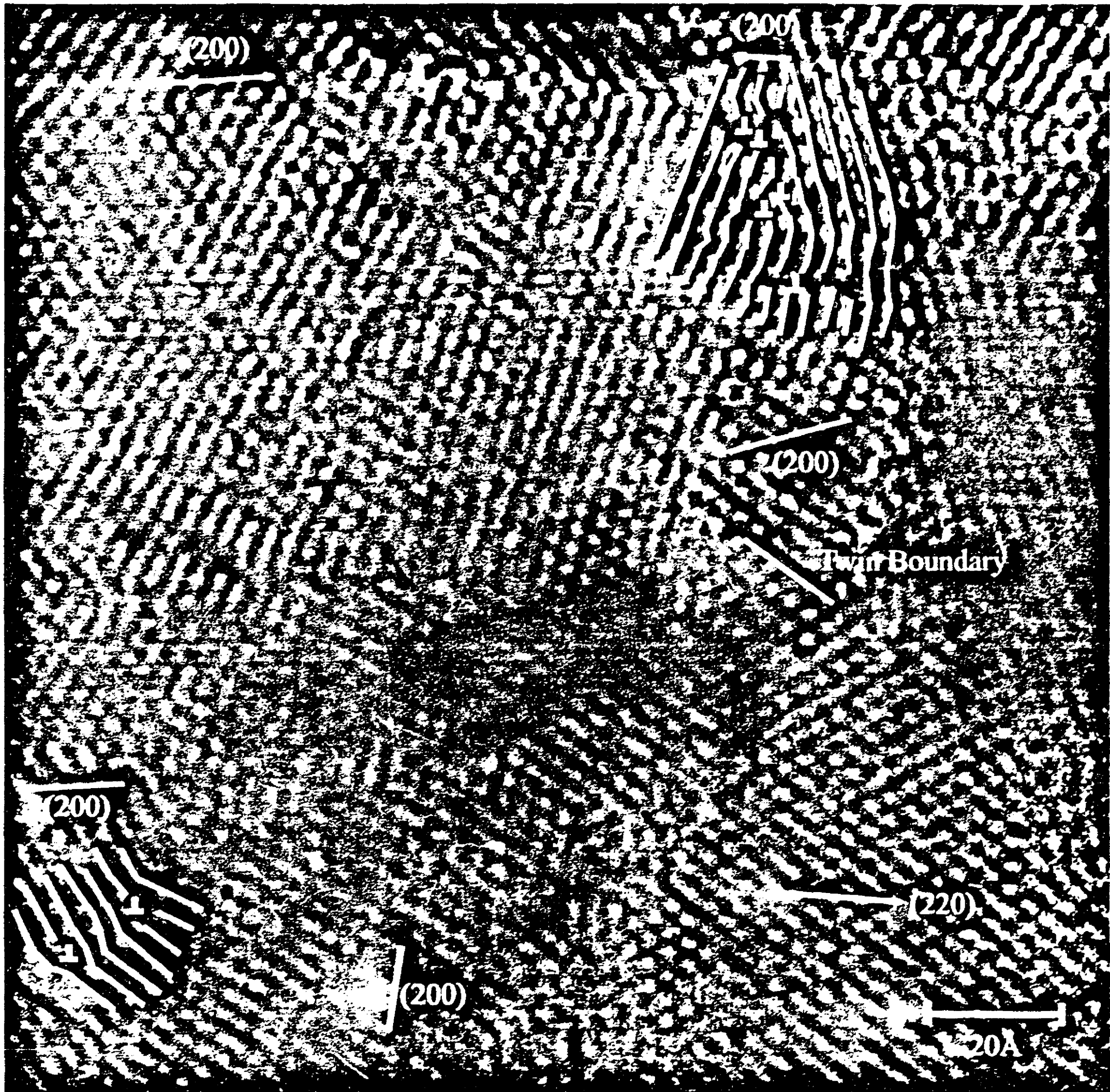

Figure 5.10 Micrograph highlighting several of the twins and dislocations present in Fig. 5.9.

condition. The optimal 2θ position was determined by scanning through the (220) pole. The specimen was then positioned at χ=0° and ϕ=0° for the first χ scan. X-ray intensity was measured as χ was rotated from 0 to 90°. The same χ scan was performed under the same conditions after the specimen was then rotated through 180° ϕ.

Combining the two resulting χ scans provides a measure of X-ray intensity along a slice across an entire hemisphere of the stereographic projection. The (220) χ scan data are presented in Fig. 5.11(a). Five peaks are visible above the background noise. Four of the five peaks correspond to the (200) biaxially aligned film. The reflections near χ=0° correspond to {220} reflections at ϕ=0° and ϕ=180° for YSZ with (200) normal to the substrate. A (220) X-ray ϕ scan was taken at χ=45° to clarify the origin of the reflections at χ=45°. The accelerating voltage and current were identical to those used for the (220) χ scan. The step size was 1° ϕ and the count time was 40s. The resulting (220) ϕ scan is shown in Fig. 5.11(b). Four (220) intensity maxima are located at ϕ=45, 135, 225, and 315°. These poles correspond to the majority of the film which is (200) biaxially aligned. The location of these poles is indicated in the (200) stereographic projection in Fig. 5.12. The reflections at 45° in the (220) χ scan correspond to minima in the (220) ϕ scan at ϕ=0 and 180° for (200) biaxially aligned material. The path traversed in the χ scan is indicated by a solid line in Fig. 5.12. The (220) positions for the intense peaks observed at χ=0° in the (220) χ scan are noted in the (220) stereographic projection in Fig. 5.12. The schematic at the bottom of Fig. 5.12 shows the orientation of {111} fringes in the cross-sectional TEM micrograph in Figs. 5.9 and 5.10 for grains with (200) normal orientation as observed along a [110] zone axis.

The remaining reflection at χ=90° can only be attributed to a film grains with (220) oriented nearly normal to the substrate. The reflection is slightly tilted toward the ϕ=0° side of the scan, the direction of the incident ion beam. The relative intensity of the (220) peak at χ=90° is nearly equal to that of the minima in the (220) ϕ scan of the (200) biaxially aligned material. This observation is consistent with the TEM evidence of (220) oriented grains at the film/substrate interface and (200) biaxially aligned material through

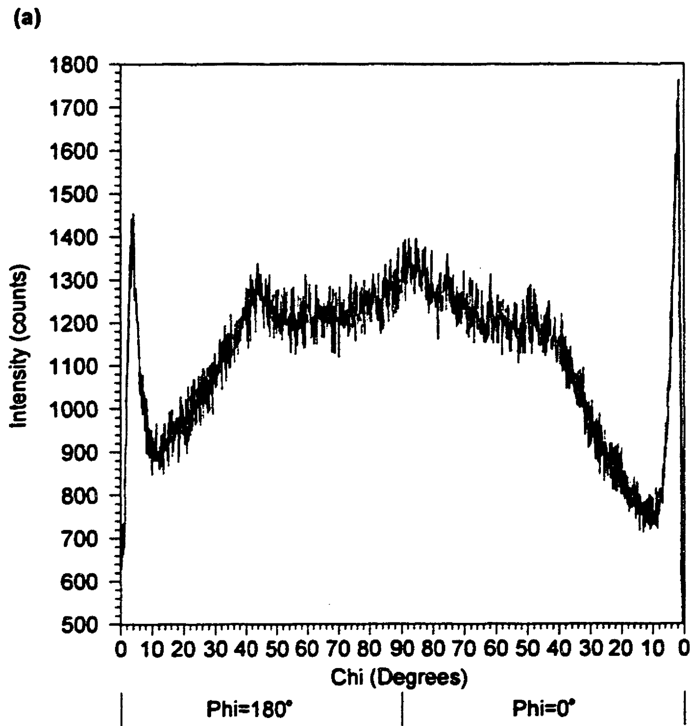

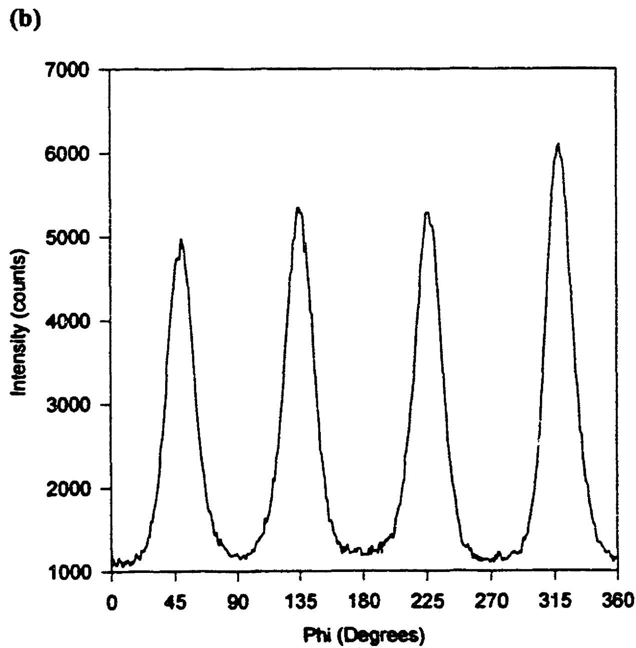

Figure 5.11 X-ray data from (a) (220) χ scan and (b) (220) ϕ scan of a biaxially aligned YSZ film fabricated by dual ion beam deposition without active substrate heating.

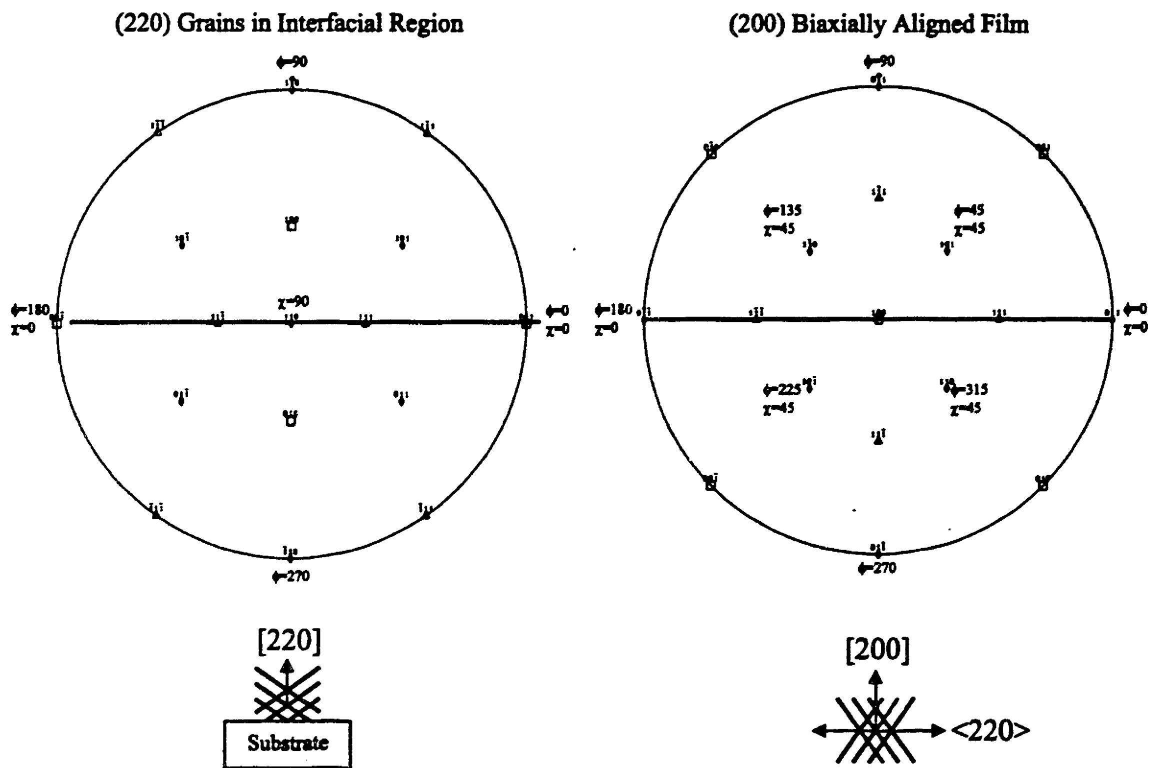

Figure 5.12 (220) and (200) stereographic projections for YSZ grains in the film/substrate interfacial region and grains constituting most of the film.

the remainder of the film. The schematic below the (220) stereographic projection shows the orientation of {111} fringes consistent with the XRD evidence in Fig. 5.11 as they appeared in Fig. 5.9.

5.3.2 Dual Ion Beam Deposition of YSZ at 600°C

5.3.2.1 35° Bombardment Angle

Quartz and silicon substrates were positioned at an angle of 35° with respect to the assisting ion source for a dual ion beam deposition at 600°C. The sputtering ion source beam current and voltage were 30mA and 1000eV, respectively. The assisting ion beam energy and fluence were 300eV and 95μA/cm^2. The deposition rate was ~0.2Å/s, as determined from the deposition time and the thickness calculated using the envelope technique of Swanepoel.[53] The YSZ films exhibited (111) preferred normal orientation on both substrates according to θ-2θ XRD as shown in Fig. 5.13. The in-plane orientation of both films was also similar as evidenced by the (111) X-ray ϕ scans in Fig. 5.14. The χ position was 20° for the ϕ scan. Three {111} reflections at χ=19.5° separated from each other by 120° ϕ should be present at this χ position for a specimen with {111} aligned normal (χ=90°). Three broad reflections are present in the (111) ϕ scans for both films. A (111) reflection is present parallel to the assisting ion beam projection at ϕ=0°. Each reflection appears to be split into pairs separated by approximately 30° ϕ. A (111) X-ray pole figure of the YSZ film on quartz is shown in Fig. 5.15. The central {111} reflection near the apex of the stereographic projection is tilted slightly away from the projection of the assisting ion beam at ϕ=0°. The {111} reflection parallel to the assisting ion beam is tilted upward from its ideal position of 19.5° χ to approximately 30° χ.

5.3.2.2 45° Bombardment Angle

Three quartz substrates and one silicon substrate were positioned at an angle of 45° with respect to the assisting ion source for another dual ion beam deposition at

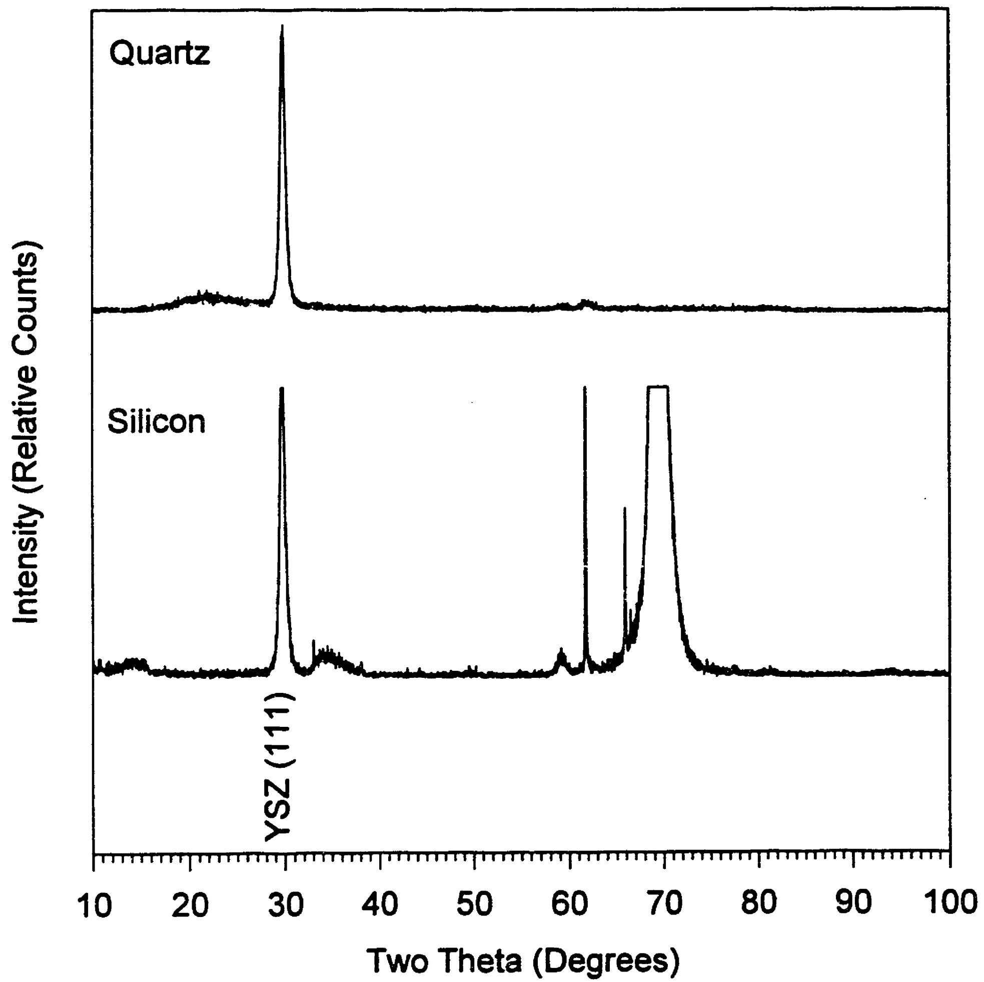

Figure 5.13 θ-2θ X-ray traces of films deposited on quartz and silicon substrates by dual ion beam deposition at 600°C with a 35° ion bombardment angle.

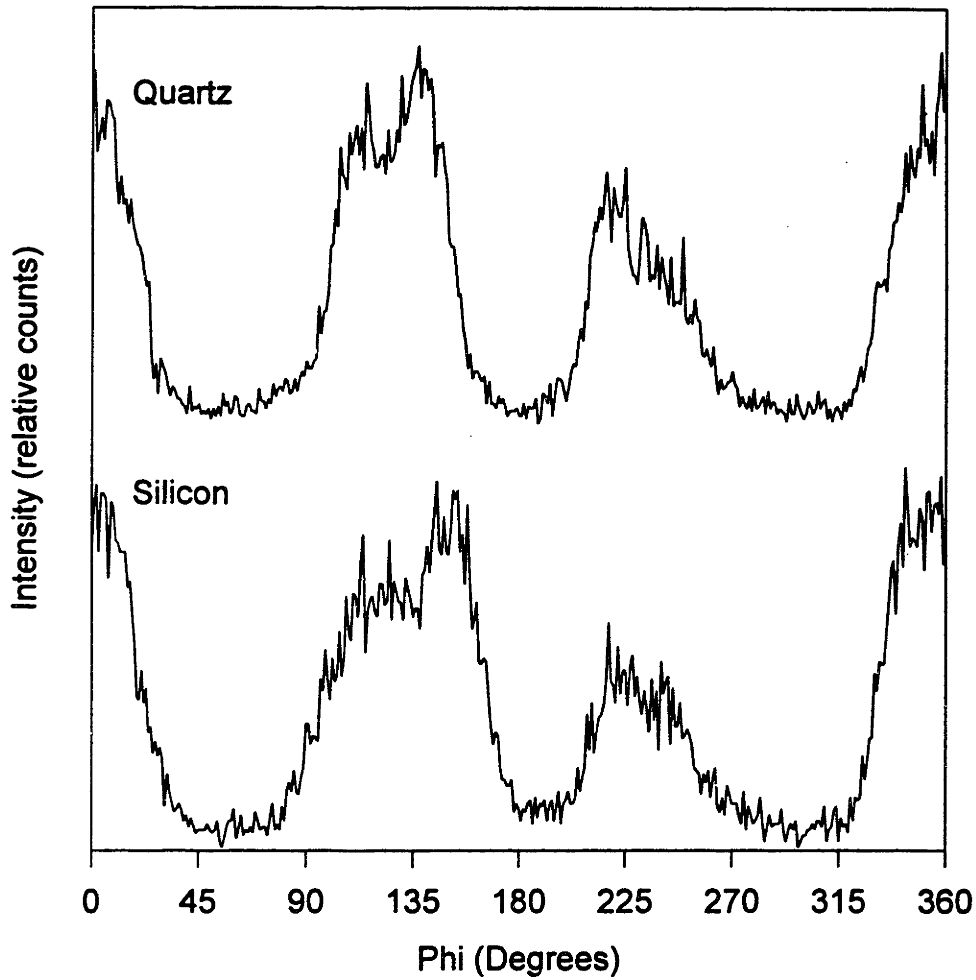

Figure 5.14 (111) X-ray ϕ scans of YSZ films deposited on quartz and silicon substrates by dual ion beam deposition at 600°C with a 35° ion bombardment angle.

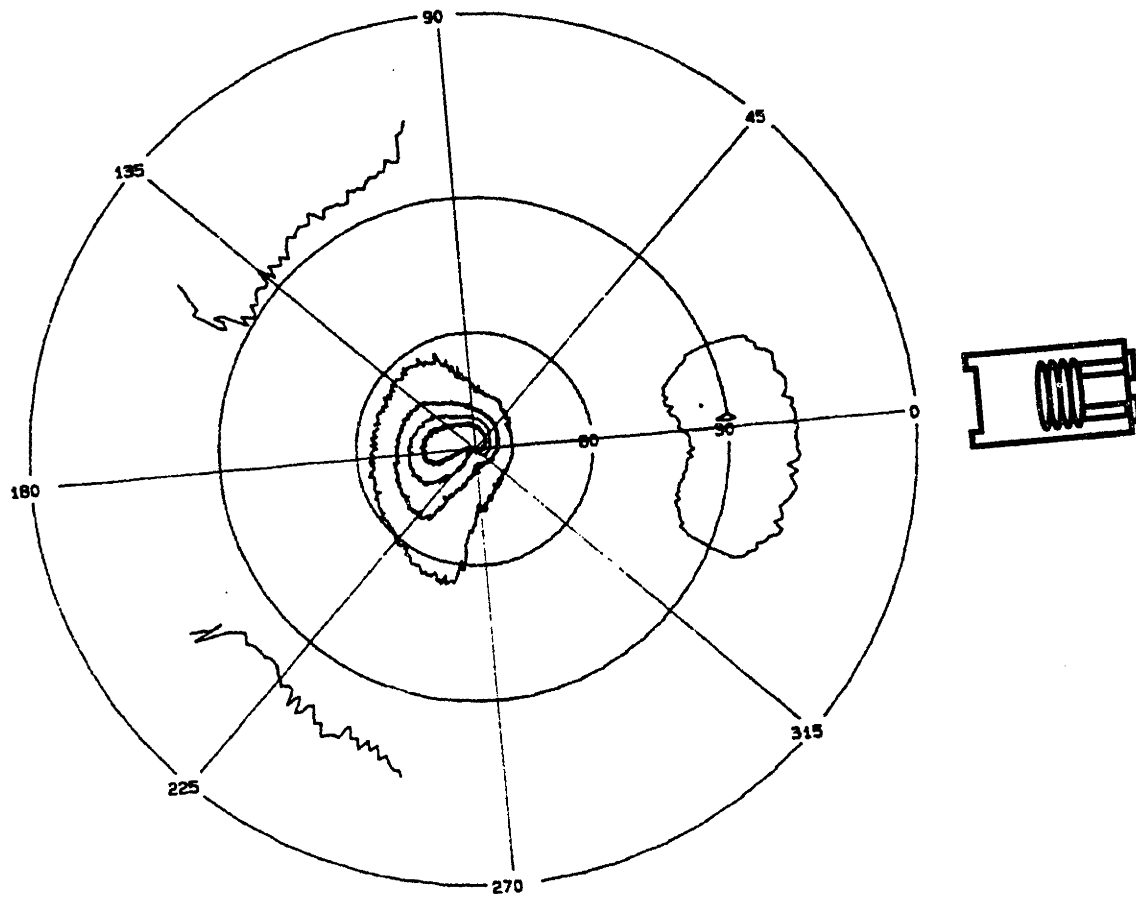

Figure 5.15 (111) X-ray pole figure of YSZ film deposited on quartz by dual ion beam deposition at 600°C with a 35° ion bombardment angle showing {111} reflection parallel to assisting ion beam at χ=35° and ϕ=0°.

600°C. The three quartz substrates were aligned vertically on the substrate block. The silicon substrate was placed adjacent to the quartz substrate furthest from the assisting ion source. The sputtering ion source beam current and voltage were 30mA and 1000eV, respectively. The assisting ion beam energy and fluence were 300eV. The ion fluence differed on the three quartz substrates, as each was positioned at a different distance from the assisting RF ion source. The assisting ion fluences were 70, 67, and 65 $\mu A/cm^2$ for the bottom, middle, and top quartz and silicon substrates, respectively. The net deposition rates varied with distance from the assisting ion source as well. The net deposition rate for the bottom, middle, and top quartz substrates were 0.21, 0.23, and 0.25 Å/s. The net deposition rate for the films deposited on the top quartz substrate and the silicon substrate should have been approximately equal based on their positions relative to the YSZ sputtering target and the assisting ion source. The θ-2θ XRD results for the YSZ films are shown in Fig. 5.16. The YSZ film deposited on the quartz substrate closest to the assisting ion source featured strongly preferred (200) normal orientation. The films deposited on the middle and uppermost quartz substrates featured (200) and (220) reflections of similar intensity. The film deposited on silicon featured strongly preferred (220) normal orientation with secondary (111) and (200) reflections.

Despite the differences among the YSZ films according to θ-2θ XRD, the in-plane orientations of the films are similar. The YSZ films deposited on the bottom quartz and silicon substrates featured the most dissimilar θ-2θ XRD traces. (111) X-ray ϕ scans taken at χ=35° indicate the in-plane orientation of grains with (200) normal orientation. The (111) X-ray ϕ scans for both films are comparable, as shown in Fig. 5.17. The {111} reflections are aligned with the ion beam projection for the films on both substrates, and both films feature a similar in-plane mosaic spread.

The X-ray pole figures for the four films are also similar. The (111), (200), and (220) X-ray pole figures for the YSZ film on silicon are shown in Fig. 5.18. The same pole figures for the YSZ film on the upper quartz specimen are shown at the bottom of Fig. 5.18. The (111) X-ray pole figure for the film on Si features two prominent reflections, one at ϕ=0° and χ=45° and the other at ϕ=180° and χ=55°. The reflection at

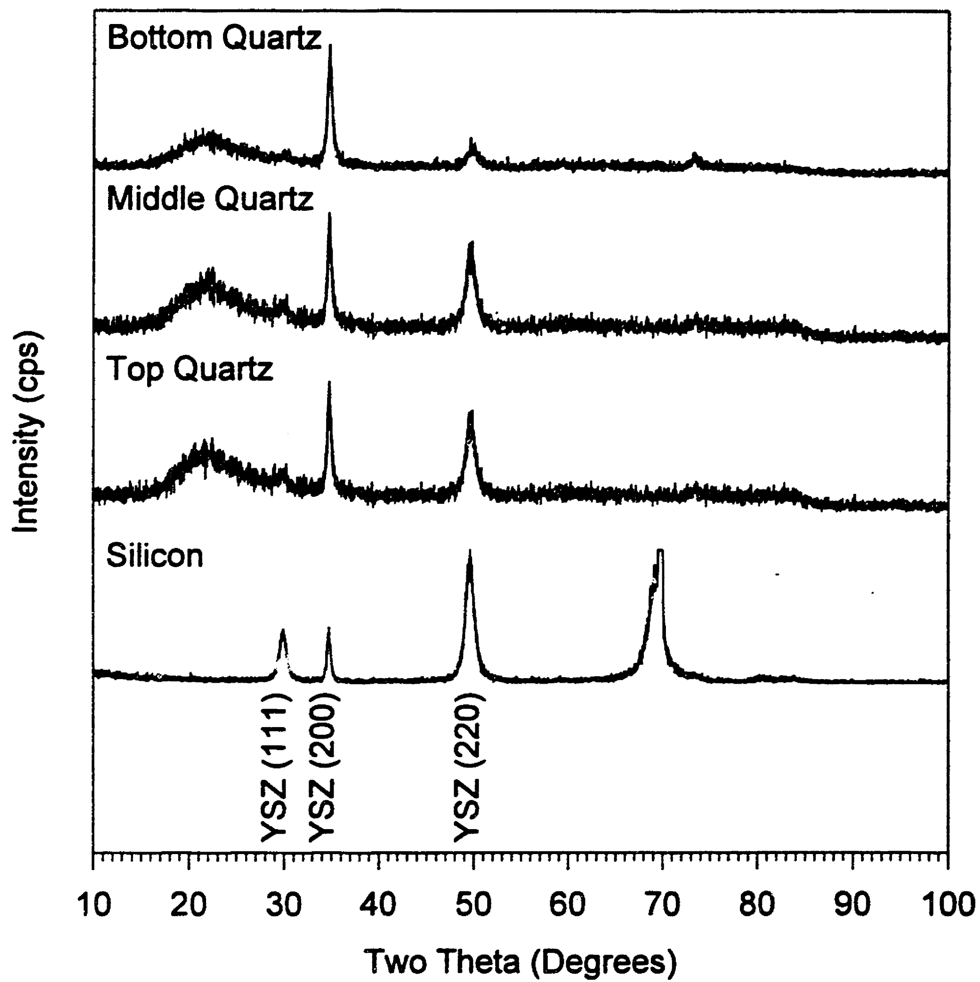

Figure 5.16 θ-2θ X-ray traces for YSZ films deposited on quartz and silicon substrates by dual ion beam deposition at 600°C with a 45° ion bombardment angle.

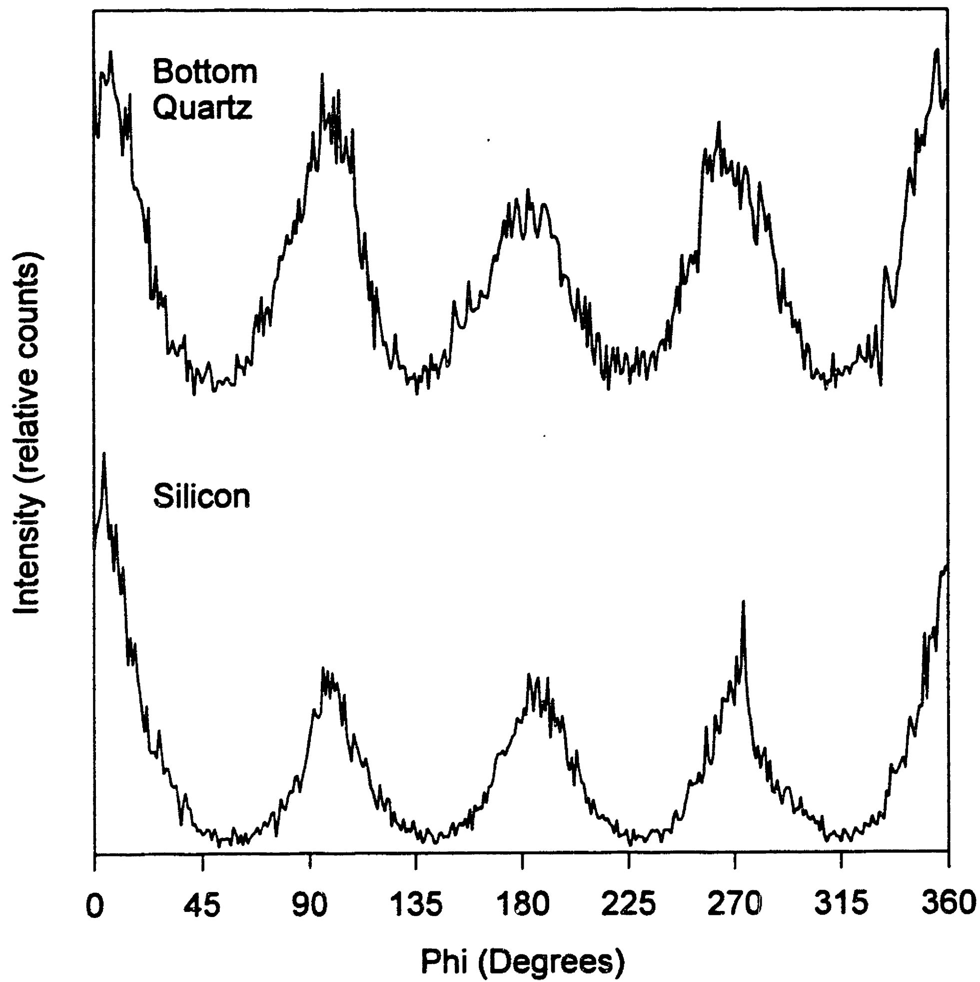

Figure 5.17 (111) X-ray ϕ scans for YSZ films deposited on quartz and silicon substrates by dual ion beam deposition at 600°C with a 45° ion bombardment angle.

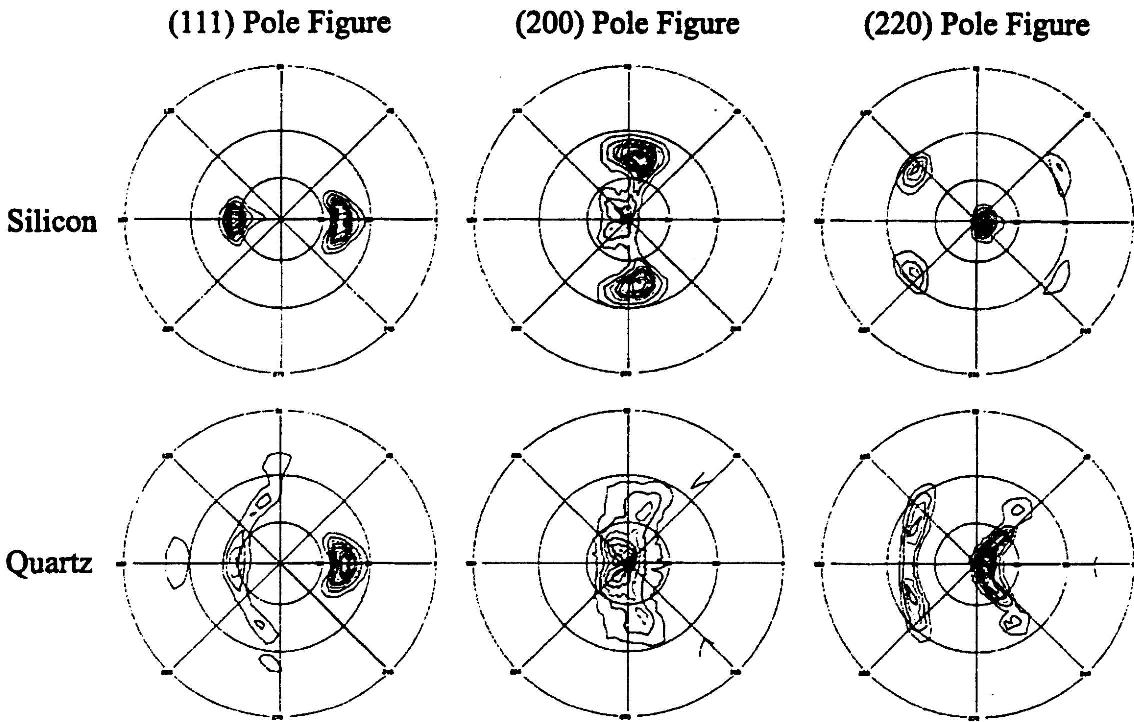

Figure 5.18 (111), (200), and (220) X-ray pole figures for YSZ films deposited on silicon and quartz substrates by dual ion beam deposition at 600°C with a 45° ion bombardment angle.

$\phi=0°$ and $\chi=45°$ remains intense while the reflection at $\phi=180°$ and $\chi=55°$ is considerably less intense in the (111) pole figure for the film on quartz. Relatively little (111) intensity is apparent at $\chi=90°$, the center of the stereographic projection, for the film on Si even though a prominent (111) reflection was observed in the θ-2θ XRD trace for this film. The (200) X-ray pole figure of the film on Si features strong reflections at $\phi=80°$ and $\chi=45°$ and $\phi=280°$ and $\chi=45°$. The (200) pole figure for the specimen on quartz features less intense reflections at these positions but significantly more intensity near the apex of the stereographic projection. Closer examination of the region around $\chi=45°$ reveals that there are two regions of high (200) intensity separated by 90° ϕ with respect to each other and 45° ϕ with respect to the incident ion beam. The two regions are tilted approximately 10° χ away from the apex at $\chi=90°$ and away from the projection of the assisting ion beam. The (220) X-ray pole for the film on Si features five reflections with the most intense reflection at $\phi=0°$ and $\chi=80°$. The (220) X-ray pole figure for the film on quartz also features five reflections. The maximum intensity is distributed among two lobes near $\chi=90°$ along $\phi=45°$ and $\phi=315°$.

5.3.2.3 SEM Microstructure Characterization

A SEM fracture micrograph of a YSZ film deposited on quartz by dual ion beam deposition at 600°C is shown in Fig. 5.19. The surface of the film is rougher than those prepared by dual ion beam deposition at low temperature. The apparent film density is comparable to that of films deposited by dual ion beam deposition without active substrate heating. There is evidence of columnar development along the cross section that was not apparent with films prepared by dual ion beam deposition at low temperature. Both the rougher surface and columnar structure are consistent with fabrication at temperatures where surface diffusion is active.

5.4 DISCUSSION: DUAL ION BEAM DEPOSITION OF YSZ

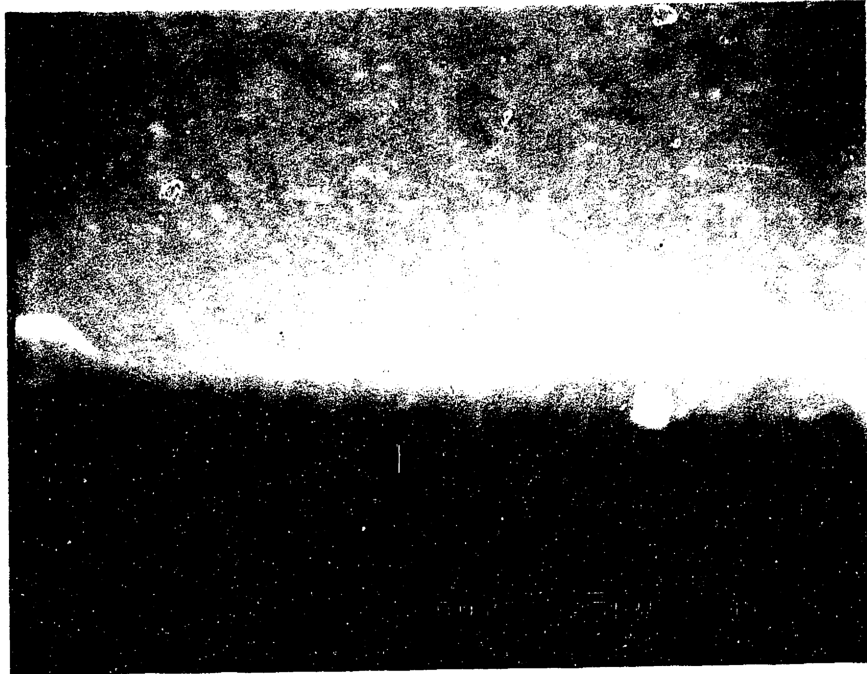

Figure 5.19 SEM micrograph of YSZ film fabricated by dual ion beam deposition at 600°C.

5.4.1 Dual Ion Beam Deposition of YSZ without Active Substrate Heating

All films fabricated by dual ion beam deposition without active substrate heating exhibited (200) biaxial alignment under all deposition conditions. The in-plane orientation of the films was similar to that noted by Iijima *et al.*[3-8] for YSZ films prepared by dual ion beam deposition under similar conditions, with {111} aligned parallel to the projection of the assisting ion source. Similar in-plane orientation was obtained with ion bombardment angles of 35° and 45°. Ion channeling is not consistent with obtaining (200) biaxial alignment with {111} aligned parallel to the assisting ion source projection with a bombardment angle of 45°. {220} would be aligned normal to the assisting ion beam in the film plane with (200) normal for an ion bombardment angle of 45° if ion channeling dictated in-plane orientation. This result is consistent with the observation of biaxial alignment for all bombardment angles for films fabricated by ion assisted e-beam evaporation.

The dependence of FWHM on r value is not straightforward. There is an apparent improvement in in-plane orientation for films deposited with relatively higher r values at the beginning of deposition. Maintaining high r values throughout deposition does not guarantee lower FWHM, as shown in Fig. 5.6 by the relatively large FWHM obtained during fabrication with a constant r value of 4.1 (Run 091495).

The microstructure of films fabricated by dual ion beam deposition without active substrate heating is polycrystalline and fine-grained, consistent with the Zone I microstructure on the Grovenor *et al.*[26] structure zone diagram for low temperature deposition. Control films fabricated without ion assist are weakly crystalline, with some (220) texture on all substrates. Grains with (220) normal orientation were observed along the film/substrate interface in Fig. 5.9 for a YSZ film deposited on quartz by dual ion beam deposition. The presence of grains with (220) normal orientation was confirmed by XRD. Biaxially aligned grains with (200) normal orientation emerged from the initial matrix of (220) grains with increased thickness. Multiple twins and dislocations were associated with the establishment of (200) biaxial alignment. Biaxially aligned (200) grains oriented approximately normal to the substrate were observed through the rest of the film. The [200] axis of many of the grains do not register with the [200] axis of

grains beneath them. These observations are consistent with renucleation occurring throughout deposition. The (200) biaxial alignment in these films is established during the transition from (220) normal orientation to (200) normal orientation, within the first 50nm of deposition. The biaxial alignment appears to remain approximately constant through the remainder of the film.

5.4.2 Dual Ion Beam Deposition of YSZ at 600°C

5.4.2.1 35° Bombardment Angle

(111) X-ray ϕ scans revealed {111} reflections split into pairs with approximately 30° ϕ separation, as shown in Fig. 5.14. The peak intensity of the (111) X-ray pole figure for the IBAD YSZ film on quartz in Fig. 5.15 was tilted approximately 10° χ away from the projection of the assisting ion beam. This tilt brings the (111) pole normally at χ=19.5° and ϕ=0° into coincidence with the assisting ion beam at χ=35° and ϕ=0°. The spacing between the peaks of the {111} reflections could be attributed to a coincident site lattice (CSL) among the YSZ grains. The lowest angle grain boundary for a coincident site lattice for rotation around [111] is the Σ13 CSL corresponding to θ=27.8°. A representation of the crystalline alignment corresponding to that CSL is shown in Fig. 5.20. The crystal is viewed along a [111] zone axis. The Zr^{4+} ions are shaded black and the O^{2-} ions are shaded gray.

5.4.2.2. 45° Bombardment Angle

(111), (200), and (220) reflections were observed in the θ-2θ XRD scans on all four substrates. Reflections from all three grain populations were observed in the X-ray pole figures of all films. All three grain populations on the silicon and quartz substrates were biaxially aligned with respect to the assisting ion beam. All three grain populations were oriented with {111} poles parallel to the assisting ion beam. The relative populations of (111), (200), and (220) grains was substrate dependent.

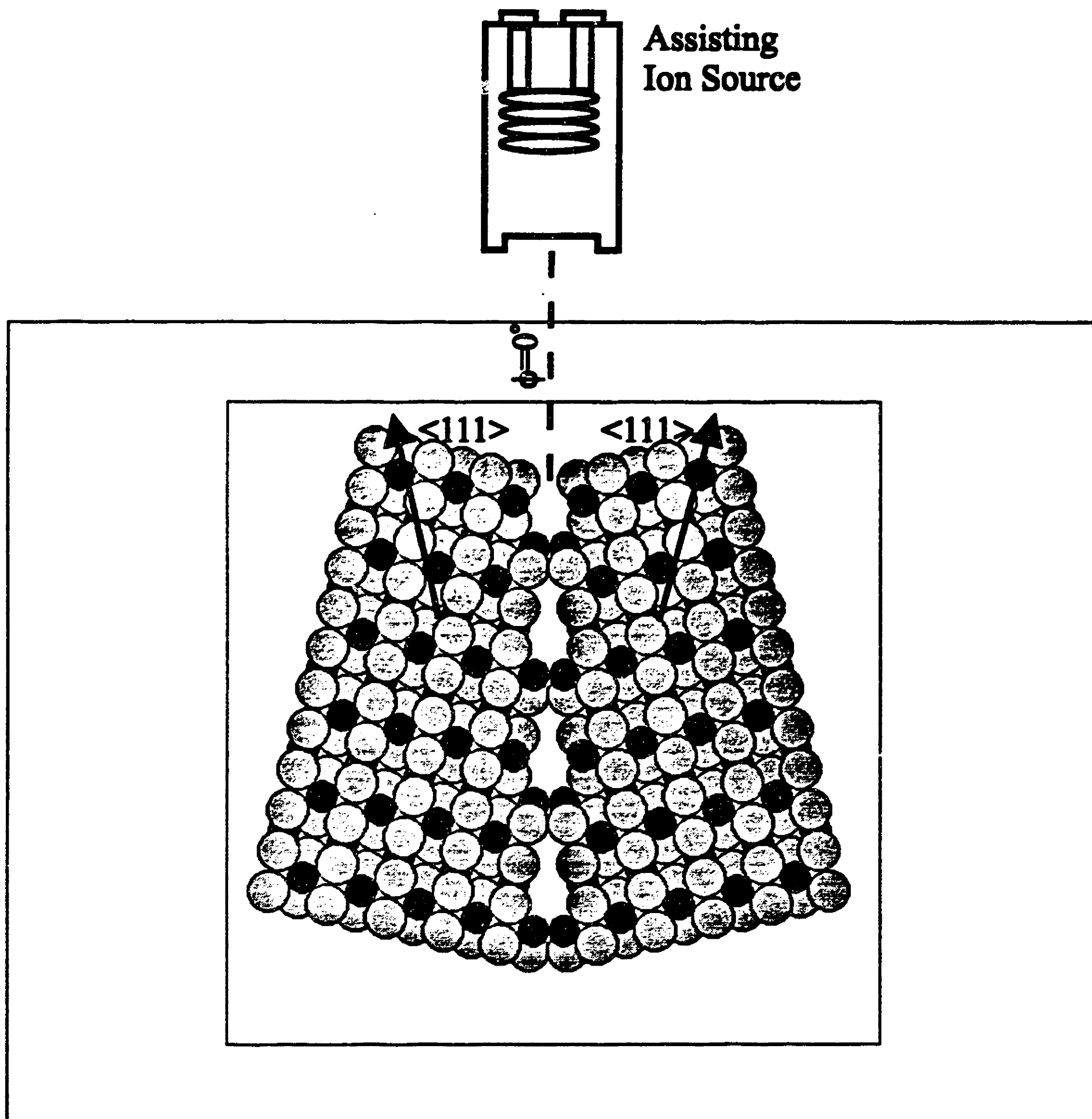

Figure 5.20 Schematic of Σ13 coincident site lattice consistent with biaxial alignment of YSZ film deposited on quartz at 600°C by dual ion beam deposition with an ion bombardment angle of 35°.

The differences in the pole figures on the respective substrates can be attributed to different relative populations of (111), (200), and (220) grains. The X-ray data are consistent with three populations of biaxially aligned grains on each substrate. The [111], [200], and [220] axes of the films are tilted from χ=90°. The direction of the tilt is specific to each grain orientation and is executed in order to bring {111} into coincidence with the assisting ion beam. The schematic in Fig. 5.21 shows how the respective grain populations are oriented in Fig. 5.18.

The reflection in the (111) pole figure at ϕ=180° and χ=55° corresponds to the [111] direction of the grains with (111) near-normal orientation. The [111] axis of the grains is tilted 25° away from the substrate normal in the direction opposite the projection of the assisting ion beam. This tilt brings a (111) pole into coincidence with the ion beam direction. Thus, the (111) pole, normally at χ=19.5°, appears at ϕ=0° and χ=45°.

Two intense lobes are present in the (200) X-ray pole figures for the films on both substrates. The relative intensity of (111) in the θ-2θ XRD trace for the film on the silicon substrate was greater than that for the film on quartz. Accordingly, the (200) reflections from (111) biaxially aligned grains poles for the film on silicon are more intense and well-defined than those in the (200) pole figure for the specimen on quartz. The two lobes near χ=90° in the (200) X-ray pole figure for the film on quartz are consistent with two populations of grains with (200) near-normal orientation, with each [200] axis tilted 10° away from the substrate normal away from the assisting ion beam direction. This tilt causes the {111} pole typically at ϕ=0° and χ=35° to be parallel to the incident ion beam. The reason why two populations would be necessary to achieve such an alignment for (200) grains is not clear. Further support for the existence of two populations of (200) grains can be obtained from the (220) pole figure for the film on quartz. The lobes of intensity along ϕ=45° and 315° can be attributed to (200) grains tilted as depicted in Fig. 5.21.

The in-plane orientation of the (220) grains is best viewed in the (220) pole figure for the film on Si. The (220) pole conventionally located at the center of the stereographic projection is titled 10° toward the projection of the assisting ion beam.

(111) Biaxially Aligned Grains

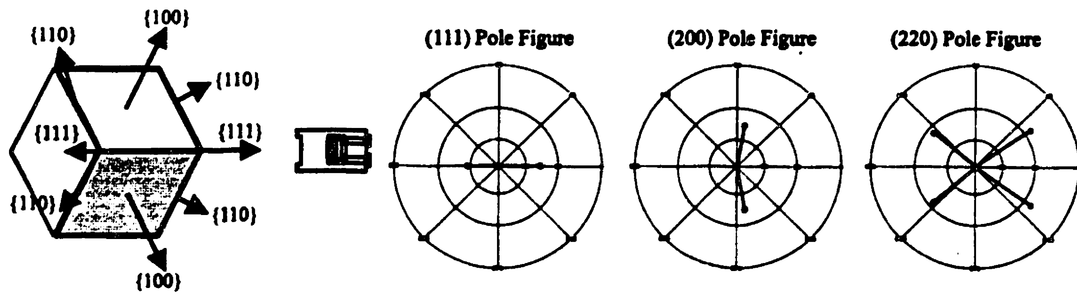

(200) Biaxially Aligned Grains

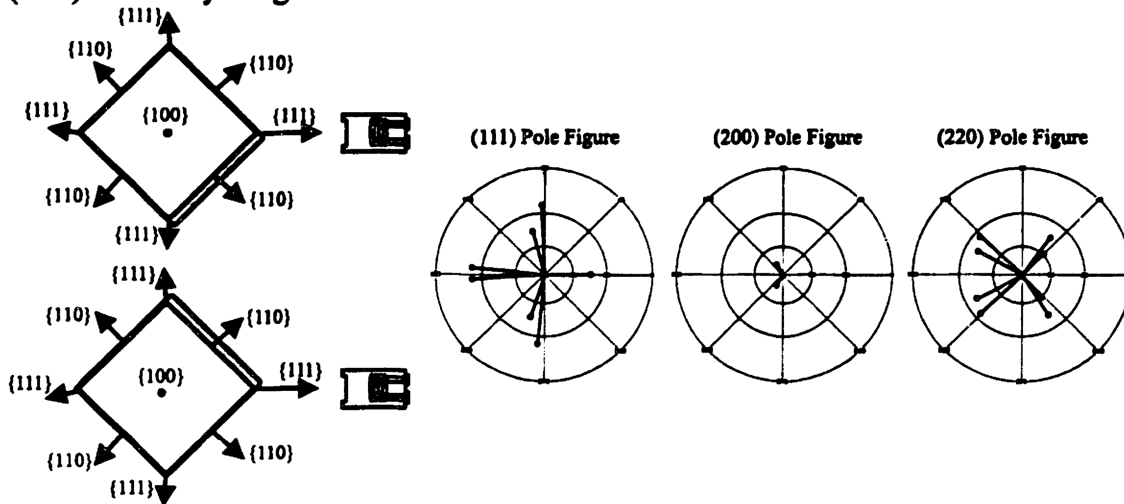

(220) Biaxially Aligned Grains

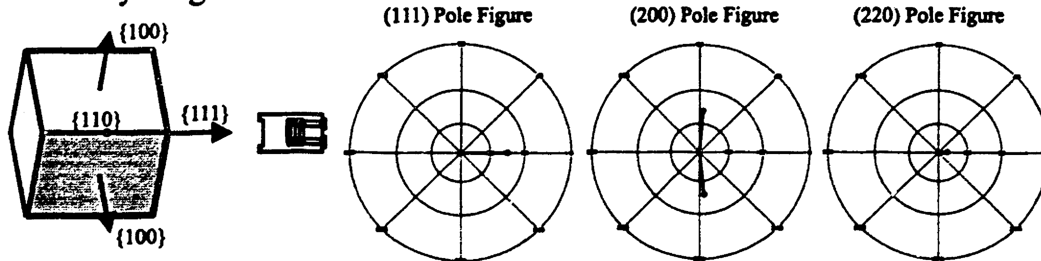

Figure 5.21 Representation of (111), (200), and (220) biaxially aligned grain populations and corresponding X-ray pole figure reflection positions.

This tilt places the {111} reflection for grains with (220) near-normal orientation parallel to the assisting ion beam. The (220) grains also contribute to the reflections observed in the (111) pole figures at ϕ=80° and χ=45° and ϕ=280° and χ=45°.

5.4.3 Film Microstructure and Comments on Dual Ion Beam Deposition Biaxial Alignment at 600°C

The observation of columns and surface relief in the films fabricated by dual ion beam deposition at 600°C are indicative of enhanced surface diffusion and grain boundary mobility. The columnar development is consistent with Zone II fabrication in the structure zone model of Grovenor *et al.*[26]

Several aspects of the nature of biaxial alignment observed at 600°C indicate that a different mechanism is responsible for the development of biaxial alignment at elevated substrate temperature compared to that operative without active substrate heating. First, the alignment exhibited by films deposited at 600°C is substrate dependent, whereas substrate-independent biaxial alignment was observed in films deposited without active substrate heating. Several defects such as twins and dislocations were observed in cross-sectional TEM micrographs of films deposited without active substrate heating, but for the most part they were localized to specific regions within the film. X-ray pole figures display the in-plane orientation representative of an entire specimen. Peak intensities of the {111} reflections were at the ideal position of χ=35° in X-ray pole figures of films with (200) normal orientation fabricated without active substrate heating, even though the (200) orientation of individual grains often deviated from the substrate normal. Reflections in the X-ray pole figures of films deposited at 600°C were split and tilted from ideal χ and ϕ positions, indicating that most of the film grains were oriented in unison in these nonideal positions. This observation is consistent with Zone II growth and granular epitaxy, where the orientation of a grain is continued with increased film thickness rather than granular renucleation where local crystallography changes continually during deposition. Film growth during dual ion beam deposition at 600°C therefore appears similar to the growth rate mode identified for ion assisted e-beam

evaporation at 600°C rather than the renucleation mode advanced for dual ion beam deposition without active substrate heating.

5.5 SUMMARY

(200) Biaxially aligned YSZ films were fabricated by dual ion beam deposition on amorphous, polycrystalline, and nonepitaxial single crystal substrates. Substrate-independent biaxial alignment was observed for films deposited without active substrate heating. Cross-sectional TEM revealed that IBAD (200) biaxial alignment develops under these conditions by twinning from an initial (220) orientation at the film/substrate interface. Substrate-dependent biaxial alignment of several YSZ orientations was observed for films deposited by dual ion beam deposition at 600°C. All orientations were biaxially aligned with (1 1 1) planes in the direction of the assisting ion beam.

CHAPTER 6
DUAL ION BEAM DEPOSITION OF LCMO

6.1 INTRODUCTION

The fabrication of biaxially aligned YSZ films by ion beam assisted deposition has been examined by several groups, including Iijima *et al.*[3-8] and Arendt *et al.*[9-12] The motivating factors for examining IBAD YSZ for high T_c applications apply to many other materials systems and applications. Few materials can be grown in large single crystal form with high purity at reasonable cost like silicon. Many electronic, optical, and magnetic thin film oxide device technologies are limited to laboratory scale due to a dearth of commercially available single crystal substrates. High deposition temperatures are often required to assure epitaxial growth on these single crystals for those instances where suitable substrates are available.

The fabrication of colossal magneoresistive (CMR) thin films is a case in point. Epitaxially laser ablated $La_{1-x}Ca_xMnO_3$ (LCMO) thin films have exhibited remarkable magnetoresistance ratios on single crystal $SrTiO_3$ substrates. Both the deposition technique and the substrate choice confine this research to small-area substrates. Commercial exploitation of this technology depends of finding a deposition technique capable of producing these LCMO films over large area, commercially viable substrates.

IBAD is a fabrication technique that could make CMR thin film devices commercially viable. LCMO is of interest in context with this thesis for several reasons. First, successful fabrication of biaxially aligned LCMO would demonstrate that oxides other than YSZ could be fabricated by IBAD. Secondly, LCMO has the perovskite crystal structure, as opposed to the fluorite structure of YSZ. Fabricating both materials by IBAD allows the influence of crystal structure on the development of biaxial

alignment to be examined and tests the generality of the IBAD biaxial alignment mechanism conclusions made based on the work on YSZ.

6.2 EXPERIMENTAL PROCEDURE

6.2.1 Dual Ion Beam Deposition of LCMO

A bulk sputtering target of was prepared by repeated grinding and reactive calcination of La_2O_3, $CaCO_3$, and MnO powder at 900°C. The process was repeated three times until complete conversion to $La_{0.67}Ca_{0.33}MnO_3$ was confirmed by θ-2θ XRD. The powder was mixed with a polyethylene glycol binder, dry pressed into a 2"x4"x1" targets, and sintered at 1400°C.

(100) $SrTiO_3$ and amorphous quartz substrates were mounted for a control deposition without ion assist using the procedures described in Chapter 3. The specimen block was placed at an angle of 35° with respect to the assisting ion source for consistency with later depositions with ion assist. Control and IBAD films fabricated with substrate temperatures below 600°C were amorphous; the films discussed in this chapter were all deposited at a substrate temperature of 600°C. The sputtering beam current was 30mA and the beam energy was 1000eV. Argon gas was flowed through the ion source. Four hours of IBAD deposition resulted in films ~3800Å thick, indicating a net deposition rate of approximately 0.26Å/s.

Several LCMO films were deposited on (100) $SrTiO_3$, (100) Si, Hastelloy, and amorphous quartz substrates at 600°C with ion assist. The sputtering ion beam conditions were identical to those used in the control deposition. The assisting ion source beam current was 30 mA, the beam energy was 75 eV, the accelerator voltage was 450V, and the neutralizer emission current was 120mA. The excess neutralizer emission current was used to neutralize both ion beams and to minimize charging on the insulating sputter target. A mixture of Ar with 8% O_2 was passed through the assisting ion source.

6.2.2 Film Characterization

Film orientation was examined using θ-2θ X-ray diffraction, four-circle diffractometry, X-ray pole figures, and X-ray phi scans using a CuK_α radiation source, as described in Chapter 3. Selected LCMO specimens was observed using scanning electron microscopy. Four point electrical resistance measurements from 77 to 298K were performed on the IBAD LCMO film deposited on quartz.

6.3 RESULTS AND DISCUSSION: DUAL ION BEAM DEPOSITION OF LCMO

6.3.1 X-Ray Diffraction

Both the control and IBAD LCMO films were epitaxial on $SrTiO_3$. The θ-2θ XRD trace for the control LCMO film sputtered on $SrTiO_3$ is shown in Fig. 6.1. The control film sputtered on quartz was polycrystalline with several intense reflections, as shown in Fig. 6.2. The films deposited by dual ion beam deposition featured (h00) biaxial alignment on all substrates. A representative θ-2θ trace for the film deposited on quartz is shown in Fig. 6.2. The (100) and (200) LCMO reflections are dominant, with small (110) and (111) reflections present. The LCMO films deposited on $SrTiO_3$, Hastelloy, and (100) Si all exhibited similar traces. The (110) X-ray phi scan for the IBAD film deposited on quartz is shown in Fig. 6.3. The positions of the {110} reflections at ϕ=45°, 135°, 225°, and 315° for {h00} aligned normal to the substrate are consistent with {111} parallel to the assisting ion beam at χ=35° and ϕ=0°. Similar phi scans were observed on all the Hastelloy and (100) silicon substrates. This is the first demonstration of IBAD biaxial alignment of a multication oxide film. The substrate-dependent biaxial alignment is similar to that noted for IBAD YSZ at elevated substrate temperature.

6.3.2 LCMO Film Microstructure

A cross-sectional SEM micrograph of the IBAD LCMO film on quartz is shown in Fig. 6.4. The film is dense, smooth, and featureless. The microstructure is very

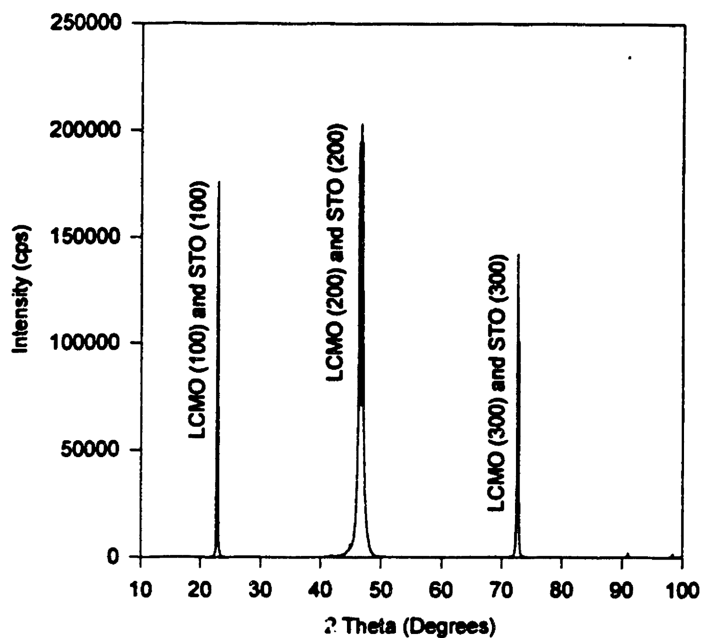

Figure 6.1 θ-2θ XRD trace of control LCMO film sputtered on $SrTiO_3$ at 600°C.

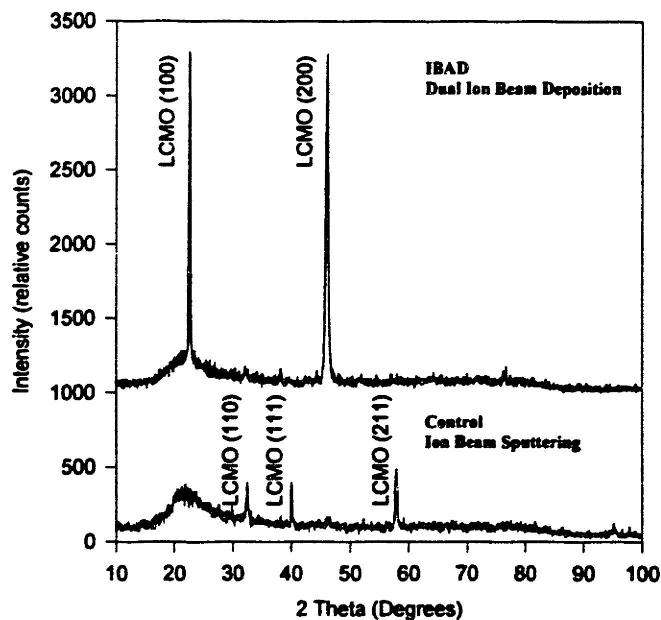

Figure 6.2 θ-2θ XRD traces of LCMO films fabricated by dual ion beam deposition at 600°C on quartz with and without ion assist.

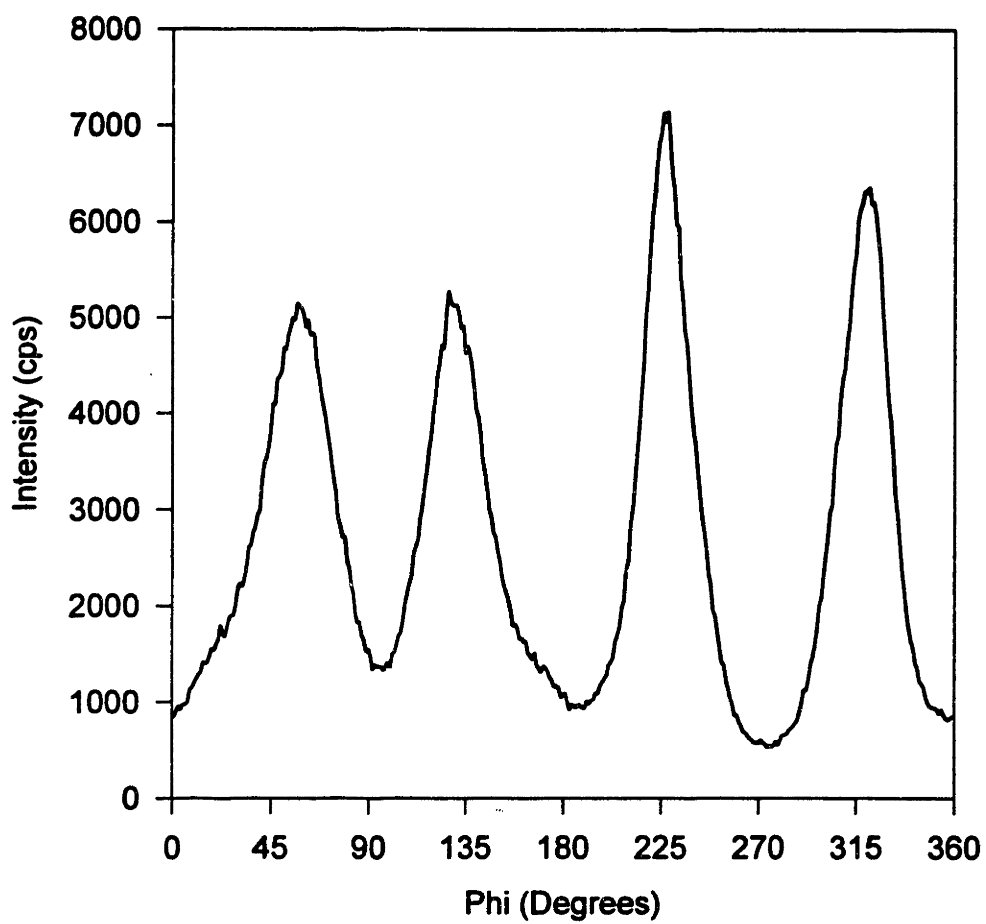

Figure 6.3 (110) X-ray ϕ scan of (h00) biaxially aligned LCMO film on quartz.

Figure 6.4 SEM micrograph of LCMO film fabricated by dual ion beam deposition at 600°C.

similar to that observed for IBAD YSZ films deposited at 600°C by dual ion beam deposition.

6.3.3 Electrical Resistance Measurements

Four-point electrical resistance measurements were taken from the IBAD LCMO film on quartz. The resistivity data is shown from 77 to 298K in Fig. 6.5. The temperature of peak resistivity was observed at 99K. The film displayed metallic-like behavior below 99K in that resistivity increased with increased temperature and semiconductor-like behavior above 99K in that resistivity decreased with increased temperature. It should be noted that the resistivity values are much greater in magnitude than those exhibited by either metals or semiconductors. The resistivity trend is characteristic of CMR behavior. The transition temperature compared favorably to the value of 95K reported by McCormack *et al.*[65] for an epitaxial LCMO film which featured a magneoresistance ratio of 127,000%.

6.4 SUMMARY

Epitaxial LCMO films were sputtered on $SrTiO_3$ with and without ion assist. (h00) Biaxially aligned LCMO films were deposited by dual ion beam deposition at 600°C on $SrTiO_3$, (100) Si, Hastelloy, and amorphous quartz substrates. The in-plane orientation of the biaxially aligned LCMO films featured {111} parallel to the assisting ion beam. The substrate-dependent biaxial alignment is similar to that observed for IBAD YSZ films deposited at 600°C. This is the first reported fabrication of a multication oxide film using IBAD.

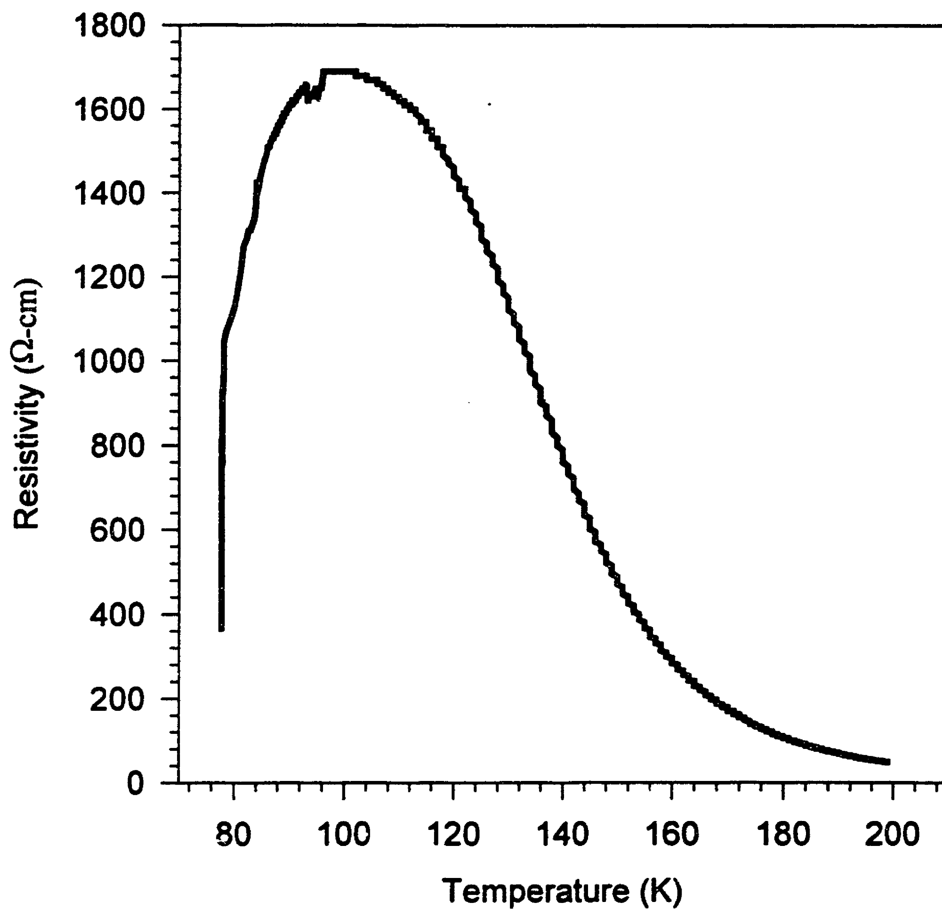

Figure 6.5 Electrical resistivity of IBAD LCMO film on quartz versus absolute temperature.

CHAPTER 7
ROLE OF THE ASSISTING ION BEAM IN THE DEVELOPMENT OF IBAD BIAXIAL ALIGNMENT

7.1 INTRODUCTION

All YSZ films deposited by ion beam assisted deposition have been shown to be biaxially aligned with both deposition techniques for all deposition rates, ion bombardment angles, assisting ion beam energies, assisting ion fluences, and substrate temperatures. The only common factor in these depositions has been the presence of the assisting ion beam. The biaxial alignment universally obtained under all IBAD parameters indicates that the assisting ion beam may be affecting film development in a common manner for all deposition conditions.

The arguments most frequently advanced for why ion beam-induced YSZ film texturing occurs during IBAD are based on ion channeling. According to the sputtering anisotropy theory of Bradley,[41] ions incident along open YSZ crystallographic directions undergo few collisions; rather, the ions traverse considerable distances into the solid before coming to rest. Grains parallel to channeling directions are, therefore, sputtered at a lesser rate relative to all other orientations which are misoriented with respect to the assisting ion beam. Ensinger[42] argues that anisotropy in radiation damage causes biaxial alignment, and that grains aligned parallel to ion channeling directions are damaged to a lesser extent than misoriented grains. Both of these arguments are examined in this chapter. First, the likelihood of ion channeling under the assisting ion beam conditions commonly employed in IBAD is investigated. Secondly, the idea of etching anisotropy based on crystalline orientation is considered. Anisotropy in damage is the third theory advanced to explain ion induced texturing during IBAD. These theories will be tested to explain the two different in-plane orientations observed for (200) biaxially aligned YSZ

films fabricated by IBAD and the in-plane orientation observed for LCMO films deposited by dual ion beam deposition.

7.2 IN-PLANE ORIENATION OF (200) BIAXIALLY ALIGNED FILMS

The fabrication of (200) biaxially aligned YSZ films by IBAD with ion assisted electron beam evaporation and dual ion beam deposition both without active substrate heating and at 600°C was detailed in Chapters 4 and 5. Two different in-plane orientations were observed for the (200) biaxially aligned films. The films fabricated by dual ion beam deposition featured (111) planes in the direction of the incident ion beam projection. This in-plane orientation was also noted by Iijima *et al.*[3-8] and Arendt *et al.*[9-12] for their IBAD YSZ films fabricated by dual ion beam deposition. The films fabricated by ion assisted electron beam evaporation at a bombardment angle of 45°, both at 600°C and without active substrate heating, featured (220) planes in the direction of the incident ion beam. It may appear that the in-plane orientation of (200) biaxially aligned films is dependent on the IBAD deposition technique, but that is not the case. (200) Biaxially aligned YSZ films with both (111) and (220) planes toward the assisting ion beam have been fabricated under different deposition conditions by ion assisted electron beam evaporation at 600°C. Four series of films were deposited with ion bombardment angles of 8, 23, 38, 48, and 63°. The IBAD parameters used for each series are detailed in Table 7.1. The ion fluences noted in Table 7.1 are the fluences measured with the Faraday cup at normal incidence to the impinging plasma. The ion fluence for each of the films within a given series is equal to this value times the sine of the ion bombardment angle. The (111) X-ray pole figures for each of the films is shown in Fig. 7.1. The nature of the in-plane alignment for each film in Fig. 7.1 is summarized in Table 7.2.

The (200) YSZ reflection was by far the most intense in the θ-2θ XRD traces for all of the films in Series 1-4. Each of the films is (200) biaxially aligned, as evidenced by the pole figures in Fig. 7.1. Films fabricated with ion assist at 8° and 23° in Series 1 exhibited (111) poles toward the assisting ion beam, while the films fabricated with bombardment angles of 38° and 48° exhibited (220) toward the assisting ion beam. The

Table 7.1 IBAD parameters used to fabricate (200) biaxially aligned YSZ films

Series	1	2	3	4
Deposition Rate (Å/s)	1.2	2.4	2.4	2.4
Ion Fluence ($\mu A/cm^2$)	18	18	18	44
Beam Energy (eV)	75	75	300	300
Ion:YSZ Molecule Ratio (r)	0.11	0.05	0.05	0.25

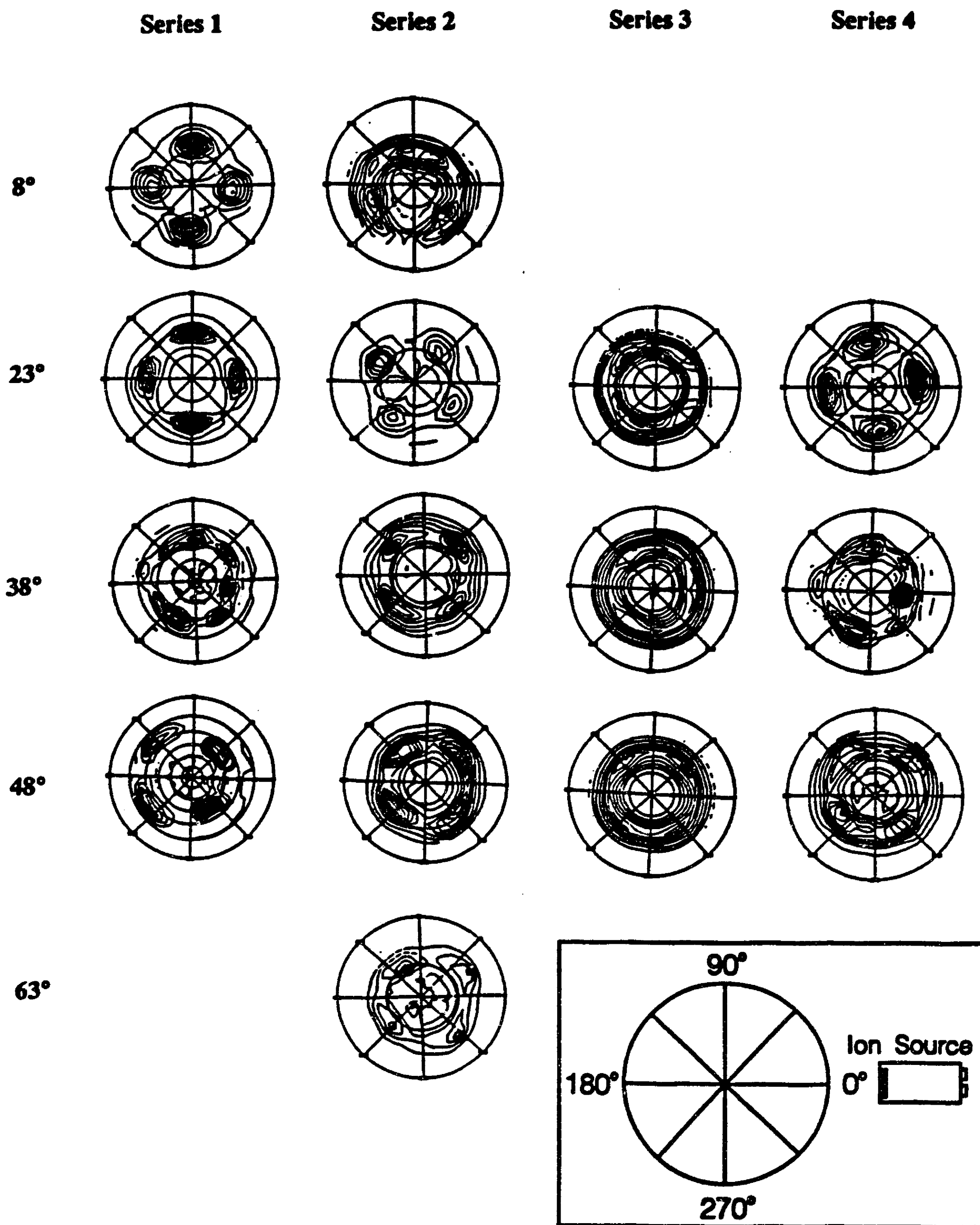

Figure 7.1 (111) X-ray pole figures of (200) biaxially aligned YSZ films fabricated at 600°C on Pyrex by ion assisted electron beam evaporation. Angle shown is the ion bombardment angle.

Table 7.2 Summary of in-plane film orientation for Series 1-4

	Series			
Bombardment Angle (°)	1	2	3	4
8	(111)	mixed		
23	(111)	(220)	(220)	(111)
38	(220); mixed	(220)	(220)	(220); mixed
48	(220)	(220)	(220)	(220)
63		(220)		

mixed - additional contributions from (311) biaxially aligned grains

deposition rate was doubled while all other IBAD parameters were held constant in Series 2; the r value was therefore halved relative to Series 1. The films fabricated at 23°, 38°, 48°, and 63° bombardment angles all featured (220) poles toward the assisting ion beam. The in-plane orientation of the film fabricated with ion assist at 23° switched from (111) to (220) in the direction of the assisting ion beam when the r value was halved. The beam energy was increased from 75 to 300eV in Series 3, with the deposition rate, ion fluence, and r value identical to those in Series 2. The in-plane orientation of the films in Series 3 remained identical in all cases to those in Series 2. IBAD with increased beam energy but the same r value did not change the in-plane orientation of the films. The r value in Series 4 was increased fivefold relative to that in Series 2 and 3 and more than twofold relative to that in Series 1. The same in-plane orientations were observed in Series 4 as were noted in Series 1 for all three films. The in-plane orientation of the films fabricated with ion assist at 23° switched from (220) toward the ion beam in Series 3 to (111) toward the ion beam in Series 4 with increased r value.

It is clear from these experiments that the in-plane orientation of (200) biaxially aligned films depends on the r value, which depends in part on the ion bombardment angle. A field plot summarizing the in-plane orientations of (200) biaxially aligned films fabricated by both IBAD techniques at both deposition temperatures is shown in Fig. 7.2. The r values on the ordinate are corrected for the ion fluences consistent with the respective bombardment angles. The in-plane orientations are located in two clear regions: (111) toward the ion beam for films fabricated with high r value while (220) is aligned parallel to the ion beam projection for films fabricated with lower r value. The boundary between (111) and (220) oriented toward the ion beam is not specific to the IBAD deposition technique, as films with (111) oriented parallel to the ion beam were fabricated by both dual ion beam deposition and ion assisted electron beam evaporation. The boundary is also not defined by the substrate temperature during IBAD. Films fabricated with nearly the same r values by ion assisted electron beam evaporation without active substrate heating at 45° bombardment angle and by ion assisted electron beam evaporation at 600°C with ion bombardment at 48° both feature (220) parallel to the ion beam projection. The field boundary between (111) and (220) planes does,

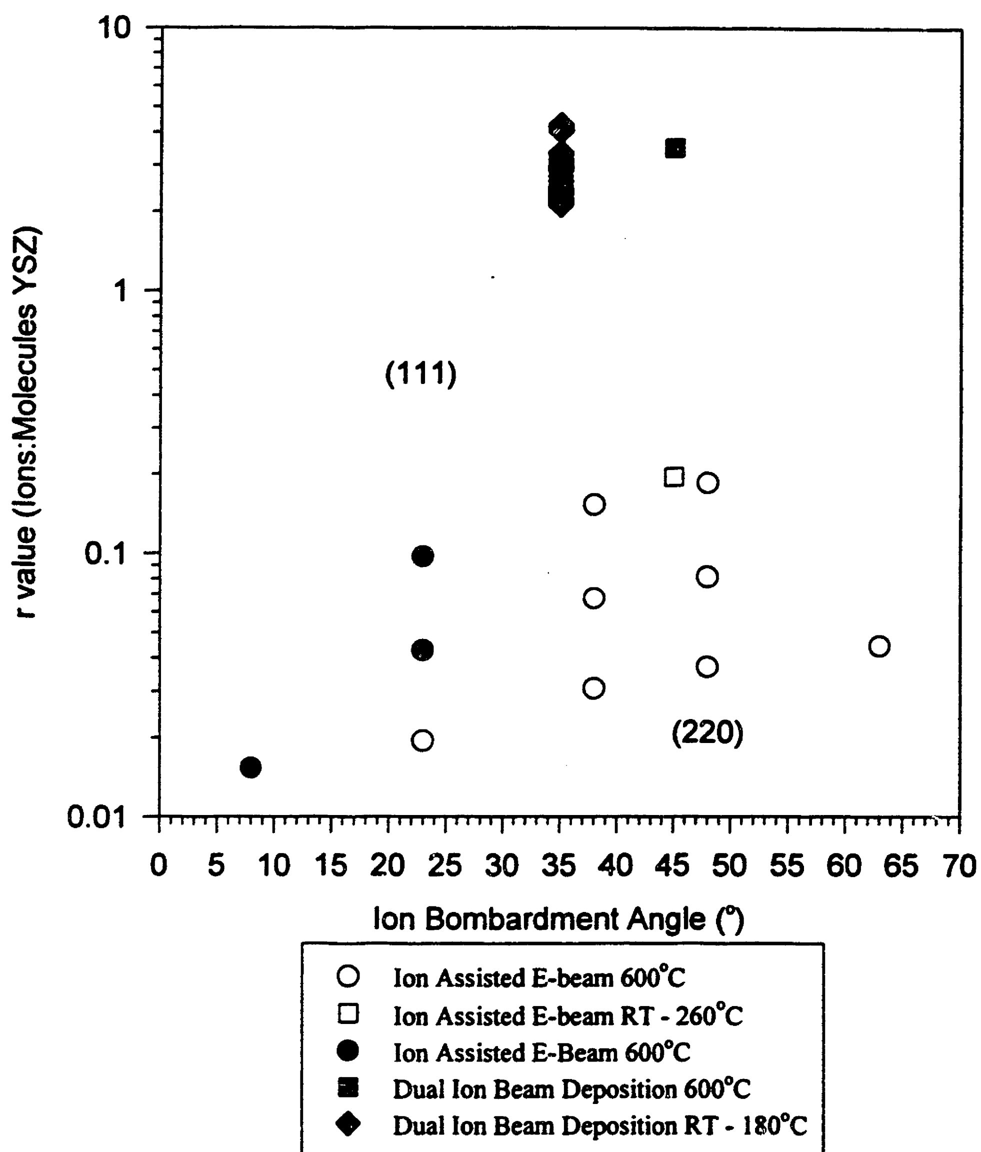

Figure 7.2 Field plot showing in-plane orientation of (200) biaxially aligned YSZ films fabricated by both IBAD techniques without active substrate heating and at 600°C. Filled symbols indicate (111) oriented parallel to assisting ion beam projection. Open symbols indicate (220) oriented parallel to assisting ion beam projection.

however, depend on the ion bombardment angle. The boundary is located at lower r values for lower ion bombardment angles.

The data in Fig. 7.2 are also consistent with the observations of Iijima *et al.*[3-8] and Arendt *et al.*[9-12] for (200) biaxially aligned films fabricated by dual ion beam deposition without active substrate heating. Both research groups always observed (111) oriented parallel to the assisting ion beam projection under the experimental conditions examined. Iijima *et al.* fabricated (200) biaxially aligned YSZ films with several ion bombardment angles.[3,6] The quoted deposition rate was 0.5Å/s. It is not clear whether this value was the gross deposition rate or the net deposition rate. No information was provided for the ion etching rates during deposition; therefore, the gross deposition rate is assumed to be 0.5Å/s for the following determination of r value. In earlier work[3], the ion fluence was 220μA/cm^2 as measured by a Faraday cup. (200) biaxially aligned films were fabricated with ion bombardment angles of 25°, 35°, 45°, and 60° from the substrate plane. In more recent work[6], ion fluences between 50 and 100μA/cm^2 were noted, and (200) biaxially aligned films were fabricated with ion bombardment angles of 25°, 30°, 35°, 40°, and 60°. An ion fluence of 75μA/cm^2 was assumed for determining the r values for this data. Arendt *et al.*[9] listed deposition rates and ion fluences of 0.4Å/s and 150μA/cm^2 and an ion bombardment angle of 35 from the substrate plane. The ion fluences were assumed to vary with ion bombardment angle in the same manner as described in Chapter 3.

Figure 7.3 includes the additional data from the Fujikura group of Iijima *et. al*[3-8] and the Los Alamos group of Arendt *et al.*[9-12] (200) biaxially aligned films with (111) planes oriented with the ion beam projection were observed for all bombardment angles for films fabricated with an r value above 1. The r values used in this thesis for dual ion beam deposition of YSZ are similar to those used by Iijima *et al.*[3-8] and Arendt *et al.*[9-12] in their IBAD fabrications. The data from Iijima *et. al*[3,6] confirm the trend of switching from (220) toward the ion beam to (111) poles toward the ion beam for IBAD fabrication with increased ion to molecule ratio at any given ion bombardment angle. The precise location of the boundary between the (111) and (220) regions in the field plot is unclear, particularly at higher ion bombardment angles. The data in Fig. 7.3 are split into two primary populations. The data for dual ion beam deposition all correspond to r values

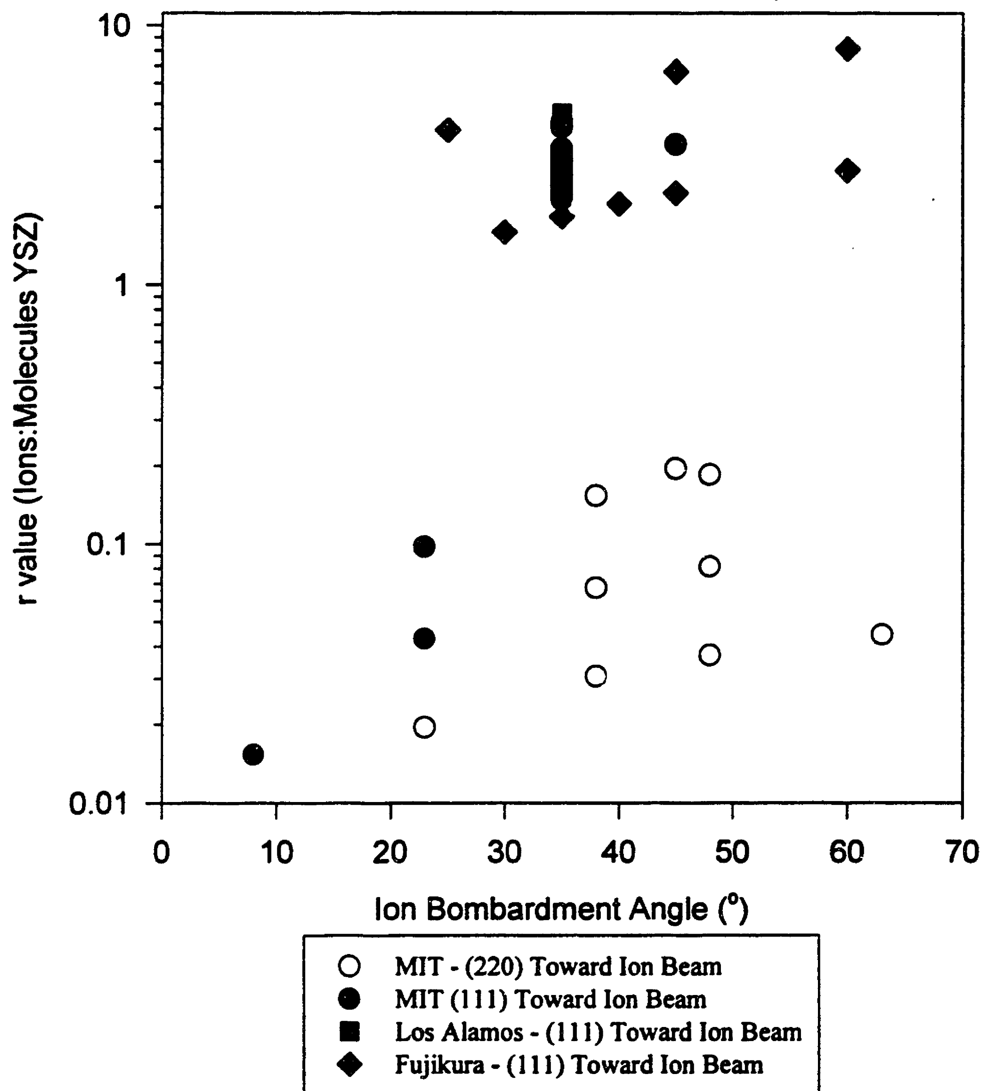

Figure 7.3 Field plot comparing results from this work to the in-plane orientation observed by Iijima *et al.*[3,6] and Arendt *et al.*[9] for YSZ films fabricated by dual ion beam deposition without active substrate heating. Filled symbols indicate (111) oriented parallel to assisting ion beam projection. Open symbols indicate (220) oriented parallel to assisting ion beam projection.

above 1 while the data for ion assisted electron beam evaporation correspond to r values below 0.25. These groupings can be attributed primarily to the deposition rates than can be attained with the respective deposition techniques. It is difficult in practice to attain gross YSZ deposition rates greater than 0.5Å/s by ion beam sputtering using a Kaufmann-type ion source, while relatively high YSZ gross deposition rates are readily attainable by electron beam evaporation.

The trend of in-plane orientation switching is consistent for both IBAD deposition techniques over three orders of magnitude in r value and over a wide range of IBAD parameters and substrate temperatures for assisting ion beam energies of 75 and 300eV. The generality of the trend suggests that the assisting ion beam is creating texture in a common manner during all depositions. It objective of the remainder of this chapter is to identify the mechanism by which the assisting ion beam induces texture during IBAD.

7.3 TEXTURING MECHANISM OF THE ASSISTING ION BEAM

7.3.1 ADESH and TRIM92 Software

Two software programs are used in this section to understand the nature of ion beam interaction with zirconia. ADESH (Atomic DEfect Simulation Handler) Version 2.1[66] and TRIM (TRansport of Ions in Matter) Version 92.12[67] were used in this investigation. ADESH facilitates modeling atomistic configurations and perturbations of materials by use of appropriate potential functions. TRIM92 is a Monte Carlo package that enables modeling ion bombardment of solids. The following sections detail the procedure used to obtain the parameters needed in the ADESH and TRIM simulations.

7.3.1.1 YSZ Lattice Constant and Density

The lattice parameters of a material are among the fundamental data needed to use ADESH, while the density of a material is needed in order to use TRIM. Common values for the lattice constant and density of YSZ are needed to facilitate agreement between the two programs. The nominal composition of both the YSZ grog used for evaporation and

the YSZ sputtering target is 8 mol% Y_2O_3 stabilized ZrO_2. It was therefore decided to use the lattice constant and density for this composition.

Scott[68] determined that all specimens containing more than 6.5 mol% Y_2O_3 were cubic and was able to calculate a linear variation in lattice parameter for cubic solid solutions for $YO_{1.5}$ compositions from 0.18 to 0.90 in ZrO_2. Following the extrapolation of this relationship to slightly lower $YO_{1.5}$ content yields a lattice parameter of 5.137Å for 8 mol% Y_2O_3 stabilized ZrO_2. This lattice parameter was used for the ADESH simulations.

The closest relevant JCPDS[69] file is number 30-1468[70] for the composition $Zr_{0.85}Y_{0.15}O_{1.93}$. The specimen was prepared by firing ZrO_2 and Y_2O_3 powder at 1400°C for 6 days with one intermediate regrinding. The specimen had a light grayish brown color, indicating that the oxygen content was substoichiometric. The reported lattice constant and density for the specimen were 5.139Å and 5.959 g/cm^3, respectively.

Hoiuchi *et al.*[71] used a YSZ crucible grown by the cold crucible method for YSZ neutron diffraction studies. The specimen was colorless and transparent and appeared optically isotropic when examined with polarized light, indicating the specimen was cubic. X-ray diffraction precession photographs indicated F-centered cubic symmetry. The chemical composition of the specimen was analyzed with an analytical electron microscope equipped with a Si(Li) solid-state detector. Quantitative analysis of the Zr and Y L_α, K_α, and K_β x-ray spectra was consistent with a chemical stoichiometry of $Zr_{0.72}Y_{0.28}O_{1.62}$. A lattice parameter of 5.158Å was determined from a spherically shaped single crystal using a four-circle diffractometer. The calculated density of the specimen was 5.824 g/cm^3.

Extrapolating from the lattice constant values and densities for the $Zr_{0.85}Y_{0.15}O_{1.93}$ and $Zr_{0.72}Y_{0.28}O_{1.62}$ compositions yield a density of 5.973 g/cm^3 for a lattice constant of 5.137Å for $Zr_{0.84}Y_{0.16}O_{2-x}$. The density used for the TRIM simulations was rounded to 6.0 g/cm^3 to reflect increased oxygen content in the IBAD YSZ films due to bombardment with reactive O_2^+ from the assisting ion beam during growth.

An idealized zirconia structure is used for both ADESH and TRIM. The composition assumed for both software packages is $Zr_{0.33}O_{0.67}$ and the crystal structure is

assumed to be the cubic fluorite structure. The yttria content needed to stabilize the cubic structure and corresponding oxygen vacancies are neglected to simplify the simulations.

7.3.1.2 Potential Function for YSZ in ADESH

The interatomic potential of YSZ was modeled using the ionic potential option of ADESH as optimized for zirconia. The potential is based on treating the Zr^{4+} and O^{2-} as point charges located in their ideal positions in the fluorite lattice. Following the treatment in the Second Edition of Introduction to Solid State Physics by Kittel[72], the total energy of any individual ion i (ϕ_i) is related to the interaction energy between ions i and j ϕ_{ij} by

$$\phi_i = \sum_j{}' \phi_{ij} \tag{7-1}$$

The prime indicates that the summation includes all ions except $j=i$. The interaction energy ϕ_{ij} is written as the sum of a crystal field repulsive potential varying as r_{ij}^{-n}, where r_{ij} is the distance between ions i and j, and a Coulomb potential:

$$\phi_{ij} = \frac{\lambda}{r_{ij}^n} \pm \frac{Z_i Z_j e^2}{r_{ij}} \tag{7-2}$$

Z_i and Z_j are the ion charges. The + sign is for like charges and the - sign is for oppositely charged ions. The repulsive term accounts for the hard ion cores resisting overlapping with the electron clouds of neighboring ion cores. The parameters λ and n are constants to be determined from observed values of lattice constant and compressibility. A potential function of similar form to equation 7-2 was used for modeling point defects in Cr_2O_3.[73]

The function in equation 7-2 converges in three dimensions only after many shells of nearest neighbors have been considered. ADESH uses an algorithm to simplify the calculation of ionic crystal energies. The function in equation 7-2 can be made to converge within a closer distance to the central ion by dealing with groups of neighboring ions with neutral, or near neutral charges.[72] The potential of a neutral assembly of ions decays faster at a given distance from the assembly compared to an group of ions with

excess charge. ADESH calculates the energy of each ion in the lattice in the following manner. The interaction energy between the ion of interest and all of its neighbors within a specific cutoff radius of the central ion is calculated using Equation 7-2. The interaction energies between the central ion and each of the neighboring ions within the cutoff radius are sorted in order of increasing ion distance from the central ion. The largest electrically neutral group of ions within the cutoff radius is determined. The energy of the ion is determined by adding the interaction energies between the central ion and the ions within the electrically neutral subset of neighboring ions. The cutoff radius used for determining the ion energies in zirconia was 4Å. An example of this calculation for determining the energy of a Zr^{4+} ion is given in Appendix A.

The total lattice energy U_o of a group of ions is calculated by repeating the summation detailed above over all ϕ, counting each pair of interactions once. The total lattice energy is the energy required at absolute zero to convert one mole of the crystal into its constituent ions at infinite separation in the gas phase.

Theoretical values of U_o and experimental values of compressibility greatly facilitate selection of appropriate λ and n values for the potential function. The theoretical value of U_o can be calculated for ZrO_2 via the Born-Haber cycle. The heat of formation of $ZrO_{2(s)}$ is conventionally measured from its constituent elements in their standard states and is equal to -1092 kJ/mol at 0K. It can also be calculated from the energy terms in a hypothetical reaction path. The first step of the reaction path involves sublimation of $Zr_{(s)}$ and the dissociation of $O_{2(g)}$ to $2O_{(g)}$:

$$Zr_{(s)} \overset{S}{\Rightarrow} Zr_{(g)} \tag{7-3}$$

$$O_{2(g)} \overset{D}{\Rightarrow} 2O_{(g)} \tag{7-4}$$

where S is the sublimation energy for $Zr_{(s)}$ (602.5 kJ/mol)[74] and D is the dissociation energy of $O_{2(g)}$ (493.6 kJ/mol).[75] The gaseous species are then ionized to the charge states present in the ZrO_2 crystal:

$$Zr_{(g)} \overset{+\sum I_{Zr}}{\Rightarrow} Zr^{4+}{}_{(g)} \tag{7-5}$$

$$O_{(g)} \overset{-E_x}{\Rightarrow} O^{2-}_{(g)} \tag{7-6}$$

where $\sum I_{Zr}$ is the sum of the first four ionization potentials for Zr (7500.2 kJ/mol)[76] and E_X is the sum of the first and second electron affinities for $O_{(g)}$ (-719.6 kJ/mol).[77] The total lattice energy U_o is evolved upon reaction of the gaseous ions to form $ZrO_{2(s)}$. The two complementary reaction paths of the Born-Haber cycle are:

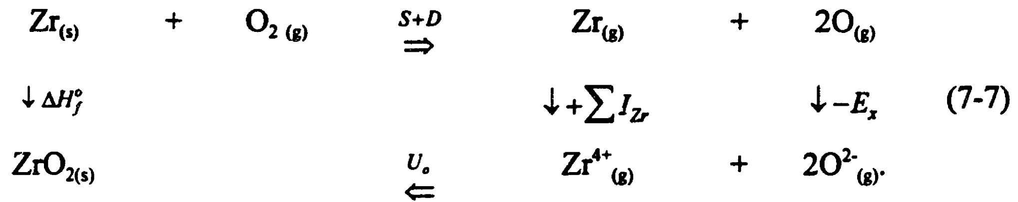

$$\begin{array}{ccccccc} Zr_{(s)} & + & O_{2\,(g)} & \overset{S+D}{\Rightarrow} & Zr_{(g)} & + & 2O_{(g)} \\ \downarrow \Delta H_f^o & & & & \downarrow +\sum I_{Zr} & & \downarrow -E_x \\ ZrO_{2(s)} & & & \underset{\Leftarrow}{U_o} & Zr^{4+}_{(g)} & + & 2O^{2-}_{(g)}. \end{array} \tag{7-7}$$

The total lattice energy can be calculated from

$$U_o = \Delta H_f^o - S - D + \sum I_{Zr} - E_X \tag{7-8}$$

and is equal to 11127.6 kJ/mol. This value is in close agreement to a value of 11195.5 kJ/mol in the literature.[78] The total lattice energy can be converted to 115.4 eV/molecule. This value can be used as a target for optimization of the parameters λ and n.

Optimal values for λ and n were determined by experimenting with a cubic zirconia computational cell using ADESH. A computational cell was created with the x, y, and z vectors corresponding to the [100], [010], and [001] crystal vectors. Periodic boundary conditions were used along [100], [010], and [001] so that the cell simulated a bulk specimen of zirconia while avoiding free surface effects. Values of 55.3 for λ and 3.2 for n substituted in Equation 7-2 resulted in an energy of -115.946 eV/molecule in the computational cell.

The validity of the potential function using these values of λ and n values was tested by calculating the bulk modulus of a computational zirconia cell cube by imposing a hydrostatic strain upon the computational cube and measuring the resulting strain energy. A tensile hydrostatic strain of 0.01 induced a strain energy increase in the computational cell consistent with a bulk modulus of 189.13 GPa. The mathematical details of this calculation are shown in Appendix B. This value was compared with experimental data for yttria-stabilized zirconia. Mizutani *et al.*[79] report a Young's

Modulus (E) of 210 GPa for 8 mol% yttria-stabilized zirconia. Ingel[80] reports a Poisson's Ratio (ν) of 0.31 for polycrystalline zirconia with 10 mol% yttria. This corresponds to a bulk modulus of 184.2 GPa. The close match between calculated lattice energy and bulk modulus calculated using ADESH with the thermodynamic crystal binding energy and experimental bulk modulus of a polycrystalline YSZ specimen supported the validity of the ADESH potential function. The potential function as given below was used to calculate the energy of both individual ions and groups of ions in zirconia crystals for several simulations in this thesis:

$$\phi_{ij} = \frac{55.3}{r_{ij}^{3.2}} \pm \frac{Z_i Z_j e^2}{r_{ij}}. \qquad (7\text{-}9)$$

7.3.1.3 TRIM92

TRIM92 is a Monte Carlo simulation program used to model ion bombardment of solids. The principal motivation in this thesis for using TRIM is to determine the average penetration depth, or range, of 75eV and 300eV argon ions in zirconia. The following sections discuss the TRIM program and the assumptions taken to determine the ion ranges in zirconia.

7.3.1.3.1 Binary Collision Approximation

TRIM is based on the binary collision approximation for ion/solid interactions. The binary collision approximation treats the movement of a ion or atom projectile in a solid as a series of successive binary collisions. A fundamental assumption used in TRIM is that the target is amorphous. This allows ion/atom and atom/atom collision partners to be selected at random, greatly simplifying the computational complexity of the program. The assumption of an amorphous target is applicable for ion energies ranging from 100eV to several MeV, depending on the ion and target atom masses. The assumption of binary ion/target collisions is less valid for ion energies below 100eV, which compromises the assumption of an amorphous target at low ion energies. TRIM nevertheless provides a satisfactory evaluation of ion ranges for low energy ions.

Two key parameters used in TRIM are the distance between successive binary collisions and the impact parameter p, which determines the energy transfer in a binary collision. The distance between successive collisions, λ_o, is equal to $N^{-1/3}$, where N is the atomic density of the target. The impact parameter determines the elastic energy transferred in a binary collision and is equal to the distance of closest approach between the centers of mass of the projectile and target atom. The impact parameter generated by TRIM is a random number between zero and p_{max}, where p_{max} is the sum of the projectile and atom atomic radii. Therefore, a collision with p=0 corresponds to a head-on collision while a collision with $p=p_{max}$ corresponds to a glancing collision where the outermost projectile and target electrons have minimal overlap. Minimal elastic energy is transferred in such a collision.

7.3.1.3.2 TRIM92 Simulation Algorithm

The simulation procedure used by TRIM is as follows. A projectile ion strikes a randomly chosen target atom. The energy transfer of the collision is determined from the value of the impact parameter. The trajectory and energy of the ion are updated after the collision. The energy transfer in the binary collision is assumed to be elastic; therefore, the ion energy after the collision is equal to its previous energy minus the energy transferred to the target atom. The new ion trajectory is calculated based on the p value of the collision. The ion then traverses another distance λ_o before colliding with another target atom. The ion inelastically loses energy while traversing λ_o due to electronic stopping of the target electron orbitals. The electronic stopping of the target is calculated based on the ion energy, the ion mass, the target atom mass, the target atom density, the target atomic number, and the Fermi velocities of the ion and target. The electronic stopping is the atomically weighted average electronic stopping powers of the constituent target atoms for compound targets. The projectile is assumed to change direction after binary nuclear collisions and move in straight paths between collisions. Projectiles therefore lose discrete amounts of energy in nuclear collisions and lose energy

continuously from electronic interactions. This sequence is repeated until the kinetic energy of the ion is reduced to zero.

The paths of recoil atoms are also tracked in TRIM. A target atom becomes a recoil atom if the elastic energy transferred in a binary collision exceeds its bulk binding energy E_b. The target atom is displaced to a stable interstitial site, leaving a vacancy behind, if the elastic energy transferred in the collision exceeds the bulk displacement energy E_d of the atom. If the energy imparted to the target atom is insufficient to dislodge it from its lattice site, the additional kinetic energy is dissipated as phonons. If the target atom becomes a recoil, its motion is treated as a projectile until its kinetic energy is reduced to zero.

7.3.1.3.3 TRIM Calculation of Ion Energy Loss and Ion Range

The ion energy lost per unit path length in the target, $\frac{dE}{dx}$, is related to the nuclear and electronic stopping cross-sections ($S_n(E)$ and $S_e(E)$) and the target atomic density N by

$$\frac{dE}{dx} = N(S_n(E) + S_e(E)). \tag{7-10}$$

When the kinetic energy of an ion decreases to zero through binary collisions and electronic energy loss the ion comes to rest in the solid. The distance traversed over the path of a projectile ion into a target is defined as the ion range R and is given by

$$R = \int_0^{E_o} \frac{dE}{N(S_n(E) + S_e(E))}. \tag{7-11}$$

Because of collisions with target atoms the path taken by an ion is not linear, but rather a random trail. Furthermore, the path is influenced by the ion angle of incidence with respect to the target. The ion range frequently noted in ion bombardment studies is not the range along the pathlength, but rather the longitudinal ion range, which is the projected distance into the solid from the surface normal to the final ion position in the target. Both the pathlength range and longitudinal range are shown in Fig. 7.4. Unless otherwise noted, range mentioned in this thesis are longitudinal ion ranges.

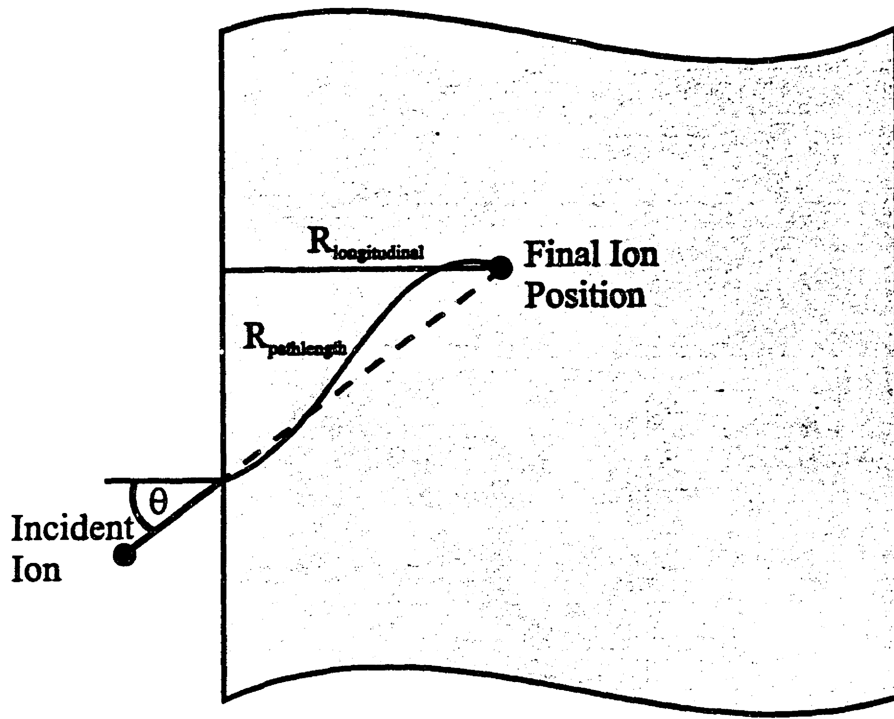

Figure 7.4 Schematic showing ion pathlength and ion range as defined in equation 7-11.

The TRIM simulations in this thesis calculated the histories of 1000 argon ions incident at several bombardment angles with energies of 75eV or 300eV. The reported range is the average longitudinal range of the 1000 ions considered in a simulation. The standard deviation of the longitudinal ranges is defined as the ion straggle. The ion range and straggle describe the statistical ion penetration depth into a target. The ion range is of particular interest for this thesis because it describes the length scale over which all of the incident kinetic ion energy is imparted into the target.

The ion range calculated by TRIM is dependent on the methods by which TRIM evaluates nuclear and electronic energy loss in a target. TRIM does not use nuclear stopping cross-sections in its determination of energy loss through binary collisions. Instead, TRIM calculates elastic energy loss based on the scattering angle θ of the projectile ion in the center-of-mass (CM) system. Figure 7.5 is a schematic of projectile/target collisions from two different reference frames: the laboratory system and the CM system. The laboratory system is a Newtonian reference frame where an incident projectile with mass M_1 and velocity v_o collides with a target atom of mass M_2. The distance of closest approach between the projectile and atom centers of mass is the impact parameter p. The projectile is scattered at an angle ϑ after the collision at reduced velocity v_1 while the target atom recoils at angle ϕ with velocity v_2.

The same binary collision can be expressed in CM coordinates in which the total momentum of the system is zero. CM coordinates are used because a complex force acting between two particles can be reduced to that of one particle moving in a central potential centered at the origin of the CM coordinates if the force between the two particles acts only along the line joining them. This enables the mutual interaction of the projectile and target atoms to be described by a potential $V(r)$ which only depends on the interatomic separation between the particles. The projectile and target atoms move at velocity v_c relative to velocities in the laboratory system. The projectile scatter angle θ in the CM system determines the elastic energy transfer.

TRIM and other Monte Carlo ion bombardment simulation programs account for nuclear energy loss during binary collisions based on general screened interatomic functions between colliding atoms rather than using the specific interatomic potentials of

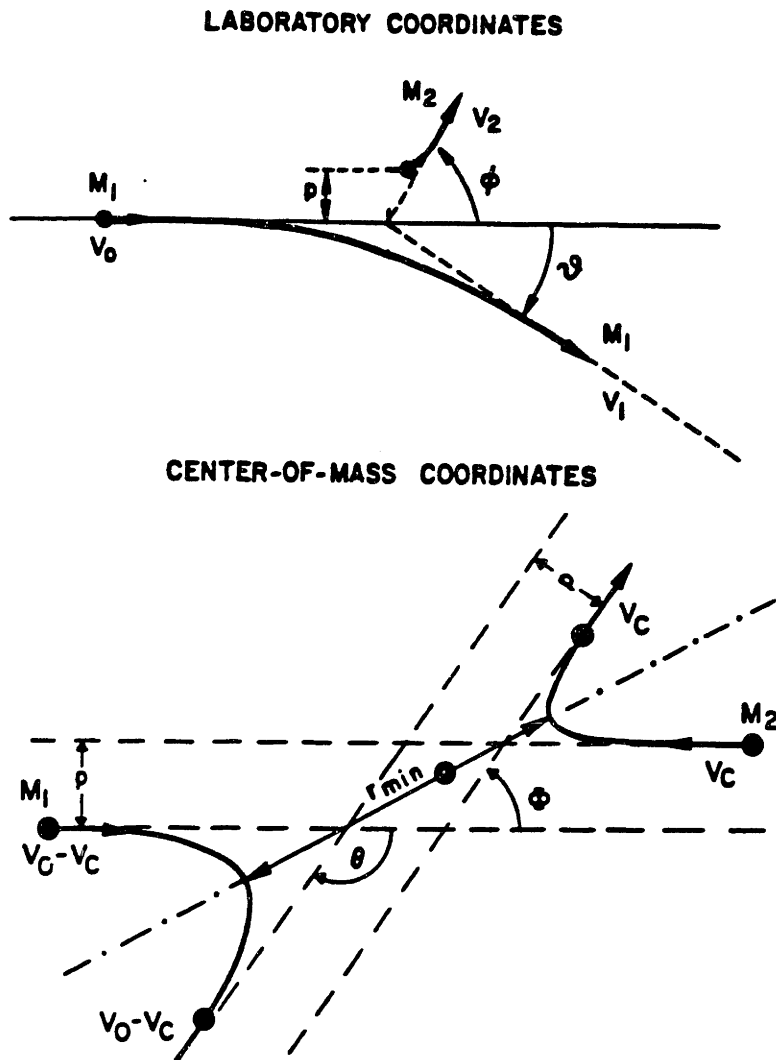

Figure 7.5 Schematic of projectile/target collisions in Newtonian laboratory coordinates and in center-of-mass coordinates (from Reference 67).

the projectile and target atoms. The screened interatomic potential function is defined as the ratio of atomic potential V on an individual atom to the potential of an unscreened nucleus:

$$\Phi = \frac{V(r)}{(Ze/r)} \tag{7-12}$$

where Z is the atom's atomic number, e is the electronic charge, and r is the radial coordinate. TRIM uses the Universal screened potential function Φ_U which is defined as

$$\Phi_U = 0.1818e^{-3.2x} + 0.5099e^{-0.9423x} + 0.2802e^{-0.4028x} + 0.2817e^{-0.2016x} \tag{7-13}$$

$$\text{with the reduced interatomic distance } x = \frac{r_{12}}{a_U} \tag{7-14}$$

$$\text{and } a_U = \frac{0.8854a_o}{Z_1^{0.23} + Z_2^{0.23}} \tag{7-15}$$

where r_{12} is the interatomic separation between the projectile (1) and target atom (2), a_o is the Bohr radius, 0.529x10^{-8}Å, and Z_1 and Z_2 are the atomic numbers of the projectile and target atoms. The screened potential function is independent of the atomic number of an atom and thus can be used to represent *all* atoms. The corresponding Universal potential used for nuclear scattering and energy loss at the low ion energies is given by

$$V(x) = \frac{Z_1 Z_2 e^2}{a_U x}\Phi_U(x). \tag{7-16}$$

This repulsive potential is used to calculate the distance of closest approach r_o for a binary collision with an impact parameter p selected at random by TRIM by

$$1 - \frac{V_{(r_o)}\left(1 + \frac{M_1}{M_2}\right)}{E_o} - \left(\frac{p}{r_o}\right)^2 = 0. \tag{7-17}$$

The projectile scattering angle θ is given by

$$\cos\left(\frac{\theta}{2}\right) = \frac{\rho_1 + \rho_2 + \delta + p}{\rho_1 + \rho_2 + r_o} \tag{7-18}$$

where ρ_1 and ρ_2 are the radii of curvature of the projectile and target atoms in the CM system and δ is a small correction term. Finally, the energy transfer T to the target atom in a single binary collision is given by

$$T = \frac{4M_1M_2E}{(M_1+M_2)^2}\sin^2\left(\frac{\theta}{2}\right) \quad (7\text{-}19)$$

The ion proceeds along a trajectory given by the scattering θ after the collision with energy E_2 given by

$$E_2 = E_1 - T \quad (7\text{-}20)$$

where E_1 was the ion energy before the binary collision.

TRIM calculates the electronic energy loss over the distance λ_o between binary collisions. The electronic energy loss ΔE_e is calculated using

$$\Delta E_e = \lambda_o N S_e(E) \quad (7\text{-}21)$$

where $S_e(E)$ is the electronic stopping cross section. Argon is considered a heavy ion compared to H and He and the mathematical treatment for heavy ions is determined by the ion velocity relative to the Fermi velocity of the target electrons. The Fermi velocity of most solids lies between $1.5\text{x}10^8$ cm/s and $3\text{x}10^8$ cm/s, corresponding to ion velocities of 25keV/amu. The velocities of Ar^+ ions with 75eV and 300eV energy are $1.9\text{x}10^{-3}$ and $7.5\text{x}10^{-3}$ keV/amu. Electronic energy loss for ions of such low energy is calculated by electronic stopping cross-sections proportional to the ion velocity. The velocity of most of the electrons in the target is far greater than the ion velocity. Consequently most of the ion/target electron interactions are adiabatic without direct energy loss.

The theory of velocity-proportional electronic stopping is based on metals, for which low energy electronic loss is caused by conduction electrons accurately described as a free electron gas. The electronic stopping for materials with a band gap should be reduced because there are fewer low-energy excitation levels available for valence electrons. The electronic stopping for materials with a band gap has been shown to be proportional to $v^{0.7}$ for Si and Ge. Electronic energy loss would be expected to be even smaller for an insulator such as zirconia.

The relative importance of nuclear and electronic stopping depends in large part on the ion energy. The reduced ion energy ε is used to calculate the nuclear and electronic stopping cross-sections. For the Universal interatomic potential function used in TRIM, the value of ε is given by

$$\varepsilon = \frac{32.53 M_2 E}{Z_1 Z_2 (M_1 + M_2)(Z_1^{0.23} + Z_2^{0.23})} \quad (7\text{-}22)$$

where E is the ion energy in keV, M_1 and M_2 are the a.m.u. masses of the projectile and target atom, respectively, and Z_1 and Z_2 are the atomic numbers of the projectile and target atoms. ε provides a measure of the relative importance of nuclear and electronic energy loss for a given ion energy. For the low ion energies considered in this thesis, the energy transferred through elastic (nuclear) collisions is far greater than that inelastically lost through electronic stopping. A schematic diagram of ion energy loss as a function of ion energy is given in Fig. 7.6 over many decades of ion energy. The peak in energy loss to elastic collisions corresponds to $\varepsilon = 0.5$ while the peak in energy loss to electronic stopping reaches a maximum at significantly higher ion energies. Nuclear elastic collisions account for the majority of ion energy loss at $\varepsilon < 0.5$. The ε values for 75eV and 300eV Ar^+ bombardment of Zr^{4+} and O^{2-} target atoms are listed in Table 7.3. Each of the ε values are far less than 0.5, indicating that nuclear (elastic) collisions with target ions dissipate the majority of a projectile ion's energy for the experiments discussed in this thesis.

7.3.1.3.4 Determination of Bulk Binding Energy and Bulk Displacement Energy

Values of the bulk binding energy E_b and the bulk displacement energy E_d are needed for individual target atoms to model a target using TRIM. These values determine the energy that must be transferred to target atoms to initiate a collision cascade of recoils in the target. These energies also influence the motion of a projectile ion in the target. The meanings of both E_b and E_d in the context of the TRIM calculation is somewhat ill-defined. The bulk binding energy is defined[81] as the energy required to remove a target atom from its lattice site by an elastic energy transfer. The final location of the target atom is not specified in the definition. The value of E_b is also uncertain. Some set $E_b = 0$ while others believe E_b should be equal to the vacancy formation energy of a target atom. In this thesis it is assumed that E_b is the equal to the negative of the interaction energy of an ion in the bulk zirconia lattice calculated using

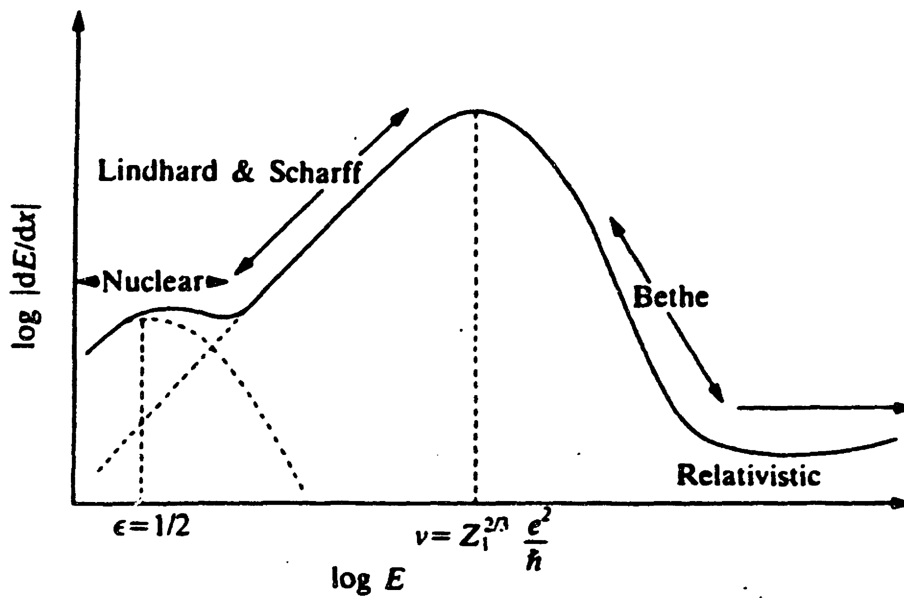

Figure 7.6 Stopping power of an ion as a function of ion energy. Nuclear stopping is the dominant ion stopping mechanism in the low energy IBAD regime (from Reference 82).

Table 7.3 ε Values for 75eV and 300eV Ar^+ bombardment of Zr^{4+} and O^{2-} in ZrO_2

Ion	ε_{75eVAr^+}	$\varepsilon_{300eVAr^+}$
O^{2-}	0.0032	0.0127
Zr^{4+}	0.0006	0.0020

equation 7-9. Thermodynamically, this is the energy needed to remove an ion from the bulk zirconia lattice to the gas phase an infinite distance away from the lattice at absolute zero. The bulk binding energies calculated using ADESH for zirconium and oxygen ions are $E_b^{Zr^{4+}}$ = 93.47eV and $E_b^{O^{2-}}$ = 11.24 eV. TRIM92 allows only one value of E_b for a compound target. The atomically averaged value of E_b used in the TRIM simulations was 38.65eV.

The bulk displacement energy E_d is the energy needed to form a stable Frenkel pair of a target atom in an interstitial site and a vacancy at the original target atom site. This energy depends on the direction of momentum of the recoiled target atom and is linked to the crystallography of the target lattice, even though TRIM assumes an amorphous target. Half of the cation sites are vacant in fluorite structure, presenting numerous interstitial sites for Zr^{4+} atoms. While numerous oxygen vacancies are present in yttria-stabilized zirconia, none of the anions sites are vacant in the ideal cubic fluorite structure assumed for ADESH and TRIM. The vacant cation sites are the only openings large enough in the idealized structure to accommodate oxygen interstitials. The energy of both Zr^{4+} and O^{2-} ions was calculated as a function of increasing distance from their initial ideal lattice sites toward vacant cation sites using ADESH. As shown in Fig. 7.7, the energy of a zirconium ion rises from -93.47 eV at its ideal site through a maximum of -22.07eV to -51.87eV at the interstitial site. The energy difference between the global energy minimum at the ideal site and the local energy minimum at the interstitial site, 41.6eV, was chosen for $E_d^{Zr^{4+}}$. There is a local energy minimum for an interstitial oxygen ion at a vacant zirconium site, as shown in Fig. 7.8; however, the energy in this interstitial site is greater than the thermodynamic zero. From a thermodynamic standpoint, the oxygen ion would be displaced an into the gas phase an infinite distance from the zirconia lattice when the O^{2-} energy reached zero. Therefore the bulk displacement energy for oxygen $E_d^{O^{2-}}$ was assumed to be equal to the bulk binding energy of 11.24eV.

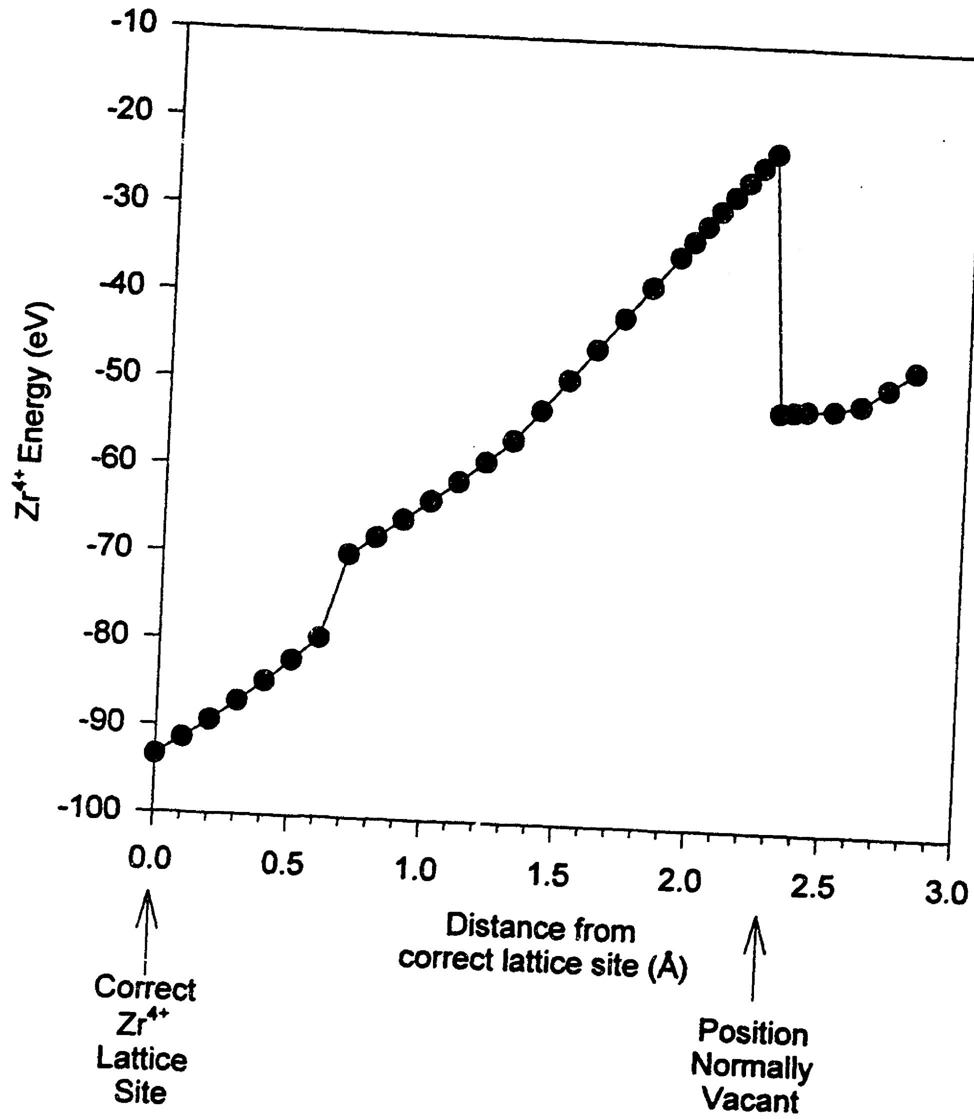

Figure 7.7 Zirconium ion energy as a function of distance from correct lattice site. Local energy minimum exists at interstitial site.

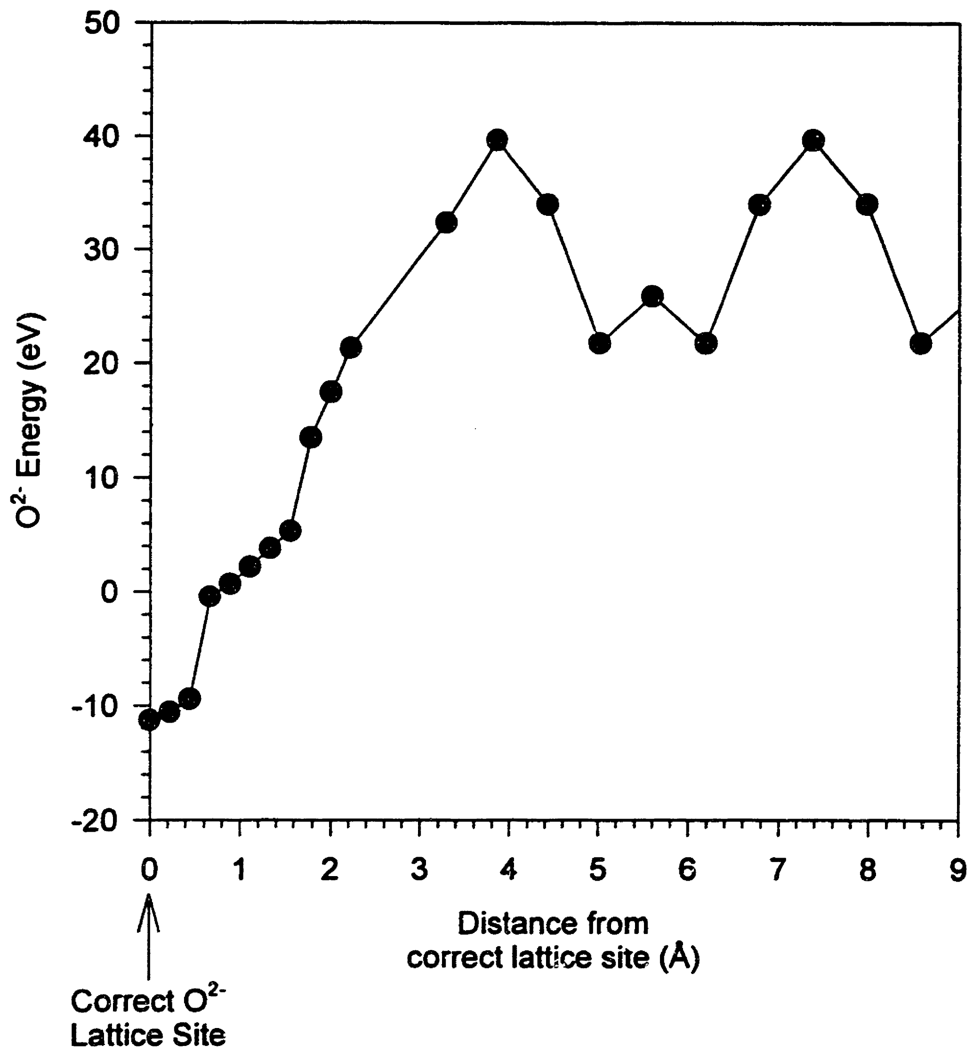

Figure 7.8 Oxygen ion energy as a function of distance from correct lattice site. Local energy minima exist only at energies greater than that needed to remove ion from lattice.

7.3.2 Ar^+ Range in Zirconia and Channeling in Zirconia and LCMO

The possibility of channeling playing a role in the development of IBAD biaxial alignment is examined in two parts. First, ion ranges are calculated for 100eV and 300eV Ar^+ bombardment of zirconia at angles from 20° through 90° using TRIM. This analysis is valid for bombardment angles that do not correspond to channeling directions in the lattice. The zirconia films of interest feature (200) normal to the substrate, so ion bombardment angles of 35° and 45° correspond to the {111} and {110} channeling directions, respectively, for the cubic fluorite structure. The likelihood of Ar^+ channeling down the {100}, {110} and {111} planes of zirconia is then examined based on the nuclear stopping cross-sections for ions with 75eV and 300eV energy.

The range of argon ions with 100eV and 300eV energy in zirconia was simulated using TRIM for ion bombardment angles of 20° through 90°, where 90° corresponded to normal incidence. The ion energy of 100eV was used instead of the 75eV energy used in many experiments in this thesis because it was the minimum energy TRIM allowed for simulation. The simulation target was zirconia of composition $Zr_{0.33}O_{0.67}$ and density 6.00g/cm^3. The bulk binding energy was 38.65eV and the displacement energies E_d were 93.47eV and 11.24eV for zirconium and oxygen ions, respectively. The histories of 1000 Ar^+ were calculated for each ion energy and bombardment angle, from which the ion range and straggle were determined. The ion ranges for 100eV and 300eV Ar^+ bombardment of zirconia is shown as a function of ion bombardment angle in Fig 7.9. The 100eV ion ranges vary from 4±2Å for 20° bombardment to 6±2Å at normal incidence. The 300eV ion ranges vary from 6±3Å for 20° bombardment to 11±5Å at normal incidence. The incident ion energy is dissipated within one zirconia unit cell for 75eV bombardment and within 2 unit cells for 300eV bombardment. The ion energy and momentum input are clearly confined to the near-surface region of the target. The ion energy is imparted within a smaller distance from the surface for bombardment at oblique bombardment angles. Ion bombardment during growth, therefore, occurs with continual modification of the film surface, with the bulk remaining unperturbed. The TRIM evidence, based on an amorphous zirconia target, indicates that the effect of argon ion bombardment is confined to the outermost two unit cells of the film.

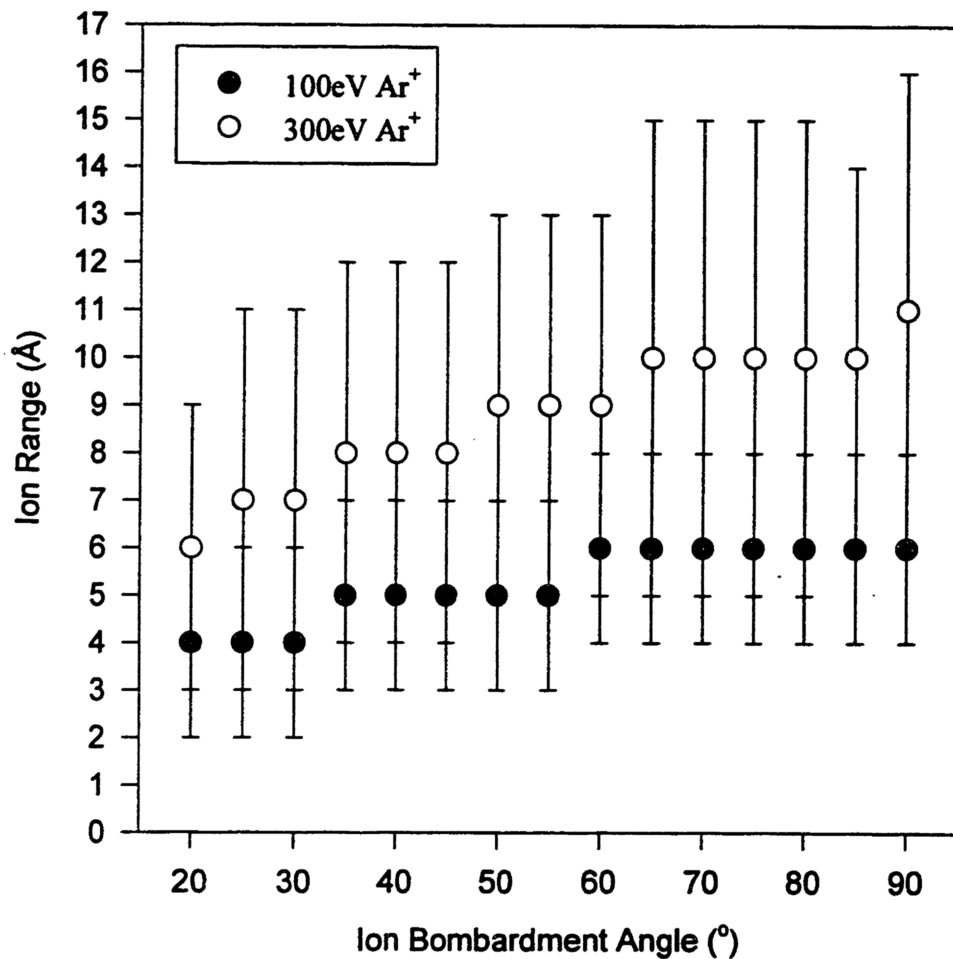

Figure 7.9 Ion ranges for 100eV and 300eV Ar^{+} incident on zirconia as a function of ion bombardment angle. Angle of 90° corresponds to normal incidence.

The (200) biaxially aligned films fabricated using IBAD are highly textured, however, and nuclear stopping cross-sections must be determined to evaluate the possibility of channeling in the textured films. The nuclear stopping cross section $S_n(E_o)$ for a particular projectile/target pair is the average energy transferred when summed over all impact parameters, so that

$$S_n(E_o) = 2\pi\gamma E_o \int_0^{p_{max}} \sin^2 \frac{\Theta}{2} p dp . \tag{7-23}$$

Θ is the scattering angle of the deflected projectile and E_o is the ion energy before the collision. γ is related to the maximum transferable energy T_{max} for a direct collision (impact parameter p=0) by

$$T_{max} = \gamma E_o = \frac{4E_o M_1 M_2}{(M_1 + M_2)^2} \tag{7-24}$$

The nuclear stopping cross section $S_n(E_o)$ can be expressed in terms of projectile and target parameters as

$$S_n(E_o) = \frac{8.462x10^{-15} Z_1 Z_2 M_1 S_n(\varepsilon)}{(M_1 + M_2)(Z_1^{0.23} + Z_2^{0.23})} \text{ eV/(atom/cm}^2\text{)}. \tag{7-25}$$

The reduced nuclear stopping $S_n(\varepsilon)$ is calculated for ε<30 using

$$S_n(\varepsilon) = \frac{\ln(1 + 1.1383\varepsilon)}{2[\varepsilon + 0.01321\varepsilon^{0.21226} + 0.19593\varepsilon^{0.5}]} . \tag{7-26}$$

The latter two equations were used to determine the nuclear stopping cross sections for Zr^{4+} and O^{2-} target ions. One can gain a physical appreciation for the magnitude of the nuclear stopping cross-section by converting the excluded area calculated for a given ion/target stopping cross-section into an equivalent nuclear stopping radius r_{nuc} about the target atom using

$$r_{nuc} = \sqrt{\frac{S_n(E_o)}{\pi E_o}} . \tag{7-27}$$

The r_{nuc} values for 75eV and 300eV Ar^+ bombardment of Zr^{4+} and O^{2-} target ions are listed in Table 7.4 along with the ionic radii reported by Shannon[83] for both ions. For

Table 7.4 Nuclear stopping cross section radii and Ionic Radii for Zr^{4+} and O^{2-}

Ion	Ionic Radius (Å)	$r_{nuc75eVAr^+}$ (Å)	$r_{nuc300eVAr^+}$ (Å)
O^{2-}	1.24	1.02	0.68
Zr^{4+}	0.98	0.86	0.62

both 75eV and 300eV bombardment the r_{nuc} values are comparable in magnitude to the ionic radii of the zirconia ions.

These r_{nuc} values are graphically depicted for the (100), (110), and (111) planes of zirconia are in Fig. 7.10. Three plots are shown for each plane: one with the ionic Zr^{4+} and O^{2-} radii, one with the r_{nuc} radii corresponding to the nuclear stopping cross-sections for 75eV and 300eV Ar^+. The plots correspond to 20Åx20Å area. All three zirconia planes are densely packed as indicated by the ionic radii. Ion channeling down a given plane is not determined by the ionic radii, but rather the nuclear stopping cross sections of the target atoms. The probability of channeling is proportional to the nonexcluded area of a given plane for a given ion energy. The fraction of nonexcluded, or open, area for all three planes are listed in Table 7.5 for 75eV and 300eV Ar^+. The (100) zirconia plane has the most nonexcluded area for both ion energies. If biaxial alignment was dictated by channeling alone, then (100) planes would be observed in the direction of the incident ion beam for both beam energies since the (100) plane is the plane most amenable to channeling. This has not been observed for zirconia films fabricated by IBAD. With (100) fixed normal to the substrate, as is the case for the (200) biaxially aligned IBAD YSZ films, the most open of the remaining crystallographic planes would be aligned with the ion beam according to the channeling argument. The (110) zirconia plane is more open relative to (111) for 75eV ion bombardment, while the (111) plane is more open for 300eV ion bombardment. Many of the fabrication conditions reported in this thesis induce biaxial alignment consistent with this argument. (110) planes are frequently observed toward the direction of the assisting ion beam for ion assisted, electron beam evaporation at 600°C with 75eV ion assist. (111) planes are always observed toward the assisting ion beam for dual ion beam deposition at both room temperature and at 600°C for 300eV Ar^+ ion assist. There are, however, many important exceptions to this trend. The (200) biaxially aligned YSZ films fabricated without active substrate heating by ion assisted, electron beam evaporation feature (110) planes toward the assisting ion beam even though the assisting ion beam energy was 300eV. As shown in Fig. 7.1, films fabricated at 600°C by ion assisted electron beam evaporation at bombardment angles of 38° and 48° featured the same in-plane alignment with ion assist of 75eV and 300eV at

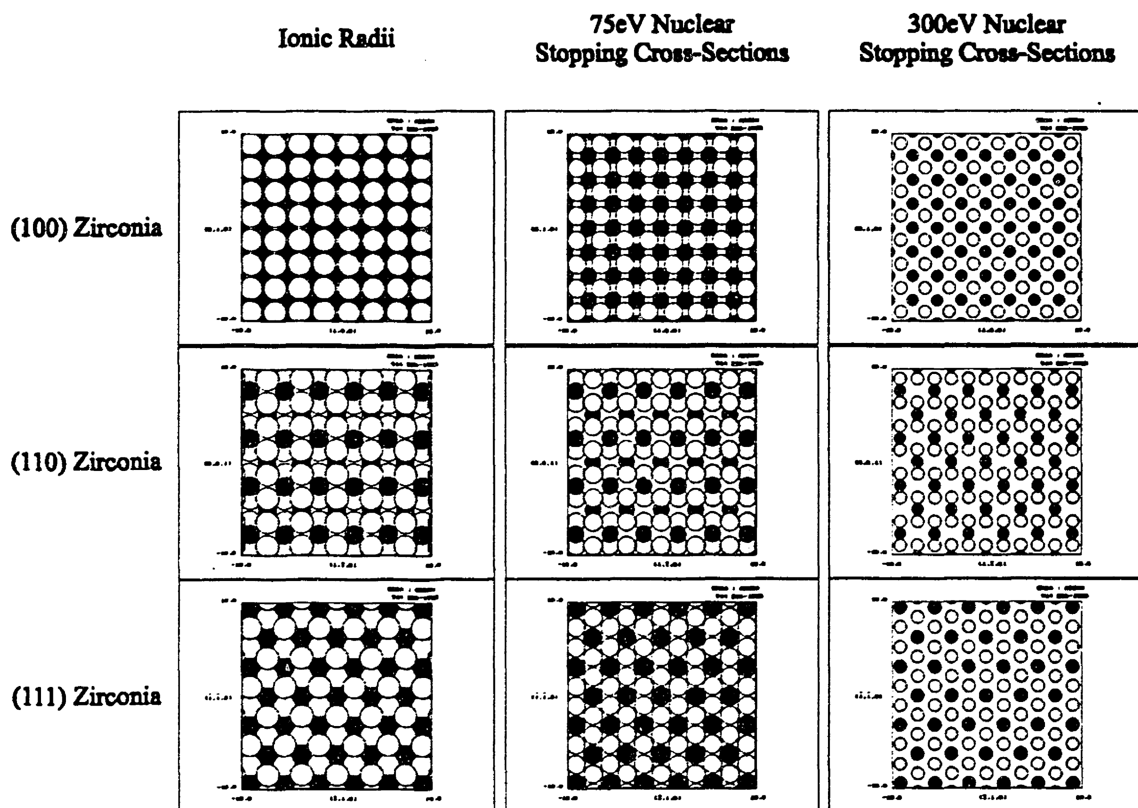

Figure 7.10 (100), (110), and (111) ZrO_2 planes with ionic radii of Shannon[83] and radii consistent with nuclear stopping cross-sections for 75eV and 300eV argon bombardment.

Table 7.5 Nonexcluded areas for zirconia planes as a function of Ar^+ energy

Zirconia Plane	75 V Ar^+	300eV Ar^+
(100)	0.240	0.643
(110)	0.199	0.559
(111)	0.142	0.619

the same r value. The in-plane orientation changed only after the ion to atom arrival ratio was changed. Although channeling is possible for assisting ion beam energies of 75eV and 300eV during IBAD, channeling does not appear to be the primary factor in creating biaxial alignment in YSZ thin films.

The nuclear stopping cross-sections for 75eV Ar^+ bombardment of La, Ca, Mn, and O were calculated and converted into nuclear stopping radii. These values are listed along with the ionic radii for La^{3+}, Ca^{2+}, Mn^{3+}, Mn^{4+} and O^{2-} for the coordination numbers in LCMO in Table 7.6. The (100), (110), and (111) planes are depicted in Fig. 7.11 with both sets of radii for the parent $LaMnO_3$ compound. Both the (100) and (110) $LaMnO_3$ planes contain nonexcluded area, while the (111) plane contains none. The (111) plane is the only plane for which channeling is not possible based upon these the calculated nuclear stopping cross-sections. This result holds if the Ca^{2+} substitution is considered as well. The (h00) biaxially aligned LCMO films feature {111} planes are direction of the assisting ion beam, as shown in Fig. 6.3. This is further evidence that channeling is not responsible for the development of IBAD biaxial alignment.

The vast majority of projectile ions come to rest in the target according to TRIM. A fraction of the ions are reflected and backscattered out of the target. The fraction of ions that remain in the target increases with increasing ion bombardment angle. Argon should be present in the YSZ films in measurable quantities if this is the case. Two films were examined using Energy Dispersive X-ray Spectroscopy (EDAX). One (Specimen 1) was fabricated on Pyrex by ion assisted electron beam evaporation at 600°C with 75eV assisting ion energy and an ion to molecule arrival ratio of 0.11. The other (Specimen 2) was fabricated by dual ion beam deposition on quartz without active substrate heating with 300eV assisting ion beam energy and an r value of 2.5. The EDAX spectra for both films are shown in Fig. 7.12. Argon was detected in both specimens. The relative atomic portions of Ar, Y, and Zr were calculated for both specimens. Oxygen was detected during the measurements but was not included in the comparison because both the quartz and Pyrex substrates contained O. The atomic ratios of Ar:Zr and Y:Zr for both specimens are listed in Table 7.7. The Ar:Zr ratio increased with r value, but not in a linear manner. The measured Y content in both films was greater than the Y to Zr ratio

Table 7.6 Ionic radii and nuclear stopping cross-section radii for LCMO

Ion	Ionic Radius (Å)	$r_{nuc75eVAr^+}$ (Å)
La^{3+}	1.50	0.77
Ca^{2+}	1.48	0.99
Mn^{3+}	0.75	0.95
Mn^{4+}	0.67	0.95
O^{2-}	1.26	1.02

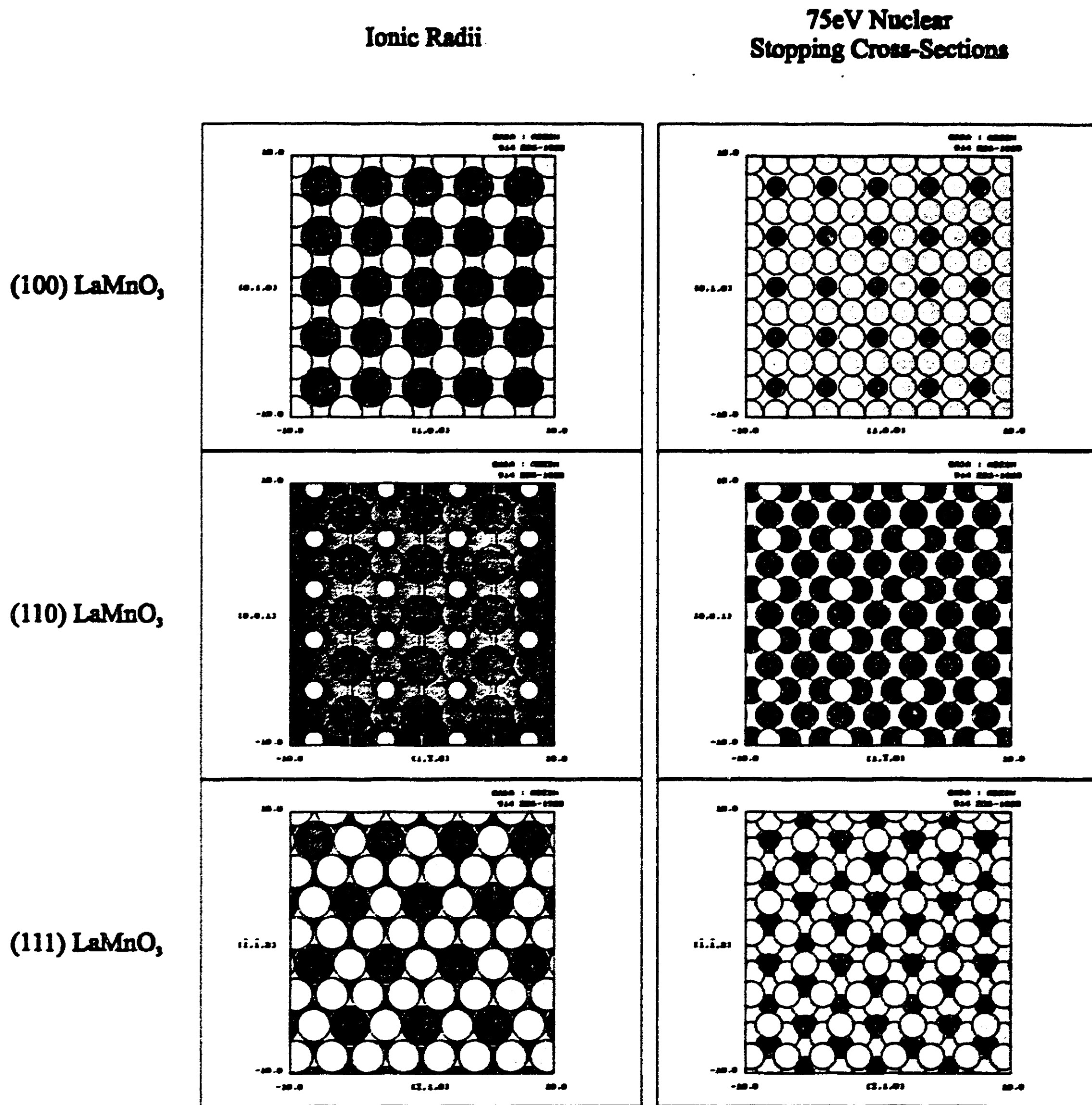

Figure 7.11 (100), (110), and (111) $LaMnO_3$ planes with ionic radii of Shannon[83] and radii consistent with nuclear stopping cross-sections for 75eV argon bombardment.

Specimen 1

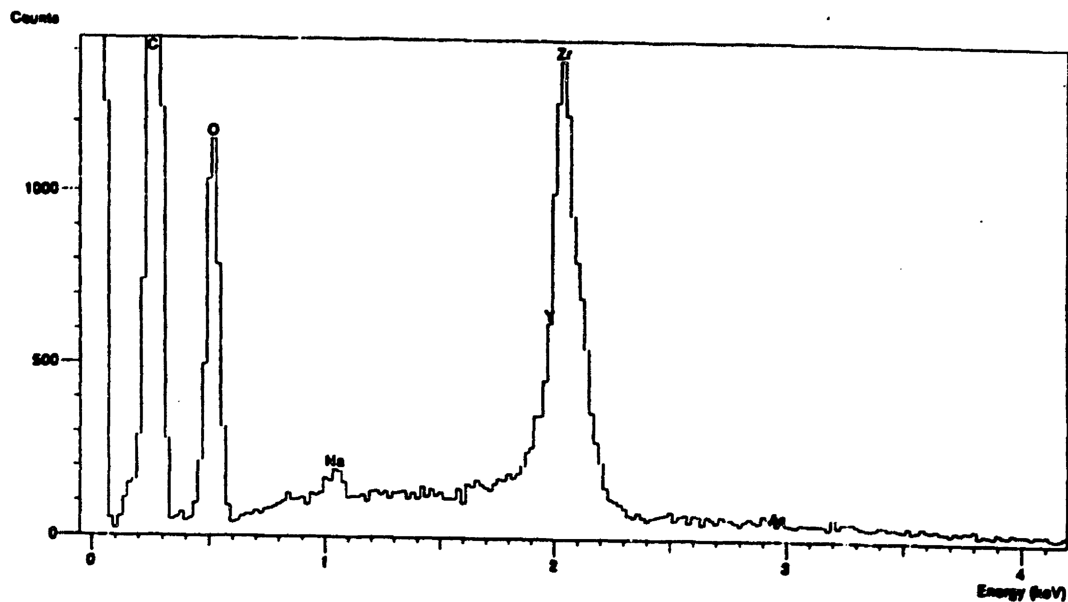

Specimen 2

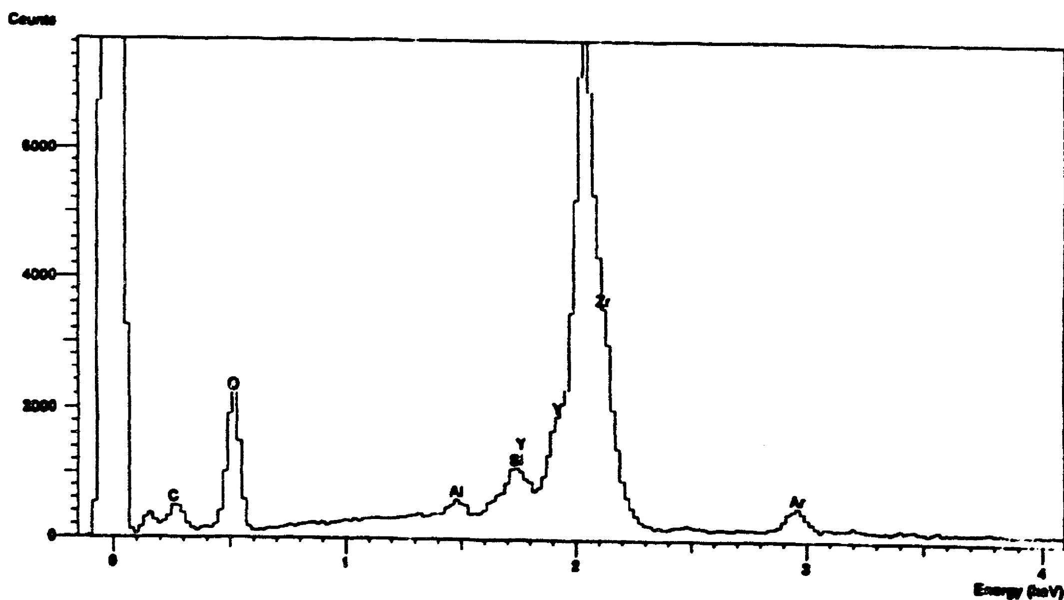

Figure 7.12 EDAX spectra of (200) biaxially aligned YSZ films fabricated by ion assisted electron beam evaporation on Pyrex at 600°C (Specimen 1) and by dual ion beam deposition on quartz without active substrate heating (Specimen 2). Argon was detected in both specimens.

Table 7.7 Chemical composition of biaxially aligned YSZ films

	Specimen 1	Specimen 2
Preparation Technique	Ion Assisted E-beam Evaporation 600°C	Dual Ion Beam Deposition 25-250°C
Ion:YSZ molecule Ratio	0.11	2.5
$\frac{Atomic\% Ar}{Atomic\% Zr}$	0.020	0.087
$\frac{Atomic\% Y}{Atomic\% Zr}$	0.285	0.325

of 0.19 for 8 mol% Y_2O_3-stabilized zirconia, suggesting that the cubic phase was fully stabilized in both films. The inclusion of argon in the lattice would presumably increase the film density, justifying the assumption of a zirconia density of 6 g/cm^3 for the TRIM simulations.

7.3.3 Etch Rate Anisotropy

It was established in the previous section that Ar^+ channeling can occur in zirconia for IBAD with 75eV and 300eV assisting beam energy. The second component of the channeling explanation of YSZ biaxial alignment is based on the assertion that crystal planes favorably aligned with respect to the assisting ion beam are sputtered at a lesser rate during deposition than planes misoriented with respect to the ion beam.

(200) biaxially aligned YSZ films have been fabricated using four distinct sets of deposition conditions: by dual ion beam deposition and ion assisted electron beam evaporation both at 600°C and without active substrate heating. The assisting ion beam conditions in these experiments ranged from 300eV and 68$\mu A/cm^2$ for dual ion beam deposition to 75eV and 13$\mu A/cm^2$ for ion assisted e-beam evaporation at 600°C. The films fabricated by ion assisted e-beam evaporation at 600°C and at room temperature both featured in-plane orientations with (110) planes parallel to the assisting ion beam projection. The films fabricated by dual ion beam deposition featured (111) planes parallel to the assisting ion beam projection. Representative specimens from each of the four IBAD deposition conditions were selected to measure etch rate anisotropy. The film thicknesses of the four specimens were measured using ultraviolet/visible spectrophotometry and calculated using the envelope technique of Swanepoel.[58] Considerable optical scattering was observed for the film fabricated by ion assisted e-beam evaporation without active substrate heating. A film thickness could not be determined for the specimen. The thickness of the other three specimens was determined. The three specimens were cut in half and mounted on a substrate block using silver paste. One half was aligned in the position in which the film had been fabricated, while the other half was azimuthally rotated 45°. One half of each specimen, therefore, had (110)

aligned parallel to the assisting ion source, while the other half had (111) facing the RF ion source. This enabled the relative ion etch rates of both in-plane orientations to be examined for three differing sets of IBAD fabrication conditions to test the hypothesis of ion etch rate anisotropy.

Faraday cup measurements were taken at normal incidence at the positions the specimens had been placed for both extremes of assisting ion beam positions. The measured ion fluence was 95μA/cm^2 for RF conditions of 300eV beam energy, 30mA beam current, 600V accelerator voltage, the assisting ion beam conditions commonly used for dual ion beam deposition.

The RF ion source was no longer able to maintain a stable 75 eV plasma at the time of the ion etch experiments under the assisting ion beam conditions used to fabricate many of the (200) biaxially aligned YSZ by ion assisted electron beam evaporation at 600°C. The RF ion fluence measured at the time of the ion etch experiments was 8.1 μA/cm^2 over the periods that the plasma was stable at 75eV. This fluence is approximately half of the value measured when the films had been fabricated. The ion source was stable at 150eV beam energy, 30mA beam current, and 450V accelerator voltage, and the corresponding measured ion fluence was 19μA/cm^2. This fluence was nearly identical to that used to fabricate the biaxially aligned YSZ films by ion assisted e-beam evaporation at 600°C.

The films were subjected to two extended ion etches. The ion bombardment angle was 45° for both experiments. The first etch was a 3.5h etch under the 150eV conditions described above. The film thicknesses were measured after the 150eV etch and remounted in the same positions. The second etch was a 0.58h etch under the 300eV conditions. The film thicknesses were again determined after the 300eV etch. The etch rates for both ion etch experiments are plotted in Fig. 7.13(a) and (b), respectively.

The relative differences in etch rate for a given film between (110) and (111) facing the incident ion beam were small in the 150eV ion etch experiment (Fig. 7.13(a)). In general, the specimens with (110) facing the ion beam had slightly higher etch rates than those with (111) toward the ion beam. There was no apparent trend to the results from the 300eV ion etch (Fig. 7.13(b)). The (110) in-plane orientation had a higher ion

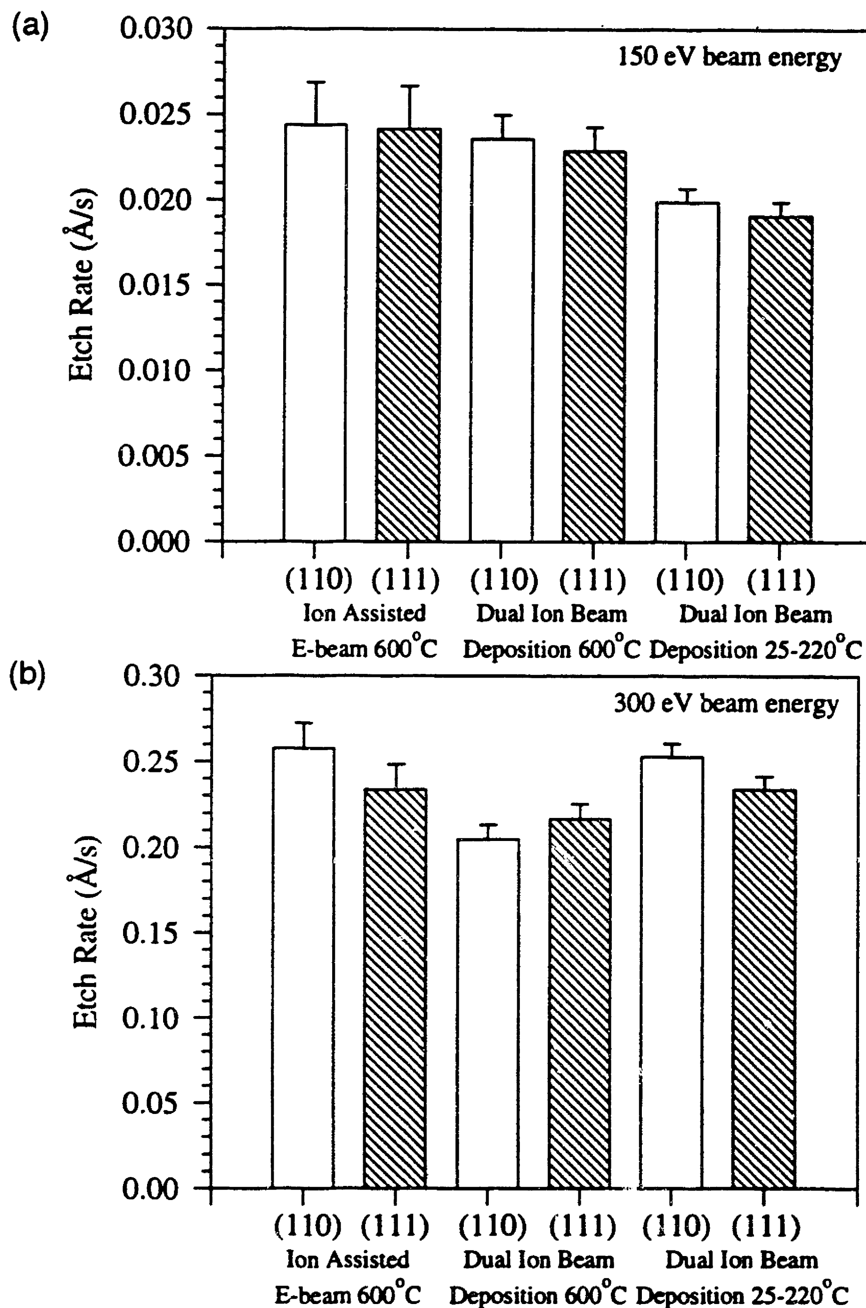

Figure 7.13 Ion etch rates of (200) biaxially aligned YSZ films for (a) 150eV beam energy and 19μA/cm^2 ion fluence and (b) 300eV beam energy and 96μA/cm^2 ion bombardment.

etch rate for two of the three specimens, but overall the relative differences in etch rate for the (110) and (111) in-plane orientations were again small. It is interesting that the ion etch rates for the 300eV ion etch were nearly an order of magnitude greater than the respective values for the 150eV etch, as the product of beam energy times ion fluence was a factor of 10 greater for the 300eV etch.

Not only were the relative differences in ion etch rate small, but many of the results ran counter to observed in-plane orientations for the respective fabrication conditions. The 300eV ion etch rate of the (110) in-plane orientation for the specimen fabricated by ion assisted e-beam evaporation at 600°C was significantly greater than that of the specimen with (111) facing the ion beam. The (110) in-plane orientation had always been observed for specimens fabricated by ion assisted e-beam evaporation at 600°C with 300eV assisting beam energy and 45° bombardment angle. Similarly, the ion etch rate of the (111) in-plane orientation was greater for the film fabricated by dual ion beam deposition without active substrate heating. The (111) in-plane orientation had always been observed toward the ion beam for films fabricated at 300eV assisting beam energy at all ion bombardment angles in the dual ion beam deposition experiments detailed in this thesis and also in the work of Iijima *et al.*[3-8] and Arendt *et al.*[9-12] It does not appear that biaxial alignment is determined by anisotropy in etch rate of different crystalline orientations based on these observations.

7.3.4 Anisotropy in Damage

Ensinger[42] advanced the idea of anisotropy in damage determining crystalline texture. He based this theory on the uniaxial texture observed for TiN and TaN thin films fabricated with ion assist at normal incidence. The in-plane orientation of the films was not reported. The argument was framed as a subset of the general ion channeling argument used to explain ion beam induced-texture. The crystal directions that are close-packed with respect to the ion beam are particularly subject to ion damage in the form of lattice rearrangements and sputtering, and that planes which survive are those most conducive to channeling. The difference between this argument and the channeling argument most frequently advanced is that the general channeling argument only

considers anisotropy in etch rate, while Ensinger's argument considers the relative differences in the capacity for crystalline planes to withstand ion induced atomic rearrangement.

The damage anisotropy argument is phrased somewhat differently in this section. The (h00) planes are fixed normal to the substrate in the biaxially aligned YSZ films fabricated by IBAD. The relevant question is why certain IBAD conditions result in films featuring (110) in-plane orientation with respect to the assisting ion beam while other conditions cause (111) in-plane alignment. The ion ranges determined by TRIM extend one or two YSZ unit cells from the surface, in the absence of channeling. The (110) and (111) planes are relatively equally conducive to channeling, based on the nonexcluded areas of both planes based on nuclear stopping cross-sections for 75eV and 300eV Ar^+ bombardment. It appears that the relevant region to consider for damage anisotropy is confined within the first few unit cells from the respective planes. The relative capacity of these planes to withstand ion damage is evaluated based on the coordination and energy of ions from the surface into the bulk for both planes using ADESH.

Computational cells were created in ADESH to represent (110) and (111) ZrO_2 surfaces. Periodic boundary conditions were maintained for the orthogonal directions normal to [$\bar{1}$10] and [111] in the respective cells. Free boundary conditions were maintained along [110] and [111] to simulate open surfaces. Each computational cell had two free surfaces, for example the (110) computational cell featured one for (110), the other for $(\bar{1}\bar{1}0)$. The ions in the computational cells were moved to a minimum energy state using the static relaxation option in ADESH. The temperature is assumed to be 0K for the procedure. Each of the ions within the computational cell were sequentially displaced by a distance ΔR from their initial position. The configurational energy of an individual ion is then calculated for twenty-seven different positions, after which the ion is placed in the position of minimum energy. The same procedure is then repeated for the next ion in the computational cell. The energy of the entire computational cell is calculated after each ion has been displaced. The procedure is repeated until the

difference in cell energies for two successive steps is less than 0.1eV. The static relaxation procedure was conducted on both the (110) and (111) computational cells using a ΔR of 0.02Å. Subsequent relaxation of the computational cell using ΔR of 0.01Å increased the cell energy. Both computational cells were therefore assumed to be fully relaxed after the static minimization procedure using ΔR of 0.02Å.

The displacements of the individual ions after the relaxation procedure were calculated for both computational cells. The computational cell was assumed to be sufficiently large when both the Zr^{4+} and O^{2-} ions featured zero displacement in the center of the computational cell. The respective {110} free surfaces in Fig. 7.14(a) were at x= -14.8Å and x=16.6Å, while the {111} free surface in Fig. 7.14(b) were at x=-6.9Å and x=9.9Å. The oxygen and zirconium ion displacement for both computational cells is shown along the cross-section of the (110) and (111) computational cells in Fig. 7.14(a) and (b). The Zr^{4+} ions featured zero displacement in both computational cells while the oxygen ions featured considerable displacements in both. This is consistent with the significantly larger Zr^{4+} interaction energy relative to O^{2-}. The O^{2-} ions in the (110) computational cell featured displacement at a depth of 12Å from the respective free surfaces, while the O^{2-} displacements terminated within 5Å from the free {111} surfaces. The oxygen ion displacements at a given distance from either free surface were greater in the (110) cell than in the (111) cell.

The ion energies after surface relaxation are of particular interest in considering the effects of ion bombardment of either surface. The energy of individual ions was calculated by the potential function and procedure described earlier in this chapter. Two caveats must be noted for calculating an ion's energy in this manner at or near a free surface. The validity of using the potential function without adding additional dipole and quadropole terms for the surface is uncertain. The validity of determining the energy of an ion using this procedure noted in Section 7.3.1.2 is uncertain, as fewer near neighbors are present than in the bulk. The energy of a specific ion is still determined by considering the largest electrically neutral assemblage of ions within 4Å of a the ion, so the results should at least be qualitatively correct for comparison between the two planes.

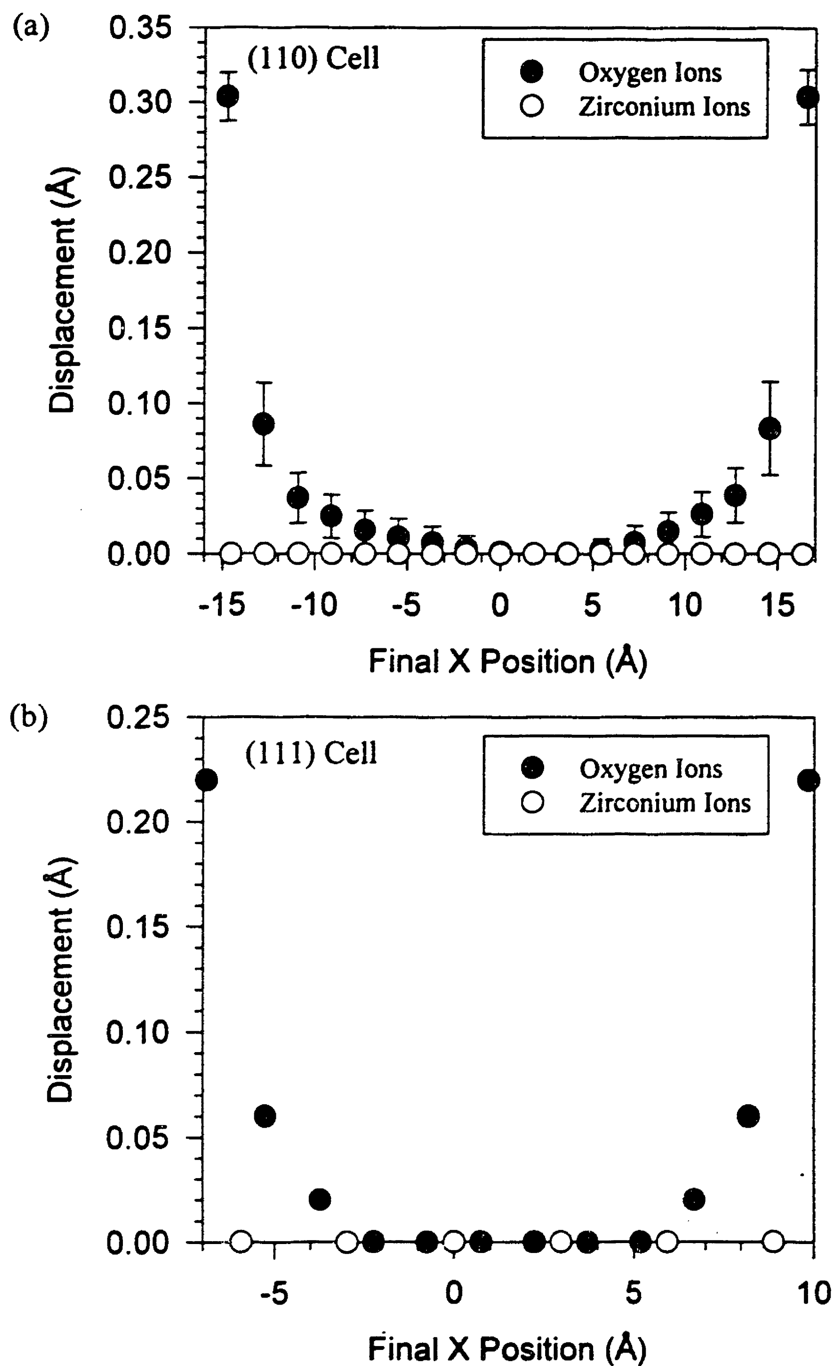

Figure 7.14 Ion displacements for (a) (110) and (b) (111) ZrO_2 computational cells.

The atomic density at the (220) surface is nearly twice the density at the (111) surface, as shown in Fig. 7.15. The atomic densities along <111> and <220> are similar beyond the surface. There are two O^{2-} ions for each Zr^{4+} on the (220) surface, while the ratio of O^{2-} to Zr^{4+} is unity at the (111) surface.

The calculated energy for zirconium ions from the (110) and (111) surfaces into the bulk are shown in Fig. 7.16(a). The Zr^{4+} energies for both cells follow approximately the same trend as a function of depth from the open surfaces. The trend converges on the bulk value of -93.47eV is within 7Å from the free surfaces. Overall, there is no discernible difference in the Zr^{4+} energies between the two computational cells.

The calculated O^{2-} energies for both computational cells are shown in Fig. 7.16(b). The bulk energy of -11.24eV is attained within 6Å of the free surfaces, and the energies for both cells follow a similar trend as a function of depth until the bulk energy value is observed. There is a significant 4eV difference in energy between oxygen ions at the (110) and (111) surfaces. The oxygen ions on the (110) surface are more susceptible to ion damage in several forms relative to those on the (111) surface, particularly sputtering. For the same relative ion to molecule arrival ratio, the (110) surface is expected to be preferentially reduced due to oxygen sputtering. Preferential ion sputtering of oxygen from metal oxide targets is well established in the SIMS literature.[84]

The relative ability of the (110) and (111) zirconia planes to withstand ion damage is not limited to preferential oxygen sputtering. Many ion/solid collisions are not sufficiently energetic to sputter target atoms, but are sufficiently energetic to induce atomic rearrangement of the target. Bonds with nearest neighbor ions must be broken before an ion can become a recoil. The resistance of an ion to atomic displacement is proportional to its number of bonds. The coordination numbers for Zr^{4+} and O^{2-} ions in bulk ZrO_2 and on the (110) and (111) ZrO_2 surfaces are shown in Table 7.8. Oxygen ions on the (110) surface are coordinated to two zirconium ions, and zirconium ions are coordinated to six oxygen ions. Oxygen ions on the (111) surface are coordinated to three zirconium ions, while zirconium ions at the surface are coordinated to seven oxygen ions. This observation also points to (111) zirconia planes being more stable against damage under more robust r values.

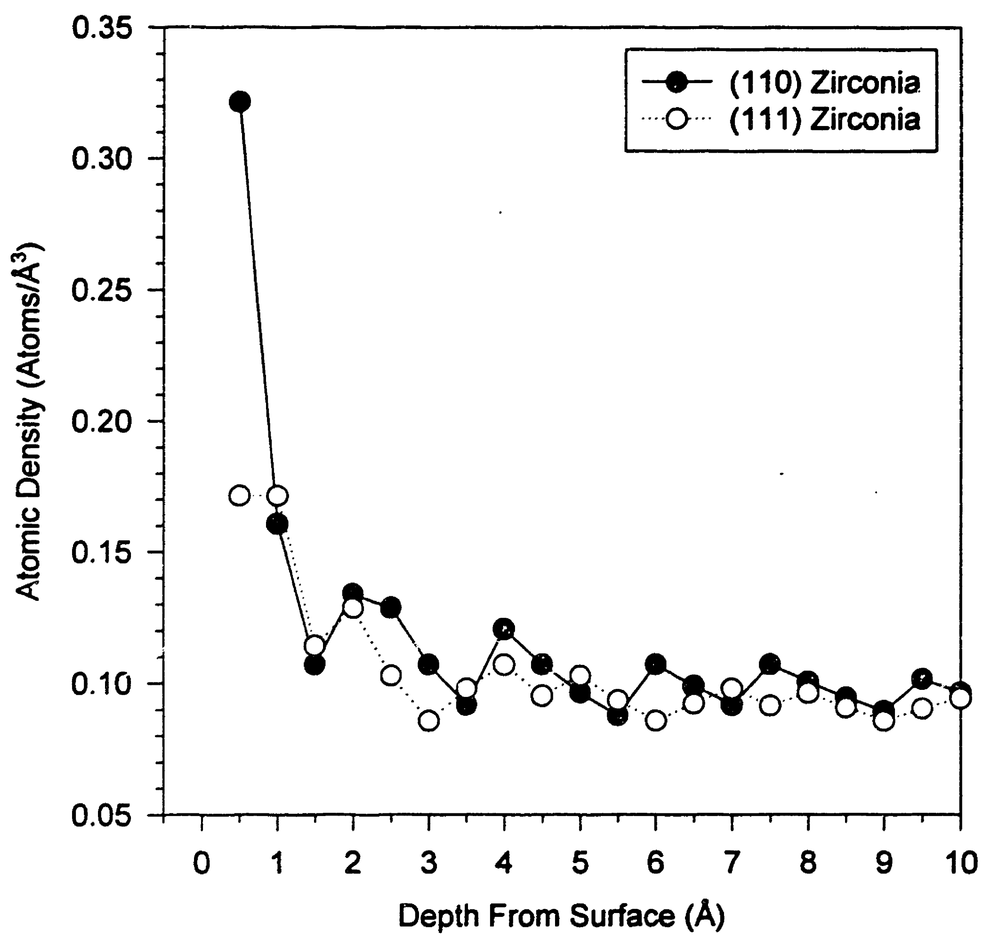

Figure 7.15 Atomic densities as a function of distance from (110) and (111) ZrO_2 surfaces.

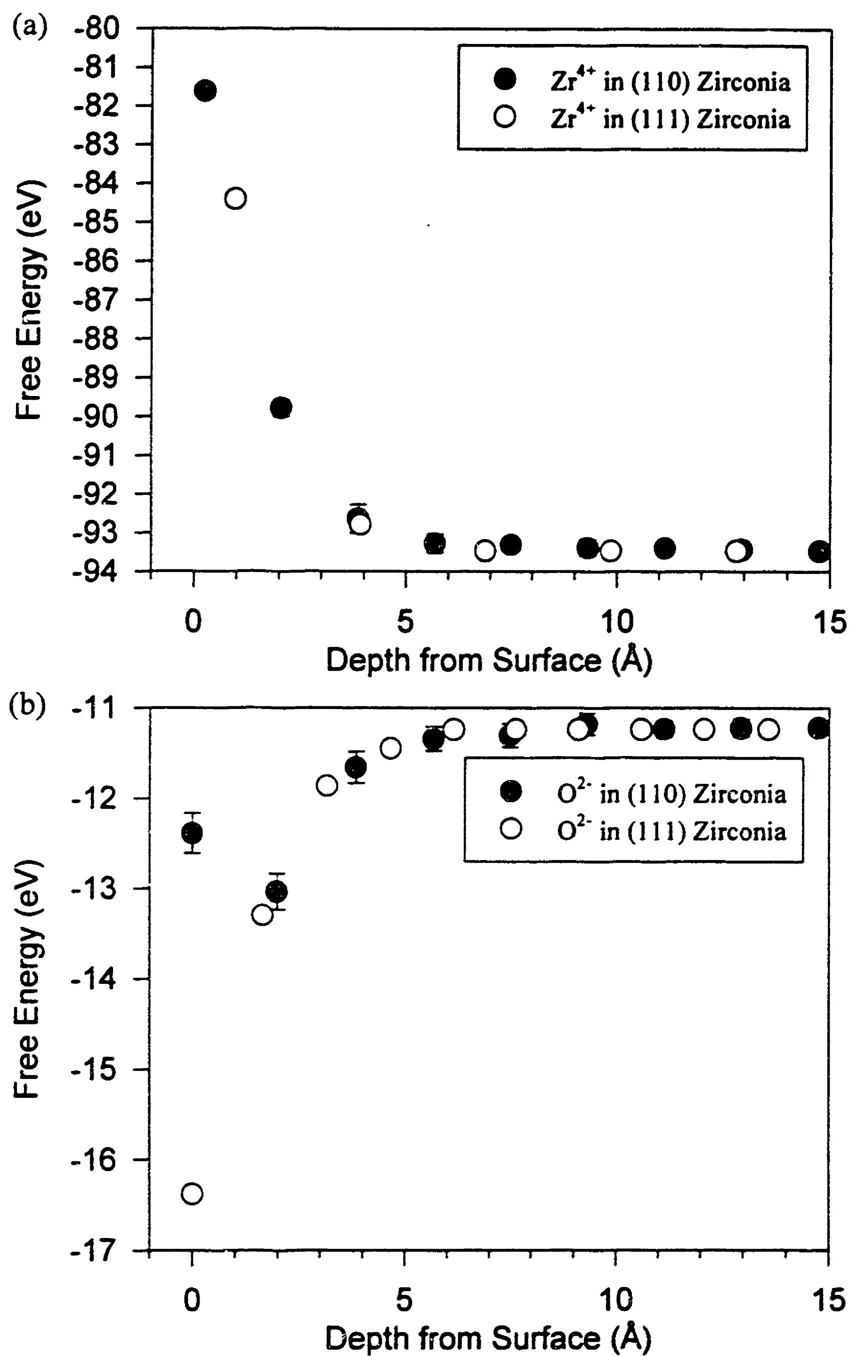

Figure 7.16 Calculated (a) Zr^{4+} and (b) O^{2-} energies from open (110) and (111) surfaces into bulk ZrO_2.

Table 7.8 ZrO_2 ion coordination numbers

Ion	Bulk	(110) ZrO_2 Surface	(111) ZrO_2 Surface
Zr^{4+}	8 O^{2-}	6 O^{2-}	7 O^{2-}
O^{2-}	4 Zr^{4+}	2 Zr^{4+}	3 Zr^{4+}

The (110) in-plane orientation is observed at low r values while the (111) in-plane orientation is observed at high r values in Figs. 7.2 and 7.3. Ensinger[42] noted that texture formation corresponds with momentum transfer per volume. A fully oxygenated (110) plane is more damage tolerant than the (111) surface at low r values because the atomic density of the (110) surface is greater, thereby distributing the assisting ion beam energy and momentum over more atoms per unit volume. The (111) plane is more damage tolerant for higher relative ion bombardment because of greater ion coordination and preferential oxygen sputtering from (110) ZrO_2. The oxygen binding energy is lower at the (110) surface, and there are twice as many O^{2-} to Zr^{4+} at the (110) surface. Both of these factors contribute to making the (111) plane more damage tolerant at high r values.

The boundary between the (110) and (111) in-plane orientations in Figs. 7.2 and 7.3 is consistent with damage anisotropy. The calculated ion range decreases with decreasing ion bombardment angle, as shown in Fig. 7.9. The change from (110) to (111) in-plane orientation occurs at lower r values for smaller ion bombardment angles because the ion energy and momentum are dissipated within a smaller volume and closer to the surface, where the O^{2-} binding energy difference between the (110) and (111) plane is greatest.

The RF ion source gas used in both the ion assisted electron beam evaporation and dual ion beam deposition work consisted of argon with 8 vol% oxygen. Some of the oxygen ionized in the ion source, but most flowed toward the growing film as molecular oxygen. The approximate arrival rate was 2.5×10^{16} O_2/cm^2s. For comparison, a deposition rate of 1.0Å/s corresponds at an YSZ arrival rate of 3×10^{14} molecules/cm^2s and an ion fluence of 50mA/cm^2 corresponds to an ion arrival rate of 3×10^{14} Ar^+/cm^2s. The molecular oxygen could have acted as a healing flux by reacting with oxygen depleted portions of the film. The boundary between the (110) and (111) regions in Figs. 2 and 3 may correspond to the r values at which damage induced reduction exceeded the supply of reactive molecular oxygen.

The observation of (111) in-plane orientation for LCMO films fabricated by IBAD is also consistent with biaxial alignment caused by anisotropy in damage. The (110) and (111) planes are the only low-index LCMO planes to consider for anisotropic

damage with respect to the off-axis assisting ion beam for (h00) fixed normal to the substrate. The parent $LaMnO_3$ compound is considered for simplicity. The coordination numbers of La^{3+}, Mn^{3+}, and O^{2-} in the $LaMnO_3$ bulk and on the (110) and (111) $LaMnO_3$ surfaces are listed in Table 7.9. The exposed (111) $LaMnO_3$ contains La^{3+} coordinated to eight O^{2-}, while La^{3+} is coordinated to 7 O^{2-} on the (110) plane. Manganese ions coordinated to 4 O^{2-} are present on the (110) surface. There are no exposed manganese ions on the (111) $LaMnO_3$ plane. The Mn^{3+} ions on the (110) surface would be expected to suffer greater ion damage relative to La^{3+} ions on either plane due to the few number of Mn-O bonds compared to the number of La-O bonds. The oxygen ion coordination number is four on both $LaMnO_3$ faces; the (111) plane features three O^{2-}bonds with La^{3+}, while only 2 La-O bonds are present at the (110) surface. These observations indicate that (110) $LaMnO_3$ is more vulnerable to ion damage than (111) $LaMnO_3$. The same arguments hold for LCMO, as Ca^{2+} substitute on La^{3+} sites.

A final argument for IBAD biaxial alignment arising from momentum transfer rather than ion channeling or anisotropic etching can be based on the work of Karpenko *et al.*,[37] in which biaxial alignment developed in Mo films conventionally sputtered on the native oxide of Si. An ion beam is essentially a directional flux of energetic particles. Atoms sputtered from a target are often quite energetic, with energies ranging from 10 to 40eV.[85] Sputtered atoms arrive at a substrate as an energetic directional flux from the sputter target. The sputtered atom energy is analogous to the energy of an individual ion, and the deposition rate is analogous to an ion fluence. Mo planes developed specific out-of-plane and in-plane relationships with respect to the sputtered Mo flux similar to the biaxial alignment exhibited by YSZ and LCMO films with respect to the assisting ion beam. (110) Mo biaxial alignment was observed at low deposition rates and low mean flux energy, while (111) Mo biaxial alignment was observed at higher deposition rates and higher mean flux energy. The orientation switch is similar to the relationship observed in IBAD YSZ films, with (110) in-plane orientation at low r value and (111) in-plane orientation with respect to the assisting ion beam at high r value.

Energetic Mo particle impingement on the growing Mo film parallels to Ar^+ impingement on a growing IBAD film. Ions dissipate energy in collision cascades before

Table 7.9 $LaMnO_3$ ion coordination numbers

Ion	Bulk	(110) $LaMnO_3$ Surface	(111) $LaMnO_3$ Surface
La^{3+}	12 O^{2-}	7 O^{2-}	8 O^{2-}
Mn^{3+}	6 O^{2-}	4 O^{2-}	None
O^{2-}	4 La^{3+} 2 Mn^{3+}	2 La^{3+} 2 Mn^{3+}	3 La^{3+} 1 Mn^{3+}

coming to rest. Sputtered adatoms also transfer excess kinetic energy to the film before being accommodated into the film lattice. Channeling is unlikely to play any role in the energy transfer of low energy sputtered Mo atoms to the B.C.C. Mo film, yet biaxial alignment similar to that in IBAD films is observed. Sputtering, much less anisotropic sputtering, is also unlikely given the low energy of the sputtered Mo flux. The sputtered flux is sufficiently energetic to induce atomic rearrangement of the Mo film surface. The observation of biaxial alignment in these films can only be attributed to momentum transfer from the sputtered Mo flux. Increasing the sputtering power to increase the Mo deposition rate is equivalent to increasing both the r value and the beam energy during IBAD. Anisotropic damage from the impinging Mo flux is the only mechanism to explain the observed orientation switch from (110) biaxial alignment to (111) biaxial alignment.

7.4 SUMMARY

IBAD biaxial alignment develops due to anisotropy of ion induced damage on various crystal surfaces. The two in-plane orientation of (200) biaxially aligned YSZ films fabricated by both ion assisted electron beam evaporation and dual ion beam deposition were combined in a field plot of ion to molecule arrival ratio versus ion bombardment angle. (110) planes are more damage tolerant at low *r* values while (111) planes are more damage tolerant at high *r* values. The data of Iijima *et al.*[3-8] and Arendt *et al.*[9-12] are consistent with the field plot. The observed IBAD YSZ and IBAD LCMO biaxial alignment does not occur due to ion channeling.

CHAPTER 8

MODEL EXPERIMENTS ON YSZ SINGLE CRYSTALS AND THE ROLE OF SUBSTRATE TEMPERATURE IN THE DEVELOPMENT OF IBAD BIAXIAL ALIGNMENT

8.1 INTRODUCTION

The fabrication and characterization of biaxially aligned YSZ films by ion beam assisted deposition on polycrystalline and amorphous substrates was detailed Chapters 4 and 5 and the role of the assisting ion beam was examined in Chapter 7. IBAD biaxial alignment for films fabricated by both deposition techniques was shown to be substrate-independent for films deposited without active substrate heating and substrate-dependent for films deposited at 600°C. The substrate crystal structure did not directly bias the development of YSZ biaxial alignment in any of the previous cases. The purpose of this chapter to investigate the development of IBAD biaxial alignment on YSZ single crystals of different orientations. The YSZ single crystal constitutes a nucleation seed acting to fix both the in-plane and out-of-plane orientation of IBAD YSZ films. These experiments will show under which deposition conditions IBAD biaxial alignment is substrate-dependent and substrate-independent in the presence of this nucleation bias. The role of substrate temperature on the development of biaxial alignment will be clarified by these experiments.

8.2 EXPERIMENTAL PROCEDURE

(100), (110), and (111) YSZ substrates were mounted on stainless steel blocks using the procedures described in Chapter 3. Films were fabricated without active

substrate heating and at 600°C substrate temperature with all other IBAD parameters held constant. The sputtering Kaufmann ion source was set to 1000eV and the sputtering beam current was PID controlled to increase the gross deposition rate linearly from 0.1Å/s initially to a final rate of 0.6Å/s for both depositions. The assisting RF ion source was set to 30mA beam current, 300eV beam energy, 600V accelerator voltage, and 120mA neutralizer emission current. The ion bombardment angle was 35°, the ion fluence was 55μA/cm^2 and the ion etching rate was approximately 0.2Å/s throughout film deposition. Ar gas flowed through the Kaufmann ion source, while a mixture of Ar and 8% O_2 flowed through the RF ion source. The film thickness was ~5500Å.

CeO_2 films were epitaxially deposited at 0.2Å/s on the IBAD YSZ films to 500Å thickness at 600°C after both depositions by electron beam evaporation without ion assist. CeO_2 and YSZ both share the fluorite crystal structure. X-ray investigation of the ceria film enabled the crystallographic orientation of the uppermost IBAD YSZ film to be examined without substrate diffraction contributions. Comparing the crystallographic orientation of the ceria layer to the X-ray information obtained from the entire YSZ film facilitates understanding of the development of biaxial alignment through the IBAD film thickness.

8.3 DUAL ION BEAM DEPOSITION ON YSZ SINGLE CRYSTALS

The IBAD YSZ films deposited at 600°C were epitaxial on the (100), (110), and (111) YSZ substrates according to θ-2θ XRD and X-ray pole figures. Two (111) X-ray φ scans are shown for each YSZ single crystal in Fig 8.1: the φ scan for the IBAD film and substrate and the scan for the ceria film epitaxially evaporated on the IBAD YSZ film. The ceria films deposited on the IBAD YSZ films at 600°C exhibited the same in-plane orientation as the respective YSZ single crystals, indicating both the IBAD YSZ and ceria films were epitaxial with the respective substrates.

Both θ-2θ XRD and X-ray pole figures revealed that both the IBAD YSZ films fabricated without active substrate heating and the evaporated ceria films featured (200)

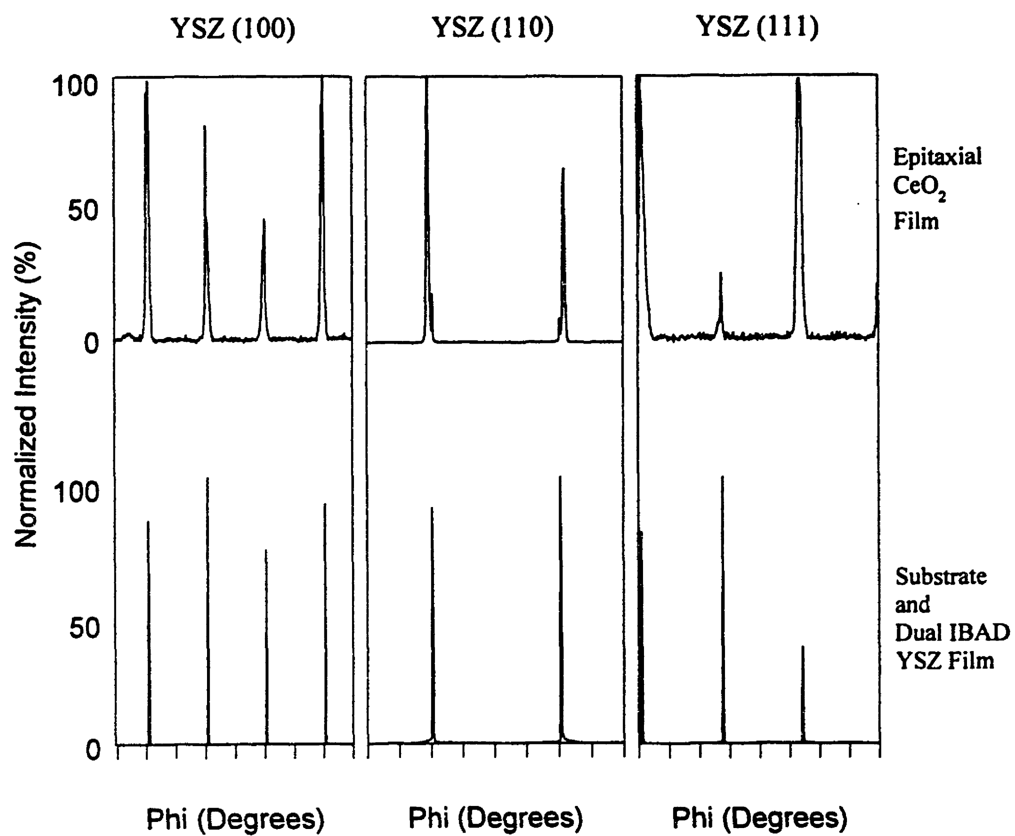

Figure 8.1 (111) X-ray φ scans of dual IBAD YSZ films, YSZ single crystal substrates, and epitaxially evaporated ceria layers for YSZ films fabricated by dual ion beam deposition at 600°C.

normal alignment on the (100), (110), and (111) YSZ substrates. The (111) X-ray ϕ scans of the epitaxial ceria layer, the IBAD YSZ film, and the respective YSZ substrates are shown in Fig. 8.2.

The orientation of the IBAD YSZ film deposited on the (111) YSZ single crystal is clearly different from that of the substrate. The (111) X-ray ϕ scan of the substrate shows the expected three-fold symmetry about the [111] axis. The (111) X-ray ϕ scan of the film shows the typical in-plane orientation observed for (200) biaxially aligned films fabricated by dual ion beam deposition. The ceria film exhibits the same four-fold symmetry as the IBAD YSZ film beneath consistent for grains with [200] normal to the substrate.

The IBAD YSZ (200) reflection overlapped the (h00) peak of the (100) YSZ substrate, as the 2θ and χ positions for the film and substrate for the (111) X-ray ϕ scan were identical. Four narrow, intense {111} reflections from the substrate are evident in the X-ray ϕ scan at ϕ=45, 135, 225, and 315°. Four broader and less intense reflections are present at ϕ=0, 90, 180, and 270°. The scale on the IBAD YSZ ϕ scan is from 0 to 4% of the maximum substrate reflection intensity to more clearly show the film reflections. The IBAD YSZ reflections are significantly broader and are distinct from the narrow reflections corresponding to the (100) YSZ substrate. It can not be determined from XRD alone whether there is an epitaxial component of the IBAD film because the film and substrate reflections occur at the same 2θ and χ positions. The (111) ceria ϕ scan features reflections at the ϕ locations corresponding to the IBAD YSZ film. If there was an epitaxial component present in the IBAD YSZ film, it did not persist to the top of the IBAD YSZ film. Only background intensity is present at the ϕ positions where the substrate {111} reflections were located in the (111) YSZ ϕ scan.

Two reflections are present in the (111) X-ray ϕ scan of the (110) YSZ substrate at χ=55°. The substrate was intentionally placed on the substrate block so that neither of the (111) reflections was parallel to the assisting ion beam projection. There are eight reflections in the (111) X-ray ϕ scan of the IBAD YSZ film. None of the reflections

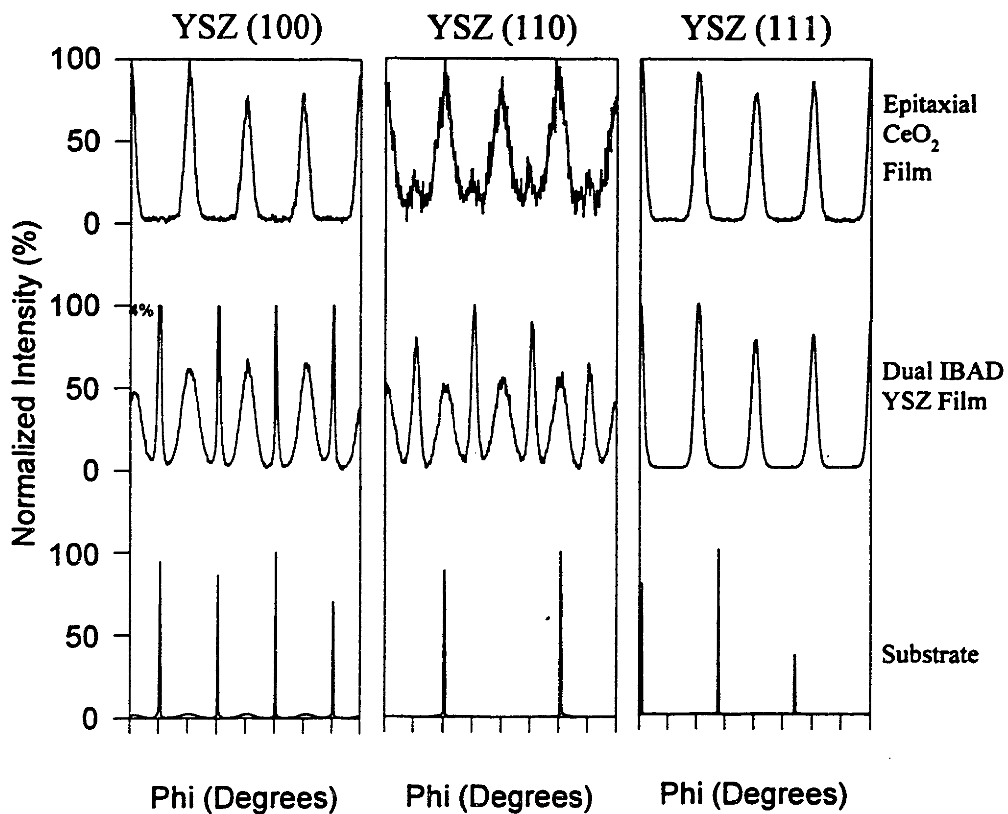

Figure 8.2 (111) X-ray ϕ scans of YSZ single crystal substrates, dual IBAD YSZ films, and epitaxially evaporated ceria layers for YSZ films fabricated by dual ion beam deposition without active substrate heating.

correspond to the (110) YSZ substrate. The four reflections at ϕ=0, 90, 180, and 270° were expected for the IBAD YSZ film. The additional reflections at ϕ=45, 135, 225, and 315° are significantly narrower than the other four reflections.

A coincident site lattice exists which is consistent with the relative orientations of the (110) YSZ substrate and the (200) grains with the narrow mosaic spread with (100) YSZ || (110) YSZ; [010] YSZ || [$\bar{1}$10] YSZ. A schematic of this coincident site lattice is shown in Fig. 8.3. This orientation has 0% misfit along the film [00$\bar{1}$] direction and 0.99% misfit along the [010] direction. The grains exhibiting this orientation are referred to as CSL grains for the remainder of this discussion. The eight reflections are also observed in the (111) ceria ϕ scan. The intensities of the four commonly observed IBAD reflections is greater relative to CSL grain reflections at ϕ=45, 135, 225, and 315° in the ceria ϕ scan compared to the YSZ ϕ scan.

A cross-sectional TEM specimen was prepared to better clarify the orientation development on the (110) YSZ substrate. Micrographs were obtained from near the middle of the IBAD YSZ film through the epitaxial ceria layer. The film amorphized during ion milling before the (110) YSZ substrate thinned sufficiently for TEM investigation of the film/substrate interface.

A bright field micrograph from the bottom portion of the thinned film is shown in Fig. 8.4. {111} Lattice fringes are visible within the grain in the right portion of the micrograph as the grain is viewed along a [110] zone axis. The [220] direction is pointed near the substrate normal through much of the grain. The orientation of this portion of the film is similar to that observed along the quartz/IBAD YSZ interface in Fig. 5.9. A square net of {100} lattice fringes is visible in the grain toward the left of the micrograph. These fringes are consistent with a (200) biaxially aligned CSL grain viewed along a [100] zone axis as shown in Fig. 8.3. The [100] direction of the grain is clearly oriented parallel to the substrate normal. The interface between the two grains is sloped toward the CSL grain. Extended areas within the film were visible in Fig. 8.3 where the IBAD grains gradually extended laterally into regions occupied by CSL grains. The IBAD grain

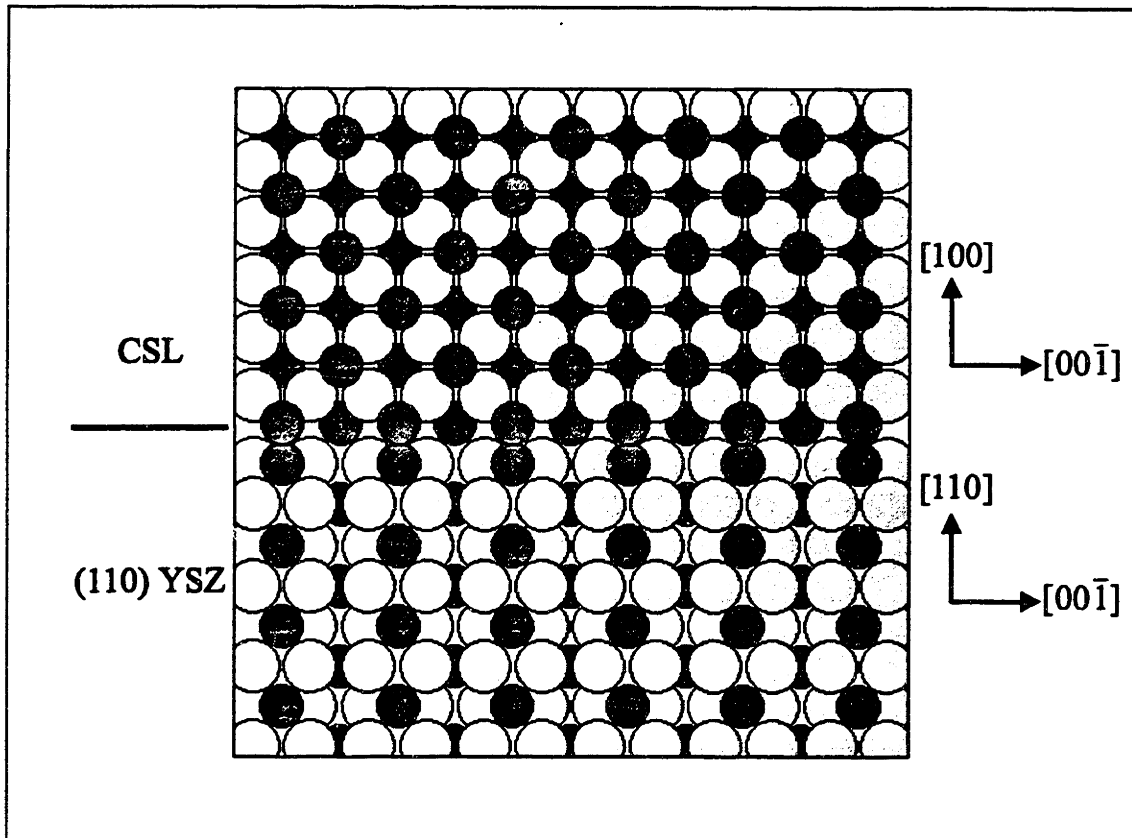

Fig. 8.3 Schematic of coincident site lattice between (200) YSZ film and (110) YSZ substrate with (100) YSZ || (110) YSZ; [00$\bar{1}$] YSZ || [00$\bar{1}$] YSZ.

Figure 8.4 Cross-sectional TEM micrograph of YSZ film deposited on (110) YSZ by dual ion beam deposition at 600°C.

twins from [220] near normal to [200] normal near the top of the micrograph. The interface between the CSL and IBAD grains remains relatively constant after the twinning event, with the interface remaining approximately parallel to the substrate.

Fig. 8.5 is a high resolution micrograph of the interface between a CSL and an IBAD grain further from the twinning event. The CSL grain is located at the left of the image while the IBAD grain is toward the right. The interface between the (200) CSL and (200) IBAD grains is crystallographically equivalent to that between the (200) CSL and (110) YSZ substrate, as the CSL and IBAD grains are viewed along [100] and [110] zone axes, respectively. A cross-sectional TEM micrograph along the ceria/YSZ interface is shown in Fig. 8.6. Both the CSL grain at the right and the IBAD grain at the left continue from the YSZ into the ceria film, as does the interface between the grains. The ceria film is epitaxial with respect to the YSZ grains beneath.

8.4 IBAD YSZ BIAXIAL ALIGNMENT ON YSZ SINGLE CRYSTALS

The epitaxial YSZ film growth observed in films fabricated at 600°C is consistent with the epitaxial LCMO growth observed for films fabricated on $SrTiO_3$ by dual ion beam deposition at 600°C. Epitaxial growth is expected on single crystal substrates at substrate temperatures where surface diffusion and granular epitaxy are active and grain boundaries are mobile. The film orientation in both cases was determined solely by the substrate crystallography rather than the assisting ion beam. The texturing bias from the assisting ion beam is insufficient to overcome the nucleation texturing bias of the substrate at elevated substrate temperatures.

The biaxial alignment observed in films deposited without active substrate heating is consistent with a granular renucleation growth mode operative at low substrate temperature. The orientation of the YSZ films deposited on the (100) and (111) YSZ substrates was unrelated to the substrate orientations, judging from the ceria (111) X-ray ϕ scan for the film on the (100) YSZ substrate and from the YSZ and ceria (111) ϕ scans for the films on the (111) YSZ substrate. These observations are consistent with

Figure 8.5 TEM micrograph showing both CSL and IBAD YSZ grains and respective orientations.

Figure 8.6 TEM micrograph along the IBAD YSZ/evaporated CeO_2 interface showing epitaxial CeO_2 growth on both YSZ granular orientations.

renucleation eliminating the crystallographic bias imposed by the single crystal substrate and biaxial alignment being determined by the assisting ion beam.

Weak (220) reflections were observed in the θ-2θ XRD traces of control films deposited without ion assist under similar fabrication conditions (Fig. 5.3), and cross-sectional TEM of a (200) biaxially aligned film fabricated without active substrate heating revealed an initial (220) near-normal orientation at the film/substrate interface. It is therefore not surprising that the (220) single crystal substrate crystallinity affected that of the IBAD film. Two populations of (200) biaxially aligned grains were observed in the film deposited on the (110) YSZ substrate. One population corresponded to the conventional biaxially aligned IBAD YSZ film orientation that was observed on the other single crystal substrates. The other corresponded to a (200) biaxially aligned CSL orientation nucleated on the single crystal substrate.

XRD and TEM observations from the film on the (110) YSZ substrate are consistent with IBAD film growth through granular renucleation at low temperature. The relative intensities of the four {111} IBAD peaks to the four {111} CSL peaks in a (111) X-ray ϕ scan reflects the relative populations of both orientations. The ratio of IBAD to CSL peak intensities was greater in the (111) X-ray ϕ scan of the epitaxial ceria cap than in the X-ray ϕ scan of the IBAD film. This result is consistent with a competition between the two populations of (200) biaxially aligned grains through the thickness of the film, with the IBAD (200) grain population having eliminated some of the CSL grains during film growth. The TEM micrograph in Fig. 8.4 shows an IBAD grain eliminating a CSL grain. These micrographs in Fig. 8.4 through 8.6 are consistent with the elimination of CSL grains primarily within the portion of the IBAD film where grains are oriented with [220] near the substrate normal.

8.5 SUMMARY

IBAD YSZ biaxial alignment was examined on single crystal YSZ substrates for films fabricated without active substrate heating and at 600°C substrate temperature. The

orientation of IBAD YSZ films deposited on (100) and (111) YSZ substrates by dual ion beam deposition without active substrate heating was shown to be substrate-independent. The YSZ film deposited on the (110) YSZ substrate exhibited two in-plane orientations, one of which corresponded to the conventional YSZ orientation and the other which corresponded to a coincident site lattice between the (200) film and (110) substrate. XRD and TEM indicated that the IBAD YSZ grains gradually eliminated CSL grains throughout deposition. The IBAD film orientations at low substrate temperature were consistent with continual granular renucleation during film growth.

Epitaxial YSZ films were deposited on (100), (110), and (111) YSZ substrates by dual ion beam deposition at 600°C. The nucleation bias of the single crystal substrates predominates the texturing effect of the assisting ion beam at elevated substrate temperature. This result was attributed to enhanced surface diffusion, granular epitaxy, and grain boundary mobility at higher substrate temperature.

CHAPTER 9
CONCLUSIONS AND FUTURE WORK

9.1 CONCLUSIONS

IBAD biaxial alignment develops due to anisotropy of ion induced damage on various crystal surfaces. The two in-plane orientations of (200) biaxially aligned YSZ films fabricated by both ion assisted electron beam evaporation and dual ion beam deposition were combined in a field plot of ion to molecule arrival ratio versus ion bombardment angle. (110) planes are more damage tolerant at low r values while (111) planes are more damage tolerant at high r values. The data of Iijima *et al.*[3-8] and Arendt *et al.*[9-12] are consistent with the field plot. The observed IBAD YSZ and IBAD LCMO biaxial alignment does not occur due to ion channeling.

Preferred normal alignment and random in-plane orientation was observed in control films sputtered and evaporated without ion assist. Such out-of-plane orientation is frequently observed in vapor deposited films and is thought to arise from surface energy minimization. Ion bombardment at off-normal incidence fixes the in-plane film orientation through ion damage minimization, thereby establishing biaxial alignment. IBAD biaxial alignment occurs so that damage tolerant planes face the assisting ion beam. The growth direction of misaligned grains changes is discrete units corresponding to the introduction of low angle grain boundaries and special boundaries in the crystal. The introduction of the low angle boundaries correspond to those growth directions with larger amounts of ion induced damage. The growth direction change occurs with highest frequency for misaligned grains and with lowest frequency for damage tolerant planes.

The accumulation of defects and sufficiently high aggregation rates to form low angle grain boundaries over a assembly of initially random nuclei will eventually create a

population of biaxially aligned grains with damage-tolerant surfaces facing the assisting ion beam. The length scale over which biaxial alignment is established will depend on

1. the relative damage tolerance of different crystal planes
2. the deposition rate relative to the defect introduction rate
3. the nucleation density and island orientation
4. the rate at which defects are annealed by atom mobility

(110) planes are more damage tolerant at low r values while (111) planes are more damage tolerant at high r values. The defect incorporation rate is proportional to the r value. The depth over which ion damage is introduced depends on the ion bombardment angle and the ion energy. The introduction of the low angle boundaries corresponded to those growth directions with larger amounts of ion induced damage. Growth direction change occurred with highest frequency for misaligned grains and with lowest frequency for damage tolerant planes.

The substrate temperature determined the IBAD film growth mode and the effectiveness of the substrate nucleation bias. IBAD film growth occurs by renucleation at low temperature. Substrate-independent biaxial alignment is observed in films fabricated without active substrate heating. High nucleation densities at low temperature favor the stochastic processes that form film texture and reduces the substrate orientation bias on the film. Low atom and grain boundary mobility prevent ion induced damage annealing and facilitate growth direction change. Localized discrete growth direction changes occur throughout deposition, even when damage tolerant planes face the assisting ion beam.

IBAD film growth occurs through growth rate competition at elevated substrate temperatures. The substrate nucleation bias persists through film deposition due to increased atom and grain boundary mobility. The nucleation bias from a single crystal substrate exceeds the ion beam texturing bias at elevated substrate temperature, and epitaxial growth occurs. Enhanced grain boundary mobility at elevated substrate temperature enables granular tilting to orient damage tolerant planes toward the assisting ion beam on nonepitaxial substrates. Fewer growth direction changes occur at elevated temperature after damage tolerant planes have been favorably oriented.

9.2 FUTURE WORK

IBAD biaxial alignment occurs so that damage tolerant planes face the assisting ion beam. The introduction of damage is necessary for the growth direction changes to occur that lead to IBAD biaxial alignment. It is desirable to achieve biaxial alignment within the shortest film thickness. It is also desirable that the uppermost portion of the IBAD film is crystallographically suitable for subsequent film deposition. Achieving biaxial alignment within a short length scale means a great deal of ion damage must be incorporated in the film to facilitate growth direction changes. The resulting high defect density is not suitable for subsequent film fabrication. It appears that IBAD fabrication should take place with two sets of r values. The initial portion of the film should be fabricated with a relatively high r value until biaxial alignment is established. The defect introduction rate should be decreased for the second portion of the film to make it a suitable crystallographic buffer layer while maintaining the orientation beneath.

The effect of r value on in-plane mosaic spread has not been established. The r value dependence is not obvious, as shown in the dual ion beam deposition work in Section 5.3.1.2. This dependence should be further investigated to establish the r value necessary to establish biaxial alignment over a short length scale. Subsequent work should focus in the minimum r value necessary to maintain the biaxial alignment with increased film thickness while decreasing the defect density in the uppermost IBAD film.

The field plots in Figs. 7.2 and 7.3 demonstrate that the same IBAD biaxial alignment mechanism is operative for ion assisted electron beam evaporation and dual ion beam deposition for both IBAD film growth modes. Commercial realization of long length coated conductors depends on the deposition rate of the IBAD YSZ film. Three IBAD technologies are being considered for coated conductor fabrication: ion assisted electron beam evaporation, dual ion beam deposition, and ion assisted pulsed laser deposition. The best aligned IBAD YSZ films have been fabricated by dual ion beam deposition. Ion assisted electron beam evaporation, however, has intrinsic advantages over both dual ion beam deposition and ion assisted pulsed laser ablation.

YSZ deposition rates of 100Å/s are attainable by both electron beam evaporation and pulsed laser ablation. Deposition rates greater than 0.5Å/s are difficult to achieve by sputtering. There are commercially available 1m long linear ion sources that can generate low energy ion fluences as high as $3mA/cm^2$. R values in the range examined in this work could therefore be realized while evaporating at 100Å/s. The assisting ion source is not a limiting factor in long length IBAD YSZ fabrication. The deposition rate and the spot size over which YSZ is deposited determine throughput. Ion assisted electron beam evaporation can generate a plume over the entire 1m tape length above a linear ion source. The sputtered YSZ plume width is proportional the sputtering ion source diameter. The spot size for pulsed laser ablation is approximately 2.5cm.

Consider continuous fabrication of 6000Å thick YSZ on a Hastelloy ribbon by the three IBAD techniques. Assume a 12cm sputtering ion source is used for dual ion beam deposition and that the resulting spot size over which 0.5Å/s deposition rate can be maintained is 12cm. The throughput that can be achieved by the three techniques is 1.4km/day by ion assisted electron beam evaporation, 36m/day by ion assisted pulsed laser ablation, and 1m/day by dual ion beam deposition. Ion assisted electron beam evaporation is clearly the most suitable technique for long length fabrication, yet it has received the least research attention of the three techniques. Future work should focus on fabricating (200) biaxially aligned YSZ films at higher deposition rates using ion assisted electron beam evaporation.

APPENDIX A: INTERATOMIC POTENTIAL CALCULATION

The interaction energy ϕ_{ij} of an individual ion is calculated in ADESH using the equation

$$\phi_{ij} = \frac{55.3}{r_{ij}^{3.2}} \pm \frac{Z_i Z_j e^2}{r_{ij}}. \qquad \text{(A-1)}$$

Calculating the interaction energy using equation A-1 of a Zr^{4+} is as follows. The interatomic distances between the ion of interest and all of the ions within 4Å are determined and the surrounding ions are ranked in order of increasing interatomic distance. The following list is obtained when considering a Zr^{4+} ion in an ideal zirconia lattice.

Ion	Distance (Å)
Central Zr^{4+}	0
Eight O^{2-}	2.224
Twelve Zr^{4+}	3.632

The largest electrically neutral subset of these ions, including the charge of the central Zr^{4+}, consists of the central Zr ion, eight oxygen ions, and three second nearest neighbor Zr^{4+}. The interaction potential for the central Zr^{4+} is therefore calculated as shown in the table below. Each pair of interactions is counted twice in the cumulative energy total. The interaction energy of an individual ion is obtained by dividing this value by two.

Ion	$\frac{55.3}{r_{ij}^{3.2}}$ (eV)	$\frac{Z_i Z_j e^2}{r_{ij}}$ (eV)	ϕ_{ij}	Number of Ions	Interaction Energy (eV)
O^{2-}	4.3	-51.8	-47.5	8	-380.1
Zr^{4+}	0.9	63.4	64.3	3	193.0
Cumulative Energy					-187.1
$\phi_{Zr^{4+}}$					-93.6

APPENDIX B: BULK MODULUS DETERMINATION

Following the treatment in Dieter[86], the elastic strain energy U_o for a general three-dimensional stress distribution is given by

$$U_o = \frac{1}{2}\left(\sigma_x\varepsilon_x + \sigma_y\varepsilon_y + \sigma_z\varepsilon_z + \tau_{xy}\gamma_{xy} + \tau_{xz}\gamma_{xz} + \tau_{yz}\gamma_{yz}\right) \tag{B-1}$$

where σ_i are tensile stresses, ε_i are tensile strains, τ_{ij} are shear stresses and γ_{ij} are shear strains. For hydrostatic strain the shear stress and shear strains are zero, $\sigma = \sigma_x = \sigma_y = \sigma_z$, and $\varepsilon = \varepsilon_x = \varepsilon_y = \varepsilon_z$. Therefore, the elastic strain energy is

$$U_o = \frac{3}{2}\sigma\varepsilon. \tag{B-2}$$

Hooke's law may be used to relate the hydrostatic strain to σ, Young's modulus E, and Poisson's ratio ν as

$$\varepsilon = \frac{\sigma}{E}(1-2\nu). \tag{B-3}$$

Rearranging yields

$$\sigma = \frac{\varepsilon E}{(1-2\nu)}. \tag{B-4}$$

The elastic strain energy can be expressed after substituting equation B-4 into equation B-2 as

$$U_o = \frac{3}{2}\left(\frac{\varepsilon^2 E}{1-2\nu}\right). \tag{B-5}$$

Bulk modulus K is defined as the ratio of hydrostatic pressure to the dilatation that it produces. It can be expressed in terms of hydrostatic stress σ and volume strain Δ as

$$K = \frac{\sigma}{\Delta}. \tag{B-6}$$

Volume strain is related to Young's modulus, Poisson's ratio and hydrostatic stress by

$$\Delta = \left(\frac{1-2\nu}{E}\right)3\sigma. \tag{B-7}$$

Therefore bulk modulus may be reexpressed as

$$K = \frac{E}{3(1-2\nu)}. \tag{B-8}$$

Equation B-5 is equivalent to

$$U_o = \frac{9}{2}\varepsilon^2\left(\frac{E}{3(1-2\nu)}\right). \tag{B-9}$$

Substituting equation B-8 into B-9 related elastic strain energy to bulk modulus as

$$U_o = \frac{9}{2}\varepsilon^2 K. \tag{B-10}$$

Rearranging equation B-10 results in

$$U_o = \left(\frac{K}{2}\right)(3\varepsilon)^2. \tag{B-11}$$

The volume change under hydrostatic strain $\frac{\Delta V}{V}$ is equal to 3ε. Therefore,

$$U_o = \left(\frac{K}{2}\right)\left(\frac{\Delta V}{V}\right)^2 \tag{B-12}$$

or

$$K = \frac{2U_o}{\left(\frac{\Delta V}{V}\right)^2}. \tag{B-13}$$

Equation B-13 was used to calculate the zirconia bulk modulus based on the strain energy increase for an imposed hydrostatic strain of 1%. $\frac{\Delta V}{V}$ was therefore equal to 0.03. A cubic computational cell containing 32 molecules of ZrO_2 was considered. Periodic boundary conditions were maintained along all the x, y, and z directions. The imposed 1% hydrostatic strain resulted in a strain energy increase of 0.018 eV/molecule.

There are four ZrO_2 molecules in a unit cell. Assuming a lattice parameter of 5.137Å, the volume of a ZrO_2 molecule is 33.9Å^3. The strain energy density U_o is therefore $5.3\text{x}10^{-4}$ eV/Å^3. Using this strain energy density and 0.03 for $\frac{\Delta V}{V}$ in equation B-13 yields a calculated bulk modulus of 189 GPa.

BIBLIOGRAPHY

1. L.S. Yu, J.M.E. Harper, J.J. Cuomo, and D.A. Smith, J. Vac. Sci. Technol. A **4**, 443 (1986).

2. L.S. Yu, J.M.E. Harper, J.J. Cuomo, and D.A. Smith, Appl. Phys. Lett. **47** [9], 932 (1985).

3. Y. Iijima, N. Tanabe, and O. Kohno, 4th International Symposium on Superconductivity, Oct. 14-17, 1991, Tokyo, Japan, edited by H. Hayakawa and N. Koshizula (Springer, Berlin) 517 (1991).

4. Y. Iijima, N. Tanabe, O. Kohno, and Y. Ikeno, Appl. Phys. Lett. **60** 769 (1992).

5. S. Aoki, T. Yamaguchi, Y. Iijima, O. Kohno, S. Nagaya, and T. Inoue, presented at Applied Superconductivity Conference, Chicago, August 24, 1992.

6. Y. Iijima, K. Onabe, N. Futaki, N. Tanabe, N. Sadakara, O. Kohno, and Y. Ikeno, IEEE Trans. Applied Superconductivity **3** 1510 (1993).

7. Y. Iijima, K. Onabe, N. Futaki, N. Sadakata, and O. Kohno, J. Appl. Phys. **74** 1905 (1993).

8. O. Kohno, Y. Iijima, K. Onabe, N. Tanabe, N. Sadakata, T. Saito, J. Yoshitomi, and S. Nagaya, 1995 International Workshop on Superconductivity Co-Sponsored by ISTEC and MRS, June 18-21, 1995, Maui, Hawaii, 210 (1995).

9. P.N. Arendt, S.R. Foltyn, X.D. Wu, J. Townsend, C. Adams, M. Hawley, P. Tiwari, M. Maley, J. Willis, D. Moseley, and Y. Coulter, Mater. Res. Soc. Symp. Proc. **341** 209 (1994).

10. S.R. Foltyn, P. Tiwari, R.C. Dye, M.Q. Le, and X.D. Wu, Appl. Phys. Lett. **63** 1848 (1993).

11. X.D. Wu, S.R. Foltyn, P. Arendt, J. Townsend, C. Adams, I.H. Campbell, P. Tiwari, Y. Coulter, and D.E. Peterson, Appl. Phys. Lett. **65** [15] 1961 (1994).

12. S.R. Foltyn, P.N. Arendt, X.D. Wu, W.R. Blumenthal, J.D. Cotton, J.Y. Coulter, W.L. Hults, H.F. Safar, J.L. Smith, and D.E. Peterson, 1995 International Workshop on Superconductivity Co-Sponsored by ISTEC and MRS, June 18-21, 1995, Maui, Hawaii, 105 (1995).

13. R.P. Reade, P. Berdahl, R.E. Russo, and S.M. Garrison, Appl. Phys. Lett. **61** [18] 2231 (1992).

14. S. Aoki, M. Fukutomi, K. Komori, and H. Maeda, J. Vac. Sci. Technol. A **12** [2], 501 (1994).

15. M. Fukutomi, S. Aoki, K. Komori, Y. Tanaka, T. Asano, and H. Maeda, Thin Solid Films **239,** 123 (1994).

16. R. Chatterjee, M. Fukutomi, S. Aoki, K. Togano, and H. Maeda, Appl. Phys. Lett. **65** [1], 109 (1994).

17. M. Fukutomi, S. Aoki, K. Komori, R. Chatterjee, and H. Maeda, Physica C **219,** 333 (1994).

18. R. Chatterjee, S. Aoki, M. Fukutomi, K. Komori, K. Togano, and H. Maeda, Physica C **224,** 286 (1994).

19. M. Fukutomi, S. Aoki, K. Komori, R. Chatterjee, K. Togano, and H. Maeda, Physica C **231,** 113 (1994).

20. N. Sonnenberg, A.S. Longo, M.J. Cima, B.P. Chang, K.G. Ressler, P.C. McIntyre, and Y.P. Liu, J. Appl. Phys. **74,** 1027 (1993).

21. K.G. Ressler, N. Sonnenberg, and M.J. Cima, Mater. Res. Soc. Symp. Proc. **316,** 953 (1993).

22. N. Sonnenberg, K.G. Ressler, P.C. McIntyre, and M.J. Cima, Mater. Res. Soc. Symp. Proc. **341,** 163 (1994).

23. K.G. Ressler, N. Sonnenberg, and M.J. Cima, J. Electron. Mater. **25** [1], 35 (1996).

24. P.C. McIntyre, K.G. Ressler, N. Sonnenberg, and M.J. Cima, J. Vac. Sci. Technol. A **14** [1], 210 (1996).

25. D.R. McKenzie, D.J.H. Cockayne, M.G. Sceats, P.J. Martin, W.G. Sainty, and R.P. Netterfield, J. Mater. Sci. **22** 3725 (1987).

26. C.R.M. Grovenor, H.T.G. Hentzell, and D.A. Smith, Acta Metall. **32** [5], 773 (1984).

27. B.A. Movchan and A.V. Demchishin, Phys. Met. Metallogr. **28,** 83 (1969).

28. J.A. Thornton, Ann. Rev. Mater. Sci. 7, 239 (1977).

29. D.A. Smith, in Structure and Properties des Joints Intergranulaires, J. Phys. **C6** (1982).

30. D.A. Smith and A. Ibrahim, Mater. Res. Soc. Symp. Proc. **317**, 401 (1994).

31. J.M. Nieuwenhuizen and H.B. Haanstra, Philips Tech. Rev. **27**, 87 (1966).

32. C.V. Thompson and R. Carel, Mater. Sci. Eng. **B32**, 211 (1995).

33. M. Volmer and A. Weber, Z. Phys. Chem. **119**, 277 (1925).

34. C.A. Neugebauer, in Handbook of Thin Film Technology, edited by L.I. Maissel and R. Glang (McGraw-Hill, New York, 1970) pp. 8-3 - 8-44.

35. A. van der Drift, Philips Res. Repts **22**, 267 (1967).

36. K.P. Fahey, B.M. Clemens, L.A. Wills, Appl. Phys. Lett. **67** [17], 2480 (1995).

37. O.P. Karpenko, M. Vill, S.G. Malhotra, J.C. Bilello, and S.M. Yalisove, Mater. Res. Soc. Symp. Proc. **317**, 467 (1994).

38. H. Windischmann, Critical Review in Solid State and Materials Science, **17** [6], 547 (1992).

39. M. Zaouali, J.L. Lebrun, and Z. Gergaud, Surface Coatings Technology, **50**, 5 (1991).

40. H.E. Roosendaal, in Topic in Applied Physics, edited by R. Behrisch (Springer, Berline, 1981).

41. R.M. Bradley, in Handbook of Ion Beam Processing Technology, edited by J.J. Cuomo, S.M. Rossnagel, and H.R. Kaufman (Noyes, Park Ridge, NJ, 1989).

42. W. Ensinger, Nucl. Instr. and Meth. in Phys. Res. B **106**, 142 (1995).

43. Corning, Inc., Corning, NY.

44. Corning, Inc., Corning, NY.

45. Haynes International, Windsor, CT.

46. Silicon Sense, Inc., Nashua, NH.

47. Commercial Crystal Laboratories, Inc., Naples, FL.

48. South Bay Technology, Inc., San Clemente, CA.

49. 3M Corporation, Minneapolis, MN.

50. SPI Supplies, West Chester, PA.

51. Temescal, Berkeley, CA.

52. Tosoh Corp., Tokyo, Japan.

53. Ion Tech, Inc., Ft. Collins, CO.

54. Union Carbide, Advanced Ceramics, Cleveland, OH.

55. Omega Engineering, Inc., Stamford, CT.

56. Sycon Instruments, Syracuse, NY.

57. Beckman Instruments Inc., Wakefield, MA.

58. R. Swanepoel, J. Phys. E **16**, 1213 (1983).

59. Commonwealth Scientific Co., Alexandria, VA.

60. Rigaku/USA, Danvers, MA.

61. Hitachi Instruments Inc., Japan.

62. JEOL USA Inc., Peabody, MA.

63. Topcon America Corp., Pleasanton, CA.

64. W.A. Tiller, in The Science of Crystallization: Macroscopic Phenomena and Defect Generation (Cambridge University Press, Cambridge, UK, 1991) pp. 301-302.

65. M. McCormack, S. Jin, T.H. Tiefel, R.M. Fleming, J.M. Phillips, and R. Ramesh, Appl. Phys. Lett. **64** [22], 3045 (1994).

66. CASA Engineering, Hopewell Junction, NY.

67. J.F. Zieglar and J.P. Biersack, in The Stopping and Range of Ions in Solids, (Pergamon Press, New York, 1985).

68. H.G. Scott, J. Mater. Sci. **10**, 1527 (1975).

69. Joint Committee on Powder Diffraction Standards (JCPDS) International Centre

for Diffraction Data, Swarthmore, PA.

70. JCPDS Powder Diffraction File Sets 29-30, (JCPDS International Centre for Diffraction Data, Swarthmore, PA, 1987) p. 1056..

71. H. Horiuchi, A.J. Schultz, P.C.W. Leung, and J.M. Williams, Acta. Cryst. B **40** 367 (1984).

72. C. Kittel, in Introduction to Solid State Physics, sixth edition (John Wiley & Sons, New York, 1986) pp.64-70.

73. P.J. Lawrence, S.C. Parker, and P.W. Tasker, Advances in Ceramics **23**, (1987) pp..

74. Janaf Thermochemical Tables Part II, Cr-Zr, Third Edition, Edited by M.W. Chase, Jr., C.A. Davies, J.R. Downey, Jr., D.J. Frurip, R.A. McDonald, and A.N. Syverud (1985) p.1850.

75. Janaf Thermochemical Tables Part II, Cr-Zr, Third Edition, Edited by M.W. Chase, Jr., C.A. Davies, J.R. Downey, Jr., D.J. Frurip, R.A. McDonald, and A.N. Syverud (1985) p.1639.

76. N.N. Greenwood, Ionic Crystals Lattice Defects and Nonstoichiometry (Butterworths, London 1968) p.183.

77. N.N. Greenwood, Ionic Crystals Lattice Defects and Nonstoichiometry (Butterworths, London 1968) p.12.

78. G. Samsonov, in The Oxide Handbook, second edition (IFI/Prenum Data Company, New York, 1982) p. 84.

79. N. Mizutani and M. Kato, Uechida Rokakuho **2**, 27 (1984).

80. R.P. Ingel, Ph.D. thesis, Catholic University, Washington, DC, 1982.

81. W. Eckstein, Computer Simulation of Ion-Solid Interactions (Springer-Verlag, Berlin 1991) p. 79.

82. P. Sigmund, in Sputtering by Particle Bombardment I, edited by R. Behrisch (Springer-Verlag, Berlin, 1981) pp. 9-71.

83. R.D. Shannon, Acta Cryst. A **32**, 751 (1976).

84. A. Benninghoven, F.G. Rudenauer, and H.W. Werner, in Secondary Ion Mass Spectrometry, (John Wiley and Sons, Inc., New York, 1987) p. 213.

85. J.M. Rigsbee, in Surface Modification Engineering Volume I: Fundamental Aspects, edited by R. Kossowsky (CRC Press, Boca Raton, FL, 1989) p. 247.

86. G.E. Dieter, Mechanical Metallurgy, Second Edition, (McGraw-Hill, New York, 1976) pp. 49-55.